Summer 8-7-2024

Modular approach to soft mobile robots

Dimuthu Kodippili Arachchige
DePaul University, darachch@depaul.edu

MODULAR APPROACH TO SOFT MOBILE ROBOTS

BY

Dimuthu Dharshana Kodippili Arachchige

A dissertation submitted to the School of Computing, Jarvis College of Computing and Digital Media of DePaul University in partial fulfilment of the requirement for the degree
of
Doctor of Philosophy

DePaul University
Chicago, Illinois

2024

DePaul University
Jarvis College of Computing and Digital Media

Dissertation Verification

This doctoral dissertation has been read and approved by the dissertation committee below according to the requirements of the Computer and Information Systems PhD program and DePaul University.

Name: Dimuthu Dharshana Kodippili Arachchige

Title of dissertation:

MODULAR APPROACH TO SOFT MOBILE ROBOTS

Date of Dissertation Defense:

August 07, 2024

Iyad Kanj, Ph.D., DePaul University
Dissertation Advisor*

Isuru Godage, Ph.D., Texas A&M University
Dissertation Co-advisor

Ljubomir Perkovic, Ph.D., DePaul University
1st Reader

Umer Huzaifa, Ph.D., DePaul University
2nd Reader

Yue Chen, Ph.D., Georgia Institute of Technology
3rd Reader

** A copy of this form has been signed, but may only be viewed after submission and approval of FERPA request letter.*

Abstract

Soft robot locomotion is a highly promising but under-researched subfield within the field of soft robotics. The compliant limbs and bodies of soft robots offer numerous benefits, including the ability to regulate impacts, tolerate falls, and navigate through tight spaces. These robots have the potential to be used for various applications, such as search and rescue, inspection, surveillance, and more. The state-of-the-art still faces many challenges, including limited degrees of freedom, a lack of diversity in gait trajectories, insufficient limb dexterity, limited payload capabilities, lack of control methods, etc. To address these challenges, this research introduces a modular approach to designing, modeling, validating, and controlling of soft mobile robots. The modular design philosophy aims at simplifying the robot construction and improving its reliability by focusing on designing and developing simpler soft robotic units. The research is conducted in two phases; (i) designing and fabricating modular soft mobile robots with different topologies and validating their fundamental locomotion gaits, and (ii) enhancing their locomotion capabilities through effective control strategies, i.e., closed-loop control.

During phase (i), inspired by spider monkeys' tails, a novel hybrid soft module is proposed. The soft module powered by pneumatics has an improved stiffness controllable range, and independent stiffness and shape control capabilities. As the first topology, soft modules are serially arranged to build soft robotic snakes (SRSs) that are wheelless, relying solely on spatial bending to achieve their movements. A kinematic model of the SRS is derived to achieve snake locomotion trajectories, namely sidewinding, serpentine, planar rolling, helical rolling, and curved surface locomotion. This is a significant improvement over the previous designs, which were either limited to planar movements or relied on wheels for locomotion. Additionally, a complete spatial dynamic model for the SRSs is proposed and experimentally validated. As the second topology, four soft modules are arranged in parallel to fabricate a soft-limbed robot that can mimic pinniped locomotion. A complete floating-base kinematic model of the proposed robot is derived to generate and experimentally validate a variety of

locomotion gaits including a novel energy-efficient locomotion mode called "tumbling". As the third topology, five soft modules are arranged serially and in parallel to fabricate a soft quadrupedal robot. Parameterized quadrupedal trajectories for crawling and trotting locomotion are derived utilizing the kinematic model of the robot. In crawling, gait models are derived to predict locomotion effectiveness, and experimental results confirm their prediction accuracy. A physics-enabled quadruped dynamic model is utilized to optimize and validate trotting locomotion trajectories. This modular approach provides a promising solution to the challenge of building high-dimensional soft robots capable of complex locomotion gaits and offers exciting possibilities for future research.

During phase (ii), closed-loop feedback control schemes are implemented to effectively manage the locomotion. Feedback control in mobile robots is important since it can track locomotion and perform dynamic locomotion adjustments necessary in real-world applications. Wireless sensors are integrated to measure the deformation of the SRS body and the quadruped limbs. The measured trajectory parameters are compared and adjusted in real-time using a Jacobian-based kinematic control system to match the intended locomotion trajectories. The results demonstrate that closed-loop controlled locomotion trajectories outperformed the previously tested open-loop control trajectories, significantly enhancing locomotion for field applications.

Keywords: Control, dynamics, kinematics, locomotion, modeling and validation, soft robots

Acknowledgments

First and foremost, I am profoundly grateful to my doctoral advisor, Dr. Iyad Kanj, DePaul University, and the co-advisor, Dr. Isuru Godage, Texas A&M University whose expertise, encouragement, and commitment to excellence have been a constant source of inspiration. Your invaluable guidance has shaped not only the trajectory of this research but also my growth as a scholar. Further, I would like to express my appreciation to the members of my dissertation committee, Dr. Ljubomir Perkovic, DePaul University, Dr. Umer Huzaifa, DePaul University, and Dr. Yue Chen, Georgia Institute of Technology, for their insightful feedback and constructive criticism throughout the research process. Their collective expertise has significantly enriched the quality of this work.

I am indebted to the Jarvis College of Computing and Digital Media, School of Computing, DePaul University, for their financial support through the Computing and Digital Media Award for doctoral studies. Additionally, I am grateful to the National Science Foundation for its research grants: IIS-2008797, CMMI-2048142, CMMI-2133019, & CMMI-2132994, and DePaul University Academic Growth Initiative Fund: 602034, which played a crucial role in funding the research work. Their investments have allowed me to pursue this endeavor with dedication and focus.

I am thankful to my lab colleagues and fellow researchers who have provided a stimulating academic environment. The exchange of ideas and collaborative spirit have been essential in shaping the intellectual foundation of this thesis. Special thanks go to my family for their unwavering support, understanding, and encouragement. I am particularly grateful to my wife, Sayuri, whose love, patience, and unwavering belief in me have been my anchor. Her sacrifices and encouragement have made this journey possible, and I am truly fortunate to have her by my side. In conclusion, I recognize and appreciate the diverse contributions of all those who have played a role, no matter how small, in the completion of this doctoral thesis. Your support has been invaluable, and I am sincerely grateful.

Contents

List of Tables

List of Figures

Publication and Content Disclaimer

Parts of the content in this dissertation have been published or are under consideration for publication as listed in Section 1.7 of Chapter 1.

Supplementary materials related to this dissertation, including codes and multimedia files that demonstrate the implementation and experimental results, are available in the GitHub repository: github.com/DimuthuDKA/PhDThesis.

Chapter 1

Introduction

1.1 Background

Soft robots are designed using pliable materials such as silicone or rubber, setting them apart from traditional robots constructed from rigid components like metal or plastic [1]. This distinct composition allows soft robots to adapt and mold to their surroundings, positioning them as ideal candidates for tasks where conventional robots may falter. Soft Robotics emerges as an interdisciplinary field, intersecting with material science, actuator and sensor technology, design and fabrication techniques, control and modeling strategies, along with studies in locomotion, manipulation, bioinspiration, and biomechanics [2]. Within this broad domain, soft robotic locomotion represents a specialized area of study focused on the innovative movement and navigation capabilities of soft robots [3]. Researchers are actively developing diverse soft robotic locomotion systems, seeking novel design and control approaches to enhance these robots' mobility. This endeavor aims to transition soft robots from the confines of laboratory research to practical, real-world applications [4]–[6]. The advent of soft robotic locomotion holds the promise of transforming the robotics field by enabling the execution of tasks previously deemed challenging or unattainable for standard mobile robots.

1.2 Motivation for Soft Mobile Robots

Soft mobile robots have a wide range of potential applications due to their unique capabilities, including flexibility, adaptability, safety, and the ability to move through challenging environments. Some of the

most promising applications of soft mobile robots include, exploration, agriculture, and manufacturing [7]. They can be used to explore challenging and hazardous environments, such as space, deep oceans, and disaster zones, where traditional robots and humans may face difficulties or danger [8]. For example, soft mobile robots could be designed to crawl through narrow passages, squeeze through small openings, and navigate uneven terrains [9]. Soft locomotive systems that have a small cross-section-to-length ratio such as soft robotic snakes, soft eel robots, etc., could be used to inspect and repair pipelines or other infrastructure in hazards (e.g. radioactive environments) or hard-to-reach locations [10].

Furthermore, soft locomotive systems can be used in a variety of ways in planetary exploration [11]. Traditional robotic exploration systems, such as rovers, face limitations in their ability to traverse rough terrains, and often require complex and expensive control systems. Soft robots, on the other hand, can use their deformable and adaptable bodies to move through environments that are difficult for traditional robots to navigate, such as caves, steep slopes, and rocky terrain [12]. Additionally, they can be designed to be lightweight and portable, making them easier and cheaper to transport to remote locations [13]. They can also be used to collect samples or perform other tasks that require a gentle touch, such as studying fragile ecosystems or conducting archaeological excavations.

Soft mobile robots have the potential to revolutionize farming practices by performing tasks such as harvesting, pruning, and plant inspection [14]. Their soft and delicate touch can help avoid damaging crops and reduce waste, and their adaptability allows them to adjust to different crop types and sizes [15]. More importantly, they can be used in manufacturing settings to perform tasks such as assembly, packaging, and quality control. Their flexibility and adaptability make them safe collaborative robots that can be employed with humans [16]. Therein, they are ideal for handling delicate and irregularly shaped objects, reducing the need for specialized machinery.

Despite this highly promising potential, soft robot locomotion is an under-researched subfield within the field of soft robotics. The state-of-the-art still faces many challenges, including limited degrees of freedom, a lack of diversity in gait trajectories, insufficient limb dexterity, limited payload capabilities, lack of control methods, etc.

1.3 Research Objectives

The core objective of this research is to **introduce a framework to systematically address the design, fabrication, modeling, locomotion trajectory generation, and control challenges of soft mobile robots**. To achieve this goal, a modular approach to soft mobile robots is proposed, which includes two phases of research activities:

i Designing and fabricating modular soft mobile robots at different topologies and validating their fundamental locomotion gaits.

ii Enhancing locomotion capabilities of the proposed robot topologies by implementing effective control strategies (i.e., closed-loop control).

1.4 Dissertation Structure

The structure of this dissertation is outlined as follows:

Chapter 1 introduces the background, motivation, research objectives, dissertation contributions, and research publications. It provides an overview of the dissertation's structure by summarizing the content of each subsequent chapter.

Chapter 2 reviews the literature on soft mobile robots within the scope of the research conducted by the author. Therein, wheelless soft mobile robots that demonstrate terrestrial locomotion are extensively reviewed in terms of types of soft mobile robots, actuation methods, locomotion trajectory generation strategies, modeling approaches, and control methods.

Chapter 3 focuses on the design and fabrication of a novel hybrid soft module and its application towards various soft mobile robot topologies, including a soft robotic snake (SRS), a tetrahedral robot, and a quadrupedal robot.

Chapter 4 presents the modeling of soft module and mobile robot topologies. It covers the kinematic modeling of the soft module and mobile robot topologies and the dynamic modeling of the SRSs. This chapter lays the foundation for trajectory generation discussed in Chapter 5.

Chapter 5 details the methods for generating locomotion trajectories for the proposed mobile robot topologies. This includes the generation of planar and spatial locomotion for SRSs, pinniped and tumbling gaits for the tetrahedral robot, and crawling and trotting gaits for the quadrupedal robot.

Chapter 6 introduces closed-loop control strategies for the SRS and the quadruped robot, including robot modifications to accommodate onboard sensors, Jacobian-based trajectory parameter control, soft module simulation, and prototype studies.

Chapter 7 presents the validation studies of the proposed locomotion trajectories and closed-loop control strategies discussed in the previous chapters. This includes validation in both simulation and experimental environments using simulation models and mobile robot prototypes.

Chapter 8 concludes the dissertation by summarizing each research study undertaken within the dissertation. It outlines the overarching conclusions and proposes directions for future research.

1.5 Dissertation Contributions

The major contributions of this research are summarized as follows:

1. Designing and fabricating a hybrid soft robotic (HSR) module that has a higher stiffness operating range and independent stiffness and pose control capabilities.

2. Proposing a novel 3-section "wheelless" soft robotic snake (SRS), generating locomotion trajectories for serpentine and planar rolling motions, and experimentally validating them on the SRS prototype. This is the first demonstration of planar rolling gaits for SRSs.

3. Designing and fabricating a novel 4-section "wheelless" SRS using HSR modules, generating locomotion trajectories for sidewinding and helical rolling motions, and experimentally validating them on the SRS prototype. This is the first demonstration of helical rolling gaits for SRSs and spatial (3D) locomotion without wheels in SRSs.

4. Presenting a complete spatial dynamic model with contact dynamics for SRSs, evaluating the model in a simulation environment, and validating the model on an SRS prototype for planar and spatial rolling gaits. This is the first validation of a spatial dynamic model for SRSs.

5. Designing and fabricating a novel pinniped robot in tetrahedral shape using HSR modules and validating sophisticated pinniped gaits. The experimental results show that the locomotion speed improvement is 38-fold compared to the state-of-the-art.

6. Proposing an energy-efficient locomotion strategy for soft robots and investigating the energy usage for locomotion. To date, this is the first study on energy estimation in soft-limbed robot locomotion.

7. Designing and fabricating a novel soft-bodied quadrupedal robot using HSR modules, generating locomotion trajectories, and experimentally validating them on the robot prototype. A systematic approach is presented to generate locomotion trajectories and a novel locomotion efficiency modeling technique is proposed.

8. Demonstrating an application of a virtual environment that has realistic Physics properties to obtain efficient dynamic locomotion on the quadruped prototype. To date, this is the fastest tethered/untethered soft-limbed robot that demonstrates dynamically stable trotting gaits using actively bending soft limbs.

9. Integrating onboard sensors and implementing closed-loop control strategies to effectively manage the locomotion of the SRS and the quadruped.

1.6 Media Appearance

The research findings of this dissertation appeared in several media outlets as follows:

- A. Wilkins, **"Robot snake that moves like a sidewinder could inspect sewage pipes,"** in *Newscientist*, Technology, March 15, 2023. Weblink: newscientist.com/article/2364216-robot-snake-that-moves-like-a-sidewinder-could-inspect-sewage-pipes.
- M. Sparkes, **"Watch a weird robot wiggle and flap like a seal moving on land,"** in *Newscientist*, Technology, April 27, 2023, Weblink: newscientist.com/article/2369472-watch-a-weird-robot-wiggle-and-flap-like-a-seal-moving-on-land.
- P. Grad, **"Robotic seal's gait may be graceless, but it could help save lives,"** in *Tech Xplore*, Robotics, April 28, 2023, Webink: techxplore.com/news/2023-04-robotic-gait-graceless.
- A. Paul, **"Seals provided inspiration for a new waddling robot,"** in *Popular Science*, Technology, May 01, 2023, Webink: popsci.com/technology/seal-soft-robot.
- T. Gururaj, **"Researchers reveal a soft-limbed robotic seal inspired by pinnipeds,"** in *Interesting Engineering*, Innovation, May 01, 2023, Webink: interestingengineering.com/innovation/robotic-seal-soft-limbed-robots-soft-robots-robotics.

1.7 List of Research Articles

The research findings of this dissertation contributed to the following journal and conference articles.

- **Peer-reviewed Journal Articles**

  J1. **D. D. Arachchige**, D. M. Perera, S. Mallikarachchi, U. Huzaifa, I. Kanj, and I. S. Godage, "Soft Steps: Exploring Quadrupedal Locomotion with Modular Soft Robots," in *IEEE Access*, vol. 11, pp. 23022–23040, 2023, doi:10.1109/ACCESS.2023.3289156.

  J2. **D. D. Arachchige**, D. M. Perera, U. Huzaifa, I. Kanj, and I. S. Godage, "Tumbling Locomotion of Tetrahedral Soft-limbed Robots," in *IEEE Robotics and Automation Letters (RAL)*, vol. 9, no. 5, pp. 4337-4344, 2024, doi:10.1109/LRA.2024.3375627.

  J3. **D. D. Arachchige**, T. Sheehan, D. M. Perera, S. Mallikarachchi, U. Huzaifa, I. Kanj, and I. S. Godage, "Efficient Trotting of Soft Robotic Quadrupeds," in *IEEE Transactions on Automation Science and Engineering (TASE)*, 2024. [In revision]

- **Journal Articles - In review**

  J4. **D. D. Arachchige**, U. Huzaifa, I. Kanj, and I. S. Godage, "Soft Robotic Snake Locomotion on Curved Surfaces," in *Journal of Soft Robotics (SoRo)*, 2024. [In review]

  J5. **D. D. Arachchige**, I. Kanj, and I. S. Godage, "Terrestrial Soft Mobile Robots: A Review," in *Bioinspiration and Biomimetics*, 2024. [In review]

- **Journal Articles - In preperation**

  J6. **D. D. Arachchige**, D. M. Perera, S. Mallikarachchi, I. Kanj, and I. S. Godage, "Soft Robotic Locomotion: A Musculoskeletal Approach," in *Science Advances Special Issue on Printed and Musculoskeletal Robotics*, 2024. [In preperation]

- **Peer-reviewed Conference Articles**

  C1. **D. D. Arachchige**, Y. Chen, and I. S. Godage, "Soft Robotic Snake Locomotion: Modeling and Experimental Assessment," in *IEEE International Conference on Automation Science and Engineering (CASE)*, Lyon, France, 2021, pp. 805–810, doi:10.1109/CASE49439.2021.9551398.

  C2. **D. D. Arachchige**, Y. Chen, I. D. Walker, and I. S. Godage, "A Novel Variable Stiffness Soft Robotic Gripper," in *IEEE International Conference on Automation Science and Engineering (CASE)*, Lyon, France, 2021, pp. 2222–2227, doi:10.1109/CASE49439.2021.9551616.

  C3. **D. D. Arachchige** and I. S. Godage, "Hybrid Soft Robots Incorporating Soft and Stiff Elements," in *IEEE International Conference on Soft Robotics (RoboSoft)*, London, UK, 2022, pp. 267–272, doi:10.1109/RoboSoft54090.2022.9762183.

  C4. **D. D. Arachchige**, D. M. Perera, S. Mallikarachchi, I. Kanj, Y. Chen, H. Gilbert, and I. S. Godage, "Dynamic Modeling and Validation of Soft Robotic Snake Locomotion," in *IEEE International Conference on Control, Automation and Robotics (ICCAR)*, Beijing, China, 2023, pp. 06–12, doi:10.1109/ICCAR57134.2023.10151763.

  C5. **D. D. Arachchige**, D. M. Perera, S. Mallikarachchi, I. Kanj, Y. Chen, and I. S. Godage, "Wheelless Soft Robotic Snake Locomotion: Study on Sidewinding and Helical Rolling Gaits," in *IEEE Intl. Conference on Soft Robotics (RoboSoft)*, Singapore, 2023, pp. 01–06, doi:10.1109/RoboSoft55895.2023.10121918.

C6. **D. D. Arachchige**, T. Varshney, U. Huzaifa, I. Kanj, T. Nanayakkara, Y. Chen, H. B. Gilbert, and I. S. Godage, "Study on Soft Robotic Pinniped Locomotion," in *IEEE/ASME International Conference on Advanced Intelligent Mechatronics (AIM)*, Seattle, USA, 2023, pp. 65–71, doi:10.1109/AIM46323.2023.10196209.

- **Conference Articles - In preperation**

C7. **D. D. Arachchige**, U. Huzaifa, I. Kanj, and I. S. Godage, "Application of Closed-loop Control for Energy-efficient Locomotion in Soft Robotic Snakes," in *IEEE International Conference on Robotics and Automation (ICRA)*, Atlanta, USA, 2025.

C8. **D. D. Arachchige**, U. Huzaifa, I. Kanj, and I. S. Godage, "Closed-loop Control of Soft Quadrupedal Robots for Discontinuous Gaits," in *IEEE International Conference on Robotics and Automation (ICRA)*, Atlanta, USA, 2025.

- **Co-authored Conference Articles**

C9. B. H. Meng, **D. D. Arachchige**, J. Deng, I. S. Godage, and I. Kanj, "Anticipatory Path Planning for Continuum Arms in Dynamic Environments," in *IEEE International Conference on Robotics and Automation (ICRA)*, Xi'an, China, 2021, pp. 7815–7820, doi:10.1109/ICRA48506.2021.9560952.

C10. A. Amaya, **D. D. Arachchige**, J. Grey, and I. S. Godage, "Evaluation of Human-Robot Teleoperation Interfaces for Soft Robotic Manipulators," in *IEEE International Conference on Robot and Human Interactive Communication (RO-MAN)*, Vancouver, Canada, 2021, pp. 412–417, doi:10.1109/RO-MAN50785.2021.9515508.

C11. D. M. Perera, **D. D. Arachchige**, S. Mallikarachchi, T. Ghafoor, I. Kanj, Y. Chen, and I. S. Godage, "Teleoperation of Soft Modular Robots: Study on Realtime Stability and Gait Control," in *IEEE International Conference on Soft Robotics (RoboSoft)*, Singapore, 2023, pp. 01–07, doi:10.1109/RoboSoft55895.2023.10122121.

C12. U. Huzaifa, **D. D. Arachchige**, M. A. Zaman, and U. Syed, "Simplified Modeling of Hybrid Soft Robots with Constant Stiffness Assumption," in *IEEE International Conference on Robotics and Biomimetics (ROBIO)*, Samui, Thailand, 2023, doi:10.1109/ROBIO58561.2023.10355009.

C13. B. H. Meng, **D. D. Arachchige**, I. Kanj, and I. S. Godage, "Path Planning for Continuum Arms in Dynamic Environments," in *IEEE International Conference on Soft Robotics (RoboSoft)*, San Diego, USA, 2024, doi:10.1109/RoboSoft60065.2024.10521950.

C14. D. M. Perera, N. Byrd, **D. D. Arachchige**, B. Vajipeyajula, K. C. Galloway, and I. S. Godage, "Curve Parametric Modeling of Planar Soft Robots," in *IEEE Intl. Conference on Mechatronics and Automation (ICMA)*, Tianjin, China, 2024. [Accepted and presented, in-press]

C15. S. Mallikarachchi, D. M. Perera, **D. D. Arachchige**, and I. S. Godage, "Design and Control of Portable Soft Robots: An Electromechanical Approach," in *IEEE International Conference on Soft Robotics (RoboSoft)*, Lausanne, Switzerland, 2025. [In preperation]

C16. K. Wang, S. Mallikarachchi, **D. D. Arachchige**, and I. S. Godage, "Body Induced Locomotion of Soft Quadrupedal Robots," in *IEEE International Conference on Soft Robotics (RoboSoft)*, Lausanne, Switzerland, 2025. [In preperation]

Chapter 2

Literature Review

2.1 Soft Mobile Robots

2.1.1 Classification

Soft mobile robots can be classified into three main categories based on their operating environments: terrestrial robots, designed for movement on land; aquatic robots, tailored for underwater environments; and aerial robots, engineered for navigating through the air. Additionally, there are robots capable of navigating in hybrid environments, such as those encompassing land, water, and air. Terrestrial robots can be further subcategorized into wheeled systems – which use wheels as their primary means of locomotion and Wheelless systems – which use various locomotion strategies, such as legged locomotion, snake-like motion, or track-based locomotion. Wheeled terrestrial robots are not suitable for all types of terrain, which has led to the development of wheelless terrestrial robots. These robots are designed for movement on rough or uneven terrain, such as sand, rocks, or steep slopes, where traditional wheeled robots would struggle to operate.

Wheelless systems can be further classified as soft-limbed and soft-limbless (or soft-bodied) robots. Soft-limbed robots are designed to move using legs. Soft-limbless robots are designed without traditional limbs or appendages, instead relying on their soft and compliant bodies to move and manipulate their environment. Figure 2.1 shows an overview of the aforementioned classification.

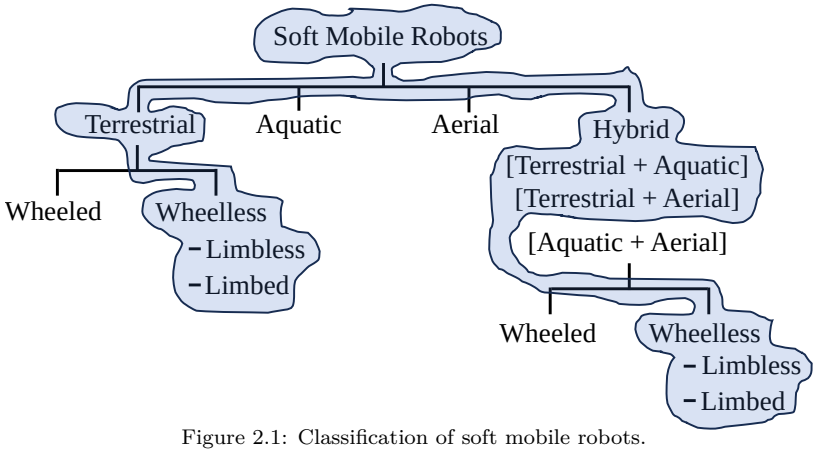

Figure 2.1: Classification of soft mobile robots.

2.1.2 Terrestrial Soft Mobile Robots

In this work, we focus on wheelless soft mobile robots that exhibit terrestrial locomotion, as illustrated in Fig. 2.2. Consequently, our review excludes aquatic, aerial, and hybrid systems lacking the capability for terrestrial movement. We explore robots with various terrestrial locomotion strategies, including jumping and climbing gaits – encompassing branch climbing, tree climbing, rod climbing, and wall climbing, among others. Additionally, we delve into amphibian-inspired robots that demonstrate terrestrial movement, drawing inspiration from creatures such as sea stars (or starfish), walruses, seals (pinnipeds), and others. Soft rolling robots are also covered in this review. Hence, the "wheelless" is referred to as the one that does not have passive or active wheels. In addition to that, robots that locomote in-body environments such as human or animal organs are not discussed here.

Building on the structure presented in Fig. 2.2, this chapter is organized into nine sections. Sec. II and Sec. III categorize the fundamental locomotion methods of wheelless terrestrial soft-limbed and soft-limbless robots, respectively. The actuation technologies of such robots are presented in Sec. IV. Sec. V explores the different modeling approaches and their unique features thereof. The trajectory generation methods are presented in Sec. VI, while the locomotion control methods are examined in Sec. VII.

2.2 Soft-Limbed Robot Locomotion

Soft-limbed robots are a favored subset within soft mobile robotics due to their ability to tackle challenging locomotive tasks. They are classified based on the number and arrangement of limbs

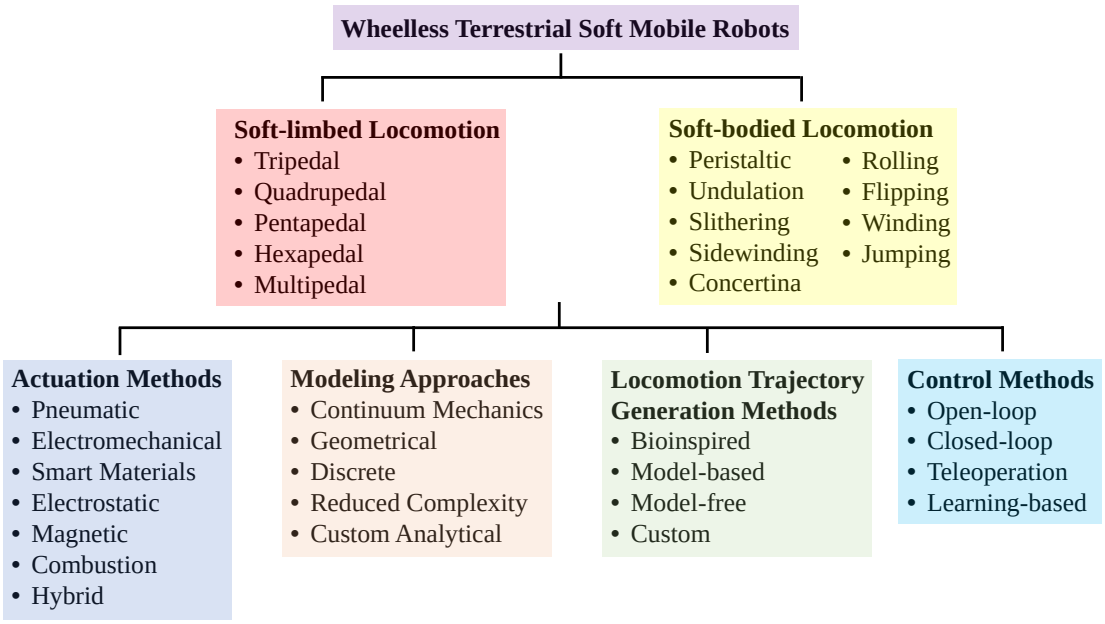

Figure 2.2: Summary of the topics discussed in this review.

into categories such as: i) tripod, ii) quadruped, iii) pentapod, iv) hexapod, and v) multipod robots. Each topology employs various locomotion methods, which are discussed in the following sections. Figures 2.3B and 2.3C show the distribution of soft-limbed robots over the years.

2.2.1 Tripedal Locomotion

Tripodal locomotion involves three legs instead of the typical four or six found in most robots, inspired by animals like spiders, crabs, and tripod fish. This form of locomotion offers certain advantages in specific situations. Several tripodal soft robot prototypes have been proposed. The authors in [17] presented a tripodal robot with tri-symmetrical limbs, operating based on the crawling gaits of a three-leg starfish. The tripod in [18] is a simple foam robot with three serially-arranged straight legs, where the outer two legs are unactuated for stability, and the central leg contracts to move the robot. Modular soft robots with four identical limbs arranged in a spatially symmetric tetrahedral topology (Fig. 2.4A) were proposed in [19]–[22]. These tetrahedral robots use three limbs for movement and one for body support, achieving gaits like steering, forward crawling, backward crawling, in-place turning, crawling-and-turning, and rolling. Additionally, the untethered tripodal robot in [23] demonstrated jumping locomotion using combustion.

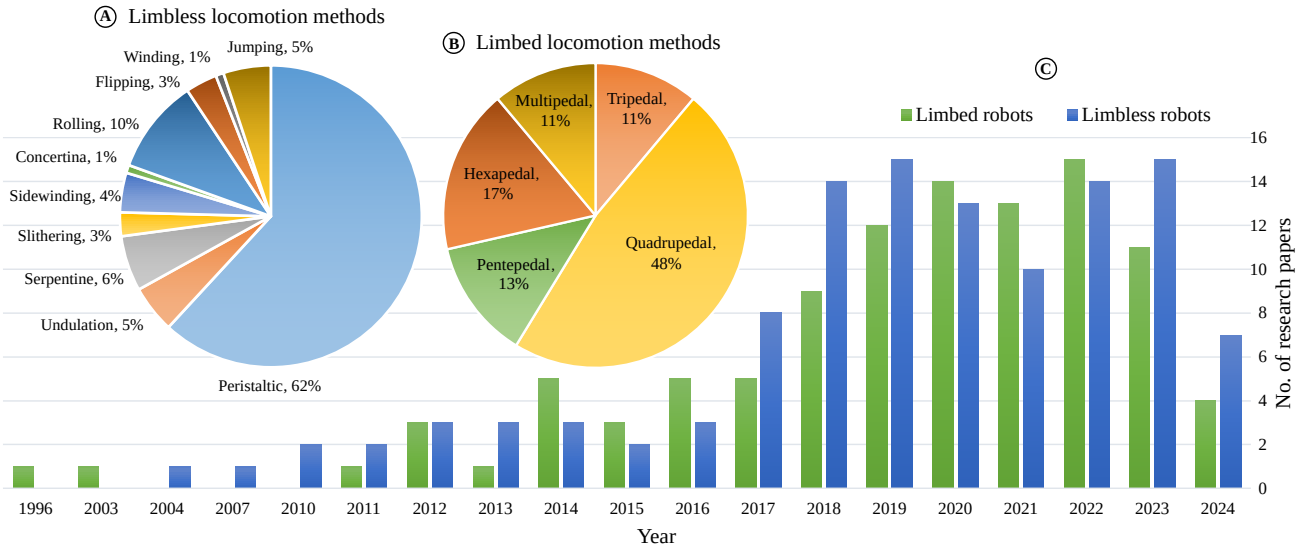

Figure 2.3: Distribution of research papers on soft mobile robots from 1996 to 2024, as considered in this review article.

2.2.2 Quadrupedal Locomotion

Soft quadrupedal robots have four limbs designed to mimic the movement of animals such as dogs and cats. This is a well-explored area within soft-limbed locomotion. These robots often have four soft limbs symmetrically anchored to either end of a rigid body [24]–[36] or a soft body [18], [37]–[45]. In some designs, such as those in [17], [18], [37], [38], [41], [42], the limbs and body are molded together as a single platform. Other prototypes have all limbs anchored to a single point or base [17], [46]–[51]. Based on limb orientation, soft quadrupeds can be categorized into straight limb (limbs under the body like mammals) [52] and flat or overhang limb (limbs out to the side like reptiles) quadrupeds [44].

A majority of flat-limb quadrupeds show crawling [17], [18], [24], [25], [27], [28], [33], [36], [37], [45], [47], [53] as their fundamental mode of locomotion. They achieve this by crawling soft limbs at different phase shifts between diagonal limb pairs [54]. Both straight and flat-limb robots exhibit various locomotion gaits, including walking [18], [26], [29], [31], [33]–[35], [38], [39], [48]–[50], [55]–[57], trotting [24], [39], [58], pacing [32], [58], back-flipping [32], bounding [32], undulation [37], and galloping [40], [58], [59]. Some quadrupeds can climb parallel rods [43], walk on inclined surfaces [18], [39], [41], navigate height obstacles [28], endure harsh environments [38], carry payloads [60], and traverse unstructured terrains [32], [36], [48], [49]. Additionally, some use terrestrial undulation for movement [37], [61]. Readers are referred to Fig. 2.4 for some of the state-of-the-art soft quadrupeds.

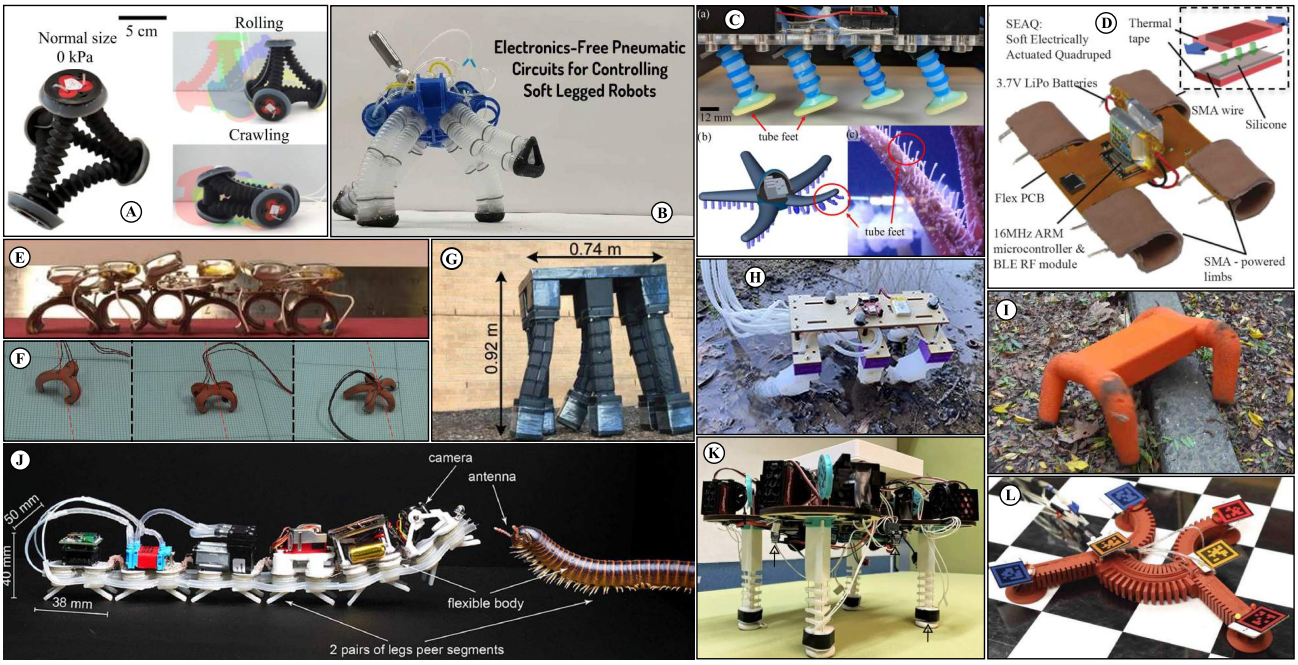

Figure 2.4: State-of-the-art wheelless terrestrial soft-limbed robots – (A) "Tetraflex" tetrahedral robot that replicates multimodal locomotion [62], (B) electronics-free quadruped in [50], (C) sea star-inspired robot that locomotes via active suction in [63], (D) "SEAQ" electrically actuated quadruped in [27], (E) SMA actuated hexapod in [64], (F) SMA actuated triped, quadruped, & pentaped in [17], (G) meter-scale hexapod in [53], (H) "SoRX" hexapod in [65], [66], (I) "Flexipod" motor-driven quadruped in [32], (J) millipede-inspired multiped in [67], (K) tendon-driven quadruped in [31], [35], [68], (L) Gecko-inspired quadruped in [41], [42], [44]. (Reproduced with permission).

2.2.3 Pentapedal Locomotion

Pentapedal robots use five legs for locomotion, offering unique advantages in stability & maneuverability due to their odd number of legs. Various soft robots have been proposed with this topology [17], [69]–[74], featuring soft limbs symmetrically anchored to a single point. The locomotion gaits of these pentapods, inspired by starfish, include crawling and rolling [17], [70], [72], [73]. They achieve continuous motion by repeating limb deformation in sequential patterns. The five-armed actinomorphic robot in [71] uses sequential crawling of its tentacle limbs for locomotion, while the pentapod in [46] moves using undulation.

2.2.4 Hexapedal Locomotion

Hexapod soft robots are popular due to their inherent locomotion stability. These robots have six limbs evenly anchored to a rectangular rigid backbone [53], [63], [65], [66], [75]–[77]. They can achieve omni-directional walking and turning [75], [76], and forward/backward walking gaits [53], [65], [75], [77], with each limb playing a crucial role in maintaining stability. The hexapod in [78] has flat limbs

for crawling locomotion via limb propulsion, while the one in [79] has limbs symmetrically anchored around a circular rigid plate for pushing-based crawling. The sea star-inspired hexapod in [63] moves using active suction, and the meter-scale hexapod in [53] uses a locomotion pattern inspired by an octopus. Some hexapod prototypes can navigate various terrains like stone, grass, sand, mud, and wood [53], [65]. Additionally, [62], [80] proposed six-legged robots that arrange their soft limbs into a closed tetrahedral shape.

2.2.5 Multipedal Locomotion

Multi-limbed soft robots, defined as having more than six limbs, vary in number from seven to dozens or even hundreds, depending on the design and application. This area is under-researched within soft-limbed locomotion. The work in [81] features a soft-bodied robot with nine reconfigurable legs, inspired by caterpillar crawling gaits. The robot in [67] is a soft millipede (Fig 2.4J) driven by 24 microfluidic actuators. Magnetically actuated millirobots with soft bodies and multiple tapered feet are shown in [82]–[86], capable of navigating uneven terrains and harsh environments, though controlling multiple legs adds complexity. Table 2.1 provides valuable insights into recent developments in soft-limbed mobile robots.

Table 2.1: Taxonomy of some recent locomotion research on terrestrial soft-limbed robots.

Research	Locomotion Method	Actuation	Modeling Approach	Trajectory Generation	Control	Power Autonomy	Limb Compliance	Max. Speed
Perera2023 [20]	Tripedal	Penumatic	CCM	Kinematic	Teleoperation	Tethered	Active	0.65 BL/s
Wang2021 [19]	Tripedal	Penumatic	CCM	Kinematic	Open-loop	Tethered	Active	3.7 mm/s
Wu2022 [36]	Quadrupedal	Pneumatic	FEM	Custom	Dynamic	Tethered	Active	0.97 BL/s
Atia2022 [34]	Quadrupedal	DEA	–	Custom	Open-loop	Tethered	Active	2.1 mm/s
Ji2022 [35]	Quadrupedal	Electromec.	Learn-based	Learn-based	Learn-based	Tethered	Active	0.05 m/s
Xia2021 [32]	Quadrupedal	Electromec.	Dynamic	Custom	Closed-loop	Untethered	Passive	2.5 BL/s
Zhu2021 [43]	Quadrupedal	Pneumatic	Kinematic	Custom	Open-loop	Tethered	Active	2.52 mm/s
Murali2021[31]	Quadrupedal	Electromec.	CCM	Kinematic	Closed-loop	Tethered	Active	2.0 BL/s
Schiller2021 [44]	Quadrupedal	Pneumatic	–	Custom	Teleoperation	Tethered	Active	0.8 BL/s
Scott2020 [73]	Pentapedal	Pneumatic	PDERM	T. Generation	Control	Tethered	Active	–
Lee2020 [74]	Pentapedal	Magnetic	–	Custom	Open-loop	Untethered	Active	0.25 BL/s
Ishida2022 [63]	Hexapedal	Pneumatic	Custom	Custom	Closed-loop	Tethered	Active	–
Li2022 [53]	Hexapedal	Pneumatic	CCM	Custom	Closed-loop	Untethered	Active	4.5 cm/min
Liu2021 [66]	Hexapedal	Pneumatic	Custom	Custom	Closed-loop	Tethered	Active	0.44 BL/s
Liu2020 [65]	Hexapedal	Pneumatic	Custom	Custom	Closed-loop	Tethered	Active	0.44 BL/s
Shao2022 [67]	Multipedal	Pneumatic	Dynamic	bioinspired	Closed-loop	Untethered	Active	1.35 BL/s
Yang2021 [85]	Multipedal	Magnetic	Modeling	Custom	Closed-loop	Untethered	Active	5 mm/s
Lu2020 [84]	Multipedal	Magnetic	–	Custom	Closed-loop	Untethered	Active	–

BL/s – body length per second

2.3 Soft-Limbless (or Soft-bodied) Robot Locomotion

Limbless soft robot locomotion refers to the movement of soft robots without traditional limbs or appendages, relying on other means of propulsion. In these robots, the body itself becomes the entire mechanism for movement. Terrestrial locomotion methods for soft-limbless robots include peristalsis, crawling, slithering, and undulation. Figures 2.3A and 2.3C show the distribution of soft-bodied robots over the years.

2.3.1 Peristaltic Movements

Peristaltic locomotion involves a robot moving forward by contracting its body in a wave-like motion, inspired by worms and snakes. In soft robotics, this is achieved by inflating and deflating body segments to create the motion, resulting in crawling locomotion [87]. Numerous soft robots utilize bio-inspired peristaltic movements, including those inspired by caterpillars [64], [88]–[97], burrowing worms [98], inchworms [99]–[114], earthworms [115]–[128], hornworms [129], [130], leeches [131], annelids [132], [133], and C. elegans [134]. Some employ passive feet [90], [135] or passive skins [136] to generate the necessary anisotropic frictional forces. Rectilinear movements of soft robotic snakes [136]–[138], where the robot moves in a straight line, also fall under peristaltic locomotion. These robots often have a shorter body length-to-diameter ratio than typical snake robots.

Some other categories of soft robot peristaltic movements include wall-climbing [139]–[145], amphibious climbing [146]–[151], worm-inspired pipe crawling [143], [152]–[158], tube climbing [150], [159]–[164], and mesh-worm crawling [165]. Figure 2.5 shows a few state-of-the-art soft-bodied robots that rely on body peristaltic in their locomotion.

2.3.2 Undulation, Serpentine, and Slithering

Soft robots mimic undulating movements of animals like worms, caterpillars, and snakes by propagating waves along their bodies. This motion is achieved through actuation methods that change the shape or volume of the robot, relying on anisotropic friction with the surface [166]. Soft robotic snakes [167]–[169] and robots inspired by C. elegans [134] and annelids [132] use undulation to move on planar surfaces.

Inspired by biological snake movements, lateral undulation is frequently used by soft robotic snakes. This involves the robot's body moving in a wave-like motion sideways or laterally rather than forward or backward. Soft robots using lateral undulation, such as those in [170]–[174], have segmented bodies where each segment can bend and flex independently. To move, the robot contracts muscles on one side while relaxing muscles on the other, causing the body to bend in the opposite direction. This method is particularly effective for moving across smooth, flat surfaces.

Serpentine locomotion involves a robot moving in a wave-like pattern from side to side, creating curves along its length. This motion propels the snake forward using muscle contractions and lateral undulation, effective for quickly moving over smooth surfaces. This type of locomotion, typical of slender-bodied snakes like garter snakes, has been replicated by soft robotic snakes with promising results in [167], [170], [175]–[178]. In some research [170], [176], serpentine and lateral undulations have been considered identical and tested for gait replications.

Slithering involves a robot using its body to slide or glide along a surface with friction-reducing adaptations. The robot moves in a serpentine pattern with lateral undulations from head to tail, distinct from undulatory locomotion, which has a more wave-like motion. Soft robots such as those in [170], [171], [174] mimic slithering locomotion.

2.3.3 Sidewinding

Snakes use sidewinding locomotion to minimize skin-ground contact, particularly in deserts. Inspired by this, soft robots achieve sidewinding motion by forming their bodies into helices [179]. The robot sequentially activates different body segments, first anchoring one end to the ground, then contracting middle segments to lift off the ground. The lifted segments move forward and re-anchor, creating a wave-like motion that propels the robot forward. This spatial locomotion gait is demonstrated well in soft robotic snake prototypes such as those in [169], [180]–[182].

2.3.4 Concertina Locomotion

Snakes use concertina movement to navigate narrow spaces or climb obstacles. This involves bunching their bodies in alternating S-shapes to extend their head and tail into an opening, then pulling the rest of their body through. Soft robotic snakes mimic this by sequentially moving sections of their body

forward, then pulling the other sections to meet them. The flexible robotic snake prototype in [169] mimics this concertina gait.

2.3.5 Rolling, Flipping, and Jumping

Limbless soft robots use rolling locomotion to move efficiently and overcome obstacles. Various designs and mechanisms exist. One type is the rolling cylinder, a cylindrical robot that deforms to roll forward. Soft robotic snakes demonstrate planar [167], [182], [183] and spatial rolling [180], [183] locomotion. Caterpillar-inspired rolling robots include designs in [93], [184]. Other prototypes like soft-wheeler robots [185], [186], isoperimetric robots [187], and magnetic grasping robots [188] mimic rolling locomotion. The robot in [64] has wedge-shaped legs inspired by caterpillar rolling gaits, while the robot in [94] uses body oscillations with six segments and five pairs of legs.

The soft robot prototypes proposed in [140], [189], [190] have the ability to flip the entire body and move in different directions. When activated, the flipping mechanism causes the robot's body to quickly deform and then return to its original shape, generating a flipping motion that propels the robot forward. Alternatively, the soft quadruped in [32] showed back-flipping through rapid rotation of its front and hind limbs, while maintaining a timed delay between them.

Soft-bodied robots, with their lightweight design, can easily perform jumping [191]–[193]. Precise tuning of jumping mechanisms balances force generation, energy efficiency, and landing stability [194]. This locomotion is advantageous for overcoming obstacles and navigating rough terrain, useful in search and rescue, environmental monitoring, and exploration. The robot in [195] achieves fast multimodal locomotion through continuous jumping, while the untethered robot in [196] uses combustion to power its jumps. Table 2.2 provides insightful details on recent developments in soft-bodied mobile robots.

2.3.6 Winding

Winding is a type of locomotion used by arboreal snakes for climbing trees. Inspired by that, authors in [197] proposed a winding-styled soft rod-climbing robot (see Fig. 2.5D) that consists of two winding actuators and a telescopic actuator. The purpose of this movement is, anchoring the robot itself to the outer surface of a rod while the remaining body actuates and pushes the robot within the rod.

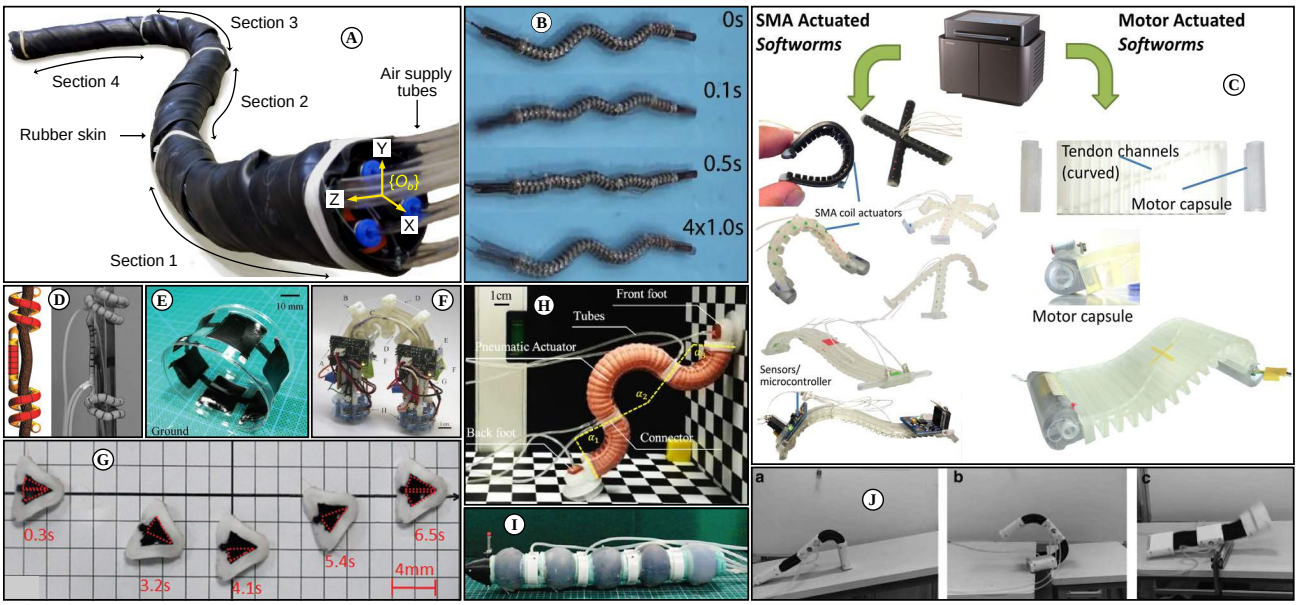

Figure 2.5: State-of-the-art wheelless terrestrial soft-bodied robots – (A) soft robotic snake in [180] that replicates helical rolling and sidewinding gaits, (B) electrically actuated snake robot in [169] replicating its concertina gait, (C) non-pneumatic soft worm robots in [130], (D) winding-styled rod-climbing robot in [197], (E) DEA-based fast rolling robot in [186], (F) "Flippy" electromechanically actuated autonomous climbing robot in [140], (G) DEA-based insect scale robot in [103] showing its running gait, (H) inchworm-inspired multimodal robot in [109] transiting between crawling and climbing locomotion, (I) earthworm-inspired modular robot in [118], (J) "Fifobots" flipping robot in [189] replicating its folding and moving gait. (Reproduced with permission).

2.4 Actuation Methods

This section categorizes soft mobile robots based on their actuation technologies. Therein, we discuss the pros and cons of each actuation technology and present how these technologies are related to robot shape, design, and locomotion methods.

2.4.1 Pneumatic Actuation

Pneumatic actuation systems commonly power and control soft mobile robots [198], using compressed air to move flexible bodies. Components include an air compressor, valves, and flexible pneumatic actuators made from materials like elastomers. These systems are lightweight and integrate well into flexible robots, providing a high range of motion and control. For instance, the 3-DoF quadrupeds in [36], [45], [48], [75] exhibit various locomotion gaits, including turning, while the pneumatic actuators in [43], [197] enable rod-climbing. Pneumatics also allow active compliance, enhancing maneuverability in dynamic situations [41], [45].

Pneumatic systems provide high-force and high-speed actuation, as seen in the cheetah-like robot in [40], which reaches 2.68 body lengths per second. They also enhance durability, as demonstrated

in robots enduring extreme conditions [176], [199]. However, they can be noisy, require compressed air, and demand precise pressure control. Onboard systems like those in [29], [38], [50], [53] offer untethered operation with lower pressure and speed, while tethered systems in [37], [40], [58], [65], [75], [200] provide higher pressure (1-4 bar) for diverse locomotion. Tethered limbless robots like those in [101], [106], [118], [119], [122], [150], [152]–[154] achieve peristaltic movement with low-pressure actuation. Vacuum-based [63], [74] and prestressed [201] systems offer lower variety and speed, often requiring additional limb support during movement [63].

2.4.2 Electromechanical Actuation

Electromechanical actuation involves using electric motors, tendons, and gears for soft mobile robot movement. Tendon-driven soft robots use flexible cables for control [26], [28], [31], [55], [56], [202]. These robots have flexible bodies segmented into sections controlled by tendons attached to motors. Actuators pull or release tendons to enable crawling, steering [120], undulating [168], slithering [140], flipping [140], or walking [35]. This method offers precise motion control and easy integration but requires many actuators, complicating design and maintenance. External actuators can limit motion range, as seen in the quadrupeds in [31], [35], making some tasks in confined spaces difficult.

The pipe crawling robot in [155], worm robot in [99], snake robots in [168], [169], and caterpillar-inspired robots in [89], [91] are tendon-driven limbless soft robots. Some robots have motorized joints for soft limbs connected to a rigid body, enabling dynamic locomotion. Examples include "SQuad" in [28] and "Flexipod" in [32], which demonstrated multiple gaits and locomotion in unstructured terrains. Robots like the pentaped in [79] and a tortoise-inspired quadruped in [25] use a crank mechanism. A limitation of these methods is that limbs are actuated only at the joints, lacking active limb compliance.

2.4.3 Smart Materials-based Actuation

Smart materials-based soft mobile robots are made of materials that have the ability to change their properties in response to external stimuli, such as temperature, light, or electric fields [203]. These materials are often called "smart" because of their ability to sense and respond to their environment. Two popular types of smart materials and their actuation methods applied in soft mobile robots are discussed, herein.

A. Shape Memory Alloy-based Actuation

Shape memory alloy (SMA) materials have the unique ability to change shape in response to temperature changes [204]. In SMA-based soft robots, the SMA material is often used in the form of wires or coils. When an electrical current is applied to the SMA wire or coil, it heats up and changes shape. As the wire cools down, it returns to its original shape, generating movement in the robot. SMA-based soft mobile robots are lightweight and capable of producing large deformations, enabling a wide range of motion. Leveraging these properties, the work proposed in [205] mimicked the terrestrial crawling of seals, and the studies in [17], [69]–[72] replicated starfish locomotion.

SMA-based robots have a slow response time due to the time required for the SMA material to heat up and change shape, resulting in slow locomotion. This slow response was observed in the quadruped and hexapod reported in [27] and [64], respectively. Additionally, limbless robots proposed in [92], [93], [104], [115], [121], [124] exhibited limited speeds. Controlling SMA-based soft robots is challenging due to the complex relationship between the input electrical signal and the resulting deformation. Due to these characteristics, achieving dynamic locomotion with SMA-actuated soft mobile robots is almost impossible.

B. Dielectric Elastomer-based Actuation

Dielectric elastomers (DEAs) are smart materials that change shape in response to an electric field [206]. Typically, the elastomer is sandwiched between two conductive electrodes, and when voltage is applied, the material compresses and expands, causing movement. Atia *et al.* [34] proposed a legged robot using reconfigurable DEAs, with legs limited to 1 DOF, resulting in low locomotion speed. However, DEAs can achieve high speeds due to their fast response time, as demonstrated by the rolling robots in [185], [186]. DEAs also offer a large deformation range, enabling diverse motions, as seen in the wall-climbing robot in [139], which exhibits climbing, crawling, and turning. DEAs are lightweight, flexible, and can be fabricated into complex shapes. They require high voltages to generate movement, making them suitable for small-scale limbless robots like caterpillars and worms [94], [96], [108], [132], [139], [207], which need limited energy for deformation and thus have restricted mobility. However, DEAs are sensitive to temperature changes and may not perform well in extreme conditions.

2.4.4 Electrostatic Actuation

Here, the principle of electrostatic attraction or repulsion between oppositely charged electrodes is used to produce movement. These robots typically consist of a soft material embedded with conductive electrodes, and the application of a voltage difference between the electrodes generates an electrostatic force that deforms the soft material and produces movement. This can be seen among limbless lightweight robots such as [100], [103], [141], [195] due to the limitations of the electrostatic force that makes the robot move.

2.4.5 Magnetic Actuation

This approach involves using magnetic fields to control the movement of robots. Magnetic particles, either ferromagnetic or paramagnetic, can be dispersed within the flexible robot material randomly or in specific patterns [208], [209]. The magnetic field is typically generated by an external source, such as an electromagnet [74], a permanent magnet [102], or a magnetic field generator [123]. By adjusting the strength and direction of the magnetic field, the embedded magnetic particles can be aligned or reoriented, causing the robot to deform or move in a specific direction [210]–[213]. This allows precise control over the robot's movement and shape. For instance, the tensegrity-based robot in [74] demonstrated multidirectional walking. These robots require less energy, reducing the need for frequent battery replacements or recharging. However, their locomotion speed is limited due to the lack of limb or body deformation (i.e., workspace). Peristaltic robots with these characteristics have been proposed in [102], [110], [111], [123], [214]–[217]. Conversely, soft milli-robots based on magnetic actuation [82]–[86] leverage many feet for superior locomotion performance. Additionally, some magnetic robots, such as the one in [191], exhibit high-speed multidirectional jumping with a simple, lightweight actuator design.

2.4.6 Combustion Actuation

The basic principle behind combustion-actuated jumping involves the controlled ignition of a fuel-air mixture within a chamber of the robot's soft body. The combustion process rapidly increases the pressure inside the chamber, causing the robot to expand and then forcefully contract, propelling it

Table 2.2: Taxonomy of some recent locomotion research on trrestrial soft-bodied robots.

Research	Locomotion Method	Actuation	Modeling Approach	Trajectory	Control	Power Autonomy	Speed
Arachch2023 [180]	Sidewinding	Pneumatic	CCM	Snake	Open-loop	Tethered	2.1 cm/s
Zhao2021 [169]	Concertina	Electromec.	Dynamic	Snake	Closed-loop	Tethered	–
Branyan2020 [172]	Undulation	Pneumatic	Custom	Snake	Open-loop	Tethered	–
Liao2020 [197]	winding	Pneumatic	Custom	Snake	Open-loop	Tethered	–
Huang2020 [131]	Peristaltic	Actuation	Modeling	Leech	Open-loop	Tethered	2.5 mm/s
Usevitch2020 [187]	Rolling	Hybrid	Kinematics	Custom	Closed-loop	Untethered	216 m/h
Wng2019 [190]	Flipping	Pneumatic	Dynamic	Custom	Closed-loop	Tethered	–
patel2023[93]	Rolling	SMA	FEM	Bioinspired	Open-loop	Tethered	1.5 BL/s
Li2021[186]	Rolling	DEA	Custom	Custom	Open-loop	Untethered	1.19 BL/s
Xu2022 [111]	Peristaltic	Magnetic	Dynamic	Worm	Open-loop	Tethered	–
Nemitz2016 [123]	Peristaltic	DEA	–	Worm	–	Tethered	2.11 mm/s
Joyee2022 [214]	Peristaltic	Magnetic	Modeling	Caterpiller	Closed-loop	Untethered	1.23 BL/s
Rozen2021 [89]	Peristaltic	Electromec.	Custom	Caterpiller	Open-loop	Tethered	–
Huang2020[131]	Peristaltic	Pneumatic	CCM	Caterpiller	Open-loop	Tethered	1.25 cm/s
Umedachi2019 [91]	Peristaltic	Electromec.	Dynamic	Caterpiller	Closed-loop	Tethered	1.5 cm/s
Das2023 [118]	Peristaltic	Pneumatic	Custom	Earthworm	Open-loop	Tethered	1.2 cm/s
Liu2019 [119]	Peristaltic	Magnetic	Custom	Earthworm	Open-loop	Untethered	0.86 cm/s
Karipoth2022[110]	Peristaltic	SMA	Custom	Inchworm	Open-loop	Tethered	–
Zhang2021 [109]	Peristaltic	Magnetic	CCM	Inchworm	Closed-loop	Untethered	2.5 mm/s
Duggan2019 [101]	Peristaltic	Pneumatic	PRBMs	Inchworm	Open-loop	Tethered	1.25 cm/s
Hu2023 [108]	Peristaltic	DEA	CCM	Inchworm	Open-loop	Tethered	1.1 mm/s

BL/s – body length per second

off the ground. For example, tripedal robots reported in [23], [218] and soft-bodied robot reported in [196] are capable of jumping powered by combustion.

2.4.7 Hybrid Actuation

Some mobile robots combine multiple actuation methods for efficient movement. For instance, the cable-driven soft quadruped in [33] uses pre-inflated pneumatic actuators, while the quadruped in [26] demonstrates autonomous locomotion with precharged pneumatic actuators. Although these robots are untethered, their actuators have low DoF (mostly 2-DoF), limiting gait variations. Usevitch *et al.* in [187] introduced an untethered octahedron truss robot made of inflated fabric tubes and motorized joints, enabling a human-scale mobile robot capable of morphing and rolling.

The "Softworm" robots reported in [130] showed SMA-actuated and tendon-driven worm robots fabricated using identical soft bodies (Fig. 2.5D). Moreover, the "OmniSkins" robots reported in [107] demonstrated rowing and inchworm locomotion using pneumatic and SMA-integrated robotic skins.

An interesting hybrid actuation method has been used by the millipede reported in [67]. It has a tendon-driven body and pneumatically actuated limbs.

2.5 Preliminary Modeling Approaches

Modeling approaches applied in soft actuators (i.e., limbs and bodies) can be classified into i) continuum mechanics models, ii) geometrical models, iii) discrete material models, iv) reduced complexity models, and v) custom analytical models [219].

2.5.1 Continuum Mechanics Models

Herein, actuators are defined by a configuration space that is infinite-dimensional and continuous, and they are based on the physical characteristics of the deformation. Typically, the deformation is subjected to a rigorous physical explanation of the kinetic and potential energy of the system.

A. Finite Element Methods

Finite element methods (FEMs) divide the actuator into a finite number of elements (i.e., mesh in Fig. 2.6A) and solve equations of motion for each element based on known input parameters such as applied forces, material properties, and boundary conditions. Typically, this is implemented as a numerical simulation in soft platforms such as COMSOL, Abaqus, ANSYS, etc. In soft robot locomotion, while most of the FEM simulations are performed to predict the actuator deformation [27], [36], [39], [40], [65], [93], [100], [152], [154], [156], there are instances where FEM is employed to verify the performance of the proposed gait models. For example, Cao et *al.* in [171] performed a FEM simulation to confirm the slithering gait of a soft robotic snake, and the results of the simulation were in close agreement with the theoretical predictions. Similarly, Bern et *al.* in [18] applied FEM to optimize the locomotion of a soft quadruped.

B. Energetic Methods

This method models the robot's behavior using energy storage and dissipation elements like springs and dampers. The stored kinetic and potential energy describes the robot's deformation and motion.

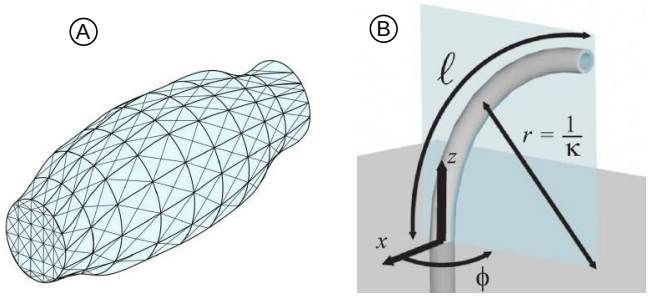

Figure 2.6: (A) Dividing actuator into a finite number of elements (i.e. a mesh) in [219]. (B) Spatial parametric representation of an actuator in [222]. (Reproduced with permission).

For example, [93] developed an analytic model using the principle of minimum potential energy to predict a bistable actuator's behavior in reconfigurable multimodal soft robots. Similarly, [40] used this approach to compare a bistable spine-based actuator's mechanical performance with its bistability-disabled counterparts, assembling a high-speed crawler.

In a different modeling perspective, energetic methods simplify continuous actuator models into a finite number of Lagrangian ordinary differential equations, preserving the variational structure. The actuator is assumed to consist of infinitesimally thin slices with constant mass and uniform linear density. The kinetic and potential energies of each slice are integrated along the length to find the total energies [220]. Assume that the total kinetic energy (**KE**) and the potential energy (**PE**) of the actuator is known, then the complete Lagrangian can be written as [221], $\mathbf{L}(\boldsymbol{q}, \dot{\boldsymbol{q}}) = \mathbf{KE}(\boldsymbol{q}, \dot{\boldsymbol{q}}) - \mathbf{PE}(\boldsymbol{q})$. Here, $\boldsymbol{q}$ defines the jointspace vector. Accordingly, the generalized equations of motion can be expressed as

$$\mathbf{M}\ddot{q} + \mathbf{C}\dot{q} + \mathbf{D}\dot{q} + \mathbf{K}q + \mathbf{G} + \mathbf{H} = \mathbf{F}_e \tag{2.1}$$

where **M**, **C**, **D**, **K**, **G**, **H**, and $\mathbf{F}_e$ are the generalized inertia matrix, centrifugal and Coriolis force matrix, damping force matrix, elastic stiffness matrix, gravitational force matrix, hysteresis matrix, and input force vector, respectively. Using this approach, Godage et *al.* in [24] expressed the dynamics of their continuum quadruped and verified its locomotion through a series of simulations. The Lagrangian approach was used by Li *et al.* in [185] and Jaryani et *al.* in [178] to obtain the EoM of their rolling robot and muscle-driven snake robot, respectively. Similarly, Wang et *al.* in [189], [190] modeled the locomotion of their flipping robots using the same approach and verified it through simulations and experiments.

2.5.2 Geometrical Modeling: Constant Curvature Models

Geometric models are based on the assumption that the deformed actuator has a resemblance to a particular geometric shape (such as the constant curvature (CC) in this case). Here, the shape is represented by a set of mathematical equations derived using curve parameters that describe the position and orientation of the actuator at any given point in time. One of the popular CC modeling approaches presented by Webster *et al.* in [222]. Therein, an actuator arc is defined by three spatial parameters; the arc length, l, the angle of bending plane w.r.t. the +X axis, $\phi \in [-\pi, \pi]$, and the curvature, k (see Fig. 2.6B). Then, the transformation from arc base to any point $\xi \in [0, l]$ of the actuator is given by (note cos=c, sin=s)

$$\mathbf{T}(k,\phi,\xi) = \begin{bmatrix} \mathrm{c}\phi\mathrm{c}k\xi & -\mathrm{s}\phi & \mathrm{c}\phi\mathrm{s}k\xi & \frac{1}{k}\mathrm{c}\phi\,(1-\mathrm{c}k\xi) \\ \mathrm{s}\phi\mathrm{c}k\xi & \mathrm{c}\phi & \mathrm{s}\phi\mathrm{s}k\xi & \frac{1}{k}\mathrm{s}\phi\,(1-\mathrm{c}k\xi) \\ -\mathrm{s}k\xi & 0 & \mathrm{c}k\xi & \frac{1}{k}\mathrm{s}k\xi \\ 0 & 0 & 0 & 1 \end{bmatrix}. \tag{2.2}$$

This CC approach has been extensively applied to model the actuators of soft tripodal robots [20], [21], quadrupeds [24], [31], [43], [45], [48], [200], hexapods [53], [75], [76], pipe crawlers [155], [156], earthworm-like robots [126], and snake robots [167], [180], [183]. This method can be easily integrated with other modeling techniques, such as FEM or pseudo-rigid body models, to provide a more comprehensive analysis of the robot's behavior as showcased by authors in [155], [156].

2.5.3 Discrete Modeling

Here, the actuator is divided into discrete elements, and each element is modeled as a separate unit. Two categories of such models exist in soft mobile robot literature: pseudo-rigid body models and discrete elastic rod models.

A. Pseudo-rigid Body Models

Pseudo-rigid body models (PRBMs) represent the soft actuator as a series of rigid segments that are interconnected through revolute, universal, or spherical joints. They can move relative to each other while maintaining their relative angles. Thus, the actuator configuration space, Q becomes

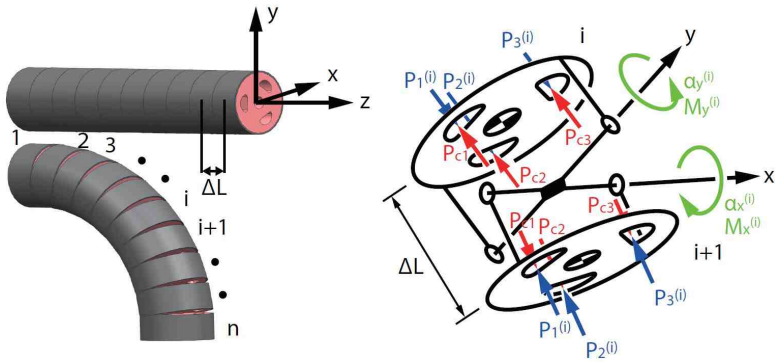

Figure 2.7: Left – A soft actuator of the pneumatically-powered tetrahedral robot in [19] is discretized into cylindrical rigid links and cardon joints between them. Right – A simplified mechanical model of the i-*th* link showing pneumatic pressure, bending torques, and joint angles. (Reproduced with permission).

$$Q \subset \mathbb{SE}(3) \times \mathbb{SE}(3) \times \mathbb{SE}(3) \ldots \times \mathbb{SE}(3)\,. \tag{2.3}$$

Authors in [19] approximated a continuous soft limb of their tetrahedral robot into n cylindrical rigid links. They are interconnected to each other via cardon joints (see Fig. 2.7). Based on this simplified model, they derived the multibody dynamics of the robot and simulated it for locomotion. Li *et al.* in [185] developed a pseudo-rigid-body model to analyze the deformation and rolling mechanism of their DEA-based rolling robot. The model was simulated on ADAMS software and verified the feasibility of the proposed rolling mechanism.

B. Planar Discrete Elastic Rod Models

The planar discrete elastic rod model (PDERM) represents the actuator as a series of connected rods with defined length, bending stiffness, and twisting stiffness, determining deformation under external forces [223]. PDERM combines geometric equations, which describe rod deformation, and dynamic equations, which describe rod motion. In [64], PDERM was combined with Lagrange's EoM to model the locomotion of an SMA-powered hexapod. Similarly, the starfish-inspired robot in [73] applied PDERM to derive the dynamic equation of the full robot.

2.5.4 Reduced Complexity Models

This refers to simplified models that capture the essential characteristics of a soft robot's behavior. Authors in [91], [103], [122] employed reduced-complexity dynamic models to model the crawling locomotion of their worm and caterpillar-inspired robots. Therein, they approximated the soft body

and muscles into mass-spring-damper systems. Rozen-Levy *et al.* in [89] modeled the body and the gripper dynamics of their branch-crawling worm robot based-on tendon actuated motor dynamics and spring-mass-damper dynamics of the body. Wang *et al.* in [190] developed a state-space model to simulate dynamics of its flipping robot. In a slightly different approach, the work reported in [70]–[72] used thermodynamic modeling to describe the heating and cooling of SMA-based limbs.

2.5.5 Custom Analytical Models

Several customized analytical modeling methods of actuators and locomotion gaits can be found in soft robotic locomotion research. They are unique for a particular mobile robot and its locomotion strategies. The magnetically actuated milli robot in [85] obtained its dynamic model through force analysis that includes magnetic pulling force, friction force, and tapping force. The electrically actuated snake robot reported in [169] was modelled based on the behavior of its individual elements such as the helical spring and the drive motor. Some work have static modeling methods such as beam theory [141], spring deflection equation [116], Euler-Bernoulli principle [79], [131], and custom geometric constraint-based model [66] applied to derive the actuator deformation and then robot motion. The work reported in [65] shows a static model based on geometric constraints for each leg.

2.6 Locomotion Trajectory Generation Methods

Trajectory generation methods are diverse, and the choice of method depends on the specific requirements of the application. They can be broadly categorized into four types: bioinspired, model-based, model-free, and custom (trial-and-error) approaches.

2.6.1 Bioinspired Methods

These approaches are inspired by animal movement patterns. Many limbless robots exhibiting peristaltic locomotion are based on biological counterparts. For instance, worm family robots such as inchworms [99]–[104], [108]–[110], [129], [154], [215], earthworms [118], [119], [121], [122], [125], burrowing worms [98], and caterpillars [64], [81], [88]–[91], [93], [94], [130], [131], [184], [214] generate locomotion through wave-like motion. These robots consist of segments that contract and expand in coordination,

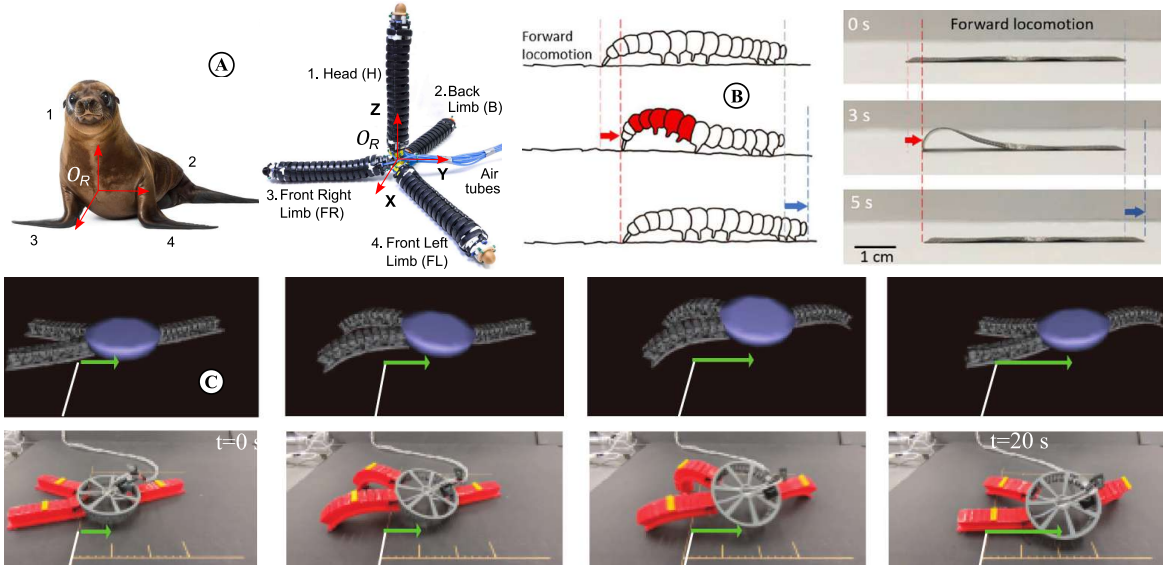

Figure 2.8: Representative locomotion trajectory generation methods – robots that replicate bioinspired, (A) pinniped [21] and, (B) caterpillar [97] gaits, (C) soft crawling robot that utilizes a reinforcement learning-based co-optimization framework to generate locomotion gaits [224]. (Reproduced with permission).

mimicking muscle movements in real animals. For example, the caterpillar robot in [214] achieved multimodal locomotion through sequential activation of magnetic forces, while the caterpillar-inspired robots in [91], [97] used module contraction and bending to produce movement (Fig. 2.8B).

Another common bioinspired method is gait analysis, which involves analyzing the way that animals move and using that information to create a mathematical model of their motion. The soft robotic snakes reported in [167]–[169], [171], [180], [183] generated their gaits by mathematically parameterizing locomotion curves of natural snakes.

Some soft-limbed robots generate bio-inspired locomotion. The high-speed crawler in [40] imitates cheetah galloping with its bistable hybrid body. The millipede robot in [67] mimics natural millipede locomotion with a 4-phase leg operation. The sea star-inspired robot in [63] uses active suction like sea stars' adhesive appendages. However, some robots mimic biological movement patterns without bioinspired trajectory generation methods [21]. Refer to Tables 2.1 and 2.2 for more details.

2.6.2 Model-based Methods

This involves using mathematical models to plan and generate motion trajectories for the robot. These models typically describe the robot's kinematics, dynamics, etc., of its motion, as well as the constraints and requirements of the task at hand.

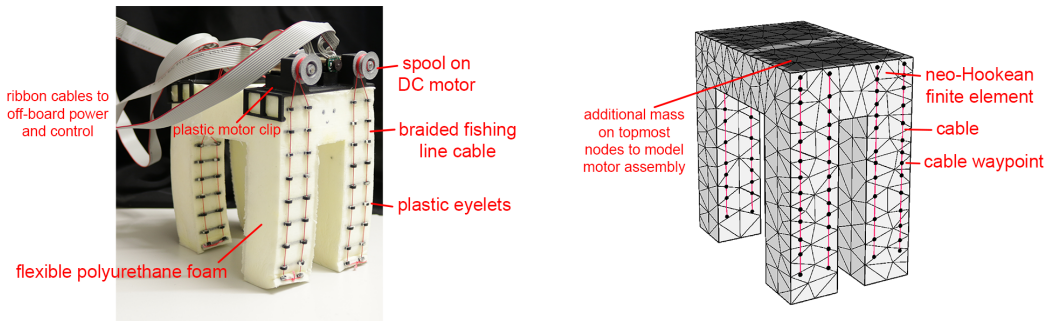

Figure 2.9: A cable-driven soft robot that employes a model-based trajectory optimization method to achieve dynamic locomotion [18]. (Reproduced with permission).

A. Kinematic Modeling-based Methods

Kinematics can accurately describe actuator deformation. Authors in [20], [21], [24], [45], [200] used curve parametric inverse kinematics for locomotion trajectories of quadrupeds and tetrahedral robots by defining limb trajectories in task space, transforming them into joint variables, and actuating limbs based on gait patterns (Fig. 2.8A). [45] experimentally validated the CC-based kinematic model with high accuracy. Similar methods generated undulation, sidewinding, and rolling gaits for snake robots in [167], [180], [183], using optimization-based inverse kinematics. The tendon-driven quadruped in [31] calculated control wire length changes for desired limb deformation. In some cases, custom kinematics, not necessarily curve parametric, assisted movement, like in the soft crawling and walking quadrupeds in [33].

B. Optimization-based Methods

Optimization methods can be used to find optimal gaits that minimize a cost function, such as energy consumption or travel time. These methods typically rely on robot dynamic models. Authors in [18] proposed a model-based trajectory optimization method for a cable-driven soft quadruped (Fig. 2.9). Therein, first, they modeled the robot using FEM. Then, forward dynamic simulations were used to predict the robot's movements and later improve it to automatically generate optimal locomotion trajectories. Arachchige *et al.* in [200] generated trotting gaits of a quadruped based on limb kinematics. Then, they simulated and optimized the gait parameters on a Physics engine-based dynamic environment. Based on optimized gait parameters, the gaits were then experimentally validated on the quadruped prototype.

C. Path Planning-based Methods

Path planning involves generating a sequence of desired poses for the robot to reach its destination, considering its compliance and environmental interactions. It defines goals and constraints, then generates feasible paths. The gecko-inspired quadruped in [42] used this approach to meet multiple goal positions on a flat surface, with constraints on position, joint variables, walking speed, and turning speed. By mapping velocity space to task space, it recursively generated optimal paths to targets. The crawling quadruped in [33] reached locations by completing cycles based on the motor's rotational angle and movement per cycle.

2.6.3 Model-free (or Learning-based) Methods

This approach generates motion trajectories without explicit mathematical models of the robot or its environment, relying instead on data-driven methods like machine learning. The robot optimizes its motion through trial-and-error based on experience. While there's extensive research on machine learning for deformation modeling of soft actuators [225], [226], few focus on soft mobile robots. Ji *etal.* [35] used deep reinforcement learning (RL) to synthesize optimal walking gaits for their quadruped [31]. In [224], a soft crawling robot utilized an RL-based co-optimization framework for gait generation (Fig. 2.8C). The authors of [105] proposed an inchworm-inspired differential drive robot and used radial basis function (RBF) neural networks to train its turning on various surfaces, resulting in a highly accurate mathematical model.

A slightly different learning approach was used to obtain locomotion of the hexapod reported in [77]. The authors used a simulation software package that offers the user separate learning and execution routines of the robot. While in the learning mode, the operator can control the individual leg tubes using a graphical user interface, which enables the customization and optimization of a specific gait. After achieving a desirable gait, the process was stored in memory and used in the robot.

2.6.4 Custom (or trial-and-error) Trajectory Generation Methods

Custom methods optimize trajectory generation for specific robot designs. The quadruped in [32] used a template with motor positions divided into constant velocity phases. The pipe-crawling robot in [155] generated trajectories via trial-and-error, using left-right body bending and uneven forward

friction. The Multigait tetrapod in [37] produced crawling and undulation by pressurizing limbs in different sequences. The quadruped in [43], tube-climbing robot in [159], hexapod in [78], and high-speed rolling robot in [186] relied on experimentation. In [92], a linear frequency increase propelled a robotic caterpillar. The "Flippy" robot in [140] (Fig. 2.5F) generated flipping and climbing gaits using a custom state machine with states: flipping, attaching, and detaching. The "SoRX " hexapod in [65] used an alternating tripod gait, ensuring the center of mass stayed within the support area formed by the three grounded legs.

Some researchers relied on extensive actuator modeling (limb or body) to achieve locomotion, as seen in the multimodal crawler [93], bionic omnidirectional wall and tube climbing robots ("BOWR," "BOTR") [131], and a walking quadruped [34]. The approach involved identifying the actuator's deformation characteristics and leveraging them for tasks like robot locomotion. More work on various custom trajectory generation methods can be found in Tables 2.1 and 2.2.

2.7 Control Methods

Control methods regulate robot movement by managing the actuation media or system (e.g., pneumatic, motor, temperature, electricity) that drives limb and body motion. We briefly discuss major control methods in wheelless terrestrial soft mobile robots.

2.7.1 Open Loop Control

This type of control system involves pre-programmed robot movements that operate independently of sensor feedback or environmental changes (Fig. 2.10B). The system generates a sequence of predefined commands that the robot executes without adapting to external inputs. Its simplicity makes it popular in soft mobile robot research (see Tables 2.1 and 2.2). Most robots in this field use open-loop sequential control systems [17], [47], [48], [69], [70], [72], [186]. For instance, the quadrupeds in [37], [50] employed manual control of pneumatic valves for limb pressure regulation. The quadruped in [43], designed to climb parallel rods, relied on air pressure regulation. The resilient quadruped in [199] demonstrated pre-programmed locomotion, while the snake robot in [169] and the rolling robot in [185] used open-loop control for multigait and fast locomotion, respectively. Robots with peristaltic movements (e.g., [91],

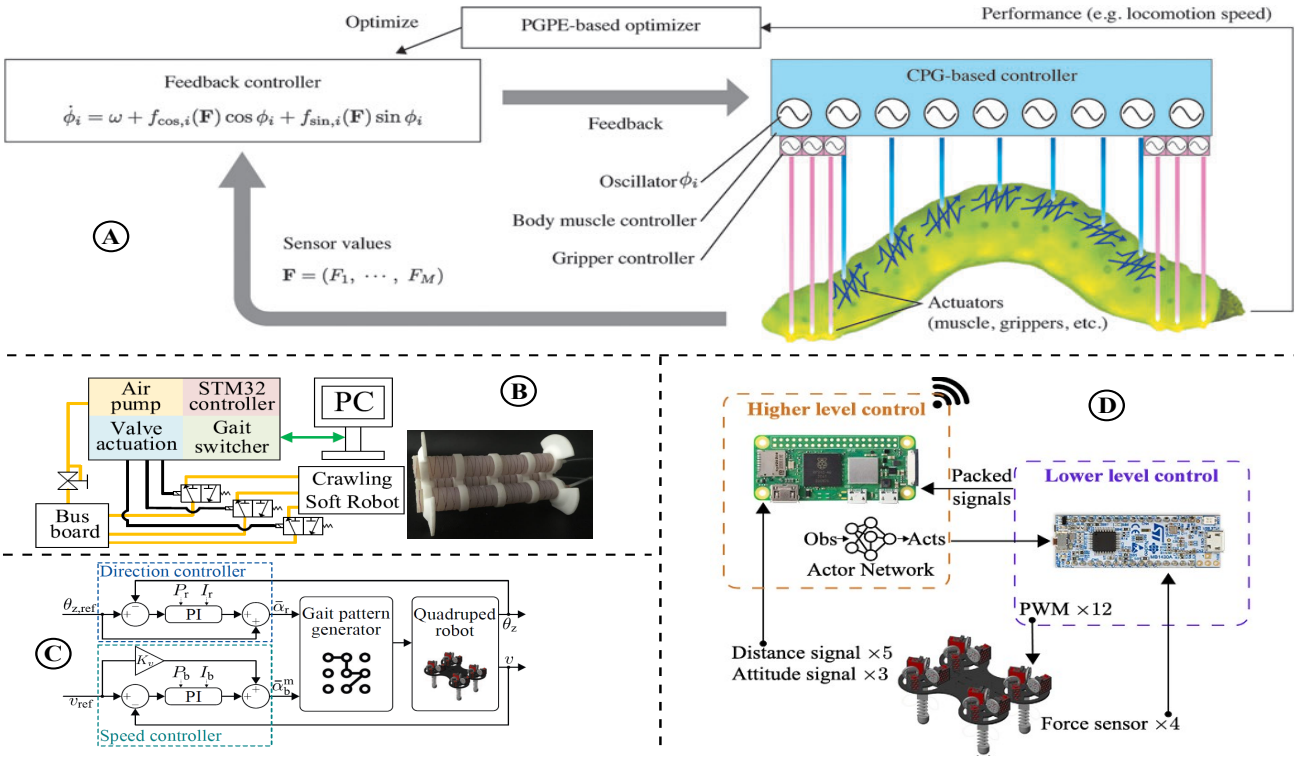

Figure 2.10: Representative control methods – (A) closed-loop control strategies in [227], (B) open-loop control method employed by the soft crawler in [156], (C) closed-loop direction and speed controllers proposed by the soft quadruped in [68], (D) control scheme used to validate learning-based locomotion trajectories of the quadruped in [35]. (Reproduced with permission).

[99], [103], [141], [154]–[156], [159]) tend to rely on open-loop control since their locomotion involves minimal body deformation. However, the lack of sensor feedback in pre-programmed movements makes these robots less adaptable to environmental changes.

2.7.2 Closed-loop Control

In closed-loop control (or feedback control), the robot's movements are regulated based on feedback from sensors and the environment (Fig. 2.10A). That is, the control system continuously monitors the robot's movements and environment and adjusts the robot's movements in real-time to achieve the desired outcome. This concept can be understood by observing the pressure control system employed by authors in [109] who proposed a multimodal worm robot (Fig. 2.5H). Therein, the sensor collects pressure data in various channels of the robot body in real-time and sends it back to compare with the input pressure (or desired pressure). Next, the controller receives the error signal in order to generate control signals, which in turn regulate the air pressure in the robot body. We discuss several sub-categories of closed-loop control systems hereunder.

A. Kinematic-based Closed-loop Control Systems

One approach to controlling soft robot locomotion is known as model-based kinematic control. This involves creating a mathematical model of the robot's kinematics and using it to design control algorithms that accurately manage the robot's movements. For example, the large-scale hexapod in [53] used a piecewise constant curvature-based kinematic model to control limb curvature and a PID regulator to handle actuator saturation and unmodeled environmental interactions. Similarly, the tendon-driven quadruped in [31] employed a kinematic controller powered by a linear–quadratic regulator (LQR) to regulate motor rotational positions that drive tendons. The isoperimetric robot in [187] used a kinematic-based PID controller to drive its rollers to desired positions. However, kinematic-based control is limited by the mathematical models, which may not accurately capture the full range of robot movements, especially in complex or dynamic environments.

B. Dynamic-based Closed-loop Control Systems (DbClCS)

Here, first, mathematical models that describe the robot's movement dynamics are obtained. They are then applied to design control algorithms that generate commands for the robot's actuators, to achieve desired motions. Similar to kinematic control, these algorithms are employed in a feedback loop that adjusts the control inputs in real-time. For example, the tortoise-inspired robot in [36] applied an empirical dynamic model to optimize motion speeds. The earthworm-inspired robot in [122] implemented a friction-based feedback control strategy that enables active friction control and supports locomotion. Therein, the authors demonstrated how the robot attains movement by employing time-varying friction controlled through feedforward mechanisms. "Flexipod" quadruped in [32] and "SQuad" quadruped in [28] used a classical joint-space position control system (a full state feedback controller) based on robot dynamics to control the motor shaft position that enabled the limb movements. Note that, dynamic-based control systems often require significant computational resources to solve the equations of motion and control the robot in real-time.

C. Custom Closed-loop Control Systems

This category of closed-loop control regulates robot movement without considering kinematics or dynamics. For example, the quadruped with active suction in [63] used closed-loop control to maintain

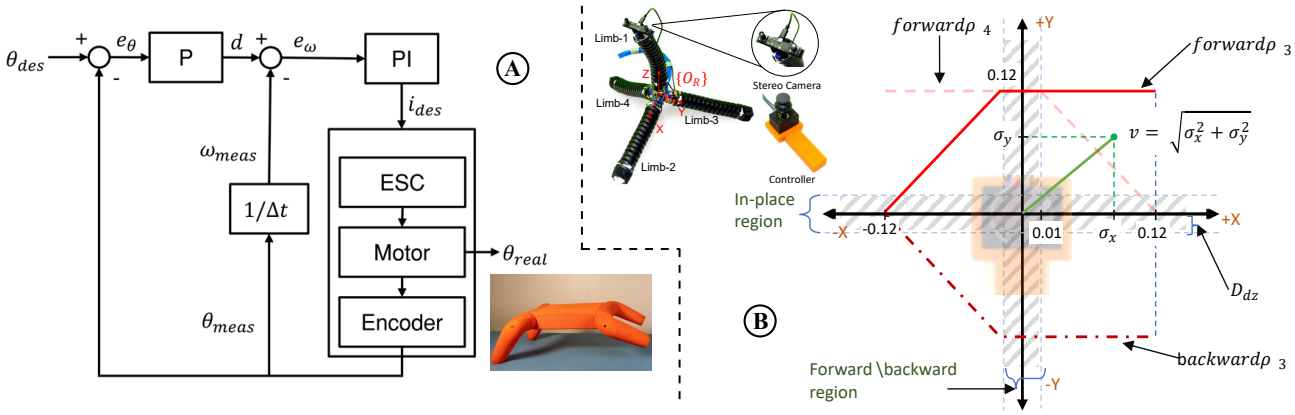

Figure 2.11: Representative control methods – (A) classical joint-space position control system used by "Flexipod" quadruped in [32], (B) teleoperating scheme applied to control the tetrahedral robot in [20]. (Reproduced with permission)

negative pressure for uniform movements. In [66], a closed-loop trajectory tracking system moved a hexapod robot along a desired path using an onboard motion-capturing system. The hexapod in [78] used a PI controller and IMU for movement regulation. The starfish-inspired robot in [73] utilized pressure sensors and visual tracking for locomotion. The gecko-inspired quadruped in [42] employed closed-loop position control in Cartesian space. FifoBots in [189] used feedback control to track flipping paths, while the robot in [110] demonstrated inch-worm and earth-worm locomotion with intrinsic strain sensors for feedback. Manwell *et al.* in [120] used a PID controller for body contraction in a worm robot. These strategies highlight the potential for task-oriented path planning.

2.7.3 Teleoperation (or Remote control)

Teleoperation allows an operator to control the movement of a soft robot from a remote location, using a computer, joystick, or other input device. This typically requires a communication link (wires, Wi-Fi, Bluetooth, Ethernet, etc.) between the robot and the operator. It can be tethered or tetherless.

A. Tethered Teleoperation

In this method, a physical connection (tether) between the robot and a remote operator allows control by sending signals through the tether, typically a wire connected to the robot. The tether provides power and communication, enabling the operator to view through the robot's sensors and control its movements in real-time. Perera *et al.* in [20] demonstrated teleoperation of a tetrahedral robot with real-time stability and trajectory control (see Fig. 2.11B). Authors in [44] developed an intuitive

interface for remote operation of a Gecko-inspired quadruped. This approach is beneficial for navigating complex environments, as the tether provides additional support and stability. However, it can also limit the robot's range of movement and mobility, making it less suitable for certain applications.

B. Untethered Teleoperation

Here, we control the robot without a physical tether. Magnetically actuated robots, like those in [82], [84], fall under tetherless teleoperating robots, as their movement is remotely controlled via magnetic fields. The millipede in [67] features tetherless remote control, with motion assisted by real-time wireless images. Examples of tetherless systems include the hybrid robotic system in [46] and the "Flexipod" quadruped in [32] (see Fig. 2.11A). These methods (tethered or tetherless) allow for human supervision and real-time decision-making, particularly useful when the robot faces unexpected obstacles.

2.7.4 Learning-based Control

The control systems can also involve machine learning algorithms that enable the robot to learn from its environment and adapt its movements accordingly. For example, a soft robot might use reinforcement learning to learn how to move through a complex environment, such as a cluttered room or a maze. In [35], a learned RL-based controller is applied to optimize the walking gaits of a quadruped (Figs. 2.10C and 2.10D). Therein, first, the controller is trained in a simulation environment. Then, the learned gait control policy was successfully implemented and tested on the quadruped prototype.

2.8 Chapter Summary

This chapter focused on wheelless soft robots, categorizing them into soft-limbed and soft-bodied types, and explored their design principles and locomotion modes. It examined various actuation methods, including pneumatic, hydraulic, and shape-memory materials, along with control strategies tailored for these flexible systems. This chapter provides a comprehensive foundation for understanding the diversity and potential of wheelless soft robots in contemporary robotics research.

Chapter 3

Design and Fabrication of Soft Modules and Mobile Robot Topologies

3.1 Hybrid Soft Robots (HSRs) or Soft Modules

3.1.1 Motivation

Soft and continuum robots are inherently compliant structures that undergo smooth and continuous structural deformation to form complex "organic" shapes [228]. Prior work has demonstrated the potential of soft robots for adaptive whole arm grasping [229], obstacle avoidance and progressive planning [230], grasping in cluttered space [231], navigation in obstructive and unstructured environments [232], human-friendly interaction [233], and locomotion [167], to name a few applications. However, despite continued research demonstrating their immense potential, they are primarily confined to laboratory settings. One of the main reasons is their lack of structural strength thereof necessary to engage in practical applications such as object manipulation or locomotion (move payload) while supporting their own weight. Soft robots are often actuated by pneumatic pressure, tendons, and smart materials [13]. An impressive number of prototypes that employ pneumatic muscle actuators (PMAs) have been proposed over the years [198]. PMAs are popular due to ease of customization, a wide operational pressure, and a high power-to-weight ratio [234]. The PMAs (typically 3) can be bundled together to construct bending robotic units – termed sections [235]. Complex soft robots such as multisection manipulators or legged robots are then fabricated by combining many such bending

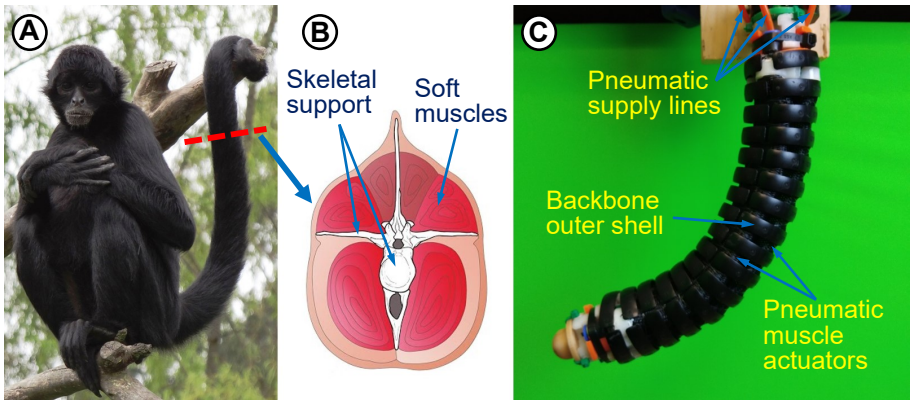

Figure 3.1: Bioinspiration – (A) spider monkey, (B) tail's muscular lining with skeletal support. (C) Proposed soft module prototype with bending.

units (sections) [236]. In addition to actuation, macro-scale PMA-powered soft robots rely on PMAs for the robot's structural integrity [237]. The PMAs stiffness is proportional to the supply pressure. Thus, a soft robot constructed from multiple PMAs exhibits variable stiffness proportional to the mean pressure of PMAs. However, the achievable stiffness in PMAs solely through pressure increase is limited. This can lead to undesirable and unpredictable behaviors (buckling) and unstable behaviors (twisting that may result in permanent structural change) during operation. In addition, PMAs undergo length change proportional to the applied pressure. Consequently, the stiffness is coupled to the robot shape. This means that it is not possible to change the robot stiffness without affecting the shape [238]. This could be a problem in applications where adaptive stiffness control during taskspace trajectory tracking.

The decoupled stiffness and pose control allow soft robots to easily adapt to task demands in situ without affecting the taskspace trajectories. However, prevalent continuum manipulators are made of sections that extend (or contract) depending on the operational mode of PMAs, morphology, etc. and are therefore subjected to length variation during operation. Consequently, they cannot independently control arm shape [239], and stiffness [240]. Hence, a new line of thinking is warranted for potentially generating technologies to bring soft robotics to practice while providing higher structural strength and better stiffness regulation to fulfill meaningful tasks without betraying compliant operation.

The usefulness of such features becomes evident when we consider a versatile biological example, such as the tail of spider monkeys (Fig. 3.1A). Their muscular arrangement – controlling the deformation of the skeletal structure underneath (Fig. 3.1B) – has embedded unique mechanical properties that

differ from conventional soft robots. Muscles (and tendons) have spring-like properties, with inherent stiffness and damping. Thus, they can seamlessly transform between modes (combinations of shape and stiffness). For instance, the tail can act as a manipulator (grasping tree branches), a support structure (standing upright), and a counterbalancing appendage (during jumping and climbing). They achieve these impressive transformations while still being "soft" to the touch because of the tail's muscular lining (Fig. 3.1B). Based on this biological example, we propose a PMA-powered hybrid soft robot (HSR – Fig. 3.1C) with a rigid-linked, highly articulable but inextensible (i.e., constant-length) backbone. The primary motivations of combining soft elements (which facilitate smooth and continuous structural deformation while being compliant and human-friendly) with stiff elements (which provide structural strength supporting high payload manipulation tasks) are to 1) increase the variable stiffness range to adapt to environmental changes and operational needs, and to 2) decouple stiffness and shape change for achieving better motion control.

3.1.2 Soft Module Design

The proposed soft module – shown in Fig. 3.1C – has two main elements, namely the backbone and PMAs, that are used to produce the decoupled stiffness and deformation control.

A. Highly-Articulable Backbone

The backbone unit used in the design is a readily available dress pack (Igus Inc, – part no: Triflex R-TRL.40) designed for cable guide applications (Fig. 3.2A). In the dress pack, high-tensile-strength plastic segments are serially connected via ball-and-socket joints (allowing free rotation about the local X and Y axes) to form a rigid-link kinematic chain. The individual segments are easily assembled or disassembled, allowing to customize the length of the backbone (i.e., section). We determined the backbone's length to be 16 cm based on its bending ability to form a subtended angle of 180° in any bending plane (Fig. 3.2A).

B. Pneumatic Muscle Actuators (PMAs)

Custom-made Mckibben type PMAs are utilized to actuate the proposed soft module [241]. We used commercially available Silicone tubes, pneumatic union connectors, braided sleeves, and heavy-duty

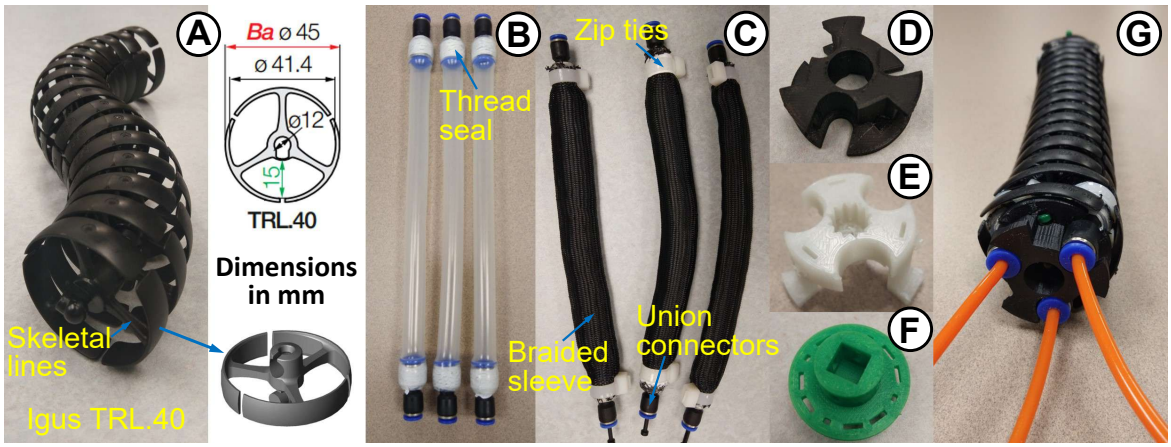

Figure 3.2: Design components of the soft module – (A) Igus Triflex R-TRL.40 dress pack, (B) silicone tubes, (C) PMAs, (D) end caps, (E) intermediate joint, (F) upper hip joint. (G) Fabricated prototype of the soft module.

zip ties to fabricate PMAs [242]. We opted for the extending-mode PMAs for their leaner physical profile as opposed to the contracting mode ones which would require a higher radius-to-length ratio. In addition, extending mode PMAs have higher normalized length variation (up to 50% compared to about 35% for contracting ones). Further, we desire comparably high operational pressures to generate increased torques to achieve high bending deformation and stiffness range. To that end, we selected a silicone tube with 11 mm of inner diameter and 2 mm of wall thickness (Fig. 3.2B). We decided on the tube's thickness based on the ability to safely operate in a pressure range (up to 5 $bars$) with an acceptable deadzone (pressure to overcome the transient radial expansion). The length of a PMA is chosen as 180 mm based on the length and backbone characteristics such that the serial joints of the backbone can bend up to 180° in any bending plane. To limit radial expansion of PMAs during operation, the diameters of constraining Nylon mesh and Silicone tubes have to match closely. Also, it increases the PMA efficiency as most of the air pressure is used for axial extension. Consequently, this further helps to reduce the PMA dead zone. To meet these design requirements, we experimentally selected high-strength Nylon braided mesh with diameters 10 mm (minimum) and 18 mm (maximum). We used 4 mm internal diameter union connectors to connect external pneumatic pressure lines to PMAs. Heavy-duty zip ties are used to secure silicon tubes, and mesh to the other end of the union connectors (Fig. 3.2C). Fabricated PMAs shown in Fig. 3.2C can extend by up to 50%, and withstand 700 kPa with a 90 kPa pressure dead zone.

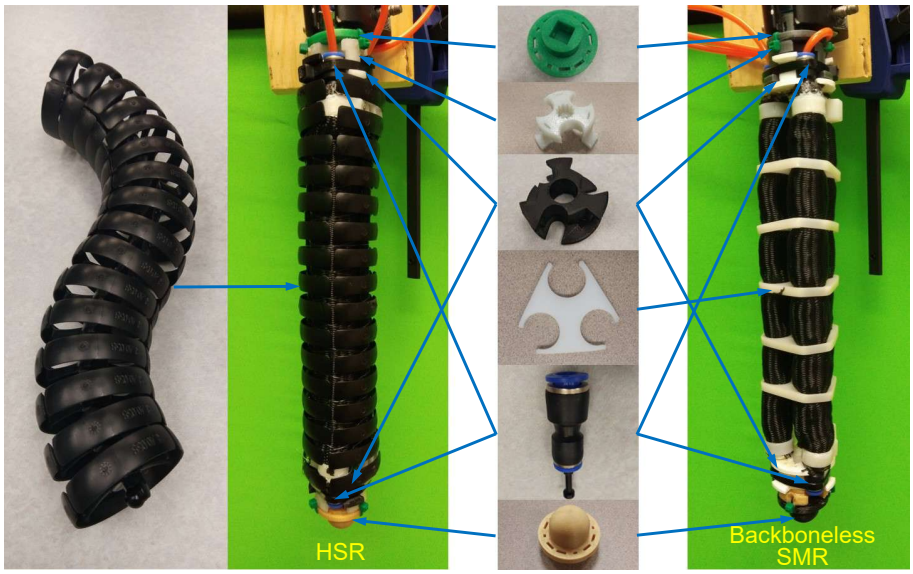

Figure 3.3: Soft module and its counterpart (backboneless unit) with their design elements.

C. Soft Module Assembly

Fig. 3.2G shows the finished prototype of the soft module. Therein, we arranged 3 PMAs within the radially symmetric cavities (or grooves) along the length of the backbone structure (Fig. 3.2-A). We designed and 3D-printed several parts (Fig. 3.2D, E, & F) to integrate PMAs into the backbone. We used two end caps (Fig. 3.2D) to axially secure the PMAs in place. High-strength fasteners then securely anchor the PMAs to the end caps at either end of the backbone. In this arrangement, the backbone constrains the PMA length change during operation, which results in a spatially antagonistic PMA configuration for an increased stiffness range. To prevent buckling and ensure uniform bending deformation during operation, we securely wrapped PMAs in parallel to the backbone using a fishing wire. The resulting fixed-length soft module has a uniform construction and exhibits omnidirectional and circular arc bending. We employed 3D-printed joints shown in Fig. 3.2E & F to connect modules to the actuation base or each other. The assembled soft module has a total length and weight of 24 cm and 0.15 kg, respectively. Apart from the fixed-length sof module with backbone, to compare operable stiffness ranges as shown in Fig. 3.3, we fabricated an identical variable-length soft module prototype without a backbone. We used identical PMAs in both prototype designs.

Next, we utilized several soft modules to assemble soft mobile robots with three different topologies, as detailed in the subsequent sections.

3.2 Soft Robotic Snakes (SRSs)

3.2.1 Motivation

Snakes are among the few reptile species that do not require limbs to locomote in various environments including, marshes, deserts, and dense vegetation. Within the powerful musculature that generates movements, snakes have a skeletal structure that protects internal organs and facilitates smooth bending to produce unique locomotion patterns [243], [244]. Further, the small cross-section-to-length ratio of snakes facilitates passing through confined and narrow spaces. Thus, robotic snakes, both rigid and soft, inspired by their biological counterparts are ideally suited for applications such as search and rescue operations and inspection tasks [245]. Soft robotic snakes (SRS) can generate smooth body deformation (bending) and are more adaptable to their surroundings than rigid robotic snakes due to their inherent compliance and continuous structures, making them the best candidate to emulate natural snake locomotion.

Snakes use friction anisotropy between snakeskin and the moving surface to generate forward propulsion necessary for planar locomotion [246]. But, typical SRS skin cannot generate anisotropic frictional forces, unless the snakeskin is improved by other means. Thus, some SRS prototypes, such as those reported in [247]–[250] utilize axially-mounted passive wheels to generate anisotropic frictional forces and achieve locomotion. The SRSs appeared in [172], [173], [175], [176] showed wheelless planar locomotion achieved through improved snakeskin with anisotropic frictional properties. There are SRSs that exhibit spatial deformation and achieve lateral undulation, sidewinding, and step-climbing gaits [251], [252]. However, they require passive wheels attached to their bodies. Wheels are cumbersome and can hinder locomotion. Additionally, wheels prevent achieving other types of snake locomotion gaits. Hence, wheeled SRSs are not suitable to study organic snake locomotion.

Note, no SRS that shows spatial rolling gaits exists. In our previous work [167], we proposed a pneumatically actuated SRS that was capable of spatial bending but was limited to achieving planar gaits including undulation and rolling. The SRS had only three bending sections and thus lacked adequate degrees of freedom (DoF) to lift the body off the ground and simultaneously maintain sufficient ground contact forces to generate a motion. Further, the bending sections do not contain a

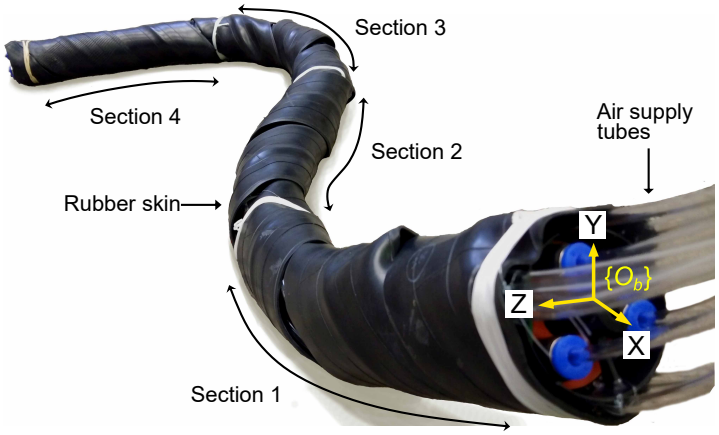

Figure 3.4: Four-section soft robotic snake prototype.

backbone and are thus subjected to length change during bending which can cause undesirable reaction forces that counteracted the forward progression.

Snakes tend to use spatial gaits when friction anisotropy does not exist (i.e., in deserts). For example, snakes use sidewinding to spatially move the body while minimizing concentrated ground contacts (similar to articulated limbs of octopi). In this work, we introduce spatial bendability as an alternative to overcome limitations associated with the anisotropic frictional forces and wheels of SRSs. Similar to snakes' spatial gaits, the idea is to maintain skin-ground contact at a minimum level. We propose an SRS prototype with four sections (Fig. 3.4) to circumvent the limitations of the previous SRS design [167]. Notably, the new SRS is inextensible as the bending sections have integrated backbones. The presence of a backbone makes the SRS design more bioinspired because similar to snakes it has a skeletal structure to support the locomotion.

3.2.2 Soft Robotic Snake Prototype

We adopt three, actuated DoF, hybrid soft module proposed in Sec. 3.1 to fabricate the 4-section SRS prototype shown in Fig. 3.4. We serially connect adjacent sections with a backbone length offset (50 mm), creating a hollow skeletal area between each section (refer to the enlarged image in Fig. 3.5A). Accordingly, the complete SRS has three identical length offsets between four sections along its body. These offsets – made as extensions of the backbone length itself – facilitate connecting pressure supply tubes to PMAs of each section while preserving the continuum nature of the complete SRS assembly. We wrap pressure supply tubes within the SRS body without obstructing its bendability as shown in

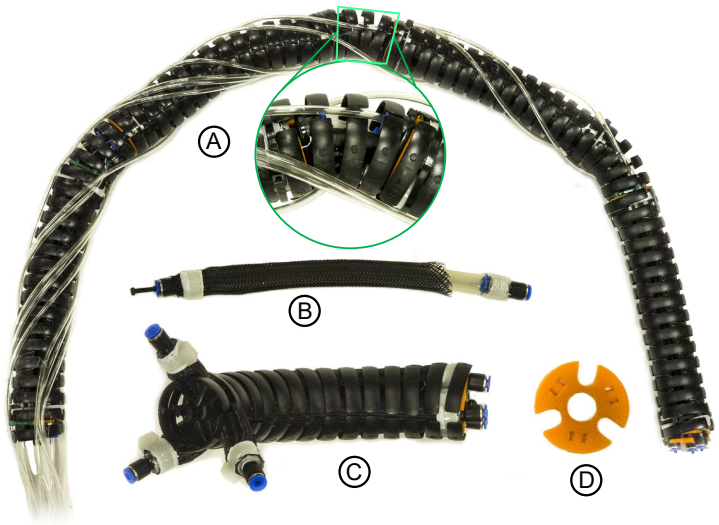

Figure 3.5: (A) SRS prototype – serially arranged four soft modules without its rubber skin showing spherically routed pressure supply tubes on the backbone outer shell. The enlarged image shows the backbone offset between adjacent sections. (B) A PMA–braided sleeve on the right side has been removed to show the Silicone tube sealed to a push-to-connect pneumatic union fitting. (C) One section with its PMA arrangement inside the backbone. (D) PMA mounting plates of each section.

Fig. 3.5A. To obtain a uniform snakeskin (hence uniform friction), a thin rubber sleeve is wrapped around the SRS body (Fig. 3.4). It covers routed pressure supply tubes and eliminates their adversarial effects during locomotion. The SRS has 12-DoF (3-DoF in each section) in total relative to its base. Physical parameters of the SRS are given in Table 3.1.

The hybrid design approach adopted here enables a higher stiffness control range with adequate structural integrity necessary for the SRS spatial locomotion [233], [253]–[258]. It should be noted, the backbone-integrated bending units (i.e., SRS sections) are heavier than the ones without a backbone. Hence, it is required to generate higher torques to overcome friction and weight during spatial bending. Thus, the presence of a backbone enables us to achieve bending at higher stiffnesses without significant torsion in SRS sections.

3.3 Soft-limbed Tetrahedral Robot

3.3.1 Motivation

Soft mobile robots are mostly designed to mimic the behavior (typically locomotive patterns) of biological creatures [6]. Compared to rigid mobile robots, the inherently compliant elements in soft mobile robots enable them to absorb ground impact forces without active impedance control [259].

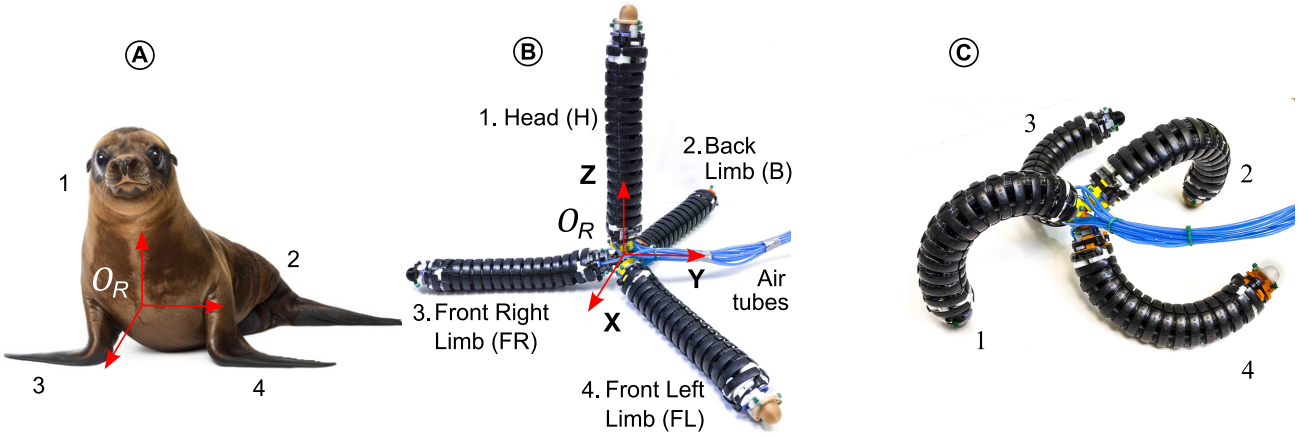

Figure 3.6: (A) Bioinspiration from pinnipeds (i.e., seals, sea lions, and walruses) that use fore flippers and body (or hind flipper) for terrestrial locomotion. Tetrahedral robot in (B) unactuated and (C) tumbling poses.

Table 3.1: Physical parameters of unactuated soft mobile robot prototype topologies.

Parameter	Robot Prototype		
	4-Section SRS	Tetrahedral	Quadruped
Length $[cm]$	110	45	32
Width $[cm]$	5	45	54
Height $[cm]$	5	30	4
Weight $[kg]$	0.94	0.69	0.85

Furthermore, their ability to deform actively and passively allows them to gain access to confined areas [9]. As a result, soft mobile robots have great potential to replace humans in performing dangerous tasks, such as nuclear site inspection [10], search and rescue operations [260], and planetary exploration [11].

Many soft-limbed robotic prototypes have been proposed to date [261]. For instance, the pneumatically actuated multi-gait robot reported in [37] uses five actuators to generate crawling and undulation gaits. However, it was only capable of preprogrammed straight locomotion without turning. The autonomous untethered quadruped in [38] is capable of carrying the subsystems (i.e., miniature air compressors, a battery, valves, and a controller). The robot can operate under adverse environmental conditions but only supports limited gaits. The quadruped in [24] can achieve various dynamic locomotion gaits such as crawling and trotting but without turning. The quadruped in [50] presents a new approach for controlling the gaits of soft-legged robots using simple pneumatic circuits without electronic components. The need for preprograming the gaits offers limited gait diversity. The soft robot prototypes reported in [17], [262] have stiffness-tunable limbs and are inspired by starfish, including its locomotion and water-vascular systems. But the low speed and low efficiency due to shape

memory alloy actuators limit their utility. The amphibious soft robot in [39] uses highly compliant limbs with no stiffness tunability and resulting in unstable and slow locomotion. The soft-limbed hexapod proposed in [75] showed the ability to derive a variety of gaits. The hexapod appeared in [65] showed the ability to traverse challenging terrains. The large number of limbs however increases the robots' complexity at the cost of limb dexterity. The soft-limbed robot proposed in [19] uses only four limbs in spatially symmetric tetrahedral topology. But due to the use of solenoid valves – binary actuation, it has limited control of the locomotion gaits. In addition, no analytical gait derivation approach was reported and only demonstrated preprogrammed locomotions.

3.3.2 Tetrahedral Robot Assembly

We propose a new soft-limbed pinniped robot to address the limitations discussed in Sec. 3.3.1. We adopt a modular design approach to increase the robustness and utilize hybrid soft limbs with improved payload and dexterous capabilities to fabricate the robot. In addition, we present a systematic approach to derive novel locomotion gaits. Further, we adopt a proportional limb bending mechanism to achieve improved workspace and control.

We connect four soft limbs using a 3D-printed tetrahedral joint to obtain the pinniped topology shown in Fig. 3.6B. Thus, the robot has 12-DoF (3-DoF per limb). The physical parameters of the tetrahedral assembly, excluding the pressure supply tubes, are provided in Table 3.1. In pinnipeds, the bulk of the mass is distributed toward the body (i.e., back end). However, we adopt this topology with symmetric mass distribution to optimize movements in all directions. Further, its spatial symmetry enables reorientation and thus better stability. Figure 3.6C illustrates an application of the tetrahedral robot for the energy-efficient tumbling locomotion as presented in our recent work [22].

3.4 Soft-limbed Quadrupedal Robot

3.4.1 Introduction

Soft mobile robots exhibit natural compliance, which can be tuned to achieve desired interactions with the environment [263]. This feature has led to the development of soft robots that can deform to adapt to various environments [261], [264]. Furthermore, recent advances in soft robotics have enabled

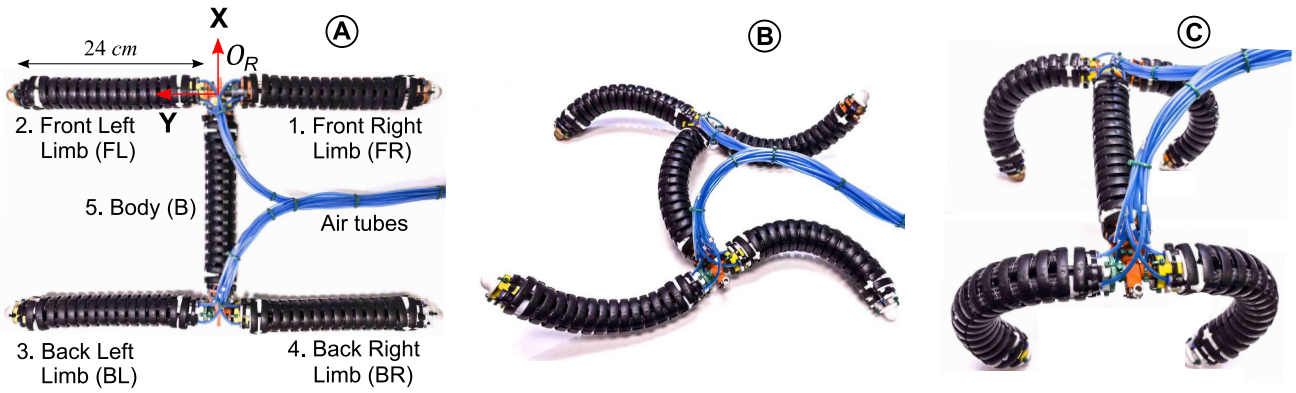

Figure 3.7: Quadrupedal robot in (A) unactuated pose, (B) crawling mode, and (C) trotting mode.

the integration of sensing and actuation capabilities, making them capable of performing tasks that were previously limited to rigid robots [265]. Soft mobile robots have the potential to perform a wide range of tasks, including inspection, surveillance, and search-and-rescue operations, by utilizing various gaits to navigate challenging and uneven terrains, which leads to an improvement in their operational reliability [4]. Nevertheless, achieving legged locomotion using soft limbs can be a complex task due to various factors such as limited deformation range and variety, inadequate control, and insufficient limb strength in existing prototypes. Hence, it is crucial to develop soft limbs that have appropriate bending stiffness and range while avoiding excessive coupling between deformation and stiffness.

3.4.2 Quadruped Prototype

The proposed quadruped (Fig. 3.7) is composed of five identical soft modules, namely, the Front Right (FR), Front Left (FL), Body (B), Back Left (BL), and Back Right (BR) limbs. In the assembly process, we utilize two hip-like joints that are 3D-printed to anchor the front and rear limbs symmetrically parallel to the body. Each PMA is pressurized independently using 4 mm Polyurethane tubes that are lightweight. These tubes are bundled and directed towards the center of gravity of the robot to minimize their effect on the robot's locomotion (Fig. 3.7A). The physical parameters of the quadruped assembly, excluding the pressure supply tubes, are given in Table 3.1. We opted for a symmetric planar limb arrangement to utilize the optimal workspace of soft limbs. The symmetric topology allows the robot to use the limbs in a similar way even if it topples. Additionally, the soft body enhances the dexterity of the robot and therefore maneuverability. For example, the soft body actuation can be used to turn the robot in a tight space with a smaller turn radius than traditional rigid-bodied soft-limbed

robots [24]. Figs. 3.7B and 3.7C show two locomotion modes that are applied to replicate quadrupedal movements as presented in [45] and [200].

3.5 Chapter Summary

This chapter focused on the design and fabrication of soft modules (or HSRs), addressing the challenges of achieving both stiffness and shape control in soft robots. By integrating soft and stiff elements, the proposed modular design enhances structural integrity and adaptability. Key components, such as the backbone and PMAs, were detailed, highlighting their roles in providing decoupled stiffness and shape control. The chapter also explored the application of modular units in assembling soft mobile robots with different topologies, including soft robotic snakes, tetrahedral soft-limbed robots, and soft-limbed quadrupedal robots. In the following chapter, we introduce modeling methodologies for the proposed soft module and mobile robot configurations.

Chapter 4

Modeling

4.1 Soft Robot (or Soft Module) Modeling

4.1.1 Soft Module Forward Kinematics

Consider the schematic diagram of the j-th soft module ($j \in \mathbb{Z}^+$) shown in Fig. 4.1A. Refer to the notations in Table 4.1. We define the soft module's body coordinate frame at the base $\boldsymbol{O_j}$ with PMA_{j1} overlapping the $+X_j$ axis. The jointspace variables of PMA_{ji} are denoted by l_{ji} and are positioned in the counterclockwise direction at an angle offset of $\frac{2\pi}{3}(i-1)$ from the $+X_j$ axis. Thus, at time t, if the initial length and length change of PMA are denoted by $L \in \mathbb{R}^+$ and $l_{ji}(t) \in \mathbb{R}$ respectively, where ($i \in \{1,2,3\}$) is the PMA number and , then $L_{ji}(t) = L + l_{ji}(t)$ denotes the length of PMA_{ji}. Therefore, the jointspace vector of the j-th module is defined as $\boldsymbol{q}_j = [l_{j1}(t), l_{j2}(t), l_{j3}(t)]^T$.

The bending of the soft module can be analyzed by assuming that the module's neutral axis (the line that runs along the center of the module) bends in a circular arc parameterized by the subtended angle, $\phi_j \in [0, \pi]$ rad, and the angle to the bending plane relative to the $+X_j$ axis, $\theta_j \in [-\pi, \pi]$ rad. The radius of this circular arc is $\frac{L}{\phi_j}$. Noting that the bending of the soft module is critical to the robot's locomotion, understanding the relationship between the PMA lengths and the curve parameters is important as controlling the PMA lengths enables the control of module shape and robot locomotion. The PMA lengths can be related to the curve parameters as given in [237] as

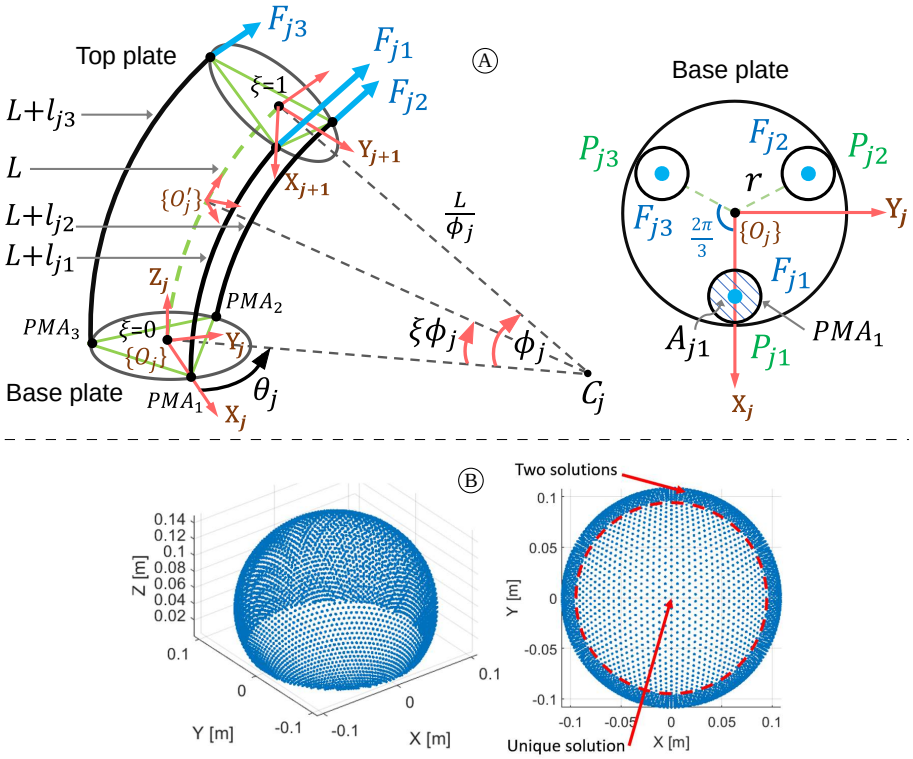

Figure 4.1: (A) Schematics of any j-th soft limb illustrating curve parameters and pneumatic pressure forces exerted on the base plate. (B) Spatial and top-down views showing the workspace symmetry of soft limb.

Table 4.1: Parameters and characteristics of the soft module.

Parameter	Details
L	Initial length [24 cm]
l_{ji}	i-th length change (or jointspace variable) of the j-th module
θ_j	Angle to the bending plane relative to the $+X_j$ axis of the j-th module $\in [-\pi, \pi]$
ϕ_j	Bending angle of the j-th module $\in [0, \pi]$
r_j	Radius of the j-th module [2 cm]
O_j	Origin of the j-th module's body coordinate frame

$$
\begin{aligned}
L + l_{ji} &= \left\{ \frac{L}{\phi_j} - r\cos\left(\frac{2\pi}{3}(i-1) - \theta_j\right) \right\} \phi_j, \\
l_{ji} &= -r_j \phi_j \cos\left(\frac{2\pi}{3}(i-1) - \theta_j\right).
\end{aligned} \tag{4.1}
$$

Note that, the inextensibility of the soft module implies that the sum of PMA length changes becomes zero, i.e., $\sum_i l_{ji} = 0$. This kinematic constraint gives rise to a relationship between the three joint variables, i.e., $l_{j1} = -(l_{j2} + l_{j3})$, which implies that the soft module forward kinematics can be obtained using just two DoFs. Employing (4.1), we can derive the curve parameters in terms of the joint variables as

$$\begin{aligned}\phi_j &= \frac{2}{3r}\sqrt{\sum_{i=1}^{3}\left(l_{ji}^2 - l_{ji}l_{j\mathrm{mod}(i,3)+1}\right)},\\ \theta_j &= \arctan\left\{\sqrt{3}\left(l_{j3}-l_{j2}\right), l_{j2}+l_{j3}-2l_{j1}\right\}.\end{aligned} \tag{4.2}$$

Following [237], ϕ_j and θ_j can be used to obtain the homogeneous transformation matrix (HTM) of any j-th soft module, $\mathbf{T}_j \in \mathbb{SE}(3)$ as

$$\begin{aligned}\mathbf{T}_j(\boldsymbol{q},\xi) &= \mathbf{R}_Z(\theta_j)\,\mathbf{P}_X\left(\frac{L}{\phi_j}\right)\mathbf{R}_Y(\xi\phi_j)\,\mathbf{P}_X\left(-\frac{L}{\phi_j}\right)\mathbf{R}_Z(-\theta_j)\\ &= \begin{bmatrix}\mathbf{R}_j(\boldsymbol{q},\xi) & \mathbf{p}_j(\boldsymbol{q},\xi),\\ 0 & 1\end{bmatrix},\end{aligned} \tag{4.3}$$

where $\mathbf{R}_Z \in \mathbb{SO}(3)$, $\mathbf{R}_Y \in \mathbb{SO}(3)$, $\mathbf{P}_X \in \mathbb{R}^3$, $\mathbf{R}_j \in \mathbb{SO}(3)$, and $\mathbf{p}_j \in \mathbb{R}^3$ denoting the rotation matrices about $+Z_j$, $+Y_j$ axes, translation matrix along the $+X_j$ axis, and the homogeneous rotation and position matrices, in order. The scalar $\xi \in [0,1]$ denotes any position on the limb's center line (Fig. 4.1A).

Fig. 4.1B shows the soft module's tip taskspace generated using the kinematic model in (4.3). It is worth reporting that, in comparison to designs without backbones (i.e., variable-length designs), the soft module's taskspace is symmetric about the +Z axis of the robot coordinate system. Whereas the taskspace of robot designs without backbones is tri-symmetric about the +Z axis. In addition, the taskspace is essentially a thin shell (without volumetric coverage). In contrast, designs without backbones have a nonzero volume due to extension (or contraction) [237]. The loss of a DoF also results in a one-to-one mapping between the jointspace and curve parameters (configuration space). This feature lets one perform the computations using curve parameters and derive jointspace solutions. This approach is not feasible with variable-length robots as the curve parameters describing the arc radius and subtended angle are coupled [237].

4.1.2 Soft Module Inverse Kinematics

The relationship between the curve parameters and taskspace coordinates at the tip (i.e., $\xi = 1$), $\mathbf{p}_j$ of (4.3), is given by

$$x_j = L\phi_j^{-1}\cos(\theta_j)\{1-\cos(\phi_j)\}, \tag{4.4a}$$

$$y_j = L\phi_j^{-1}\sin(\theta_j)\{1-\cos(\phi_j)\}, \text{ and} \tag{4.4b}$$

$$z_j = L\phi_j^{-1}\sin(\phi_j), \tag{4.4c}$$

where x_j, y_j, and z_j are the position vector elements w.r.t. the soft limb body coordinates frame, $\{\boldsymbol{O_j}\}$.

Recall that, because of the length constraint imposed by the backbone (Sec. 3.1.2), there are only two kinematic DoFs. Thus we can use two taskspace variables, x_j and y_j, to derive the curve parameters θ_j and ϕ_j. This can be done by solving for (4.5) that maps taskspace to curve parameters. Note that, there is no closed-form solution to (4.5). Thus, in this work, we utilize MATLAB's 'fmincon' constrained optimization routine to solve it.

$$\theta_j = \arctan(y_j, x_j), \tag{4.5a}$$

$$\phi_j^{-1}\{1-\cos(\phi_j)\} = L^{-1}\sqrt{x_j^2+y_j^2}. \tag{4.5b}$$

4.1.3 Soft Module Jointspace Jacobian

Jacobian relates the changes in the jointspace curve parameters, (θ_{ji}, ϕ_{ji}), to the changes in lengths, l_{ji}. Combining the results in (4.1) with the kinematic constraint, $l_{j1} = -(l_{j2}+l_{j3})$, Jacobian, J, with respect to θ_{ji} and ϕ_{ji} for l_{ji} can be obtained as

$$J = \begin{bmatrix} \frac{\partial l_1}{\partial \theta} & \frac{\partial l_1}{\partial \phi} \\ \frac{\partial l_2}{\partial \theta} & \frac{\partial l_2}{\partial \phi} \end{bmatrix} \tag{4.6}$$

Substituting the partial derivatives, we get

$$J = \begin{bmatrix} r\phi\sin(\theta) & -r\cos(\theta) \\ 0.5r\phi(-\sin(\theta)-\sqrt{3}\cos(\theta)) & 0.5r(\cos(\theta)-\sqrt{3}\sin(\theta)) \end{bmatrix} \tag{4.7}$$

This is the reduced 2×2 Jacobian matrix that captures the independent relationships of the system.

4.1.4 Soft Module Kinetostatics

Refer to the force, F_{ji}, exerted on the base plate due to the distributed pneumatic pressure, P_{ji} of PMAs, as depicted in Fig. 4.1A. An imbalance in pressure across PMAs generates a force disparity, leading to a net torque at the tip relative to $\{O_j\}$, inducing the bending of the limb. Following standard sign convention, the X, Y, Z components of the torque M_{ji}, generated by each F_{ji}, can be written as

$$M_{ji}|_X = 0F_{j1} + rF_{j2}\sin\left(\frac{\pi}{3}\right) - rF_{j3}\sin\left(\frac{\pi}{3}\right), \tag{4.8a}$$

$$M_{ji}|_Y = -rF_{j1} + rF_{j2}\cos\left(\frac{\pi}{3}\right) + rF_{j3}\cos\left(\frac{\pi}{3}\right), \tag{4.8b}$$

$$M_{ji}|_Z = 0. \tag{4.8c}$$

Assuming a uniform cross-sectional area A_{ji} exists in each PMA, then $F_{ji} = P_{ji}\ A_{ji}$ and, (4.8) can be further deduced as

$$M_{ji}|_X = \frac{\sqrt{3}A_{ji}r}{2}\left(P_{j2} - P_{j3}\right), \tag{4.9a}$$

$$M_{ji}|_Y = \frac{A_{ji}r}{2}\left(-2P_{j1} + P_{j2} + P_{j3}\right). \tag{4.9b}$$

Utilizing results in (4.9), the net bending torque which incorporates pneumatic actuation pressures, is expressed by (4.10), where K_b represents the bending stiffness.

$$M_{ji}|_{Net} = \sqrt{\left(M_{ji}|_X\right)^2 + \left(M_{ji}|_Y\right)^2} = K_b\phi_j. \tag{4.10}$$

4.2 Soft Robotic Snake (SRS) Modeling

4.2.1 SRS Kinematics

In the proposed SRS, the kinematics of a single SRS section can be serially extended to obtain the kinematics of the complete SRS. The kinematics of a single section (or module) has been in detail discussed in Sec. 4.1 [254], [266], [267]. Herein, we extend it to obtain the kinematics of the SRS skin. Considering any j-th section ($j \in \{1, 2, 3, 4\}$) of the SRS, Fig. 4.1 illustrates the kinematic diagram thereof. Due to redundant kinematic DoF in soft modules (Sec. 4.2.1), we can express the jointspace variable for the i-th section as $q_j = [l_{j1}, l_{j2}]^T$. By adopting modal kinematics proposed in [237], we can derive the homogeneous transformation matrix (HTM), $\mathbf{T_j} \in \mathbb{SE}(3)$ of any point on the surface (skin)

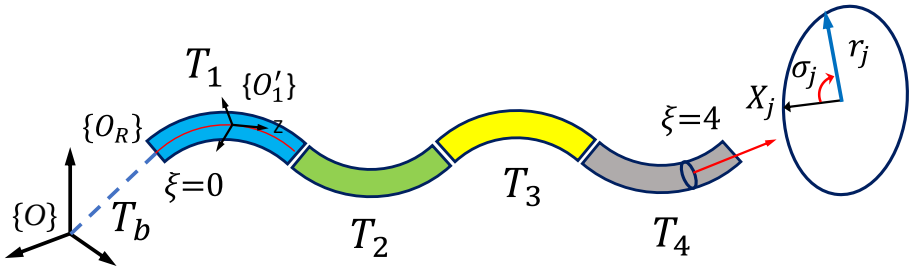

Figure 4.2: 4-section SRS showing the global, robot, and local coordinates frames and kinematic parameters.

of the i-th section as

$$\mathbf{T}_j\left(\boldsymbol{q}_j,\xi_j\right)=\begin{bmatrix}\mathbf{R}_j\left(\boldsymbol{q}_j,\xi_j\right) & \mathbf{p}_j\left(\boldsymbol{q}_j,\xi_j\right)\\ \mathbf{0} & 1\end{bmatrix}\begin{bmatrix}\mathbf{R}_z\left(\sigma_j\right) & \mathbf{0}\\ \mathbf{0} & 1\end{bmatrix}\begin{bmatrix}\mathbf{1} & \mathbf{p}_x\left(r_j\right)\\ \mathbf{0} & 1\end{bmatrix}, \tag{4.11}$$

where $\mathbf{R}_j(\sigma_j)\in\mathbb{SO}\left(3\right)$ and $\mathbf{p}_j\in\mathbb{R}^3$ denotes the rotation matrix and position vector of a point on the neutral axis.

A point on the skin of the i-th section is obtained by translating HTM in (4.11) by $\mathbf{R}_z\in\mathbb{SO}\left(3\right)$ and $\mathbf{p}_x(r_j)\in\mathbb{R}^3$ where $\sigma_j\in[0,\ 2\pi]$ and $r_i\in\mathbb{R}$ are the angular offset (Z^+) and the position offset (X^+) of the surface point from the neutral axis. $\xi_j\in[0,1]$ is a selection factor for points along the neutral axis such that 0 gives the base point and 1 gives the tip location. When the SRS moves, its base at $\{O_b\}$ floats on the global coordinate frame, $\{O\}$. By combining a floating-base coordinate frame, $\mathbf{T}_b$, we define the kinematic model of the complete SRS as

$$\mathbf{T}\left(\boldsymbol{q}_b,\boldsymbol{q}_r,\xi\right)=\mathbf{T}_b\left(\boldsymbol{q}_b\right)\prod_{j=1}^{4}\mathbf{T}_j\left(\boldsymbol{q}_j,\xi_j\right)=\begin{bmatrix}\mathbf{R}\left(\boldsymbol{q}_b,\boldsymbol{q}_r,\xi\right) & \mathbf{p}\left(\boldsymbol{q}_b,\boldsymbol{q}_r,\xi\right)\\ \mathbf{0} & 1\end{bmatrix}, \tag{4.12}$$

where $\boldsymbol{q}_r=[\boldsymbol{q}_1,\boldsymbol{q}_2,\boldsymbol{q}_3,\boldsymbol{q}_4]\in\mathbb{R}^{12}$ is the vector that contains all joint variables and $\xi=[0,4]\in\mathbb{R}$ selects a point along the SRS (i.e., SRS base at $\xi=0$, and SRS tip at $\xi=4$). $\boldsymbol{q}_b=[x_b,y_b,z_b,\alpha,\beta,\gamma]\in\mathbb{R}^6$ defines translation and angular offsets of $\{O_b\}$ relative to $\{O\}$ (Fig. 4.2).

4.2.2 SRS Dynamics

For the dynamic modeling, we consider the 3-section version of the SRS prototype shown in Fig. 3.4. The SRS dynamic modeling includes two components; robot-ground contact dynamics which includes

the distributed contact dynamics along the robot snakeskin and complete SRS dynamics which presents the equations of motion (EoM) of the SRS.

A. Robot-Ground Contact Dynamics

We extend the dynamic model derived for variable–length multisection continuum robotic manipulators reported in [221] to model the SRS considered here. However, the dynamic model cannot be directly utilized for modeling the SRS. Because, therein, the continuum manipulator has a fixed base whereas SRS achieves locomotion via different gaits. In addition, the model does not handle external forces. But, similar to snakes, the SRS achieves locomotion when its skin-like outer layer makes distributed contact with a surface and generates reaction forces via friction.

Hence, we modify the model reported in [221] to include a floating coordinate frame to support locomotion modeling and distributed contact dynamics and use it as a snake. The utility of moving coordinate systems on soft locomoting robots has been explored in [24], [268]. However, implementing continuous contact dynamics is computationally inefficient. We use a discrete model with an array of finely distributed contact points defined along the periphery of the SRS by introducing two parameters, $\xi \in [0, 3]$ and $\sigma_j \in [0, 2\pi]$ which discretize the SRS surface into 31 points axially and 10 points radially as shown in (4.11) and (4.12). This results in 310 contact points on the outer layer of the SRS. We compute the reaction forces of those points when contact conditions are met using a spring-damper ground model (Fig. 4.3). We define a ground contact condition as when the z coordinate of a contact point with respect to $\{O\}$ is negative, i.e., $z < 0$, [269]. As long as this condition is met, the reaction forces are continuously computed and added to the SRS dynamic model as follows. Without losing generality, let the z component of the ground reaction force at any contact point (defined by ξ_j and σ_k), be $F_{jk|z}$ and given by

$$F_{jk|z} = -\frac{1}{2}\left(1 - \text{sign}\left(z\right)\right)\left(K_g z + B_g \dot{z}\right), \tag{4.13}$$

where K_g and B_g are the ground stiffness and damping coefficients, respectively.

Here, we assume that the ground stiffness is sufficiently large (i.e., high K_g) and thus z is negligible such that our point-contact model is valid. To achieve locomotion, there must be net reaction forces on the $X - Y$ plane (Fig. 4.3). From standard ground friction models, we can compute the complete

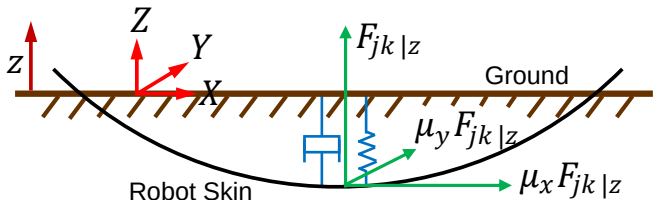

Figure 4.3: Contact dynamic model (condition for the ground contact: $z < 0$). The displacements are exaggerated for visualization.

reaction force F_{jk} as

$$\mathbf{F}_{jk} = F_{jk|z} \begin{bmatrix} \mu_x \text{sign}\,(\dot{x}) & \mu_y \text{sign}\,(\dot{y}) & 1 \end{bmatrix}^T, \tag{4.14}$$

where μ_x and μ_y are the static reaction coefficients in the X and Y directions respectively.

B. Complete SRS Dynamics

We assume that an SRS section is made of a set of infinitesimally thin slices with constant mass and uniform linear density. Using the floating base kinematics derived in (4.12), we calculate the kinetic and potential energies of a thin slice and integrate them to find the total energies of bending sections. We then apply the Lagrangian mechanics-based recursive computation scheme proposed in [221] to derive the EoM of the SRS as

$$\mathbf{M}\ddot{q} + (\mathbf{C} + \mathbf{D})\,\dot{q} + \mathbf{G} = \begin{bmatrix} 0 \\ \boldsymbol{\tau}_e \end{bmatrix} + \sum_{j\in\xi, k\in\sigma} \mathbf{J}_{jk}^T \mathbf{F}_{jk}, \tag{4.15}$$

where $\mathbf{M} \in \mathbb{R}^{15\times15}$ is the generalized inertia matrix, $\mathbf{C} \in \mathbb{R}^{15\times15}$ is the centrifugal and Coriolis force matrix, $\mathbf{D} \in \mathbb{R}^{15\times15}$ is the damping force matrix, and $\mathbf{G} \in \mathbb{R}^{15}$ is the conservative force vector. Here, $\boldsymbol{\tau}_e \in \mathbb{R}^9$ defines the pressure force vector and $\mathbf{J}_{jk}$ defines the Jacobian, which maps $\mathbf{F}_{jk}$ into jointspace $\boldsymbol{q}$. Note that, this dynamic model does not consider the hysteretic effects as it is negligible compared to the damping effect [221].

In the recursive formulation employed here, the terms in (4.15) can be separated into contributions from each j^{th} SRS bending section. For instance, the generalized inertia matrix can be written as $\mathbf{M} = \sum_{j=1}^{3} \mathbf{M}_j$ where $\mathbf{M}_j$ is the inertia matrix of the j^{th} SRS bending section given by

$$[\mathbf{M}_j]_{uv} = m_j \int_{\xi_j} \frac{\partial \boldsymbol{p}_j^T}{\partial \boldsymbol{q}_u} \frac{\partial \boldsymbol{p}_j}{\partial \boldsymbol{q}_v}, \tag{4.16}$$

where m_j is the mass of the j^{th} section, and $\{u, v\} \in \mathbb{Z}^+ \wedge [1, \cdots, 15]$ denotes the matrix element index.

For any j^{th} SRS section, the elements of the centrifugal and Coriolis force matrix, $\mathbf{C}_j \in \mathbb{R}^{15\times15}$ can be derived from the partial derivatives of $\mathbf{M}_j$ as reported in [221],

$$[\mathbf{C}_j]_{vu} = \sum_{h=1}^{15} {}_{vuh}\left(\mathbf{M}_j\right)\dot{q}_h, \text{and} \tag{4.17}$$

$$[\mathbf{M}_j]_{vuh} = \frac{1}{2}\left(\frac{\partial[\mathbf{M}_j]_{vu}}{\partial q_h} + \frac{\partial[\mathbf{M}_j]_{vh}}{\partial q_u} - \frac{\partial[\mathbf{M}_j]_{hu}}{\partial q_v}\right). \tag{4.18}$$

Recursively, $\mathbf{C} = \sum_{j=1}^{3}\mathbf{C}_j$ gives the complete centrifugal and Coriolis force matrix.

Damping force matrix, $\mathbf{D}_i$ for any j^{th} SRS section can be written as a diagonal matrix such that, $\mathbf{D}_i = diag([D_{j1}, D_{j2}, D_{j3}]) \in \mathbb{R}^{3\times3}$. Then, $\mathbf{D} = \sum_{j=1}^{3}\mathbf{D}_j$ gives the complete damping force matrix.

The conservative force vector for any j^{th} SRS section, $\mathbf{G}_j$ can be written as

$$\mathbf{G}_j = \mathbf{K}_j q_j + m_j \int_{\xi_j} \frac{\partial \boldsymbol{p}_j^T}{\partial q_j}\boldsymbol{g}, \tag{4.19}$$

where $\mathbf{K}_j$ is the elastic stiffness coefficient matrix of any j^{th} SRS section. It can be written as a diagonal matrix such that, $\mathbf{K}_j = diag([K_{j1}, K_{j2}, K_{j3}]) \in \mathbb{R}^{3\times3}$. $\boldsymbol{g} = [0, 0, g]^T$ is the gravitational acceleration vector.

Employing the recursive approach, the complete conservative force vector can be written as $\mathbf{G} = \sum_{j=1}^{3}\mathbf{G}_j$. The readers are referred to [221] for a detailed derivation of the EoM.

4.3 Soft-limbed Tetrahedral Robot Modeling

Refer to the schematic of the robot shown in Fig. 4.4A. Utilizing (4.3), the HTMs of limbs, $\mathbf{T}_{Limb_j} \in \mathbb{SE}(3)$ relative to the robot coordinates frame, $\{\boldsymbol{O}_R\}$, located at the geometric center of the tetrahedral joint can be expressed as

$$\mathbf{T}_{Limb_1}(q_1, \xi) = \mathbf{T}_1(q_1, \xi), \tag{4.20a}$$

$$\mathbf{T}_{Limb_2}(q_2, \xi) = \mathbf{R}_Y\left(\frac{\pi}{2} + \delta\right)\mathbf{R}_Z(\pi)\,\mathbf{T}_2(q_2, \xi), \tag{4.20b}$$

$$\mathbf{T}_{Limb_3}(q_3, \xi) = \mathbf{R}_Y\left(\frac{\pi}{2} + \delta\right)\mathbf{R}_Z\left(\frac{5\pi}{3}\right)\mathbf{T}_3(q_3, \xi), \tag{4.20c}$$

$$\mathbf{T}_{Limb_4}(q_4, \xi) = \mathbf{R}_Y\left(\frac{\pi}{2} + \delta\right)\mathbf{R}_Z\left(\frac{7\pi}{3}\right)\mathbf{T}_4(q_4, \xi), \tag{4.20d}$$

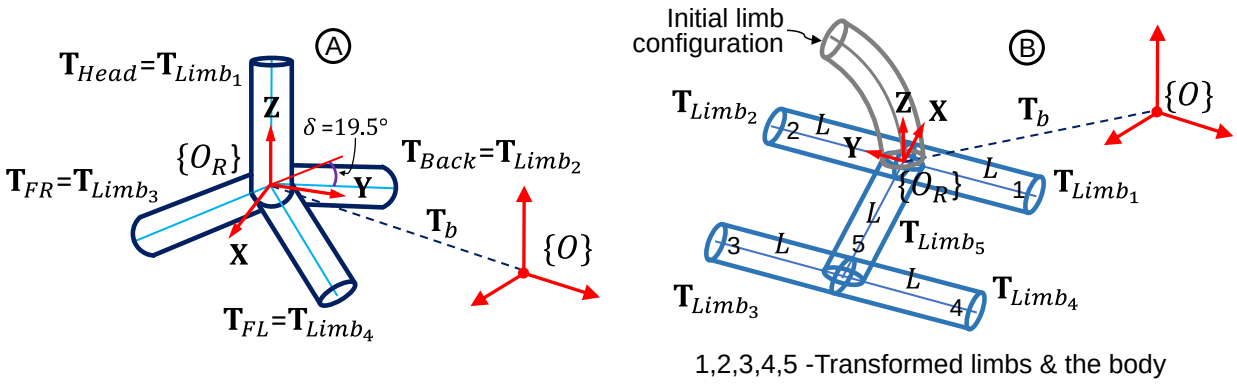

Figure 4.4: Schematic of the (A) tetrahedral and (B) quadruped robots showcasing the transformations at the limb level.

where δ is 19.47° (Fig. 4.4A) computed from the tetrahedral geometry. The complete kinematic model of the j-th limb of the robot can be obtained utilizing (4.20) with a floating-base coordinate frame, $\mathbf{T}_b \in \mathbb{SE}(3)$ as below.

$$\mathbf{T}_{Limb_j}(q_b, q_j, \xi) = \mathbf{T}_b(q_b)\,\mathbf{T}_{Limb_j}(q_j, \xi), \tag{4.21}$$

$$\mathbf{T}_b(q_b) = \begin{bmatrix} \mathbf{R}_Z(\alpha)\,\mathbf{R}_Y(\beta)\,\mathbf{R}_X(\gamma) & \mathbf{p}_b \\ 0 & 1 \end{bmatrix}. \tag{4.22}$$

Herein, $q_b = [x_b, y_b, z_b, \alpha, \beta, \gamma]$ with $[\alpha, \beta, \gamma]$ and $\mathbf{p}_b = [x_b, y_b, z_b]^\mathsf{T}$ denote the orientation and translation variables of $\{\boldsymbol{O}_R\}$ relative to the global coordinate frame $\{\boldsymbol{O}\}$.

4.4 Soft-limbed Quadrupedal Robot Modeling

Refer to the soft modules assembled as a quadruped in Fig. 4.4B. The robot coordinate frame, $\{\boldsymbol{O}_R\}$ is positioned at the anchoring point of FR and FL limbs with the body (Limb B). HTMs of four limbs and the body, $\mathbf{T}_{Limb_j} \in \mathbb{SE}(3)$ relative to $\{\boldsymbol{O}_R\}$ can be expressed as

$$\begin{aligned}
\mathbf{T}_{Limb_1}(q, \xi) &= \mathbf{R}_X\left(\frac{\pi}{2}\right)\mathbf{R}_Z\left(-\frac{\pi}{2}\right)\mathbf{T}_1(q_1, \xi) \\
\mathbf{T}_{Limb_2}(q, \xi) &= \mathbf{R}_X\left(-\frac{\pi}{2}\right)\mathbf{R}_Z\left(\frac{\pi}{2}\right)\mathbf{T}_2(q_2, \xi) \\
\mathbf{T}_{Limb_5}(q, \xi) &= \mathbf{R}_Y\left(-\frac{\pi}{2}\right)\mathbf{R}_Z(\pi)\,\mathbf{T}_5(q_5, \xi) \\
\mathbf{T}_{Limb_3}(q, \xi) &= \mathbf{T}_{Limb_5}\mathbf{R}_X\left(-\frac{\pi}{2}\right)\mathbf{R}_Z\left(\frac{\pi}{2}\right)\mathbf{T}_3(q_3, \xi) \\
\mathbf{T}_{Limb_4}(q, \xi) &= \mathbf{T}_{Limb_5}\mathbf{R}_X\left(\frac{\pi}{2}\right)\mathbf{R}_Z\left(-\frac{\pi}{2}\right)\mathbf{T}_4(q_4, \xi)
\end{aligned} \tag{4.23}$$

where $\{\mathbf{R}_X, \mathbf{R}_Y, \mathbf{R}_Z\} \in \mathbb{SO}(3)$ are homogeneous rotation matrices about the $+X_j$, $+Y_j$, $+Z_j$ axes. $\mathbf{T}_j \in \mathbb{SE}(3)$ is the result in (4.3). Similar to (4.21), a floating-base coordinate system, $\mathbf{T}_b \in \mathbb{SE}(3)$ can be incorporated with (4.23) to obtain the complete kinematic model of any j-th limb of the robot as given in (4.24).

$$\mathbf{T}_{Limb_j}(q_b, q, \xi) = \mathbf{T}_b(q_b)\,\mathbf{T}_{Limb_j}(q, \xi) \tag{4.24}$$

4.5 Chapter Summary

This chapter focused on the modeling of soft robots, starting with the forward and inverse kinematics of soft modules to understand and control their movements based on PMA lengths. It discussed the kinetostatics of the modules, analyzing internal forces and torques. The chapter extended the modeling to the kinematic and dynamic aspects of the soft robotic snake, and detailed the complete kinematics of the tetrahedral and quadrupedal robot. In the subsequent chapter, the proposed modeling approaches are utilized to generate locomotion trajectories for soft mobile robots.

Chapter 5

Locomotion Trajectory Generation

5.1 Trajectory Generation of Soft Robotic Snake

5.1.1 Methodology

We generate locomotion trajectories to move the soft robotic snake (SRS). Snakes show periodic locomotion, and hence, their locomotion gaits can be modeled as periodic mathematical curves. First, we mathematically model the desired locomotion gait (i.e., trajectory) on the global coordinate frame (i.e., robot taskspace). Next, one period of the identified trajectory curve (i.e., the mathematical curve) is discretized and the curve at discretized locations is projected onto the robot coordinate frame; this is referred to as trajectory sampling and coordinate transformation (from the global frame to the local frame). Finally, the inverse kinematic solution of (4.12) is applied to convert the local taskspace (i.e., local curve points – x, y, z) into jointspace variables required to actuate the robot.

5.1.2 Defining SRS Locomotoin Trajectories

A. Sidewinding Gait

A time-series (t) sidewinding curve shown in Fig. 5.1A, is given by,

$$\begin{aligned} y(t) &= A_y \sin(2\pi f_y t), \\ z(t) &= A_z \sin(2\pi f_z t + \beta), \end{aligned} \tag{5.1}$$

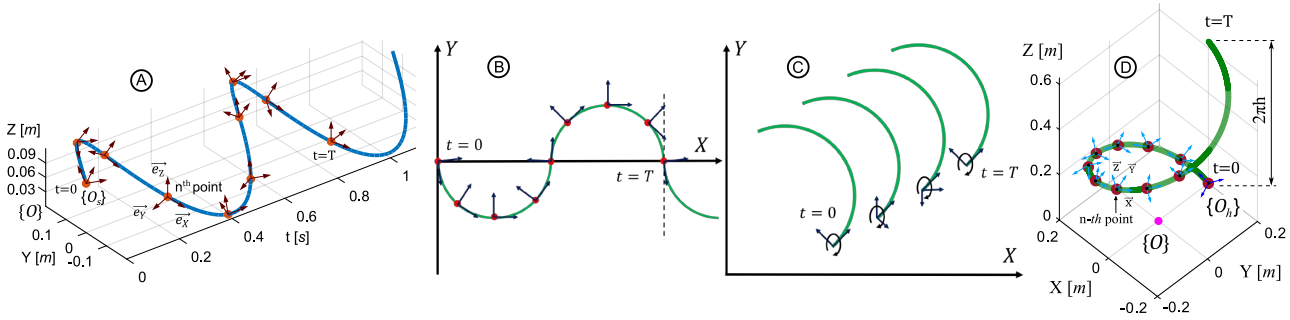

Figure 5.1: Periodic discretization of (A) sidewinding, (B) serpentine, (C) planar rolling, and (D) helical rolling trajectories relative to the global frame, $\{O\}$.

where A_y, A_z, and f_y, f_z define amplitudes and frequencies of y and z curve segments, respectively. Herein, β denotes the phase shift between two curve segments.

B. Serpentine Gait

The serpentine curve is given by

$$x(s) = \int_0^s \cos(a\cos(b\sigma) + c\sigma)\, d\sigma$$
$$y(s) = \int_0^s \sin(a\cos(b\sigma) + c\sigma)\, d\sigma \tag{5.2}$$

where $a = -\frac{pi}{4}$, $b = \frac{pi}{4}$, $c = 0$, and $z(s) = 0$.

Figure 5.1B shows the progression of the serpentine gait in one cycle. The dots along the serpentine curve denote the origin of the robot coordinate frame at the sampling time instances.

C. Planar Rolling Gait

The rolling gait can be modeled as a mathematical curve – in this case, the displacement of a circular arc with radius r_R, in the rolling gait. Figure 5.1C shows the taskspace trajectories of outward rolling locomotion. One cycle of the rolling gait is defined as the rotation of the curve about its longitudinal axis (Z-axis in the robot coordinate frame), and the robot displacement on the $X-Y$ plane is due to the thickness of the robot that can be derived as $2\pi r_i$, where r_i is the radii of soft modules. From one period of a gait, we derive spatial shapes from the curve at different time intervals within one locomotion cycle to obtain different spatial shapes resembling the snake shape at each of those instances.

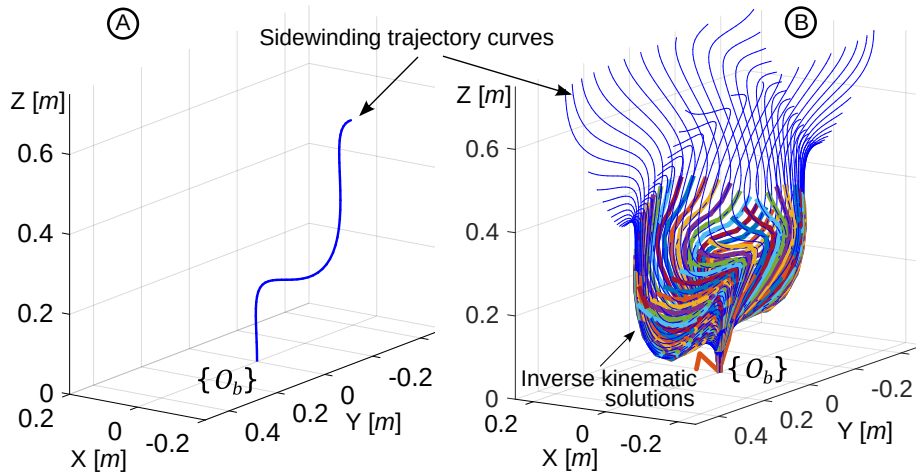

Figure 5.2: In sidewinding trajectory – (A) a discretized curve at $t = 0$ projected onto the robot coordinate frame, $\{O_b\}$, (B) generated trajectory curves after projecting all discretized curve points onto $\{O_b\}$ and matched jointspace trajectories (i.e., inverse kinematic solutions).

D. Helical Rolling Gait

Helical rolling (i.e., 3D/spatial rolling) is an extension of the planar rolling. We utilize a general formulation of a helix, as shown in Fig. 5.1D, to parameterize the taskspace for helical rolling as

$$\begin{aligned} x(t) &= A\cos(2\pi f t), \\ y(t) &= A\sin(2\pi f t), \\ z(t) &= 2\pi h f t, \end{aligned} \tag{5.3}$$

where $A \in \mathbb{R}^+$ and $f \in \mathbb{R}^+$ are the radius and frequency of the helical wave, respectively. And $h \in \mathbb{R}^+$ is the pitch, defined by $2\pi h$, that represents the separation between consecutive turns along the Z-axis.

5.1.3 Deriving SRS Taskspace Trajectories

Consider the sidewinding curve depicted in Fig. 5.1A. To derive the task-space trajectory, we isolate the portion of the mathematical curve to depict one cycle, which can be achieved by taking the period of the locomotion, $\tau = \frac{1}{f}$. First, we uniformly discretize the curve at marked locations such that those points designate the origin of the robot coordinate frame, $\{O_b\}$ at the discretized time instances. Next, we derive local coordinate frames at each point relative to $\{O\}$. At any n^{th} point, the local coordinate frame can be defined as a tangential line to the curve (let it be local X) and a line normal to that (let it be local Y). If $\overrightarrow{e_X}$ and $\overrightarrow{e_Y}$ define unit vectors along the local X and local Y, respectively, then $\overrightarrow{e_X} \times \overrightarrow{e_Y}$ gives the unit vector along the local Z. We encapsulate this orientation data with the discretized

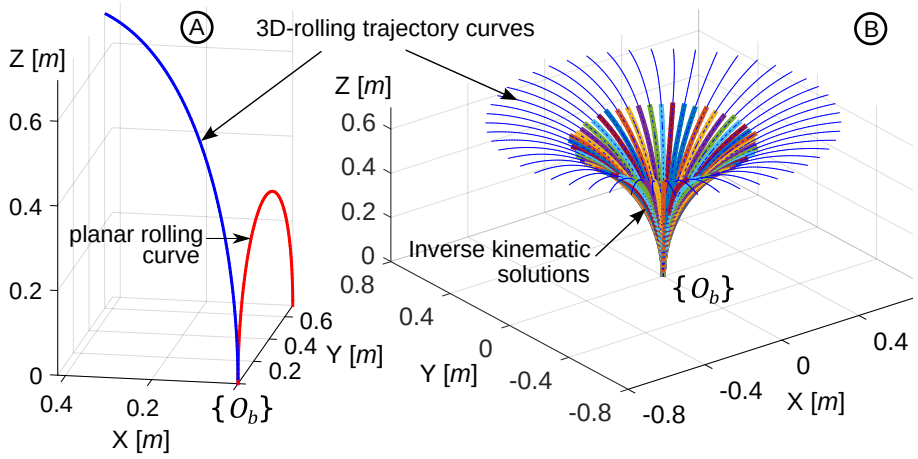

Figure 5.3: (A) A trajectory curve projected onto $\{O_b\}$ in planar and helical rolling. (B) Projected total trajectory curves onto $\{O_b\}$ and generated jointspace trajectories (inverse kinematic solutions) in helical rolling.

position data to derive the local HTM at each point relative to $\{O\}$ along the curve. Then, these local HTMs at each instance are utilized to project the sidewinding curve onto $\{O_b\}$. Figures 5.2A and 5.3A show the projection of the taskspace curve of the sidewinding and helical rolling gaits at the time instance, $t = 0$ onto $\{O_b\}$, respectively. Similar to that, all subsequent taskspace curves at each discretized time instance within the trajectory period, T are projected onto $\{O_b\}$ as depicted by thin blue lines in Fig. 5.2B and 5.3B. This process is repeated for other locomotion gaits as well.

5.1.4 Obtaining SRS jointspace Trajectories

We obtain the SRS joint variables by mapping the trajectory curves at $\{O_b\}$ (i.e., local taskspace curves) into the SRS jointspace using inverse kinematics [270], [271]. However, it is impossible to obtain closed-form inverse kinematic solutions for multi-section continuum robots [237] such as the 4-section SRS proposed here. For that reason, we formulate the solution for the inverse kinematics as an optimization problem between the desired local trajectory curves and the SRS forward kinematics [268]. Therein, we apply the kinematic model in (4.12) to obtain uniformly distributed points (61 points – 15 per section) along the SRS neutral axis. Correspondingly, the cost function is formulated as

$$f_{cost} = \sum_{k=1}^{61} \left\| \mathbf{p}\left(0, q, \xi_k\right) - f_{gait}\left(s\right) \right\| + \sum_{j\in\{1,2,3\}}^{i\in\{1,2,3,4\}} l_{ij}^2, \tag{5.4}$$

where, $\xi_k = \xi$ given in (4.12) is discretized into 61 points along the SRS and $f_{gait}\left(s\right)$ is the trajectory curve (with $s = 61$ discretized points) to which the SRS should fit.

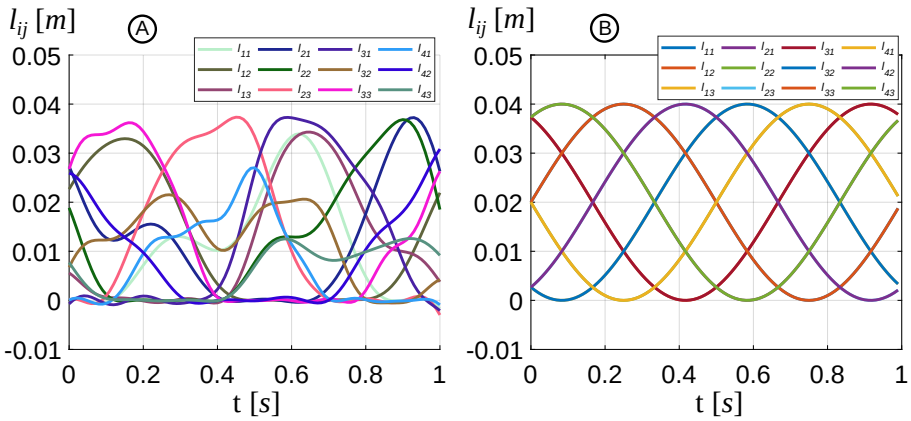

Figure 5.4: Optimization results, i.e., matched jointspace trajectories (length changes) for (A) sidewinding and (B) helical rolling gaits. In helical rolling, the length variables of section 1 and section 4 overlap each other due to the phase shift applied.

The latter term of (5.4) ensures the stability and the smoothness of the optimized solution. We implemented (5.4) using MATLAB's global constrained optimization routine. Figures 5.2B and 5.3B show the matched SRS shapes (thick multi-color lines) with the projected taskspace curves (thin blue lines) for the sidewinding and helical rolling gaits, respectively. This process is repeated for other locomotion gaits as well. Figures 5.4A and 5.4B show optimization results, i.e., jointspace trajectories (or length changes) for sidewinding and helical rolling gaits during one cycle. Here, the SRS actuation rate (i.e., gait frequency) and the SRS bending can be controlled by adjusting the gait period and the jointspace amplitude, respectively.

5.1.5 Special Case: Obtaining SRS Locomotion on Curved Surfaces

Herein, we propose a specialized locomotion gait that involves the SRS wrapping itself onto a curved surface (Fig. 5.5A), leveraging continuous and distributed contact points to ensure a secure grip during locomotion. To enable effective traversal on this surface, the SRS must address specific challenges: (a) establishing a secure spatial grip on the curved surface, (b) executing locomotion while sustaining a consistent grip, and (c) adapting to variations in surface steepness. The wrapping pose constrains the robot, limiting deformation on or outside the curved surface [180]. Herein, we establish a general formulation for wrapping a snake robot around a cylindrical surface helically utilizing the helical rolling gait proposed in Sec. 5.1.2.

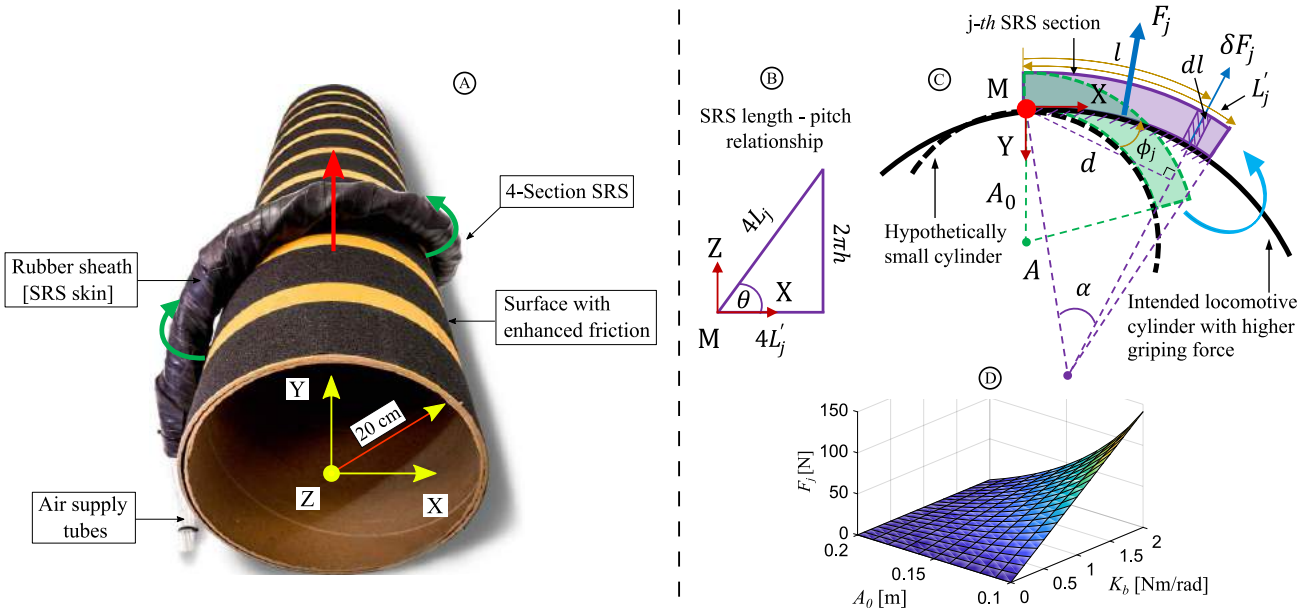

Figure 5.5: (A) Soft robotic snake (SRS) prototype showcasing locomotion on a cylindrical surface. (B-D) Gripping force applied by the SRS on the locomotive surface.

A. Generalizing Jointspace Trajectories for Curved Surface Locomotion

The locomotion trajectory generation discussed in Secs. 5.1.3 and 5.1.4 is time-consuming and requires recalculation if gait parameters need to be changed during locomotion. For instance, variations in the surface curvature lead to changes in the helical curve radius used for trajectory generation and subsequently affect the jointspace projection thereof. This constrains the ability to dynamically adjust locomotion trajectories in situ, limiting the utility of SRS in real-world scenarios. Thus, we parameterize and generalize the jointspace trajectory to dynamically accommodate surfaces with varying curvature or steepness.

Without loss of generality, a time-series, t, sinusoidal jointspace trajectory of the $i\text{-}th$ PMA of the $j\text{-}th$ SRS module, as depicted in Fig. 5.4B, can be parameterized as

$$l_{ji} = a_{ji} \sin\left(2\pi b_{ji} t + c_{ji}\right) + d_{ji}, \tag{5.5}$$

where $\{a_{ji}, b_{ji}, c_{ji}, d_{ji}\} \subseteq \mathbb{R}$ denote the trajectory amplitude, frequency, phase shift, & offset, respectively.

Assuming no vertical offset, d_{ji} can be neglected. Based on the SRS operating limits, we uniformly discretize the helical radius, A in (5.3), over the interval $[0.1, 0.4]$ and collect a set of jointspace trajectories, using the optimization-based IK solution process proposed in Sec. 5.1.4. The coefficients

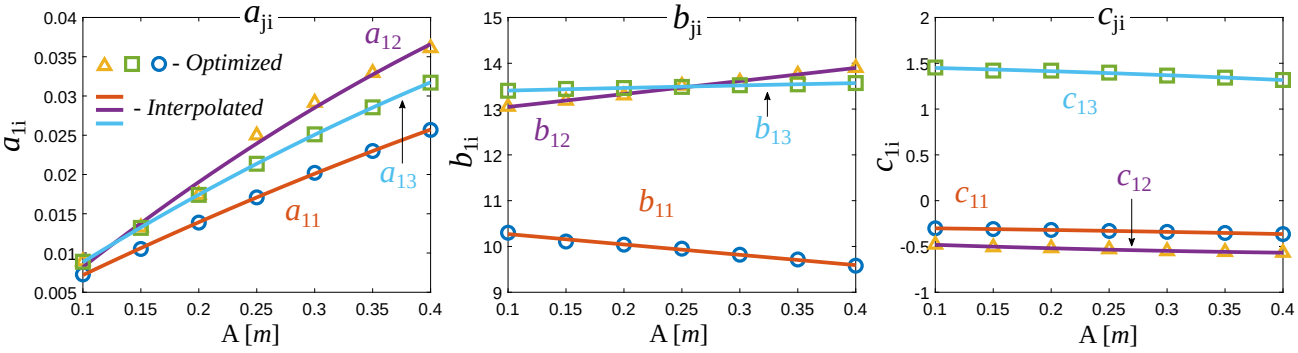

Figure 5.6: Variation in jointspace coefficients of the first SRS module under various helix radii.

a_{ji}, b_{ji}, and c_{ji} are then plotted against A. Figure 5.6 illustrates the coefficients for each PMA of the first SRS module. We use MATLAB curve-fitting tool [272] to approximate these relationships to quadratic polynomials, as depicted in Fig. 5.6. The process is repeated for the jointspace trajectories of all SRS modules. Table 5.1 shows the generalized jointspace coefficients as a function of the helical radius, A, for the entire SRS. By applying these results into (5.5), the SRS locomotion trajectories can be readily computed for any A, without recomputing.

B. Deriving Gripping Force on Curved Cylindrical Surfaces

SRS locomotion relies on distributed contact forces to generate movement. The ability to precisely control and modulate gripping force is essential to prevent slipping during traversal on curved and, especially, sloped surfaces, thereby minimizing the risk of falls. This section investigates how we can control the gripping force by mathematically modeling its key contributing factors. This model then allows one to dynamically adjust gripping force in response to varying terrain conditions, consequently to prevent slips and ensure stable locomotion.

Consider a cylindrical surface with a radius, A, as depicted in Fig. 5.5C. Given the stiffness and conformity of soft robots, we hypothesize that gripping force can be increased by deriving the trajectory for a cylindrical surface with a smaller radius than A. To that end, we focus on the SRS length-pitch relationship illustrated in Fig. 5.5B, obtained by unwrapping the cylindrical surface onto which the SRS wraps itself. In this context, the pitch, $2\pi h$, extends across the total length of the robot, $4L_j$, denote by the hypotenuse of the triangle where L_j represents the length of the j-th SRS module. We project the length of the SRS onto a plane normal to the cylindrical surface, denoted by $4L_j^{'}$ in Fig. 5.5B.

Table 5.1: Generalized trajectories of the SRS in curved surface locomotion.

SRS module	Jointspace variable	Jointspace Coefficients
1	l_{11}	$a_{11} = -0.02775A^2 + 0.07567A - 0.0001023$ $b_{11} = 0.05714A^2 - 2.289A + 10.5$ $c_{11} = -0.156A^2 - 0.1317A - 0.2872$
	l_{12}	$a_{12} = -0.06859A^2 + 0.1289A - 0.004006$ $b_{12} = 0.1143A^2 + 2.783A + 12.77$ $c_{12} = 0.4362A^2 - 0.5052A - 0.4359$
	l_{13}	$a_{13} = -0.04806A^2 + 0.1004A - 0.0007149$ $b_{13} = -0.1714A^2 + 0.6314A + 13.34$ $c_{13} = -0.4362A^2 - 0.2216A + 1.475$
2	l_{21}	$a_{21} = -0.08105A^2 + 0.1257A - 0.001387$ $b_{21} = -10.48A^2 + 0.9352A + 13.72$ $c_{21} = -0.05333A^2 + 0.1427A - 2.104$
	l_{22}	$a_{22} = 0.02606A^2 + 0.07243A + 0.00429$ $b_{22} = -8.076A^2 + 7.77A + 11.69$ $c_{22} = -5.935A^2 + 0.8326A + 0.2196$
	l_{23}	$a_{23} = -0.04876A^2 + 0.09007A + 3.086e\text{-}05$ $b_{23} = 8.552A^2 - 9.096A + 12.97$ $c_{23} = -32.08A^2 + 5.293A + 3.13$
3	l_{31}	$a_{31} = -0.08309A^2 + 0.1188A - 0.001545$ $b_{31} = -14.99A^2 + 2.607A + 14.51$ $c_{31} = 0.4343A^2 - 0.5354A - 1.983$
	l_{32}	$a_{32} = -0.08137A^2 + 0.139A - 0.004173$ $b_{32} = -5.752A^2 + 7.528A + 11.53$ $c_{32} = -6.188A^2 - 1.981A + 1.48$
	l_{33}	$a_{33} = 0.01152A^2 + 0.06804A - 0.0003943$ $b_{33} = 28.1A^2 - 7.445A + 11.04$ $c_{33} = -0.2041A^2 - 2.357A + 1.694$
4	l_{41}	$a_{41} = -0.01408A^2 + 0.06396A - 0.001089$ $b_{41} = -9.465A^2 - 0.201A + 12.46$ $c_{41} = -5.29A^2 - 1.606A + 0.1178$
	l_{42}	$a_{42} = -0.09095A^2 + 0.1296A - 0.00678$ $b_{42} = 31.63A^2 - 8.807A + 11.85$ $c_{42} = -3.585A^2 - 1.394A + 1.621$
	l_{43}	$a_{43} = -0.05472A^2 + 0.08219A - 0.002598$ $b_{43} = 3.981A^2 + 1.851A + 11.15$ $c_{43} = 0.1143A^2 - 5.003A + 3.648$

Accordingly, the length $L_j^{'}$ of the $j\text{-}th$ SRS module can be expressed as

$$L_j^{'} = \tfrac{1}{2}\sqrt{4L_j^2 - \pi^2 h^2}. \tag{5.6}$$

In Fig. 5.5C, $L_j^{'}$ is highlighted in green. It has curved inward following the trajectory generated in relation to a hypothetical cylindrical surface with a higher curvature, A_0^{-1}. The smaller original curvature A^{-1} has caused $L_j^{'}$ to bend about its anchoring point, M, forming the shape shown in purple. Due to this mismatch of resulting bending, a uniform reaction force, F_j is generated from the combined effect of surface contacts along $L_j^{'}$, as depicted in Fig. 5.5C.

Without loss of generality, consider the infinitesimally small length segment, dl, located at a distance, l from the anchoring point, M, along the length, $L_j^{'}$. A bending torque is induced on dl by the point gripping force, δF_j, as a result of the cylinder radius change from A_0 to A. Accordingly, the distributed bending torque, τ_j, along $L_j^{'}$ can be written as

$$\tau_j = \int_0^{L_j^{'}} (\delta F_j d)\, dl = K_b \phi_j, \tag{5.7}$$

where d is the normal distance to M, K_b is the bending stiffness, and ϕ_j is the change in the bending angle of $L_j^{'}$ resulting from the variation in the cylinder's radius.

Considering geometrical arc properties in Fig. 5.5C, d and ϕ_j can be obtained as

$$d = A \sin\left(\frac{l}{A}\right), \tag{5.8}$$

$$\phi_j = \left(\frac{1}{A_0} - \frac{1}{A}\right) L_j^{'}. \tag{5.9}$$

Applying results in (5.8) and (5.9) into (5.7) yields

$$\tau_j = F_j A \int_0^{L_j^{'}} \sin\left(\frac{l}{A}\right) dl = \left(\frac{1}{A_0} - \frac{1}{A}\right) K_b L_j^{'}. \tag{5.10}$$

By solving (5.10), F_j can be deduced as

$$F_j = \frac{\beta K_b}{A\,(1 - \cos(\beta))} \left(\frac{1}{A_0} - \frac{1}{A}\right), \tag{5.11}$$

where $\beta = \frac{\sqrt{4L_j^2 - \pi^2 h^2}}{2A}$.

According to (5.11), F_j is proportional to K_b and A_0 as illustrated by the surface plot in Fig. 5.5D. Note that, K_b is a function of the common mode pressure in PMAs as demonstrated in [253]. The applicability of the gripping force is evaluated in Chapter 7.

5.2 Trajectory Generation of Soft-limbed Tetrahedral Robot

5.2.1 Generating Pinniped Locomotion Trajectories

A. Fundamental Limb Motion

The locomotion gaits derived here are inspired by the terrestrial crawling of pinnipeds (Fig. 5.7A). In this work, we leverage on the cyclic nature of limb movements in pinnipeds and derive locomotion trajectories based on movements of individual limbs. We use limb kinematics in Sec. 4.1 to parameterize and derive circular taskspace movement of the limb tip as the fundamental limb motion. For any j-th soft limb – shown in Fig. 5.7B – we define a circular trajectory of radius ρ at d distance from the limb's origin, $\{O_j\}$, and period, τ. At time t, the tip position relative to $\{O_j\}$ is given by

$$x_j = \rho \sin\left(-\tfrac{2\pi t}{\tau}\right), \; y_j = \rho \cos\left(-\tfrac{2\pi t}{\tau}\right), \; z_j = d. \tag{5.12}$$

We apply uniformly distributed $t \in [0, \tau]$ values on (5.12) to obtain a 100-point taskspace trajectory corresponding to the circular limb motion. We transform the taskspace trajectory to configuration space trajectory using the inverse kinematic model described in Sec. 4.1. Subsequently, (4.1) is used to map the configuration space trajectory (θ_j, ϕ_j) to the jointspace trajectory (l_{ji}).

B. Effect of Center of Gravity

The center of gravity (CoG) of the robot helps stabilize locomotion [273]. We compute the robot CoG to investigate and regulate locomotion stability. From [274], the CoG of a limb, $\mathbf{c}_j \in \mathbb{R}^3$, relative to its body coordinate frame $\{O_j\}$ is

$$\mathbf{c}_j(q_j) = \int_0^1 \mathbf{p}_j(\xi, q_j) d\xi. \tag{5.13}$$

Substituting $\mathbf{p}_j$ in (4.4) into (5.13), $\mathbf{c}_j(q_j)$ can be derived as

$$\mathbf{c}_j(q_j) = \frac{L}{\phi_j^2} \begin{bmatrix} \cos(\theta_j)\,(\phi_j - \sin(\phi_j)) \\ \sin(\theta_j)\,(\phi_j - \sin(\phi_j)) \\ (1 - \cos(\phi_j)) \end{bmatrix}. \tag{5.14}$$

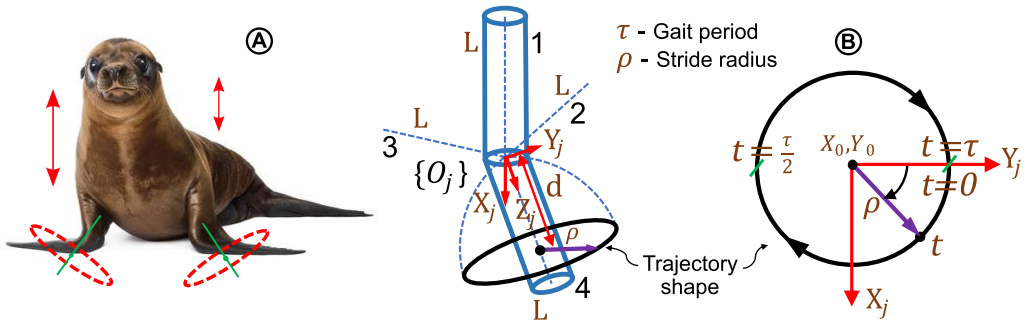

Figure 5.7: (A) Pinniped crawling with limb, body, and head movements. (B) Fundamental motion trajectory of a soft limb.

Utilizing the results in (4.20) and (5.14), CoG relative to the robot coordinate frame, $\{O_R\}$, denoted by $\mathbf{C}_j \in \mathbb{R}^3$, can be obtained. If the mass of the j-th limb is m_j, then CoG of the robot relative to $\{O_R\}$, $\mathbf{C}_R \in \mathbb{R}^3$, can be written as

$$\mathbf{C}_R(q_j) = \frac{1}{\sum_{j=1}^{4} m_j} \sum_{j=1}^{4} m_j \mathbf{C}_j(q_j). \tag{5.15}$$

C. Forward Crawling

We generate forward crawling locomotion by simultaneously (i.e., with zero phase offset) replicating the limb motion derived in Sec. 5.2.1 in FR and FL limbs as illustrated in Fig. 5.8A. Therein, we move the robot in $+X$ direction, by giving anticlockwise and clockwise motion trajectories to FR and FL limbs w.r.t. the local coordinate frames thereof, respectively. However, achieving forward crawling is challenging as there is, unlike pinnipeds with their relatively massive bodies, no body (or support limb) to counterbalance the angular moment generated by crawling forelimbs. Because of that, forward crawling in the proposed robot can induce instability.

We circumvent this limitation by controlling the CoG position given by (5.15) to obtain a more stable forward crawling gait as described below. Refer to Fig. 5.8E for the limb movements and CoG trajectories during a forward crawling cycle. We cyclically and proportionally bend the Head (H) limb towards the moving direction from a straight position ($\phi = 0°$) to a value computed using (5.15), $\phi = 90°$, during a locomotion cycle (Fig. 5.8E). This dynamic CoG control approach stabilizes the movement by counteracting instantaneous torque imbalances. We generate an additional thrust from the Back (B) limb (located on the opposite side) by actuating it in a manner that supports forward propelling. Therein, the B limb is gradually bent in a linear trajectory against the moving floor (Fig.

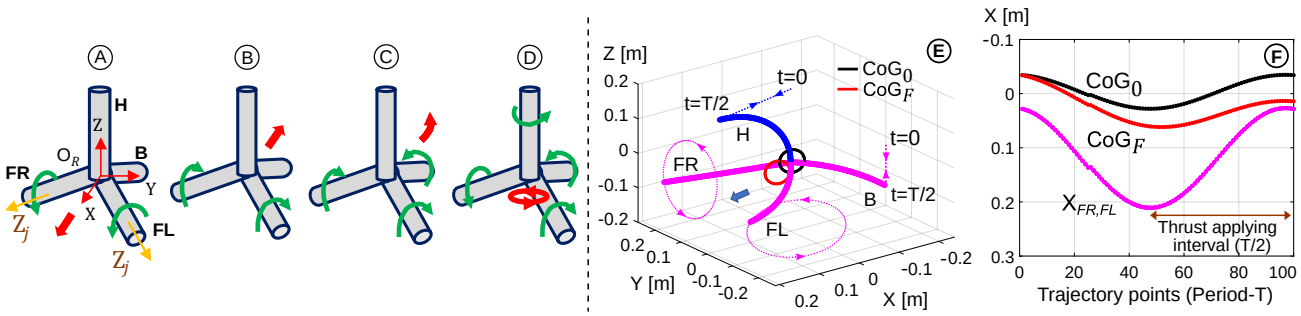

Figure 5.8: Limb trajectories – (A) forward crawling, (B) backward crawling, (C) crawling-and-turning (leftward), (D) in-place turning (counterclockwise). In forward crawling – (E) spatial limb displacements and computed CoG trajectories, (F) CoG components and crawling limb tip displacements along the moving direction (i.e., $+X$ axis) relative to O_R.

5.8A). As a consequence, the resultant limb displacement torque increases. Readers are referred to the experimental video on forward crawling to further understand the above limb actuating mechanism.

The impact of H and B limb actuation on crawling thrusts can be visualized by tracking the robot CoG and limb movements as shown in Figs. 5.8E and 5.8F. The CoG_0 denotes the CoG trajectory when H and B limbs are not actuated. When they are actuated, CoG_0 shifts towards the moving direction ($+X$) as noted by CoG_F in Fig. 5.8E. Figure 5.8F shows computed CoG_0, CoG_F, and crawling limb tips (X_{FR}, X_{FL}) in the moving direction relative to O_R. During the crawling thrust applying interval (i.e., ground contact period), the robot CoG converges and closely follows crawling limb tips as noted by CoG_F in Fig. 5.8F. It causes an increase in the weight-induced torque supported by the crawling limbs (FR & FL). As a consequence, with the increase in ground-limb reaction forces, the crawling thrusts increase.

D. Backward Crawling

The backward crawling is referred to as moving in the $-X$ direction (Fig. 5.8A). Here, the limb motion derived in Sec. 5.2.1 is simultaneously applied to FR and FL limbs in the opposite direction to that of the forward crawling, i.e., FR and FL limbs are given clockwise and anticlockwise motion trajectories respectively, as illustrated in Fig. 5.8B. We keep the Head (H) limb bent in the $-X$ direction (i.e., backward) for shifting the robot CoG toward FR and FL limbs for improved stability and generating more thrust from the increased weight (reaction forces) at the limbs-ground contact [19]. Concurrently, the Back (B) limb is bent upward (in the $+Z$ direction of O_R) to reduce the contact surface and minimize the frictional resistance [19].

E. Crawling-and-Turning

Pinnipeds use peristaltic body movement to propel forward since the bulk of the body weight is distributed towards the back (body) [275]. But, the proposed soft robot design has a symmetric weight distribution and thus it is difficult to maintain stability while propelling forward. As a consequence, the robot shows limited frontal movements. Conversely, when propelling backward, the torque imbalance is countered by the Body (i.e., B limb). It enables the use of the B limb in turning only in backward movements. Therefore, we opt to achieve turning in the backward direction. To achieve turning locomotion, we additionally actuate the B limb similarly to straight crawling limbs (FR & FL) discussed in Sec. 5.2.1. For example, a clockwise trajectory of the B limb results in a leftward turn (Fig. 5.8C), while changing the direction of the B limb to anticlockwise results in a rightward turn. We replicate the B limb motion with different stride radii to control the turning effect.

F. In-place Turning

In-place turning is referred to as the rotation about the robot $+Z$ axis (Fig. 5.8A). It is achieved by crawling all ground-contacting limbs in the same direction of rotation (clockwise/counterclockwise) as shown in Fig. 5.8D. Additionally, we actuate the Head (H) limb in the same direction of rotation in a circular trajectory at the same angular velocity. In that way, we shift the CoG of the Head (H) limb into the direction of rotation and support the turning. We can reverse the direction of in-place turning by reversing the direction of crawling in all limbs.

5.2.2 Generating Tumbling Locomotion Trajectory

A. Motivation for Tumbling

The pursuit of energy-efficient locomotion in soft-limbed robots remains uncharted. Achieving this requires exploring novel designs and locomotion modes that withstand environmental challenges. Nature offers valuable insights, as some organisms exhibit energy-efficient locomotion [6]. For instance, dung beetles use tumbling to transport dung balls efficiently. Similarly, tumbleweeds roll across landscapes, and some caterpillars tumble by curling into a ball and rolling downhill as a defense mechanism. Similar to biological creatures, soft robots can adopt unconventional locomotion modes like tumbling

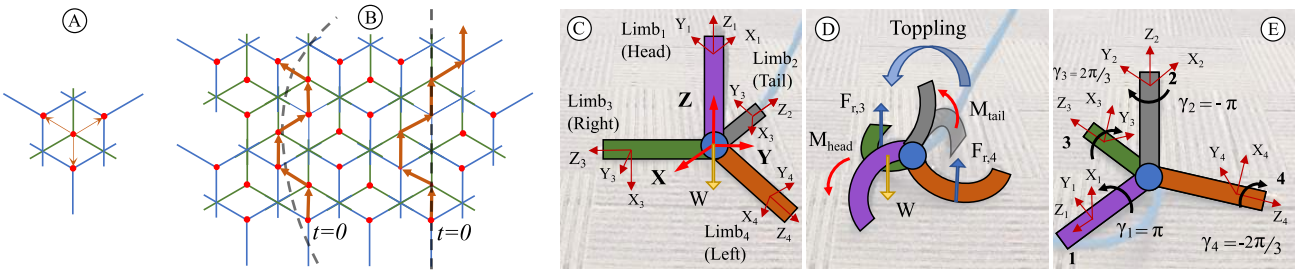

Figure 5.9: Discrete Tumbling Locomotion – (A) shows the three directions in which the robot can tumble, with green lines indicating the robot's initial pose. (B) illustrates the robot's workspace, with red dots representing the points where the robot can move (i.e., the movement of the robot's center of gravity). The black dotted lines denote desired straight and curvilinear paths. (C) An initial tumbling pose, (D) an intermediate tumbling pose, and (E) a tumbled pose. The black arrow and γ_i indicate the required direction and magnitude of rotation to maintain the standard frame orientation.

and flipping due to their deformable structures. These methods require minimal energy as the robot uses its compliant body to roll. They offer advantages such as high maneuverability, orientation correction, adaptability to rough terrain, impact resilience, and safe interactions. Tumbling enhances maneuverability, allowing tight turns and agile movements, and helps in effective orientation correction if the robot falls. The robot's flexibility provides impact resistance by absorbing and distributing forces during collisions. The previously proposed crawling locomotion is not an energy-efficient way of moving as it wastes a substantial amount of energy for friction due to distributed contacts of crawling limbs. In this section, we extend crawling and systematically look into a novel discrete locomotion gait named tumbling.

B. Tumbling Strategy

Tumbling is an unconventional method of movement where the robot intentionally induces rolling or flipping motions to navigate through its environment. Due to the spatially symmetric limb structure, the tumbling of the tetrahedral robot generates a discrete locomotion pattern. This motion creates discrete points in Cartesian space following a honeycomb structure as illustrated in Figs. 5.9A and 5.9B. Therein, any locomotion trajectory (such as the highlighted straight and curvilinear paths) can be realized by moving the robot across discrete points marked in red color.

In tumbling, the robot's center of gravity (CoG) is moved beyond the balance triangle to topple the robot [276]. This is achieved by bending the tail against the floor (i.e., downward) and the head towards the moving direction (i.e., forward), simultaneously in a linear trajectory as illustrated in Figs. 5.9C, 5.9D, and 5.9E. Consequently, the generated angular moments in each limb (M_{head}, M_{tail}) tip over

the robot around ground contact points. In order to guarantee the completion of a rolling cycle, the robot must be given an adequate amount of angular momentum towards the tumbling direction. This is attained by reversing the bending direction of the tail towards the moving direction (i.e., forward) at the time the robot completes its rolling cycle. Additionally, the left and right limbs crawl and move the robot forward while shifting the ground contact closer to the CoG facilitating the robot's translation [20]. Herein, head, tail, and left-right limbs undergo 3 distinct movements that can be parameterized by the curve parameters (θ_i, ϕ_i in Sec. 4.1) of each limb.

Let the $\vec{p_i} = [x_i, y_i]$ be the Cartesian coordinate vector of the heel of any i-th limb relative to its own coordinate frame, $\{O_i\}$. Then, the taskspace, (x_i, y_i) of a circular limb heel trajectory is given as presented in [21] as

$$\begin{aligned} x_i &= \rho_i \cos(\alpha_i), \\ y_i &= \rho_i \sin(\alpha_i), \end{aligned} \tag{5.16}$$

where ρ_i is the trajectory stride radius and $\alpha_i = \frac{2\pi t}{T}$ is the angular displacement of the i-th limb at a time, t within the trajectory period, T.

The proposed limb motions can be repeated to obtain multiple tumbling cycles. Therein, based on the new tumbling direction, limbs' linear and circular trajectory taskspace is transformed via corresponding Z axis rotations, Rz as

$$\vec{\hat{p}_i} = Rz(\gamma_i) \cdot \vec{p_i} \tag{5.17}$$

where $\hat{p}_i$ is the remapped taskspace of the i-th limb and γ_i is the corresponding rotation angle needed to reorient the limb frame in the next tumbling cycle. γ_i is determined by taking into account the tetrahedron geometry, current robot orientation, and next tumbling direction. Figure 5.9E illustrates the aforementioned remapping according to the corresponding angle offsets of each limb. For example, during the previous tumbling cycle, limb-4 rotated $\frac{2\pi}{3}$ around the $Z+$ axis. Therefore, to maintain the standard frame orientation, we must rotate the frame $-\frac{2\pi}{3}$ around the $Z+$ axis.

5.3 Trajectory Generation of Soft-limbed Quadrupedal Robot

5.3.1 Generating Quadruped Crawling Trajectories

A. Straight Crawling

The fundamental limb motion for the crawling locomotion of the quadruped is identical to the one proposed for the tetrahedral robot in Sec. 5.2.1. In subsequent derivations, refer to the symbols listed in Table 5.2 for clarity. Here, we describe the initial pose of the robot and the approach for achieving locomotion by maintaining a phase shift between diagonal limb pairs.

Table 5.2: Quadruped crawling: nomenclature of locomotion trajectory generation.

Symbol	Definition
ρ	Trajectory stride radius
T	Trajectory period
ω_k	Phase shift between diagonal limb pairs
$\omega_{FL}, \omega_{FR}, \omega_{BL}, \omega_{BR}$	Phase shift of front left, front right, back left, and back right limbs, respectively
$F_{FL}, F_{FR}, F_{BL}, F_{BR}$	Locomotion thrusts of front left, front right, back left, and back right limbs, respectively
D	Linear straight moving distance
d	Trajectory stride distance
G	Center of gravity
η_k	Locomotion efficiency
V_k	Average robot speed of straight locomotion
$\Omega_{in-place}$	Angular speed of in-place turning
r_{ip}	In-place turning radius
ρ_I, ρ_O	Inner and outer stride radii
r_ρ	Turning arc radius
Φ	Angular rotation for turning
Ω_{stride}	Average angular speed
φ	Body actuation angle for turning
T_{err}	Locomotion trajectory error
P_{error}	Robot speed prediction error

We start with an unactuated pose where the robot is lying flat on the ground (see Fig. 3.7A). The approach used for achieving locomotion is similar to the crawling gaits of tetrapods such as lizards, i.e., maintain a phase shift (ω_k) between diagonal limb pairs. Refer to Fig. 5.10A for the trajectory definitions/notations. At $t = 0$, we initiate the FR and BL limbs with phase shifts $\omega_{FR} = \omega_{BL} = 0$ (diagonal limb-pairs). Similarly, we initiate the FL and BR limbs with phase shifts $\omega_{FL} = \omega_{BR} = \omega_k$ (diagonal limb-pairs). Following the results in (5.12), the taskspace parameters of FL and BR limbs relative to the limb's coordinate frames can be written as

$$x_j = \rho_j \sin\left(-\frac{2\pi t}{T} + \omega_k\right), \; y_j = \rho_j \cos\left(\frac{2\pi t}{T} + \omega_k\right), \; z_j = d. \tag{5.18}$$

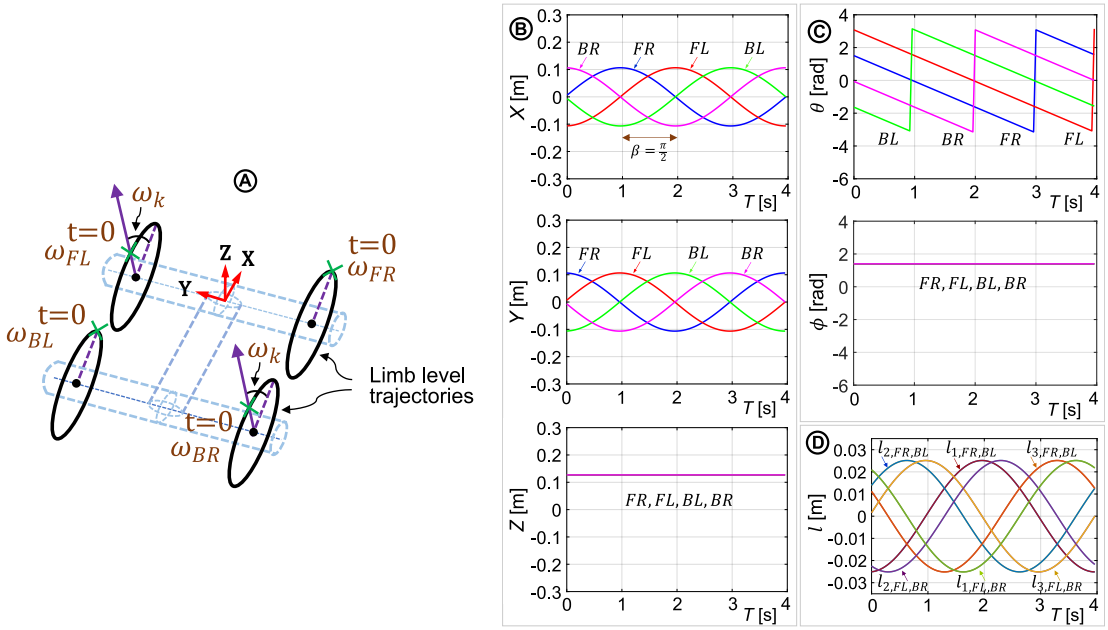

Figure 5.10: (A) Configuration of limb level trajectories. During straight locomotion ($T = 4\ s, \rho = 0.1\ m, \omega_k = \frac{\pi}{2}\ rad$), the following visualizations are presented: (B) taskspace, (C) curve parametric jointspace, and (D) variable-length jointspace trajectories of four limbs relative to their respective limb coordinate frames.

To achieve straight motion, identical trajectories are applied in diagonal limb pairs while the robot body (Limb B) is kept straight or unactuated (i.e., $\theta_5 = \phi_5 = 0$). Figures 5.10B, 5.10C, and 5.10D illustrate the taskspace, curve parametric jointspace, and variable-length jointspace trajectories of the four limbs, respectively, relative to limbs' coordinate frames at a straight motion for $T = 4\ s$, $\rho_j = 0.1\ m$, and $\omega_k = \frac{\pi}{2}\ rad$.

The locomotion speed is calculated based on the straight locomotion gait shown in Fig. 5.11A. During the stance phase, all limbs generate uniform locomotion thrusts, $F_{FR} = F_{FL} = F_{BL} = F_{BR} = F$, for a constant stride radius, $\rho_{FR} = \rho_{FL} = \rho_{BL} = \rho_{BR} = \rho$, causing the robot to move forward a linear distance, D. Under ideal conditions, D can be approximated to twice the stride radius, i.e., $D = 2\rho$. To evaluate the contribution of each limb pair during the stance phase, locomotion thrusts (F) are analyzed under different phase shifts, $\omega_k \in \{0, \frac{\pi}{4}, \frac{\pi}{2}, \frac{3\pi}{4}, \pi\}\ rad$, as illustrated in Fig. 5.12.

At $\omega_k = 0\ rad$, both limb pairs synchronously move the robot a distance, 2ρ, during the stance period, $\frac{T}{2}$. Hence, the average robot speed along the $+X$ direction at $\omega_k = 0\ rad$ during a period, T can be written as $V_1 = \eta_1 \left(\frac{2\rho}{T}\right)$, where η_1 defines the locomotion efficiency at $\omega_k = 0\ rad$ accounting for the frictional and energy losses due to the assumed ideal conditions. Similarly, at $\omega_k = \pi\ rad$, two limb pairs sequentially apply equal locomotion thrusts during the period, T, making the ideal moving

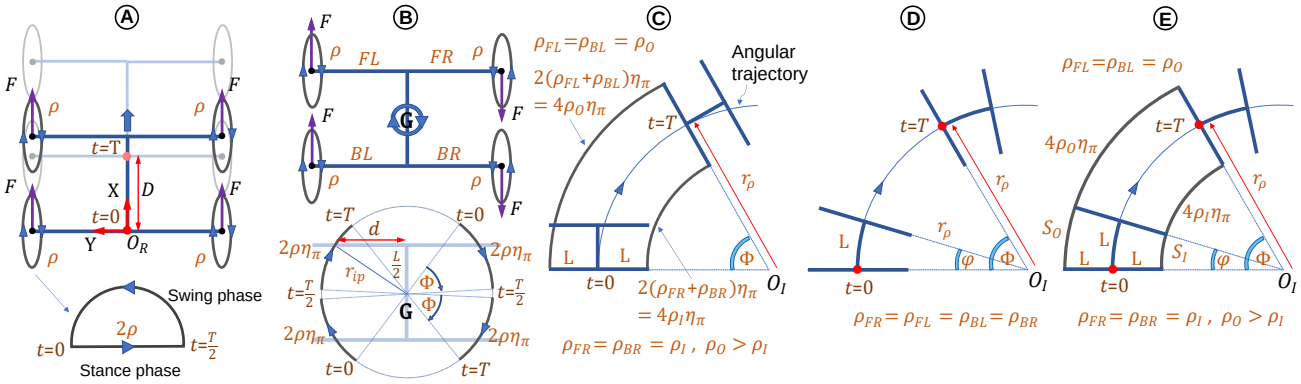

Figure 5.11: Modeling of different gaits – (A) straight locomotion, (B) in-place turning, (C) locomotion with differential strides, (D) locomotion with body bending, and (E) general locomotion combining differential strides and body bending.

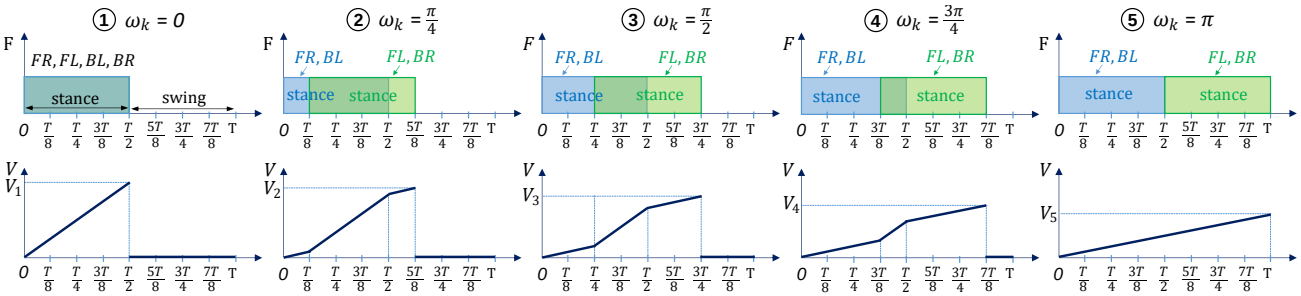

Figure 5.12: Straight locomotion stance and robot speed variations during stance and swing phases of diagonal limb pairs under different phase shifts (ω_k).

distance twice that of the distance at $\omega_k = 0\ rad$. Accordingly, the average robot speed at $\omega_k = \pi\ rad$ can be written as $V_5 = \eta_5 \left(\frac{4\rho}{T}\right)$, where η_5 defines the locomotion efficiency at $\omega_k = \pi\ rad$. Referring to Fig. 5.12, the average robot speed, V_k, along the $+X$ direction at any phase shift, $\omega_k \in [0, \pi]$, can be written as

$$V_k = \eta_k \left(1 + \frac{\omega_k}{\pi}\right) \frac{2\rho}{T} \tag{5.19}$$

where η_k defines the locomotion efficiency with $k \in \mathbb{Z}^+$.

B. Crawling and In-Place Turning

In-place turning is a type of rotation about the Z axis (Fig. 5.10A). It can be achieved by reversing the direction of rotation (counterclockwise to clockwise) of the limbs on one side of the robot with $\omega_k = \pi\ rad$ phase between diagonal limb pairs. To turn counterclockwise, the rotation direction of the limbs on the left side is reversed and vice versa. The rotation direction of a limb can be reversed by reversing the X_j task space of the fundamental trajectory motion (i.e., x_j becomes $-x_j$) at $t = 0$

(Fig. 5.7B). The rate and effectiveness of rotation can be controlled by varying the trajectory stride, ρ_j (Sec. 5.2.1).

Consider the in-place turning gait shown in Fig. 5.11B. In this gait, the left and right limbs are given uniform locomotion strides ($\rho_{FR} = \rho_{FL} = \rho_{BL} = \rho_{BR} = \rho$) in opposite directions. Because of that, crawling thrusts generate a net angular torque, resulting in rotation about the robot's geometric center, G. During the stance phase, a diagonal limb pair moves the robot a displacement of 2ρ, which is approximated to a circular arc distance. Due to a phase shift of $\omega_k = \pi\ rad$, two limb pairs move the robot a total arc distance of $(\eta_\pi)\, 4\rho$ during the period T. Here, η_π defines the locomotion efficiency at $\omega_k = \pi\ rad$. Accordingly, the robot's angular speed about G, $\Omega_{in-place}$, can be calculated as

$$\Omega_{in-place} = \eta_\pi \left(\frac{4\rho}{T r_{ip}} \right) \tag{5.20}$$

where r_{ip} is the in-place turning radius (Fig. 5.11B) which can be obtained from

$$r_{ip} = \sqrt{d^2 + \left(\frac{L}{2} \right)^2} \tag{5.21}$$

with d as the trajectory stride distance given in (5.18).

C. Crawling with Differential Strides

The second method for turning the robot while moving involves using different stride radii on the left and right limbs, with a straight body module. This method is illustrated in Fig. 5.11C, where a differential stride gait is shown. The principle used here is similar to that used in turning a vehicle, where the inner wheels turn more tightly than the outer wheels to achieve the desired turn.

To implement this principle in quadrupedal locomotion, different stride radii are chosen for the left and right limbs based on the direction of the turn. When the outer stride radius is greater than the inner one (i.e., $\rho_O > \rho_I$ in Fig. 5.11C), the robot moves in a rightward angular trajectory, and vice versa for leftward turning. As in the previous method, the contribution of a limb to locomotion is approximated as a circular arc with an equivalent stance displacement of 2ρ, and the robot turns about its arc center at O_I during the period T. Referring to the arc geometries in Fig. 5.11C, the turning arc radius, r_ρ, can be derived as follows.

$$r_\rho = L \left[\frac{\rho_O + \rho_I}{\rho_O - \rho_I}. \right] \tag{5.22}$$

Subsequently, from r_ρ in (5.22), the angular rotation, Φ can be found and hence the average angular speed, $\Omega_{stride} = \frac{\Phi}{T}$ can be obtained as

$$\Omega_{stride} = \eta_\pi \left[\frac{2(\rho_O - \rho_I)}{TL}. \right] \tag{5.23}$$

All turning gaits are actuated at $\omega_k = \pi \ rad$, hence the locomotion efficiency, η becomes η_π.

D. Crawling with Body Bending

In this method of turning, the robot changes its moving direction by bending its body while maintaining the same limb stride radii (Fig. 5.11D). The idea is to change the relative orientation of the front and rear hip joints, which are otherwise parallel to each other. The limb pairs can be actuated using two independent actuator signals (6-DoF), while the robot body must be actuated using a separate actuator signal (3-DoF), bringing the total DoF to 9. By leveraging body deformation, the same turning effect can be achieved with fewer actuators.

To obtain the body bending angle (φ in Fig. 5.11D) required for locomotion with differential strides, we derive r_ρ and Φ as described in Section 5.3.1 and bring them forward to Fig. 5.11D. We approximate the average angular speed of the locomotion with body bending gait to that of the locomotion with differential strides gait given by (5.23). Under this assumption, the required body actuation, φ, can be obtained as

$$\varphi = \frac{L}{r_\rho}. \tag{5.24}$$

It should be noted, when the robot locomotes with differential strides or body bending, it may slip sideways due to the straight body or unequal turn radii of inner and outer limbs.

E. General Crawling Combining Differential Strides and Body Bending

In this approach, we combine locomotion with differential strides (Sec. 5.3.1) and body bending (Sec. 5.3.1) to effectively achieve the same turning effect without possible slipping, as shown in Fig. 5.11E. First, we determine the stride radius adjustment required to eliminate slipping when the robot bends its body for turning. According to Fig. 5.11E, if the body has to bend φ amount to track

its desired angular trajectory, the ratio between stride radii can be obtained as

$$\frac{\rho_O}{\rho_I} = \frac{1+\varphi}{1-\varphi}. \tag{5.25}$$

From (5.25), for a known inner stride radius, ρ_I, adjusted outer stride radius, ρ_O can be computed. Subsequently, similar to (5.23), the angular speed of the combined turning gait, Ω_c can be obtained as

$$\Omega_c = \eta_\pi \left[\frac{4\rho_I \varphi}{(1-\varphi)TL}. \right] \tag{5.26}$$

In Chapter 7, we evaluate the above gait modeling approach by comparing model outputs with the experimental results.

5.3.2 Generating Quadruped Trotting Trajectories

A. Motivation for Trotting

To date, most soft mobile robots use slow, statically stable gaits like crawling [5], which can be inefficient for certain field applications. High-speed, dynamically stable gaits (e.g., trotting, galloping) are limited in soft-limbed robots [3]. Researchers have added more limbs, such as in soft hexapods, to bolster payload and achieve stable gaits, but this increases design and actuation complexity. Fewer limbs (e.g., 4 instead of 6) require stronger legs to support body weight, yet most proposed soft limbs are overly pliant. Soft limb deformation can be active or passive, with passive actuation reducing the robot's effective DoF and dexterity. Actively bending soft limbs can achieve high-speed, dynamically stable locomotion, squeeze through narrow spaces, and improve maneuverability. However, these robots have not yet achieved meaningful dynamic gaits due to inadequate limb structural strength [39], [58].

B. Fundamental Limb Motion for Trotting

Without loss of generality, we derive a fundamental limb trajectory for one limb and, with appropriate phase shifts, apply to other limbs to generate quadrupedal locomotion. Herein, we consider that the limb heel follows the fundamental trajectory profile shown in Fig. 5.13. It is formed by a circular arc with a radius, ρ (swing phase) and a chord drawn at an angular offset, $\pm\varphi \in [0, \pm\pi]$ from the $+X_0$ axis of the trajectory (stance phase). We position the trajectory origin, $\{x_0, y_0\}$ at $\{x_d, 0, d\}$ relative to the limb's origin at O_j. Referring to notations in Fig. 5.13, the trajectory starts at time, $t = 0$ from

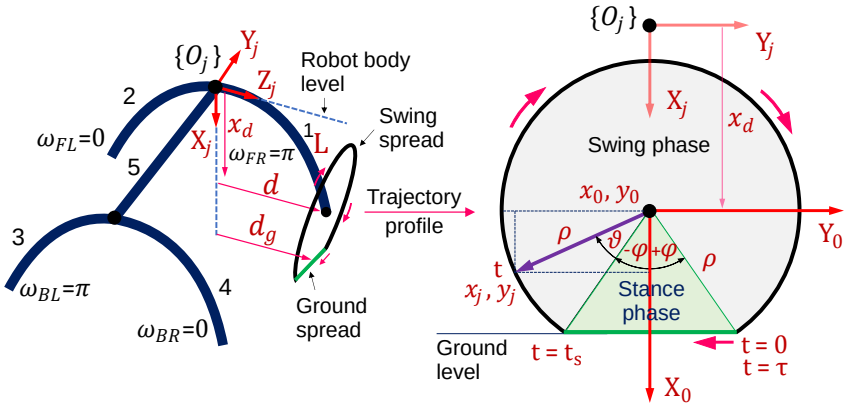

Figure 5.13: Definitions of fundamental limb trajectory.

the angular offset, $+\varphi$ and follows a clockwise direction with a period τ. The limb heel traces stance and swing phases at a uniform angular speed at time intervals, $0 \leq t < t_s$ and $t_s \leq t < \tau$, respectively. Herein, t_s defines the time period of the stance. The $X-Y$ projection of the taskspace of any j-th limb at time, t relative to $\{O_j\}$ can be obtained as

$$x_j = \begin{cases} x_0 + \rho\cos(\varphi), & 0 \leq t < t_s \\ x_0 + \rho\cos(\varphi + \vartheta), & t_s \leq t < \tau \end{cases} \tag{5.27}$$

$$y_j = \begin{cases} y_0 + \left(1 - \frac{2t}{t_s}\right)\rho\sin(\varphi), & 0 \leq t < t_s \\ y_0 - \rho\sin(\varphi + \vartheta), & t_s \leq t < \tau \end{cases} \tag{5.28}$$

where ϑ is the swing angle at time, t measured from $t = t_s$ in the clockwise direction during $t_s \leq t < \tau$.

The Z – component of the trajectory taskspace, z_j relative to the coordinate frame of the limb is given by (4.4). However, given the limited kinematic DoFs of a soft limb, only the X, Y – components can be solved [45]. Hence we disregard the Z – component. The duty cycle, D, between the stance and swing phases can be defined as

$$D = \frac{t_s}{\tau}. \tag{5.29}$$

Considering uniform angular speed, ϑ can be deduced as

$$\vartheta = 2\pi\left(\frac{t}{\tau} - D\right). \tag{5.30}$$

Further, ground spread, s can be related to the trajectory stride radius, ρ as

$$s = 2\rho\sin(\varphi). \tag{5.31}$$

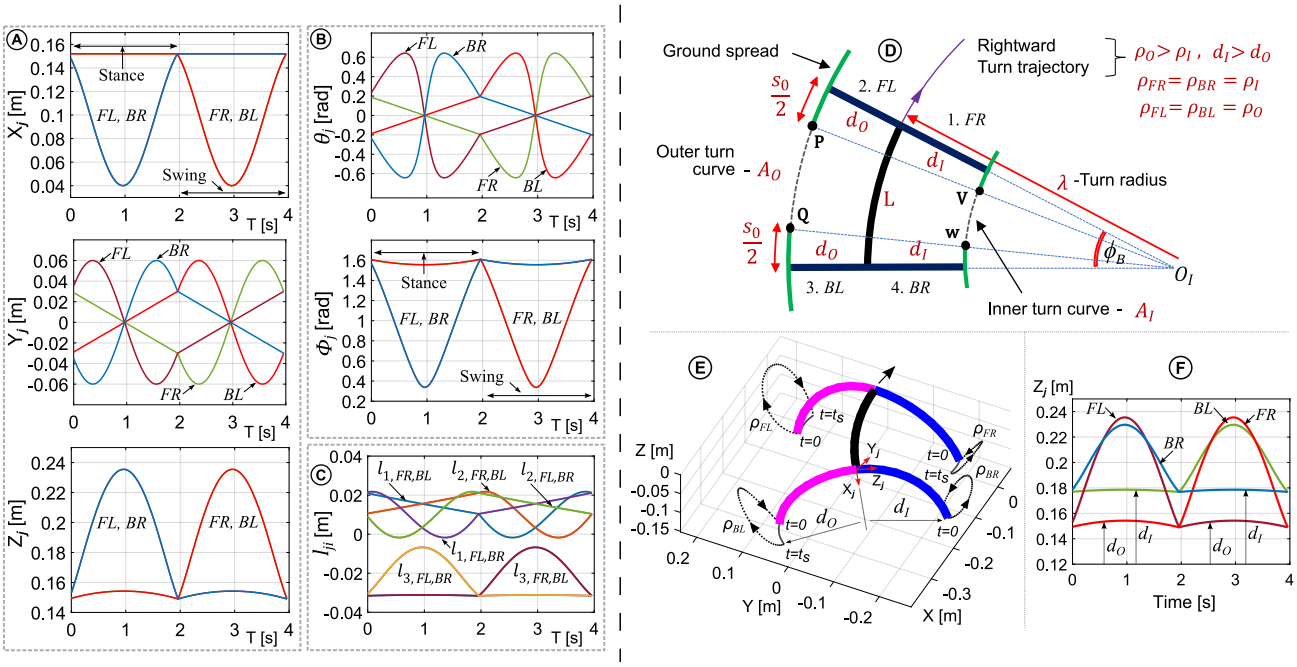

Figure 5.14: Trajectory outputs – (A) $X-Y-Z$ taskspace, (B) curve parameters and, (C) joint variables of four limbs relative to individual coordinate frames of limbs, $\{O_j\}$ at $X_d = 10\ cm$, $\rho = 6\ cm$, $D = 0.2$, $\tau = 4\ s$, and $\Delta t = 1.34\ s$. (D) Modelling turning locomotion (rightward turn). (E) Quadruped rightward turn with body bending and differential limb strides. (F) Change in horizontal limb heel distance relative to $\{O_j\}$ according to differential limb strides.

We discretize the limb taskspace trajectory, (x_j, y_j) into uniformly distributed 100 points within $[0, \tau]$ corresponding to the limb tip movement in Fig. 5.13. The taskspace is then transformed to a 100-point trajectory of curve parameters, $(\theta_j,\ \phi_j)$ utilizing the inverse kinematics given in (4.5b). Subsequently, we apply (4.1) to transform $(\theta_j,\ \phi_j)$ into joint variables, l_{ji}. We use identical limb trajectories at each limb and actuate respective joint variables to achieve locomotion in the quadruped as described in Sec. 5.3.2.

C. Generating Straight Trotting

Trotting is a fast two-beat gait where diagonal limb pairs are lifted and struck the ground at $\pi\ rad$ phase shift between each beat [277]. We achieve straight trotting locomotion by replicating the limb trajectory obtained in Sec. 5.3.2 with phase shifts, $\omega_{FR} = \omega_{BL} = \omega_d = \pi$ in FR, BL limbs and $\omega_{FL} = \omega_{BR} = 0$ in FL, BR limbs (Fig. 5.13). Accordingly, taskspaces of FR and BL limbs in (5.27) and (5.28) are modified as

$$x_{1,3} = \begin{cases} x_0 + \rho\cos(\varphi + \omega_d) & 0 \le t < t_s, \\ x_0 + \rho\cos(\varphi + \vartheta + \omega_d) & t_s \le t < \tau, \end{cases} \tag{5.32}$$

$$y_{1,3} = \begin{cases} y_0 + \left(1 - \frac{2t}{t_s}\right)\rho\sin(\varphi + \omega_d) & 0 \le t < t_s, \\ y_0 - \rho\sin(\varphi + \vartheta + \omega_d) & t_s \le t < \tau. \end{cases} \tag{5.33}$$

In order to maintain stability, we ensure that at least one diagonal limb pair is always at the stance phase, i.e., on ground during the stance-swing transition in a trajectory cycle. We achieve this by introducing a time shift, Δt such that $t_s = t_s + \Delta t$ letting a diagonal limb pair to initiate its limb trajectory with a time delay relative to the other one. Note that, Δt depends on the limb actuation frequency, f (or trajectory period, $\tau = 1/f$) and stance period, t_s. Accordingly, to satisfy above ground contact requirement, we compute Δt as

$$\Delta t = \tau(k - D) \tag{5.34}$$

where k ($> D$) is a scalar that relates Δt into τ and D based on limb trajectories of diagonal limb pairs.

During straight locomotion, the robot body is maintained at straight mode (i.e., $\theta_B = \phi_B = 0$) all the time. Figure 5.14 shows trajectory outputs (A – taskspace, B – curve parameters, and C – joint variables) of limbs in relation to their origins with $X_d = 10\ cm$, $\rho = 6\ cm$, $D = 0.2$, $\tau = 4\ s$ ($f = 0.25\ Hz$), and $\Delta t = 1.34\ s$. We verify the proposed locomotion trajectory through kinematic simulations performed in MATLAB. Please refer to Quadruped-Trotting-Multimedia to see them.

D. Generating Trotting-and-Turning

For a given turn radius and a turn direction, we assume that the range of motion of a limb on the ground (i.e., ground spread) follows a turn curve as depicted in the rightward turn in Fig. 5.14D. The turning herein can be analogized to turning a four-wheeled automobile. Therein, inner and outer wheels follow turn curves with different radii. Since inner wheels follow a smaller turn curve, they make a tighter turn than outer wheels. We can replicate this phenomenon in the quadruped by giving different ground spreads for left and right limbs according to the desired turn direction and the turn radius. Note that, the ground spread, s is proportional to the trajectory stride radius, ρ as given in

(5.31). Accordingly, in Fig. 5.14D, when trajectory radii of outer (or left) limbs are larger than the inner (or right) limbs (i.e., $\rho_O > \rho_I$ with $\rho_O = \rho_{FL} = \rho_{BL}$ and $\rho_I = \rho_{FR} = \rho_{BR}$), the robot moves in a rightward angular trajectory. Conversely, when the inner limb radii are larger, the robot turns leftward. When turning, we adjust the spatial deformation of the robot body, ϕ_B and $\theta_B = \pm\frac{\pi}{2}$, to match the turn angle. It prevents the robot from slipping sideways.

Figure 5.14E spatially visualizes the aforementioned turning philosophy. The horizontal limb heel distance or distance to the ground spread relative to the corresponding body coordinate frame, $\{O_j\}$ (i.e., d_O or d_I in Figs. 5.14D and 5.14E) can be found from the trajectory taskspace, z_j (i.e., d_g in Fig. 5.14D) during the stance interval. For subsequent derivations, consider the notations in Fig. 5.14D. For known d_O, d_I and the desired turn radius, $\lambda(> d_O, d_I)$, the ratio between outer and inner turn curve lengths can be derived as

$$\frac{A_O}{A_I} = \frac{\lambda + d_O}{\lambda - d_I}. \tag{5.35}$$

By accounting ground spreads of outer limbs, s_0 and inner limbs, s_I, the length ratio between $P-Q$ and $V-W$ turn curves can be expressed as

$$\frac{A_O - s_0}{A_I - s_I} = \frac{\lambda + d_O}{\lambda - d_I}. \tag{5.36}$$

Results in (5.31), (5.35), and (5.36) relate the robot turn curve lengths to stride radii as

$$\frac{A_O}{A_I} = \frac{\rho_O}{\rho_I}. \tag{5.37}$$

Utilizing results in (5.35) and (5.37), we adjust the trajectory stride radii of two sides as

$$\rho_O = \left(\frac{\lambda + d_O}{\lambda - d_I}\right)\rho_I. \tag{5.38}$$

Additionally, the robot's body bending, ϕ_B can be adjusted as

$$\phi_B = \frac{L}{\lambda}. \tag{5.39}$$

Figure 5.14F shows the variation of the horizontal limb heel distance relative to $\{O_j\}$ based on different trajectory strides (ρ_O, ρ_I) of outer and inner limbs. We obtained those results by applying a turning radius, $\lambda = 40\ cm$ with $X_d = 10\ cm$, $D = 0.2$, $\rho_I = 4\ cm$, and $\tau = 4\ s$ ($f = 0.25\ Hz$). Utilizing (5.38) and (5.39), we found $\rho_O = 6\ cm$ and $\phi_B = 37.2°$, respectively.

5.4 Chapter Summary

This chapter focused on generating locomotion trajectories for the soft mobile robots. The methodologies involved modeling desired gaits as periodic mathematical curves/shapes, discretizing them, and using inverse kinematics to convert taskspace into jointspace variables. For the SRS, sidewinding, serpentine, rolling, and helical rolling gaits were illustrated. For the tetrahedral robot, first, inspired by pinniped crawling, various crawling gaits were generated, and then a novel energy-efficient tumbling locomotion gait was explored. The quadrupedal robot's crawling and trotting trajectories were modeled, incorporating phase shifts between diagonal limb pairs for efficient locomotion. In the subsequent chapter, closed-loop control strategies are introduced for the proposed locomotion gaits.

Chapter 6

Closed-loop Control of Soft Mobile Robots

6.1 Motivation and Significance

The motivation behind closed-loop control of soft mobile robots stems from the need to enhance their adaptability, stability, and overall performance in locomotion. The deformable nature of soft mobile robots poses challenges in ensuring precise and predictable locomotion, especially in unpredictable surroundings. Closed-loop control systems, which incorporate feedback mechanisms to continuously adjust the robot's behavior based on sensory information, are pivotal in addressing these challenges. By integrating sensors that monitor the robot's surroundings, internal states, and external forces, closed-loop control facilitates real-time adjustments in the robot's gait, shape, and interaction with the environment. This enables soft mobile robots to adapt to varying terrains, obstacles, and tasks, ensuring stable locomotion and enhancing their overall maneuverability and functionality. The significance of closed-loop control lies in its ability to improve the robot's robustness, responsiveness, and autonomy, thereby expanding its applicability in various domains. For example, in industrial settings, these robots can efficiently manipulate objects of various shapes and sizes, contributing to flexible and agile manufacturing processes. Moreover, in disaster scenarios, these robots can be deployed to traverse unpredictable terrains, locate survivors, and deliver aid effectively, enhancing the efficiency of search and rescue operations.

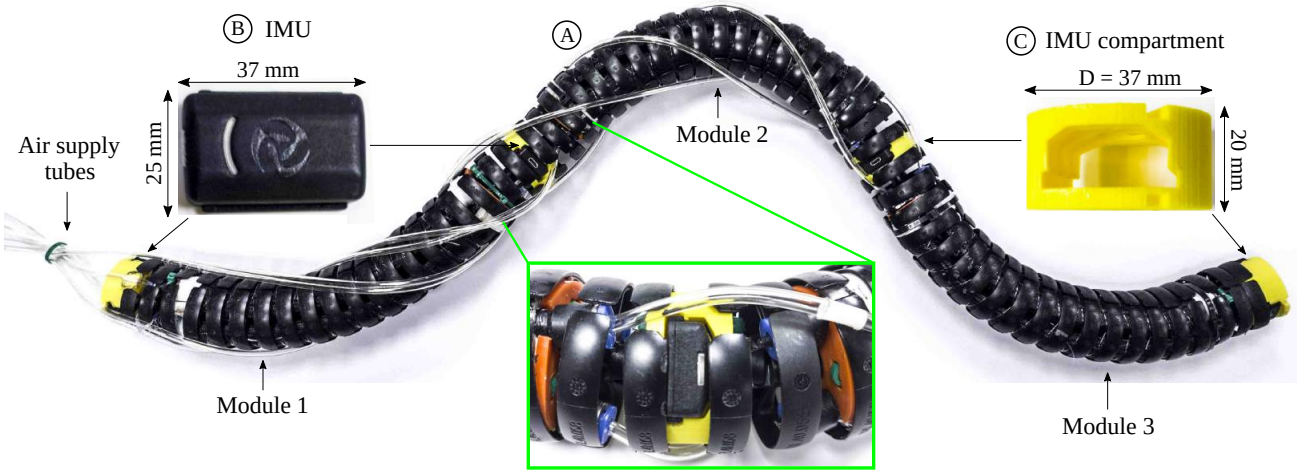

Figure 6.1: (A) Modified SRS prototype with closed-loop control implementation, showcasing key design elements. The enlarged view highlighting the placement of onboard sensors between adjacent sections within the SRS body. (B) Wireless Inertial Measurement Unit (IMU) sensors used for capturing deformation. (C) Sensor compartment.

Overall, closed-loop control of soft mobile robots not only addresses the challenges associated with their deformable nature but also unlocks their full potential in a wide range of applications. By providing greater stability, adaptability, and responsiveness, this control mechanism paves the way for the integration of soft robots into various industries and critical tasks, revolutionizing the way robots interact with their environment and enhancing their practical significance in diverse real-world scenarios.

6.2 Closed-loop Control of Soft Robotic Snake

Noting the lack of closed-loop control mechanisms in soft mobile robots, as highlighted in the literature review presented in Sec. 2.7, we propose a feedback control method to effectively manage the locomotion of the SRS introduced in Sec. 3.2. The SRS locomotion trajectory considered herein is planar rolling (refer to Sec. 5.1.2), and our objective is to maintain the desired bending curvature of the SRS sections during locomotion. The following sections detail our proposed strategy for achieving this.

6.2.1 SRS Prototype Modifications

The SRS prototype proposed in Sec. 3.2 is modified to accommodate the onboard sensors that are used to measure the deformation (i.e., orientation and bending curvature) of individual sections. Figure 6.1A shows the modified 3-section SRS prototype showcasing its design elements. To measure

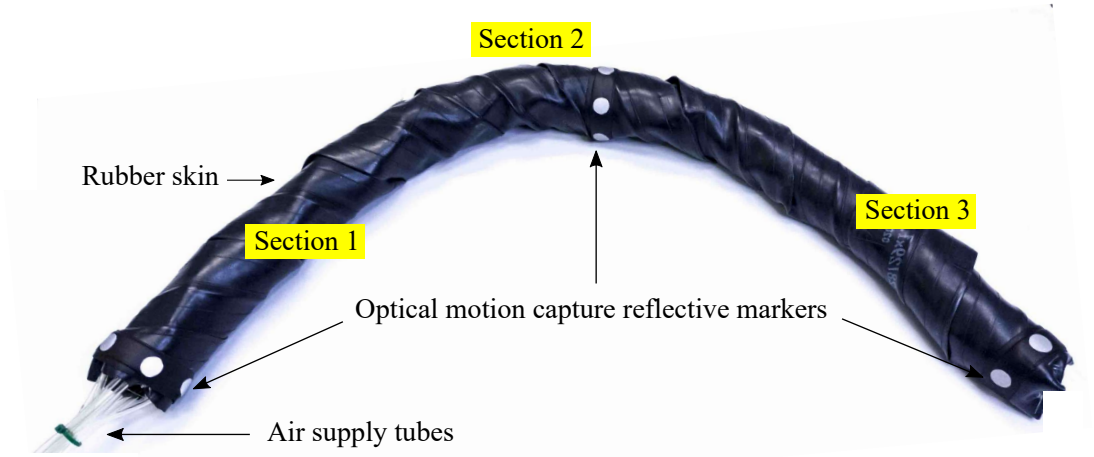

Figure 6.2: Three-section SRS prototype equipped with reflective markers for motion capture.

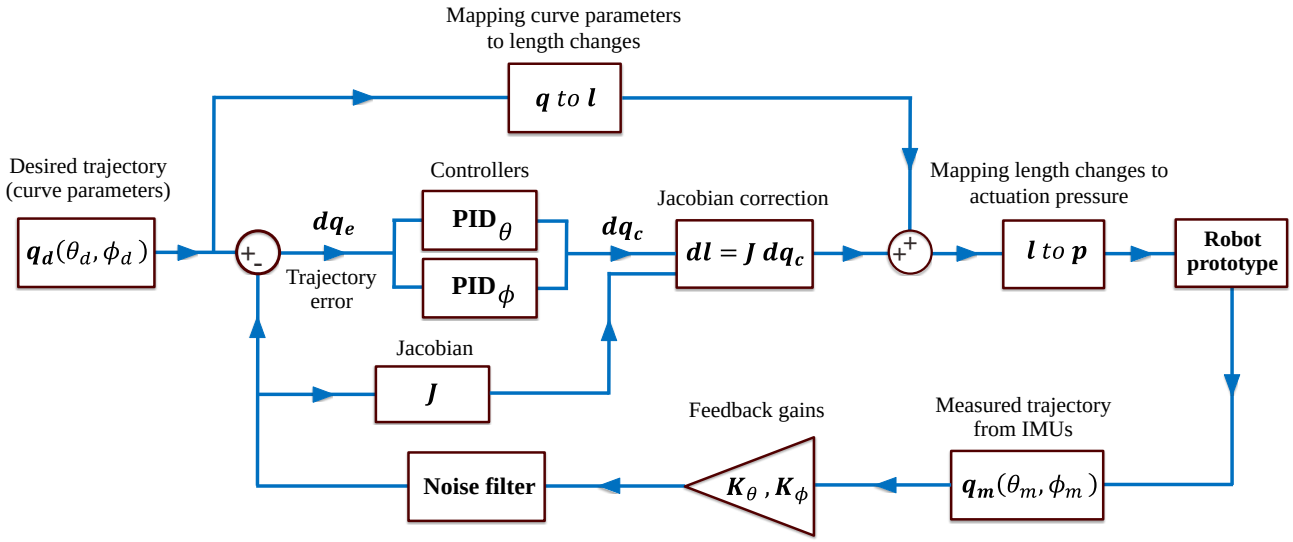

Figure 6.3: Proposed closed-loop control system for the SRS prototype.

the deformation, we use 3-Space Mini Wireless Inertia Measurement Units (IMUs) from Yost Labs, Inc, USA (Fig. 6.1C). Four IMUs are serially attached within the SRS body at uniform intervals, starting from the base and extending to the tip of each section, utilizing the 3D-printed sensor compartments (Fig. 6.1D). An IMU primarily provides the orientation data of its current location. We integrated this orientation data into the kinematic model of a soft module as presented in [237], to obtain the curve parameters (θ, ϕ in (4.2)) in real-time. This serial arrangement of IMUs allows us to undertake the relative measurements, resulting in the curve parameters of individual SRS sections. Figure 6.2 shows the SRS prototype after wrapping it with a thin rubber sleeve. We position optical reflective markers within the SRS body to capture its motion.

6.2.2 SRS Control Strategy

We propose jointspace control of SRS for planar rolling. Figure 6.3 provides the schematics of the complete control system. The desired curve parameters of the rolling trajectory are compared against the trajectories measured by IMUs. The trajectory error, dq_e, is then adjusted using Proportional Integral Derivative (PID) controllers. Note that each curve parameter is managed by a separate PID controller due to their vastly different behavior patterns during rolling. This approach allows for separate tuning of controller gains, resulting in improved accuracy.

Next, the adjusted deformation error, dq_c, is mapped to length changes as $dl = J\ dq_c$, where J is the jointspace Jacobian given in (4.7). Subsequently, this adjusted length change, dl, is added to the current length change and mapped to actuation pressures to actuate the SRS. The curve parameters measured by the IMUs are processed through a moving average noise filter to suppress excessive noise. Additionally, two feedback gains, $\{K_\theta, K_\phi\}$, are used to adjust discrepancies in each measured signal, as shown in Fig. 6.3. The feasibility of the above control strategy is evaluated in subsequent sections.

6.2.3 Testing Control System for Fundamental SRS Motion in a Soft Module within a Simulation Environment

First, we implemented the proposed control strategy in Sec. 6.2.2 within the MATLAB Simulink environment before deploying it in the SRS prototype. Here, we focus on controlling a separated soft module (i.e., an individual section of the SRS) rather than the assembled SRS. Our plan is to test the control system for an individual soft module in both simulation and experimental settings, and then extend it to control the SRS motion. Simulations allow us to evaluate the significance of individual control components and their contributions to achieving effective control of a soft module. Accordingly, the control system in Fig. 6.3 is modified to accommodate simulations, as shown in Fig. 6.4. In this setup, the SRS prototype is replaced by the soft module's kinematic model. To make the simulation as close to real-life experiments as possible, we added a noise of 0.2 rad, consistent with the noise recorded during measurements. Additionally, we incorporated a transport delay of 0.05 s for the feedback signal and sampled it at 30 Hz to mirror real-life experiments. A dead zone of 1 bar was included to represent the actual dead zone of PMAs in the soft module [183]. In line with the practical implementation, the forward signal was sampled at a higher rate of 60 Hz (see Fig. 6.4).

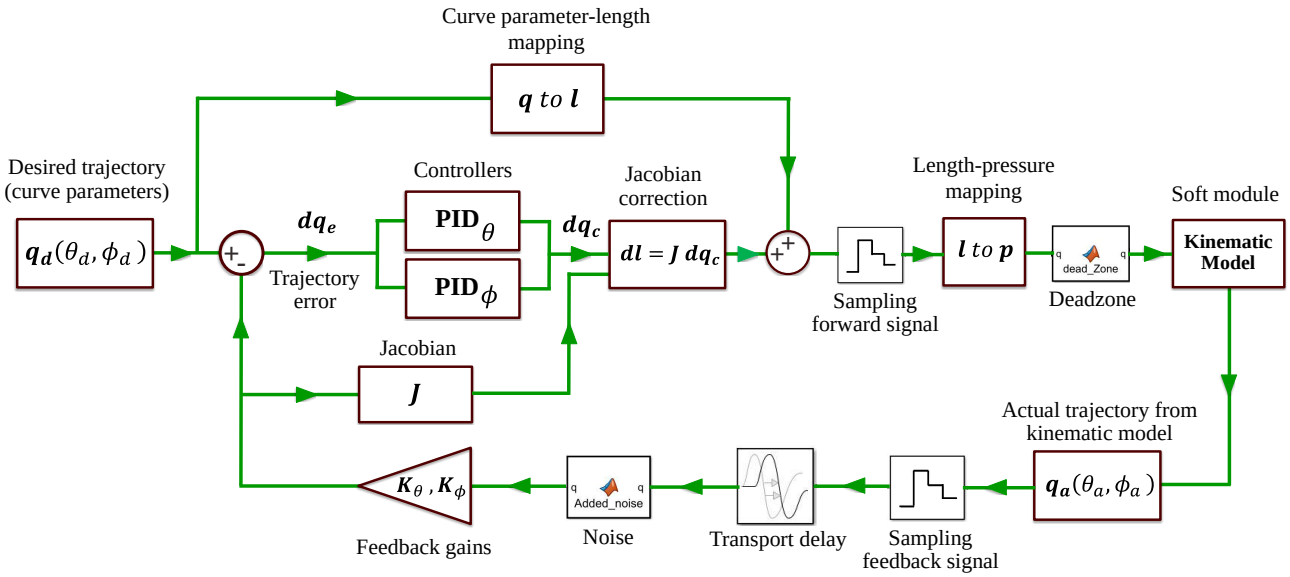

Figure 6.4: Modified control system for testing the fundamental SRS motion in a soft module within MATLAB Simulink.

Table 6.1: Optimized controller gains in soft module simulation for fundamental SRS motion.

Actuating Frequency, f $[Hz]$	**Bending Curvature,** ϕ $[rad]$	**Feeback Gains**		**PID$_\theta$ Gains**			**PID$_\phi$ Gains**		
		K_θ	K_ϕ	K_P	K_I	K_D	K_P	K_I	K_D
0.3	$\pi/12$	1.00	1.00	0.10	0.25	0.05	0.10	0.15	0.00
	$\pi/6$								
0.6	$\pi/12$	1.00	1.00	0.10	0.35	0.10	0.10	0.20	0.05
	$\pi/6$								

An SRS planar rolling trajectory was generated by varying the orientation, θ, from $0 \rightarrow \pi$, and then from $-\pi \rightarrow 0$ rad, while keeping the bending curvature, ϕ, at a constant value [167]. The soft module was simulated for planar rolling trajectories generated under two bending curvatures, $\phi = \{\frac{\pi}{12}, \frac{\pi}{6}\}$ rad, and two actuation frequencies, $f = \{0.3, 0.6\}$ Hz, that reflect SRS prototype testing. During the simulations, the PID controller and feedback gains were tuned in real-time on a trial-and-error basis to obtain the best control performance within the Simulink environment. Table 6.1 gives the optimized controller gains, and Fig. 6.5 shows the simulation results under the aforementioned bending curvature – actuation frequency combinations. Table 6.2 also provides the Root Mean Square Error (RMSE) of the controlled signal in each simulation. The results indicate that the proposed control scheme demonstrates robustness under various simulation conditions (i.e., bending curvature and actuation frequency combinations), as the RMSE for both θ and ϕ remains below 7°.

Given that θ shows a discontinuous behavior (shifting from π to $-\pi$) within a period, the straightforward deduction of θ can lead to misleading error calculations. We handled this issue by calculating

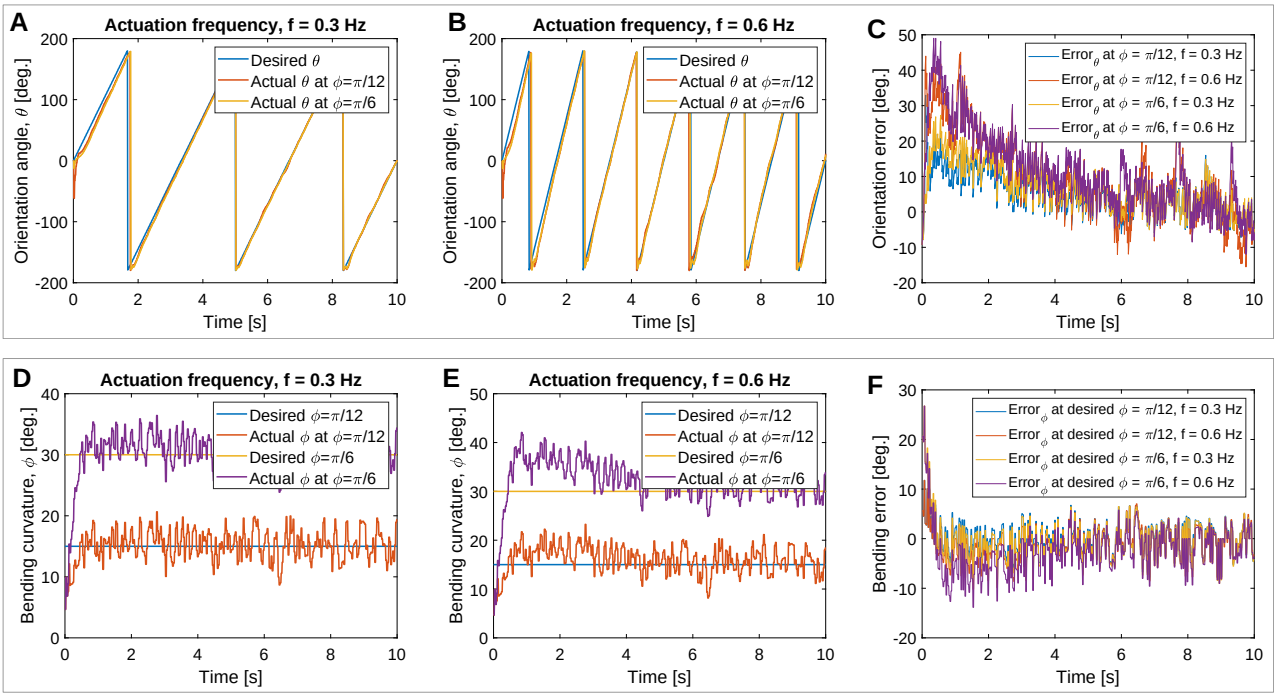

Figure 6.5: Simulation results of soft module control, i.e., desired and actual trajectories of orientation angle, θ, under bending curvatures, $\phi = \{\pi/12, \pi/6\}$ at actuation frequencies, (A) $f = 0.3\ Hz$, (B) $f = 0.6\ Hz$, and (C) respective angular error. (D), (E), and (F) show the controller performance for the bending angle, ϕ, under the same conditions.

Table 6.2: Controller performance: soft module simulation for fundamental SRS motion.

Actuating Frequency, f $[Hz]$	**Bending Curvature,** ϕ $[rad]$	**Jointspace RMSE**$_\theta$ $[deg]$	**Jointspace RMSE**$_\phi$ $[deg]$
0.3	$\pi/12$	2.21	3.29
	$\pi/6$	3.39	5.02
0.6	$\pi/12$	3.65	4.52
	$\pi/6$	4.21	6.25

the angular difference of the error in a way that it wraps around correctly at the discontinuities as presented by Algorithm 1. First, it calculates the absolute differences between desired and actual angles, considering both direct and wrapped-around differences to determine the minimum error (refer to lines 3-4). Depending on the minimum error, it then computes the error vector and adjusts for any angular dependency (refer to lines 5-11). Errors below a threshold of 0.01 are set to zero to account for negligible deviations (refer to lines 12-17). This approach ensures precise evaluation of angular deviations, which is critical for accurate trajectory tracking and correction in spherical coordinate systems.

Algorithm 1 Trajectory Error Computation

Require: θ_d (desired theta), ϕ_d (desired phi), θ_a (actual theta), ϕ_a (actual phi)
Ensure: *error_theta*, *error_phi*, *angular_error_theta*, *angular_error_phi*

$q_d \leftarrow [\theta_d, \phi_d]$
$q_a \leftarrow [\theta_a, \phi_a]$
$abs\_diff\_1 \leftarrow |\theta_d - \theta_a|$
$abs\_diff\_2 \leftarrow |\mod(\theta_d, 2\pi) - \mod(\theta_a, 2\pi)|$
if $abs\_diff\_1 < abs\_diff\_2$ **then**
    $error \leftarrow q_d - q_a$
    $theta\_dep \leftarrow \theta_d$
else
    $error \leftarrow \mod(q_d, 2\pi) - \mod(q_a, 2\pi)$
    $theta\_dep \leftarrow \mod(\theta_d, 2\pi)$
end if
if $|error[0]| < 0.01$ **then**
    $error[0] \leftarrow 0$
end if
if $|error[1]| < 0.01$ **then**
    $error[1] \leftarrow 0$
end if
$error\_theta \leftarrow error[0]$
$error\_phi \leftarrow error[1]$
$angular\_error\_theta \leftarrow \mod(\theta_d - \theta_a + \pi, 2\pi) - \pi$
$perecenteage\_error\_theta \leftarrow |angular\_error\_theta/\pi| \times 100$
$angular\_error\_phi \leftarrow \mod(\phi_d - \phi_a + \pi, 2\pi) - \pi$
$perecenteage\_error\_phi \leftarrow |angular\_error\_phi/\pi| \times 100$
$error\_norm \leftarrow \text{norm}(error)$
return *error_theta*, *error_phi*, *angular_error_theta*, *angular_error_phi*

6.2.4 Testing Control System for Fundamental SRS Motion in a Soft Module Prototype

Based on the results of the soft module simulation in Sec. 6.2.3, we deployed the proposed control scheme in a soft module prototype utilizing the experimental setup shown in Fig. 6.6. This testing is significant as it provides an opportunity to evaluate the fundamental motion trajectory of the SRS in an individual limb prototype and adjust the controller parameters prior to deploying the controller in the SRS prototype.

An IMU is attached to the soft module's heel via a dedicated limb-heel sensor compartment (Fig. 6.6). We adopted identical testing parameters (i.e., bending curvature and actuation frequencies) similar to the simulation. For the prototype testing, we used the optimized controller gains as the baseline to initiate the controller. However, we found that the optimized controller gains from the simulations needed further optimization to achieve better performance. Accordingly, Table 6.3 provides the updated controller gains, while Fig. 6.7 and Table 6.4 present the experimental outcomes

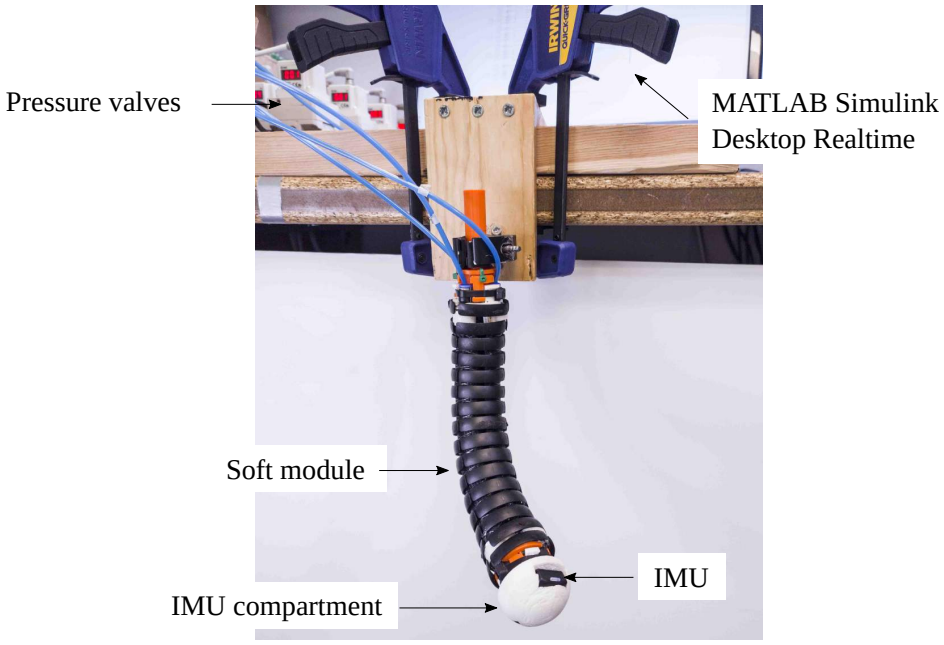

Figure 6.6: Experimental setup for testing control system in a soft module prototype.

and recorded controller errors (with and without controller), respectively. We computed the error reduction percentage in jointspace, E [%], as defined by (6.1), and recorded it in Table 6.4 to further validate the controller's action quantitatively.

$$E\ [\%] = \frac{E_{No\ Control} - E_{With\ Control}}{E_{No\ Control}} \times 100. \tag{6.1}$$

Our initial control assumption was that jointspace control would enable us to manage the soft limb's taskspace trajectory. To test this, we actuated the soft limb prototype in both open-loop (no control) and closed-loop (with control) configurations and recorded the soft limb's taskspace position using a motion tracker system (Vicon Inc, USA). The actuation frequency of the soft limb was set to 0.3 Hz, with the bending curvature maintained at 30°. Figure 6.8 illustrates the recorded task space curves. The error reduction percentage was found to be approximately 25 %, demonstrating the impact of the closed-loop control.

Values in Table 6.3 indicate that when the actuation frequency varies, the gains must be re-tuned. Results in Table 6.4 show that the controller can achieve an RMSE margin of 10° in soft module prototype testing. The error reduction percentage remains approximately 20 % for θ, while it stays around 35 % for ϕ. It should also be noted that the controller error increases (i.e., error reduction

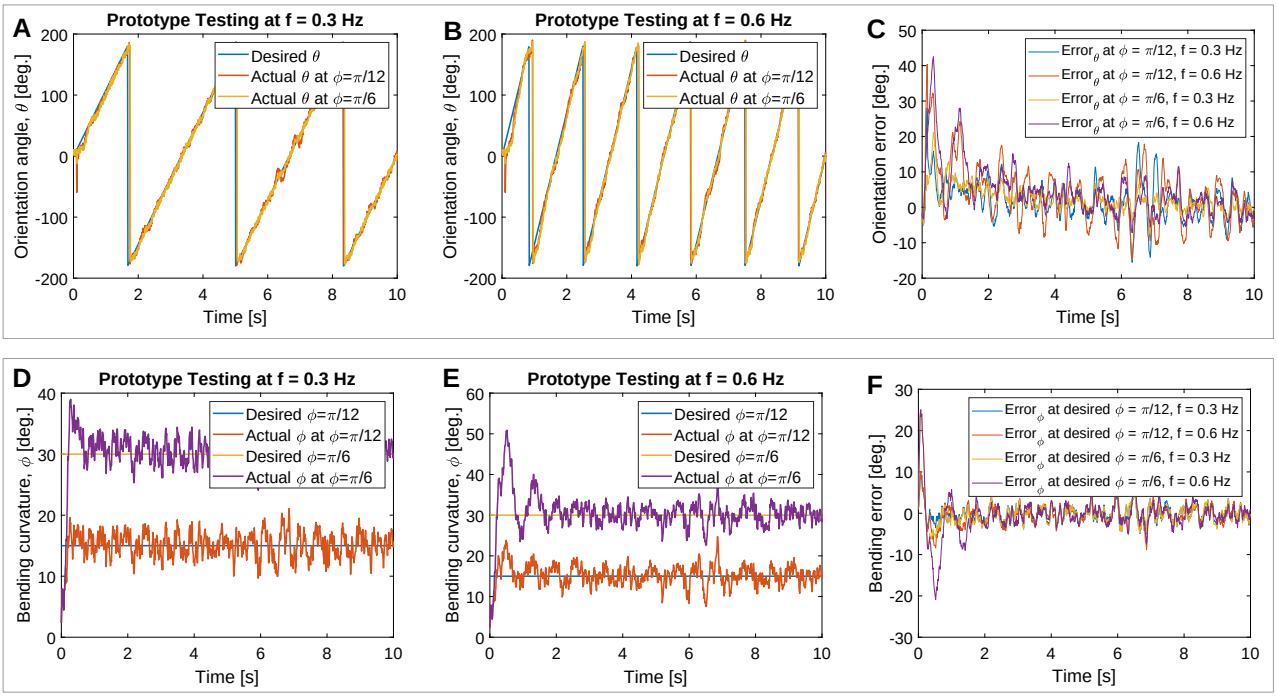

Figure 6.7: Experimental results of soft module prototype control, i.e., desired and actual trajectories of orientation angle, θ, under bending curvatures, $\phi = \{\pi/12, \pi/6\}$ at actuation frequencies, (A) $f = 0.3\ Hz$, (B) $f = 0.6\ Hz$, and (C) respective angular error. (D), (E), and (F) show the controller performance for the bending angle, ϕ, under the same conditions.

percentage decreases) with the actuation frequency, which is apparent due to the controller's inability to handle fast actuation rates because of the transport delays in the feedback signal. A multimedia file demonstrating the control of the soft module prototype with real-time trajectory tracking is included in SRS Control-Multimedia. The above simulation and prototype results are brought forward and experimentally validated the locomotion on the SRS prototype in Sec. 7.2.4, Chapter 7.

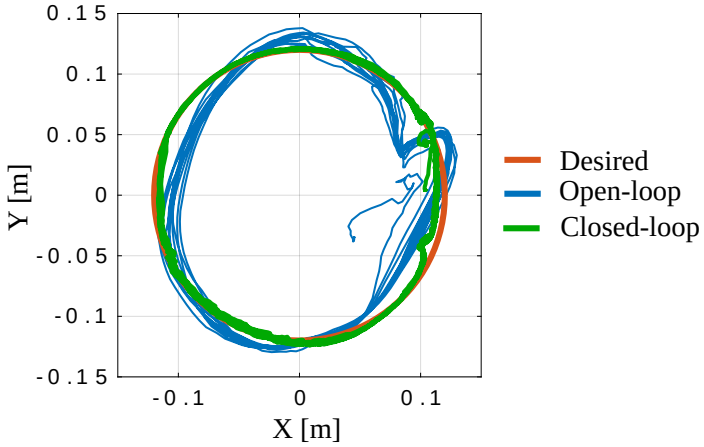

Figure 6.8: Taskspace performance of the controller for fundamental SRS motion tested on the soft module prototype.

Table 6.3: Optimized controller gains in soft module prototype and SRS prototype actuation.

Actuating Frequency, f $[Hz]$	**Bending Curvature,** ϕ $[rad]$	**Feeback Gains**		**PID$_\theta$ Gains**			**PID$_\phi$ Gains**		
		K_θ	K_ϕ	K_P	K_I	K_D	K_P	K_I	K_D
0.3	$\pi/12$	1.00	1.10	0.20	0.35	0.10	0.20	0.15	0.05
	$\pi/6$								
0.6	$\pi/12$	1.00	1.10	0.30	0.35	0.20	0.20	0.20	0.10
	$\pi/6$								

Table 6.4: Controller performance: soft module prototype actuation for fundamental SRS motion.

Actuating Frequency, f $[Hz]$	**Bending Curvature,** ϕ $[rad]$	**Jointspace RMSE$_\theta$** $[deg.]$			**Jointspace RMSE$_\phi$** $[deg.]$		
		NC	**WC**	**E [%]**	**NC**	**WC**	**E [%]**
0.3	$\pi/12$	4.89	4.19	16.7	6.08	4.61	31.9
	$\pi/6$	5.88	4.93	19.3	8.97	6.77	32.5
0.6	$\pi/12$	5.11	4.17	22.5	7.96	5.82	36.8
	$\pi/6$	7.31	5.89	24.1	10.0	7.19	39.1

NC - No Control, WC - With Control

6.3 Closed-loop Control of Soft-limbed Quadruped

We extend the proposed joinstpace control scheme of the SRS in Sec. 6.2.2 for controlling the trotting gait of the quadruped presented in Sec. 5.3.2. Our objective is to maintain the desired fundamental limb trajectory of each limb during the trotting movement.

6.3.1 Quadruped Control Strategy

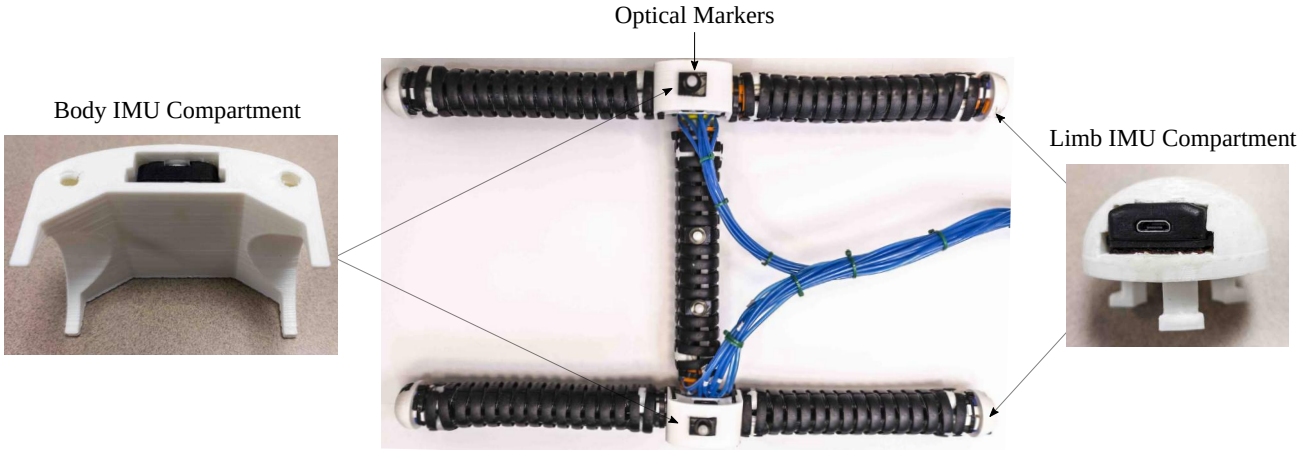

Figure 6.9: Modified quadruped prototype featuring newly added onboard sensor compartments.

Similar to the SRS in Sec. 6.2, it is required to measure the limb orientation and bending curvature (i.e., limb deformation) during locomotion. To achieve this, the quadruped prototype proposed in Chapter 3 is updated to accommodate onboard IMU sensors, as shown in Fig. 6.9. This setup includes

two body IMU compartments fixed to the quadruped body and four limb IMU compartments fixed to each limb heel. All compartments are 3D-printed. The IMUs fixed at the body level are used to independently measure the relative limb deformation. Here, we propose an identical control system similar to the one presented for the SRS in Fig. 6.3 as the control scheme for the quadruped.

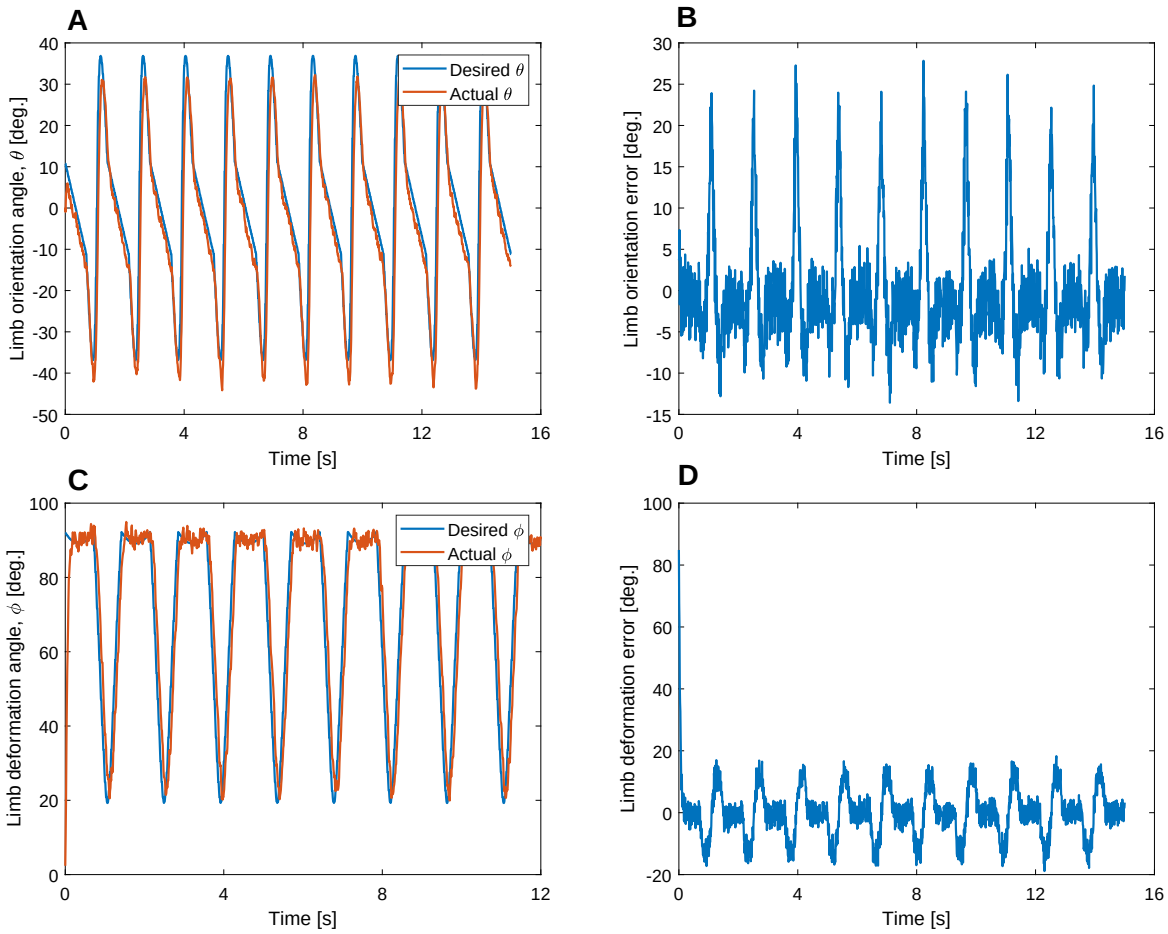

Figure 6.10: (A) Simulation results of controlling the fundamental limb trajectory of a trotting gait under optimized gait parameters. (B) Corresponding control error.

6.3.2 Testing Control System for Fundamental Limb Movement within a Simulation Environment

Following the testing procedure outlined in Sec. 6.2.3, we tested the fundamental trotting gait for the soft module's kinematic model within the MATLAB Simulink environment using the modified control system shown in Fig. 6.4. The gait parameters used in the simulation are based on the optimized trotting parameters presented in Table 7.21, Chapter 7. Figure 6.10 shows the simulation results

when the gait is operated at the optimized actuation frequency, $f = 0.7\ Hz$. To obtain these results, the controller gains were tuned in real-time, and Table 6.5 presents the optimized gains for trotting. Re-tuning of gains was necessary due to changes in the shape of the locomotion trajectory and the actuation frequency. The results in Fig. 6.10 show that the actual limb trajectory closely follows the desired one. We found the RMSE of limb orientation, θ, and bending curvature, ϕ, to be within the margin of error, 11° and 8°, respectively. The respective error reduction percentages were 15 % and 25 %.

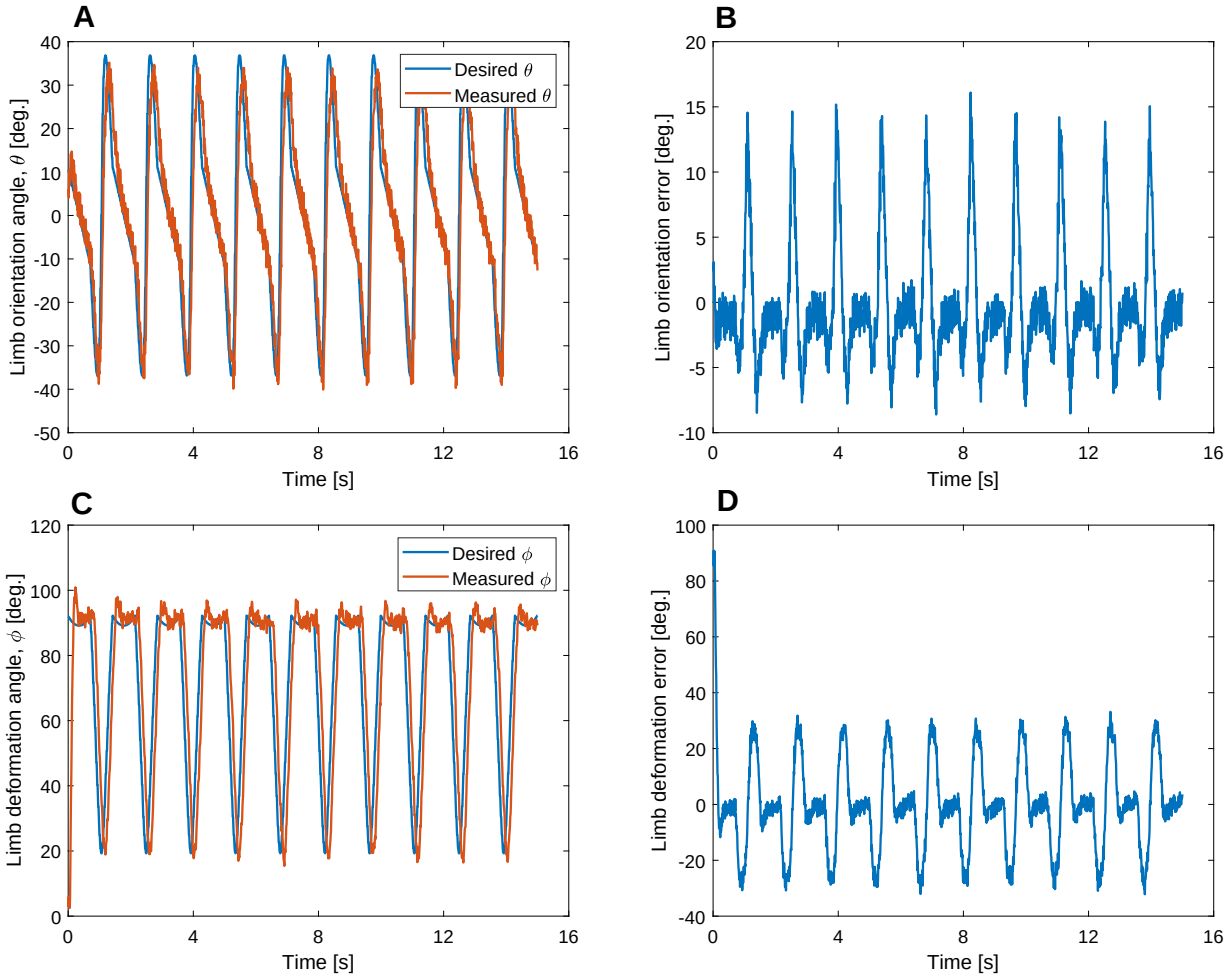

Figure 6.11: (A) Experimental results of controlling the fundamental limb trajectory of a trotting gait in a soft module prototype under optimized gait parameters. (B) Corresponding control error.

Table 6.5: Optimized controller gains in soft-limb and quadruped prototype testings for trotting trajectory.

Feedback Gains		**PID$_\theta$ Gains**			**PID$_\phi$ Gains**		
$\mathbf{K}_\theta$	$\mathbf{K}_\phi$	$\mathbf{K}_P$	$\mathbf{K}_I$	$\mathbf{K}_D$	$\mathbf{K}_P$	$\mathbf{K}_I$	$\mathbf{K}_D$
1.05	1.21	0.30	0.42	1.15	0.25	0.10	0.05

6.3.3 Testing Control System for Fundamental Limb Movement in a Soft-limb Prototype

Simulation results presented in 6.3.2 are brought forward for testing the fundamental limb trajectory in the soft module prototype. This is a repetition of the test conducted on the fundamental motion of SRS locomotion in Sec. 6.2.4. For this purpose, we used the experimental setup shown in Fig. 6.6 and applied the same trotting limb trajectory used in the soft module simulation in Sec. 6.3.2. Figure 6.11 shows controller performance during the testing. The RMSE of limb orientation, θ, and bending curvature, ϕ, were reported to be less than, 20° and 12°, respectively, at all times. The error reduction percentage for θ remained approximately at 18 %, while it stayed at 30 % for ϕ. It must be noted that, unlike in the simulation, the experimental results show a higher margin of error leading to lower error reduction percentages. This is expected due to non-linear characteristics, hysteresis, dead zones, and other unaccounted losses in the soft module prototype. Despite these factors, the results show that the actual jointspace closely follows the desired trajectory, demonstrating the controller's engagement. Quadruped Prototype testing and further validations of these results are presented in Sec. 7.4.3, Chapter 7.

6.4 Chapter Summary

This chapter discusses the closed-loop control of soft mobile robots, emphasizing its significance in enhancing adaptability, stability, and performance by using feedback mechanisms to adjust behavior based on sensory information. For the SRS, a feedback control method for planar rolling locomotion was proposed, involving onboard sensors to measure deformation and orientation, and jointspace control using PID controllers. This system was tested successfully in a simulation environment. Similarly, for the soft quadruped robot, a control scheme was developed to maintain the desired limb trajectory during trotting, with onboard IMU sensors measuring limb deformation. Simulation tests showed minimal error between actual and desired trajectories. The next chapter will address the experimental validation of these control systems.

Chapter 7

Simulation and Experimental Validation

7.1 Validation of Soft Module

7.1.1 Experimental Setups

A block diagram of the experimental setup is shown in Fig. 7.1. The air compressor provides a constant 8 *bar*, input air pressure. Each PMA pressure is controlled by an SMC ITV3000 (Orange Coast Pneumatics, Inc. USA) digital proportional pressure regulator. Input pressure commands, generated by a MATLAB Simulink Desktop Real-time model, communicated to pressure regulators via an NI PC-6704 data acquisition card. To capture the HSR taskspace movement, three wireless 6-DoF trackers are used (Polhemus G4 wireless – Polhemus, Inc. USA). We mounted trackers at either end – base and tip – as well as at the mid-point of the HSR (Figs. 7.2A and 7.2B) and recorded the tracking data at 100 Hz. The complete experimental setups for both HSR and the variable-length counterpart (i.e., a soft robot without a backbone) are shown in Fig. 7.2.

7.1.2 Validating Stiffness Control Range Improvement

This section assesses the impact of backbone integration on the improvement of controllable stiffness range with respect to the robot designs with and without backbone, shown in Figs. 7.2A and 7.2B, respectively. To limit the torsional deformation during operation, we constrain the bending of both

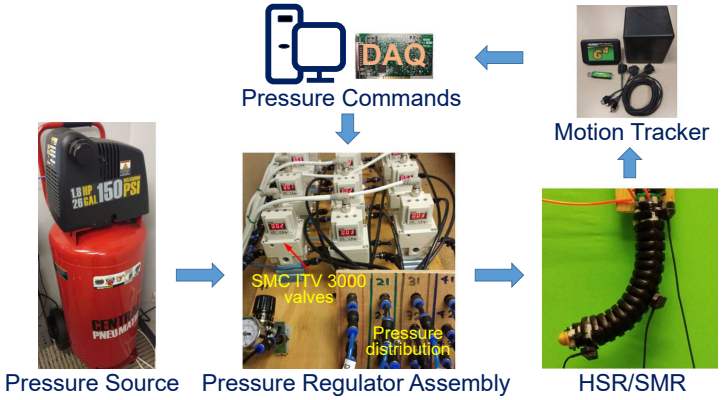

Figure 7.1: Experimental setup of the HSR and backboneless soft robot (SMR).

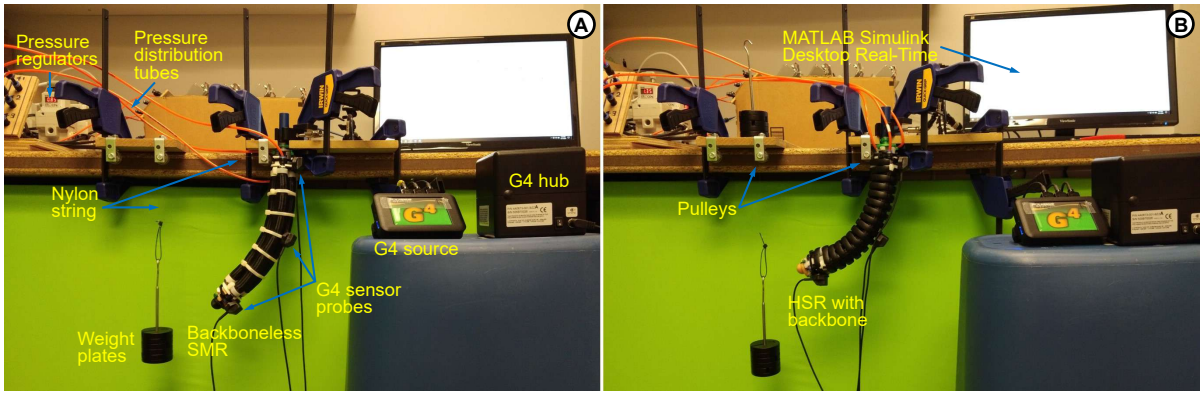

Figure 7.2: Experimental setups to obtain bending stiffness in, (A) soft robot without backbone, (B) proposed HSR (with backbone).

designs to a plane. We achieved this by simultaneously supplying the same pressure commands to two PMAs. This results in planar bending deformation, as shown in Fig. 7.3. The other pressure input counteracts the bending and, due to the antagonistic PMA arrangement and fixed-length constraint, controls the stiffness. We use an experimental approach to estimate the stiffness. Thus, we can use the same arrangement and limit outside influences associated with setup changes. Further, as we replicate the same test in both soft robot designs with identical actuator arrangements, we can extrapolate and generalize the results for omnidirectional bending across both designs. The supply pressure combinations that were applied in these tests are shown in Table 7.1. To comply with the limitations of the experimental setup, the pressure combinations are chosen such that the bending is unidirectional, as shown in Fig. 7.3. We achieve this behavior by setting a higher or equal pressure value to P_2 pressure component (corresponds to the pressure of two simultaneously actuated PMAs). In this experiment, we use pressure combinations outlined in Table 7.1 for both designs. Upon applying each pressure combination, we utilized a pulley arrangement to provide a bending torque perturbation.

Table 7.1: Stiffness variation in soft module with and without backbone.

Bending stiffness $[Nmrad^{-1}]$ without backbone

P_1 [bar] \ P_2 [bar]	0.0	0.5	1.0	1.5	2.0	2.5	3.0
3.0	x	x	x	x	x	x	1.39
2.5	x	x	x	x	x	1.22	1.32
2.0	x	x	x	x	0.94	1.07	1.12
1.5	x	x	x	0.62	0.71	0.86	0.92
1.0	x	x	0.49	0.57	0.63	0.70	0.73
0.5	x	0.42	0.46	0.51	0.59	0.62	0.62
0.0	0.39	0.40	0.43	0.48	0.53	0.58	0.61

Bending stiffness $[Nmrad^{-1}]$ with backbone

P_1 [bar] \ P_2 [bar]	0.0	0.5	1.0	1.5	2.0	2.5	3.0
3.0	x	x	x	x	x	x	3.21
2.5	x	x	x	x	x	2.60	2.84
2.0	x	x	x	x	1.76	1.96	2.40
1.5	x	x	x	0.97	1.26	1.63	1.87
1.0	x	x	0.70	0.82	0.97	1.21	1.45
0.5	x	0.56	0.68	0.75	0.82	0.93	1.24
0.0	0.52	0.54	0.62	0.70	0.79	0.90	1.12

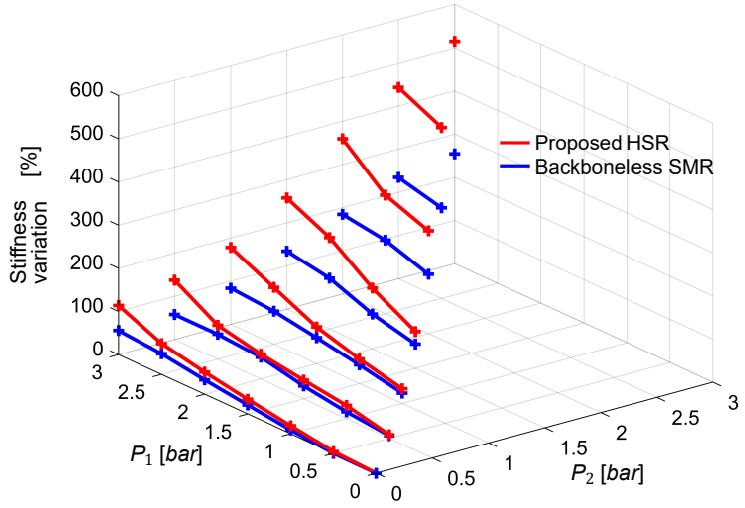

Figure 7.3: Percentage change of bending stiffness in two soft robot designs.

Note that the torque perturbation is normal to the neutral axis of the prototype (Fig. 7.2). We recorded the change in bending angle ($\Delta\phi$) due to the torque perturbation ($\Delta\tau$). Note that the motion tracker system provides taskspace data in terms of positions and orientations. We used the kinematic model in Sec. 4.1.1 to derive the arc parameters, ϕ, and θ from the taskspace data. We calculated the bending stiffness (K) using $K = \frac{\Delta\tau}{\Delta\phi}$. We repeated the same procedure with similar pressure inputs on the variable-length soft robot (i.e., no backbone) design.

Stiffness variation computed through perturbation tests is presented in Table 7.1-left for the backboneless soft robot and in Table 7.1-right for the proposed HSR. The percentage bending stiffness variation with respect to the natural bending stiffness – at $P_1 = 0$ *bar* and $P_2 = 0$ *bar* – is shown in Fig. 7.3. The percentage increase of the bending stiffness in the soft robot without a backbone is $\frac{(1.39-0.39)}{0.39} \times 100\ \% = 256.41\ \%$. Similarly, the percentage bending stiffness increase in the proposed HSR is $\frac{(3.21-0.52)}{0.52} \times 100\ \% = 517.31\ \%$. The results show that the bending stiffness increase in the

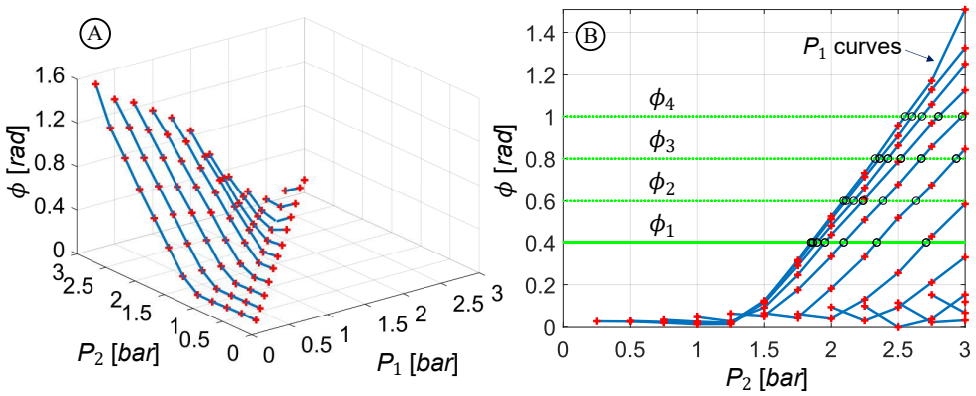

Figure 7.4: (A) Shape-pressure mapping of HSR. (B) Extracting pressure combinations for identified planner bending shapes.

Table 7.2: Shape-pressure-stiffness mapping of soft module.

HSR shape ϕ $[rad]$	Pressure combinations		Bending stiffness
	P_1 $[bar]$	P_2 $[bar]$	$[Nmrad^{-1}]$
0.4	0.50	1.86	0.63
	0.75	1.90	0.81
	1.00	1.96	1.11
	1.25	2.09	1.32
0.6	0.50	2.11	0.71
	0.75	2.17	0.85
	1.00	2.24	1.40
	1.25	2.39	1.71
0.8	0.50	2.36	0.86
	0.75	2.42	1.42
	1.00	2.52	1.90
	1.25	2.67	2.18
1.0	0.50	2.60	1.56
	0.75	2.68	1.98
	1.00	2.80	2.33
	1.25	2.98	2.58

proposed HSR is about 100% higher than that of the variable-length soft robot. Note that both designs have comparable natural stiffness (when applied pressures are 0). This result is expected because both designs use identical PMAs and physical arrangements sans the backbone. Thus, the results conclusively demonstrate that the backbone integration enhances the operational bending stiffness range without betraying bending or compliance capability. With the added benefit of on-demand stiffening capability, it supports tasks requiring structural strength, such as variable payload handling.

7.1.3 Validating Decoupled Stiffness and Deformation Control

We empirically evaluated the independent stiffness and shape controllability of the proposed HSR using the experimental setup in Fig. 7.2B. First, we recorded the shape variation (ϕ) against a range of

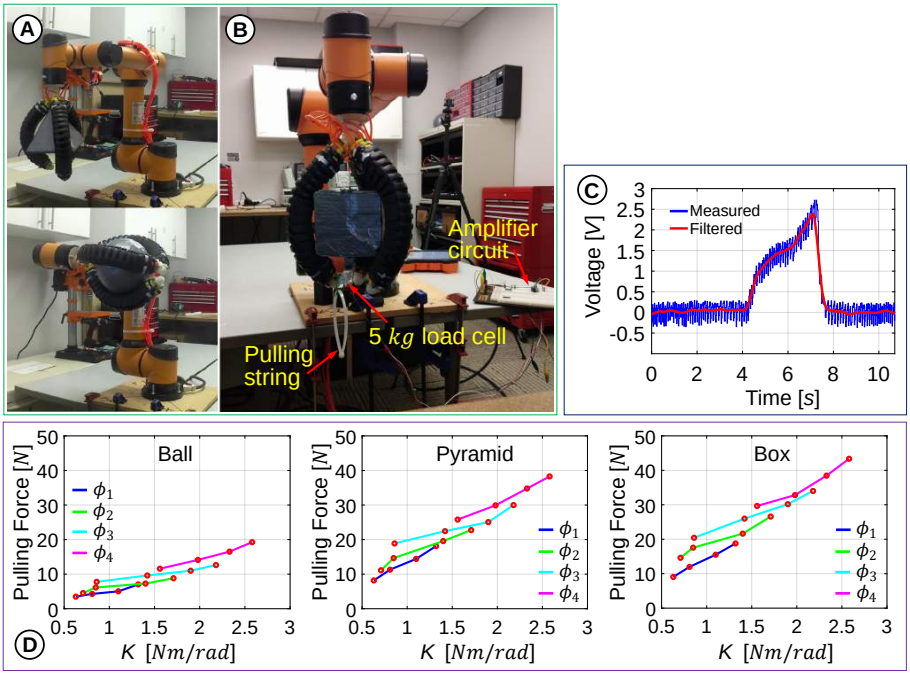

Figure 7.5: (A) Proposed variable stiffness gripper with pyramid and ball objects. (B) Force test experiment with box object. (C) Pulling force reading. (D) Failure forces of three objects.

actuation pressure combinations (P_1, P_2) using the motion tracking system under no-load conditions. Note that, here, we applied bidirectional bending similar to Section 7.1.2. Fig. 7.4A shows the recorded shape variation, and Fig. 7.4B shows the 2D plot of it. Marked bending shapes $(\phi_1 - \phi_4)$ in Fig. 7.4B show that along a particular bending plane (say ϕ_1), we can extract several corresponding pressure combinations (highlighted in circles). Next, we applied a load profile and measured the corresponding bending stiffness (similar to Sec. 7.1.2) for four extracted pressure combinations on ϕ_1 bending plane. Subsequently, we repeated the procedure for other bending planes (ϕ_2, ϕ_3, &, ϕ_4), and Table 7.2 shows extracted pressure combinations and recorded bending stiffness values. The table data reveals that different stiffness values are recorded for the same bending angle under different pressure combinations indicating independent stiffness and shape controllability of the proposed HSR.

7.1.4 Application Example: A Soft Robotic Gripper

We combined three HSR units to fabricate a tri-fingered soft robotic gripper shown in Fig. 7.5A [253]. We conducted the experiment shown in Fig. 7.5B to quantify the effect of decoupled stiffness and shape control for improving grip quality without exerting pressure on objects. We quantify grip

quality utilizing the external force perturbation needed to release an object from the grip. In that respect, higher forces indicate a better grasp. Three objects with geometrically varying surfaces but with the same smoothness (pyramid, ball, and box – approximately 100 g weight) were gripped by applying pressure combinations recorded in Table 7.2 to HSR fingers. In each actuation, an external pulling force is applied to the object via an attached cable until the grip fails. We coupled a 5 kg load cell to record failure forces. Fig. 7.5C shows a typical force sensor output during the test. Therein, we uniformly increase the force while recording the force sensor data until the grip fails. Then we apply a 50-sample moving average to filter the noise in force sensor data and measure the peak value (failure force). Fig. 7.5D presents maximum failure forces against each object's stiffness variation. The plots show that under the same finger shape (same ϕ), the grip failure force increases with the bending stiffness for each object. Moreover, higher bending (i.e., firmer grip $\rightarrow \phi_1 < \phi_2 < \phi_3 < \phi_4$) has recorded higher failure forces for each object. Further, pulling the ball and box recorded relatively the smallest and largest failure forces, respectively. This is due to the fact that ball and box have the relatively lowest and the highest irregular surfaces among the three object shapes. The force test results reveal that the proposed HSR units are useful in applications where independent stiffness and shape control are desired.

7.2 Validation of Soft Robotic Snake Locomotion

7.2.1 Validating General Locomotion Trajectories

A. SRS Experimental Setup

The experimental setup employed in validation studies is shown in Fig. 7.6. The air compressor provides steady 8 bar pressure to 12 digital proportional pressure regulators (SMC ITV3050) that are then connected to individual PMAs (12 PMAs in 4 sections) of the SRS. The MATLAB Simulink Real-Time model computes the length changes and generates $0-10$ V voltage signals via a data acquisition card (National Instruments PCI-6221) to control the pressure regulators in real-time at 20 Hz. During each test, the SRS prototype was actuated on a carpeted floor with uniform friction. Note that, the jointspace trajectories (i.e., length changes of PMAs) obtained in Fig. 5.4 should be converted into actuation pressure trajectories and input to PMAs via the experimental setup (Fig. 7.6) to obtain

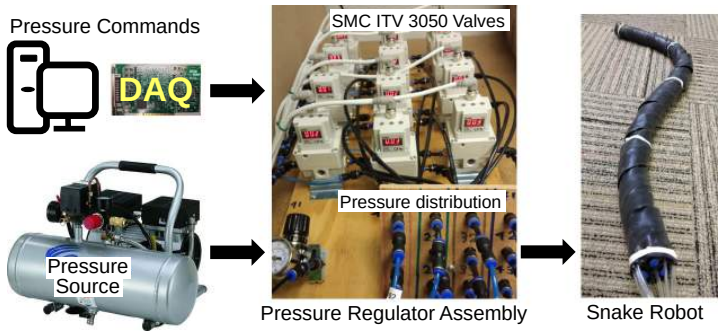

Figure 7.6: SRS experimental setup.

the SRS locomotion. We adopted the jointspace – pressure mapping reported in [167] to generate corresponding pressure inputs.

B. Testing Sidewinding Gait

We tested the SRS's ability to achieve sidewinding locomotion by applying different pressure amplitude and frequency combinations. We initiated the testing at pressure ceiling, $p = 3\ bar$, and actuation frequency, $f = 0.25\ Hz$. We chose those values because we found that low pressures ($p < 3\ bar$) onto PMAs could not provide an adequate bending in SRS sections and low frequencies ($f < 0.25\ Hz$) could not provide an adequate forward momentum for moving, hence the robot was unable to show meaningful locomotion. Thus, the SRS testing was repeated by increasing the pressure ceiling and frequency by 0.25 bar and 0.05 Hz steps, respectively. We observed that the SRS can achieve a fairly stable sidewinding gait at 4 bar – 1.00 Hz. It was further revealed that high frequencies ($f > 1.25\ Hz$) result in incomplete sidewinding trajectories because those exceed the operational bandwidth of PMAs. On the other hand, a high-pressure ceiling ($p > 4\ bar$) overbent sections result in twisting hence the distorted trajectories. The SRS movements were video recorded using a fixed camera station. Fig. 7.7A shows the progression of the SRS during its sidewinding movement at $4\ bar - 1.00\ Hz$ pressure ceiling – frequency combination. Complete videos of the experiments are given in the multimedia repository at SRS-General-Multimedia.

C. Testing Helical Rolling Gait

For testing helical rolling gait, we adopted the same procedure applied in the sidewinding testing. Accordingly, we initiated the testing at $p = 3\ bar$ pressure and $f = 0.25\ Hz$ frequency combination,

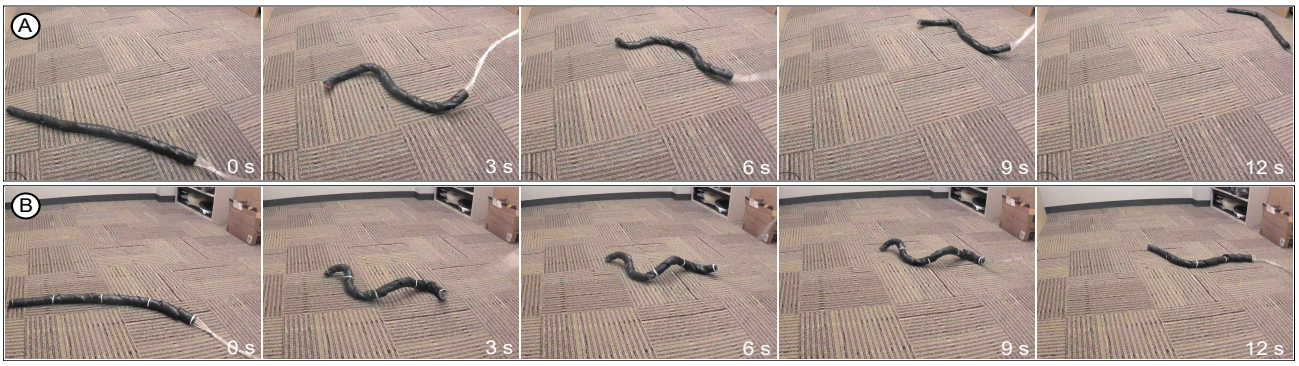

Figure 7.7: The SRS progression for (A) sidewinding gait at 4 $bar - 1.00\ Hz$, and (B) helical rolling gait at 4 $bar - 0.50\ Hz$.

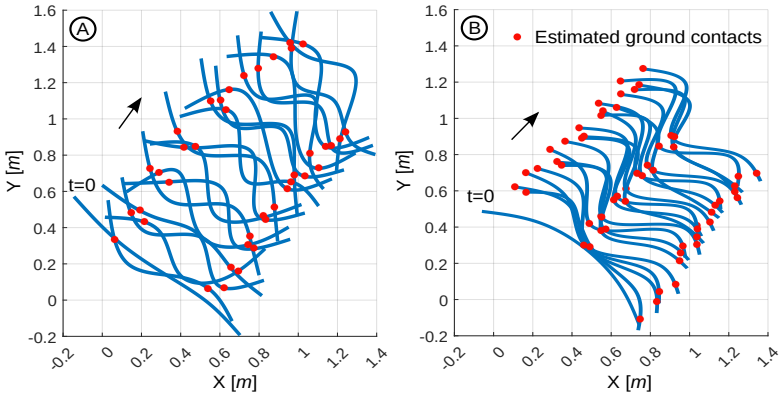

Figure 7.8: Locomotion tracking – (A) sidewinding and (B) helical rolling.

and increased values on a trial-and-error basis. It must be noted that the choice for the pressure ceiling depends on the properties of custom-made PMAs and overall SRS assembly including the length of pressure supply tubes. Similar to the sidewinding testing, the SRS recorded its best helical rolling trajectory replication at 4 *bar* pressure amplitude. However, unlike the sidewinding trajectory, we observed that the SRS was capable of achieving helical rolling throughout the applied frequency range ($0.25\ Hz < f < 1\ Hz$) at all times. When the frequency was gradually increased from 0.25 Hz to 1 Hz, the out-of-plane bending amplitude of the rolling trajectory (i.e., the displacement along the Z axis of $\{O\}$) decreased. This was expected since low-frequency actuation allows PMAs to realize the desired bending profile – i.e., at a low actuation rate, air pressure reaches to PMAs in due time through long pressure supply tubes. Fig. 7.7B shows the progression of the SRS during its helical rolling at $4\ bar - 0.5\ Hz$, pressure – frequency combination in which the SRS showed the best gait replication. Please refer to the video file that shows the helical rolling gait at low-medium-high frequencies and different amplitudes.

Table 7.3: Locomotion performance in sidewinding and helical rolling gaits.

Gait Type	Travelling velocity $[cms^{-1}]$	
	V_x	V_y
Sidewinding	13.38	14.12
Helical rolling	04.56	07.27

We employed the image processing method (perspective image projection) reported in [167] to estimate the robot displacement on the actuated plane (on the X-Y plane) using video feedback and geometric blocks on the carpeted floor as illustrated in Fig. 7.8. Correspondingly, we computed the SRS velocities shown in Table 7.3. It shows that the SRS replicated the sidewinding locomotion faster than the helical rolling. This is obvious since the SRS replicated sidewinding trajectory only at higher frequencies ($\approx$ 1 Hz). On the contrary, the SRS replicated its best helical rolling trajectory at mid-range frequencies (≈ 0.5 Hz). As expected, the SRS maintained skin-ground contacts at three points during helical rolling (Fig. 7.8B). The SRS was expected to maintain skin-ground contacts at two points during sidewinding locomotion (Fig. 7.8A). In reality, even though the SRS touches the ground at more points, the skin-ground contact has been dramatically reduced.

D. Testing Serpentine Gait

Serpentine and planar rolling gaits were validated using our initial SRS prototype, which is made of three extension mode soft modules, as presented in [167], [183]. Figures 7.9A, 7.9B, and 7.9C show how the SRS behaves during serpentine motion at 2 $bar - 0.25$ $Hz, 4$ $bar - 0.25$ Hz, and 4 $bar - 1.00$ Hz, pressure-frequency combinations. Refer to the media files at SRS-General-Multimedia to see the videos of the experiments. Therein, we did not observe any meaningful serpentine locomotion in the axial direction. Further, it is discovered from the numbers indicated in Table 7.4 under the traveling velocity of the serpentine gait. Here, the robot wobbles around without making any progress. This is a common problem with snake robots[172]. It is mainly due to insufficient friction difference in the robot skin in normal and tangential directions. In the real world, snakes have different friction coefficients in these directions. In our robot, the skin is made of a rubber surface, resulting in the same friction coefficient in all directions. Therefore the robot cannot generate a forward propagation force in the axial direction. As expected, it does not result in any forward locomotion with serpentine patterns. This is one of the main reasons why the prior work involving planer SRS [247]–[251], [278]–[280] use wheels. The wheels generate low friction in the axial direction and high friction in the normal direction.

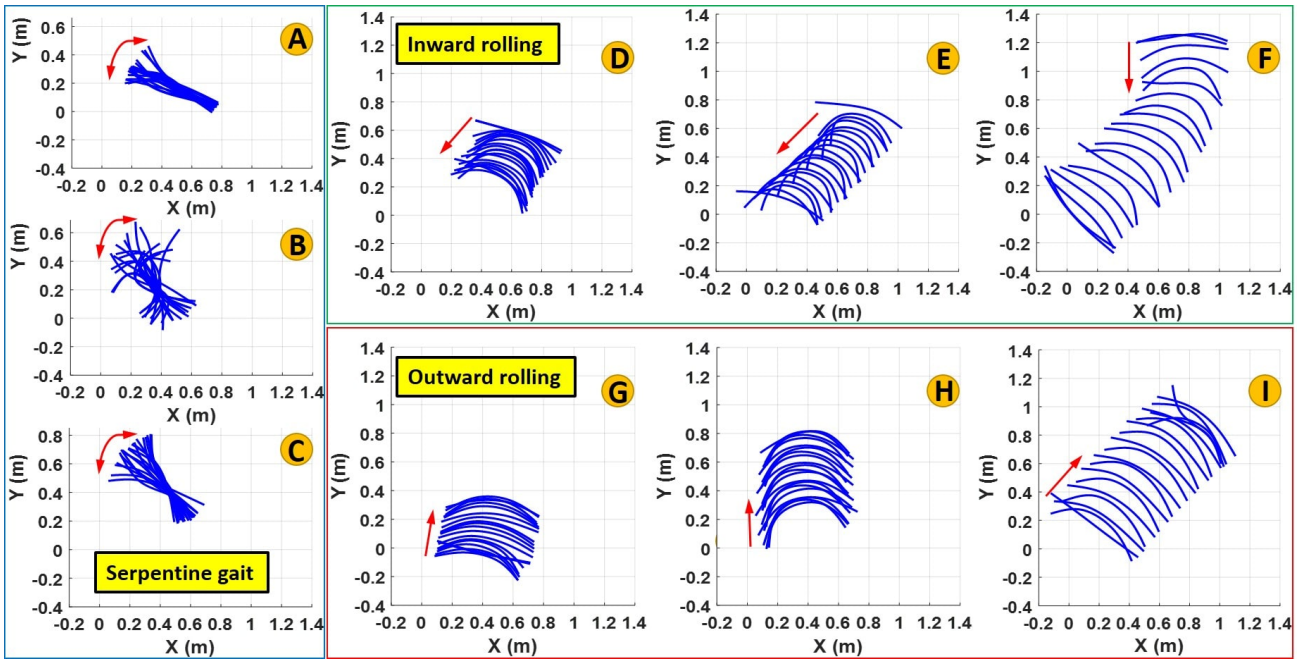

Figure 7.9: Tracking of robot movement for serpentine gait at (A) 2 $bar - 0.25\ Hz$, (B) 4 $bar - 0.25\ Hz$, and (C) 4 $bar - 1.00\ Hz$ pressure-frequency combinations; Inward rolling gait at (D) 2 $bar - 0.25\ Hz$, (E) 3 $bar - 0.50\ Hz$, and (F) 4 $bar - 1.00\ Hz$; and Outward rolling gait at (G) 2 $bar - 0.25\ Hz$, (H) 3 $bar - 0.50\ Hz$, and (I) 4 $bar - 1.00\ Hz$.

E. Testing Planar Rolling: Inward Motion

Figures 7.9D, 7.9E, and 7.9F show how the robot behaves during inward rolling at 2 $bar - 0.25\ Hz$, 3 $bar - 0.50\ Hz$, and 4 $bar - 1.00\ Hz$, pressure-frequency combinations. We observed that the robot could successfully replicate inward rolling locomotion at all pressure and frequency combinations except at a pressure as low as 1 bar. At 2 bar, when the moving frequency was as high as 1 Hz, the robot occasionally flipped back in the opposite direction. Further, the robot shows a low bending curvature at higher actuation pressure and frequency combinations. This is mainly due to air pressure not reaching the PMAs in realtime through long pneumatic lines. In both inward and outward rolling gaits, the highest traveling velocity is observed when the applied pressure-frequency combination is at its maximum value, i.e., 4 $bar - 1.00\ Hz$ (Table 7.4). Unlike serpentine gait, we demonstrate that SRS locomote successfully via rolling gaits. Here, the friction is applied in the rolling direction and supports rolling without interference, similar to moving a wide and continuous wheel. We observed similar performance in reverse rolling (Sec. 7.2.1).

Table 7.4: Traveling velocity of the SRS for serpentine and planar rolling gaits.

Pressure amplitude (bar)	**Frequency** (Hz)	**Travelling velocity** (cms^{-1})					
		Serpentine		**Inward rolling**		**Outward rolling**	
		v_x	v_y	v_x	v_y	v_x	v_y
1.0	0.25	0.00	0.00	0.00	0.00	0.00	0.00
	0.50	0.00	0.00	0.00	0.00	0.00	0.00
	0.75	0.00	0.00	0.00	0.00	0.00	0.00
	1.00	0.00	0.00	0.00	0.00	0.00	0.00
2.0	0.25	0.07	0.13	1.14	2.21	0.44	2.20
	0.50	0.12	0.16	2.11	3.21	1.29	2.02
	0.75	0.14	0.21	2.98	3.99	2.15	1.82
	1.00	0.08	0.14	3.43	4.32	3.01	1.48
3.0	0.25	0.28	0.43	3.99	4.87	3.33	2.08
	0.50	0.49	0.65	4.05	5.72	5.69	0.12
	0.75	0.59	0.71	5.16	5.89	4.21	2.19
	1.00	0.28	0.55	5.23	7.89	4.89	1.91
4.0	0.25	0.76	0.36	3.12	7.55	4.03	3.91
	0.50	0.63	0.28	4.16	9.11	5.79	2.78
	0.75	0.21	0.27	4.98	9.67	6.39	4.55
	1.00	0.09	0.18	5.61	10.11	6.56	6.75

F. Testing Planar Rolling: Outward Motion

Figures 7.9G, 7.9H, and 7.9I show how the robot behaves during inward rolling at 2 $bar - 0.25$ Hz, 3 $bar - 0.50$ Hz, and 4 $bar - 1.00$ Hz, pressure-frequency combinations. Table 7.4 shows the calculated traveling velocity of all three locomotion gaits based on image tracking results in Fig. 7.9. Here, the robot performs outward rolling towards the opposite of its curve opening. The robot cannot perform very well as much as in the other direction. The friction is applied opposite the rolling direction, and the friction force interferes with the generated rolling thrust. This is proved by relatively low velocities recorded in Table 7.4.

The tracking results in Fig. 7.9 show that the SRS replicates the three locomotion gaits very well. When the actuation pressure is low at 1 bar regardless of frequency or the locomotion gait type, the robot showed almost no movements. This is mainly due to the associated $1.0 - bar$ deadzone present in PMAs where no length change was observed and, therefore, no bending. Starting from 1.5 bar, the SRS starts to replicate all locomotion gaits well. The best replication of serpentine gait is observed at 4 $bar - 0.25$ Hz pressure-frequency combination, as presented in Table 7.4. At 2 bar pressure and $0.25 - 0.50$ Hz low-frequency combinations, the SRS shows considerably slow serpentine patterns. At low frequencies, when pressure increases from 2 to 4 bar, the serpentine pattern improves. However, at higher frequencies, the pressure amplitude distorts the gait pattern replication, as presented in Fig.

7.9C. This is due to these fast pressure changes not reaching PMAs in realtime through long pneumatic lines. Therefore the caused propagation delay interferes with replication patterns.

7.2.2 Validating Soft Robotic Snake Locomotion on Curved Surfaces

A. SRS Testing Setup

The SRS prototype is tested on two cylinders (cardboard concrete building form tubes) with outer radii, $A = 0.15$, 0.20 m and length, 1.5 m (see Fig. 7.11). The position and orientation of cylinders are adjusted based on specific testing scenarios as detailed below. To improve friction on the cylinder outer surfaces, we attached anti-slip abrasive tapes with medium grit. This ensures adequate friction between the SRS rubber skin and the locomotive surface, facilitating enhanced traction. The robot actuation entails mapping jointspace trajectories to actuation pressures. Following[45], corresponding pressure trajectories are applied to each PMA while maintaining the input pressure ceiling at 3.5 bar, utilizing the experimental setup outlined in [180].

B. Validating Gripping Force Model

We employ the experimental setup shown in Fig. 7.10A to empirically validate the gripping force derived in (5.11). The cylinder, with diameter $A = 0.20$ m, is mounted horizontally. The SRS engages in locomotion using a trajectory derived for a cylindrical surface with diameter $A = 0.20$ m while maintaining a stationary pose. A horizontal pulling force is progressively applied by a pulling string attached to the SRS skin until the SRS releases its grip. We securely affixed a calibrated 10 kg load cell in conjunction with an instrumentation amplifier to measure pulling force.

We selected the testing values for hypothetically smaller cylinder radii and the helix pitch as $A_0 = \{0.1, 0.125, 0.15, -0.175, 0.2\}$ m and $2\pi h = 0.6$ rad, respectively. These values are within the operational range of the SRS on the testing cylinder. The jointspace variable values needed to actuate the SRS at each A_0 were derived utilizing the results given in Table 5.1. The jointspace (i.e., PMA length changes) values were transformed into actuation pressure values as described in [45]. Following that, we ran the snake for a single cycle and stopped for grip force sensing to ensure interference from initial conditions for static gripping at each A_0 independently. Figure 7.10B depicts the force readings and the corresponding grip failure points for each A_0 conditions. We used a moving average filter to

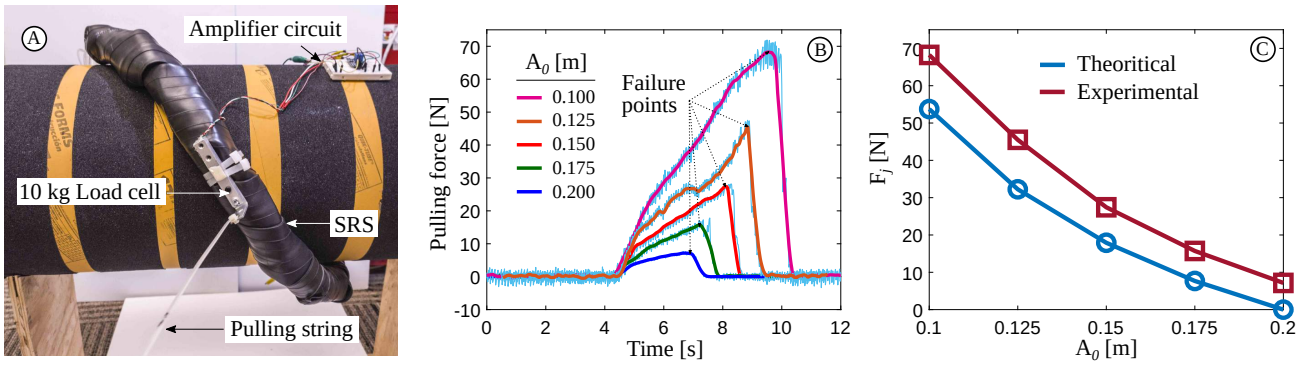

Figure 7.10: Validating gripping force model – (A) experimental setup for estimating gripping force, (B) recorded pulling force with corresponding failure points used to determine gripping force, (C) comparison between theoretical and experimental gripping forces.

mitigate noise in the force readings (represented as thick lines). We approximated the force at failure point as the gripping force. As depicted in Fig. 7.10B, an increase in A_0 from 0.1 to 0.2 decrease both the gripping force. This observation is consistent with the model in (5.11), where lower A_0 results in higher gripping forces.

In Fig. 7.10C, we compare the empirical and theoretical gripping forces. To compute the theoretical F_j from (5.11) requires K_b. As K_b depends on common-mode actuation pressure of PMAs, following the pressure-stiffness mapping reported in [253], we computed the average pressure within an actuation cycle to estimate $K_b = 0.98\ Nmrad^{-1}$. Figure 7.10C shows that theoretical and empirical force estimates follow the same trend, with the latter being higher. This discrepancy can be attributed to the unaccounted surface friction between SRS and curved surface that contribute for additional resistance to pulling.These results substantiate the observations predicted by the gripping force model derived in (5.11). Note that the goal of this test is solely to observe and confirm proportional relationships predicted by (5.11).

C. Testing SRS Locomotion on Curved Surfaces

For testing the SRS, various combinations of gait parameters were selected from the following data sets. The locomotion frequency $f \in \{0.40, 0.60, 0.80\}\ Hz$ (within the bandwidth of PMAs) and the pitch $h \in \{0.12, 0.14, 0.16\}$ based on the SRS prototype specifications. Applying the combinations of f and h values into (5.3) yielded the helix pitch values presented in Table 7.5. To compute the gripping force, A_0 was determined as $A_0 \in \{0.10, 0.15, 0.20\}\ m$ which are within the estimated gripping force region in Sec. 7.2.2. We utilized the results in Table 5.1 to compute locomotion trajectories for above

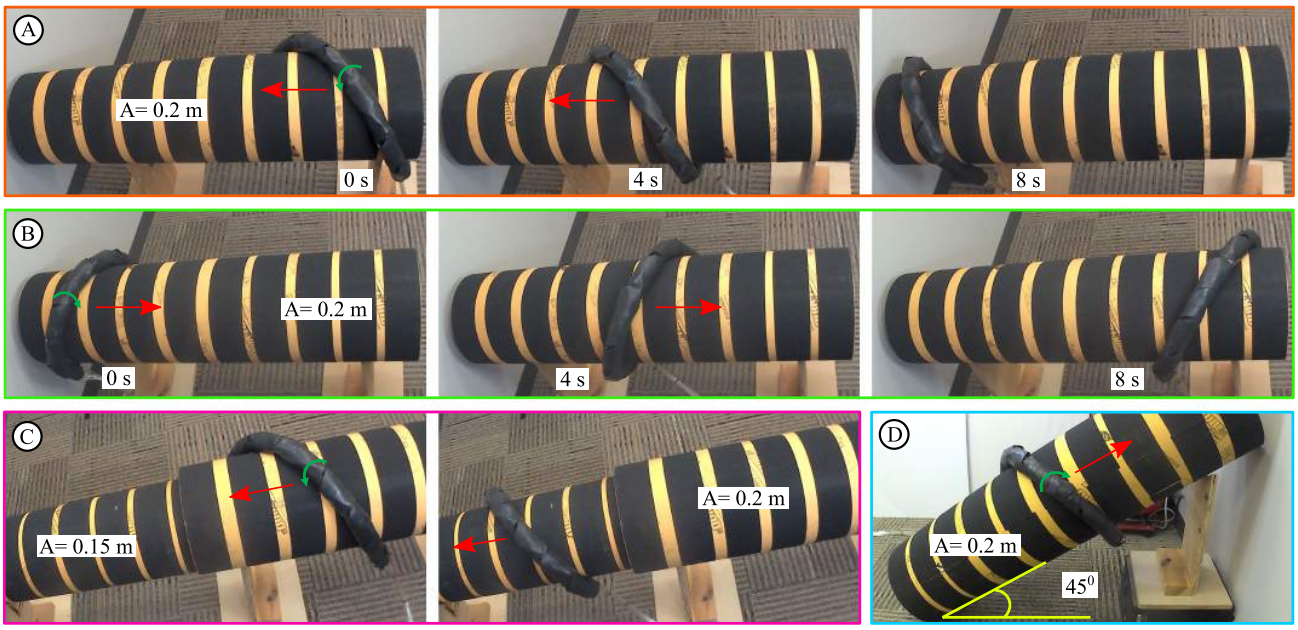

Figure 7.11: The SRS progression for (A) forward and (B) backward motion on a cylinder with a radius, $A = 0.20\ m$. (C) SRS crossing from a large cylinder ($A = 0.20\ m$), to a small cylinder ($A = 0.15\ m$). (D) SRS moving on an inclined cylinder. The actuating frequency (f) and pitch ($2\pi h$) for all motions are set at 0.60 Hz and 0.6 rad, respectively.

A_0. By applying nominal A_0, K_b, and L_{ji} values into (5.11), the gripping forces were computed as given in Table 7.5.

1) Assessing Locomotion Speed

The first test setup includes a horizontally mounted cylinder with $A = 0.20\ m$ at 0.4 m height (Fig. 7.11A). We tested both forward and backward locomotions for each trajectory parameter combinations listed in Table 7.5. The corresponding locomotion speeds were computed using time to navigate a fixed distance along the cylinder. Additionally, the SRS tests were recorded on video using two stationary cameras covering either side of the cylinder. Figures 7.11A and 7.11B show the SRS progressions in forward and backward motions, respectively, for $f = 0.8\ Hz$, helix pitch, 0.6 rad, and $F_{ji} = 0$. This parameter combination represented the optimal configuration, delivering the highest locomotion speed. Table 7.5 also presents the locomotion speeds of all experiments for forward motion, which are generally comparable to those for backward motion due to the symmetrical locomotion pattern.

We observe that SRS locomotion trajectories under increased pitch become distorted leading to SRS to slip, showcasing decreased stability. An increased pitch has spaced-out helical curve. Given

Table 7.5: SRS locomotion performance on curved surfaces: forward motion.

Theoretical gripping force F_{ji} $[N]$	**Actuation frequency -** f $[Hz]$								
	0.40			0.60			0.80		
	Pitch - $2\pi h$ $[rad]$								
	0.40	0.60	0.80	0.40	0.60	0.80	0.40	0.60	0.80
	Moving speed $[cm/s]$								
53.8 $[A_0 = 0.10\ m]$	8.9	11.0	9.2	9.3	11.4	9.6	9.2	12.6	10.2
17.9 $[A_0 = 0.15\ m]$	9.2	12.1	10.4	9.7	12.6	10.1	10.3	13.9	11.0
0 $[A_0 = 0.20\ m]$	9.9	13.6	11.2	10.8	14.5	11.8	11.2	15.5	12.2

the fixed length of the SRS, as a result, this causes reduced wrapping around the cylinder. Hence, the contact between the SRS skin and the underlying surface becomes more rectilinear which leads to a loss of gripping force. The resulting slipping or lost of traction render it difficult to maintain the taskspace locomotion trajectory then collectively contribute to decreased movement stability. The data in Table 7.5 reveals the influence of gripping force, with higher gripping force corresponding to lower recorded moving speeds consistently.

On the other hand, when the helix pitch is low, we have higher gripping force and movement stability but the distance covered along the locomotion axis per revolution is relatively low leading to reduced speed. This is due to the inevitable increase in frictional resistance when the force is large, leading to a reduction in speed. This explains how the SRS achieved its peak speed at the moderate pitch value of 0.6 rad, the highest actuation frequency of 0.80 Hz, and the lowest gripping force of 0 N. Refer to the supplementary file at SRS-Curved-Multimedia for a more comprehensive view of experimental results.

2) Testing Adaptability on Varying Curvature Surfaces

The second test aims to demonstrate the capability of SRS to dynamically adjust its locomotion in response to changes in surface curvature (Fig. 7.11C), leveraging the proposed generalization scheme in Sec. 5.1.5. Here, the SRS was actuated using the optimal parameters identified during the previous experiment. The results indicated that the SRS is capable of traversing cylinders of different curvatures.

3) Testing Locomotion on Inclined Curved Surfaces

The third and final experimental evaluation, shown in Fig. 7.11D, assesses ability of SRS to navigate an inclined cylindrical surface. Our findings indicate that the SRS can ascend a cylinder inclined at

45° with gait parameters; $f = 0.8\ Hz$, helix pitch, 0.6 rad, and $F_{ji} = 53.8\ N$. Note that, herein, the SRS showcased climbing with an increased gripping force, thereby validating the effectiveness of the gripping force mechanism for locomotion on curved surfaces.

7.2.3 Validating Soft Robotic Snake Dynamic Model

We validate the dynamic model for a 3-section SRS prototype, as presented in [167], [183]. We carry out the dynamic model validation in three steps. In the first step, we implement the dynamic model as a numerical model and apply planar and helical rolling locomotion trajectories derived in Sec. 5.1 and simulate them in a contact-enabled simulation environment. The second step involves the application of the same locomotion trajectories tested in the first step to the actual SRS hardware and experimentally evaluated for gait replications. In the last step, we qualitatively and quantitatively compare the numerical model outputs with experimental results and validate the dynamic model.

A. Dynamic Model Simulation

We implemented the SRS dynamic model derived in Sec. 4.2.2 as a numerical model and provided jointspace trajectories of planar and spatial/helical rolling (Fig. 5.4B) as inputs to test for gait simulations. The numerical model was implemented in the MATLAB 2021a programming environment, and simulations were recorded. MATLAB's ODE15 solver is selected for solving the (4.15) due to the stiff nature of the complex, high-DoF dynamic systems such as the one presented here. Herein, jointspace trajectories (i.e., length changes) are converted into pressure trajectories and then applied as force inputs ($= pressure \times sectional\ area\ of\ PMAs$) (Sec. 7.2.3). We approximated PMA elastic stiffness limiting values as $K_{i1} = 1900\ Nm^{-1}\,\forall i \in \{1, 2, 3\}$ (rounded to the nearest 100) and the damping coefficients as $D_{i1} = 90\ Nm^{-1}s\,\forall i \in \{1, 2, 3\}$ (rounded to the nearest 10) following an experimental procedure similar to the one proposed in [221]. We assumed that the robot actuating floor (Fig. 7.13) has uniform friction. We experimentally approximated the ground stiffness as $K_g = 1000\ Nm^{-1}$, damping as $B_g = 130\ Nm^{-1}s$ and, static frictional coefficients as $\mu_x = 0.6,\ \mu_y = 0.2$. The gravitational acceleration was set as 9.81 ms^{-2}.

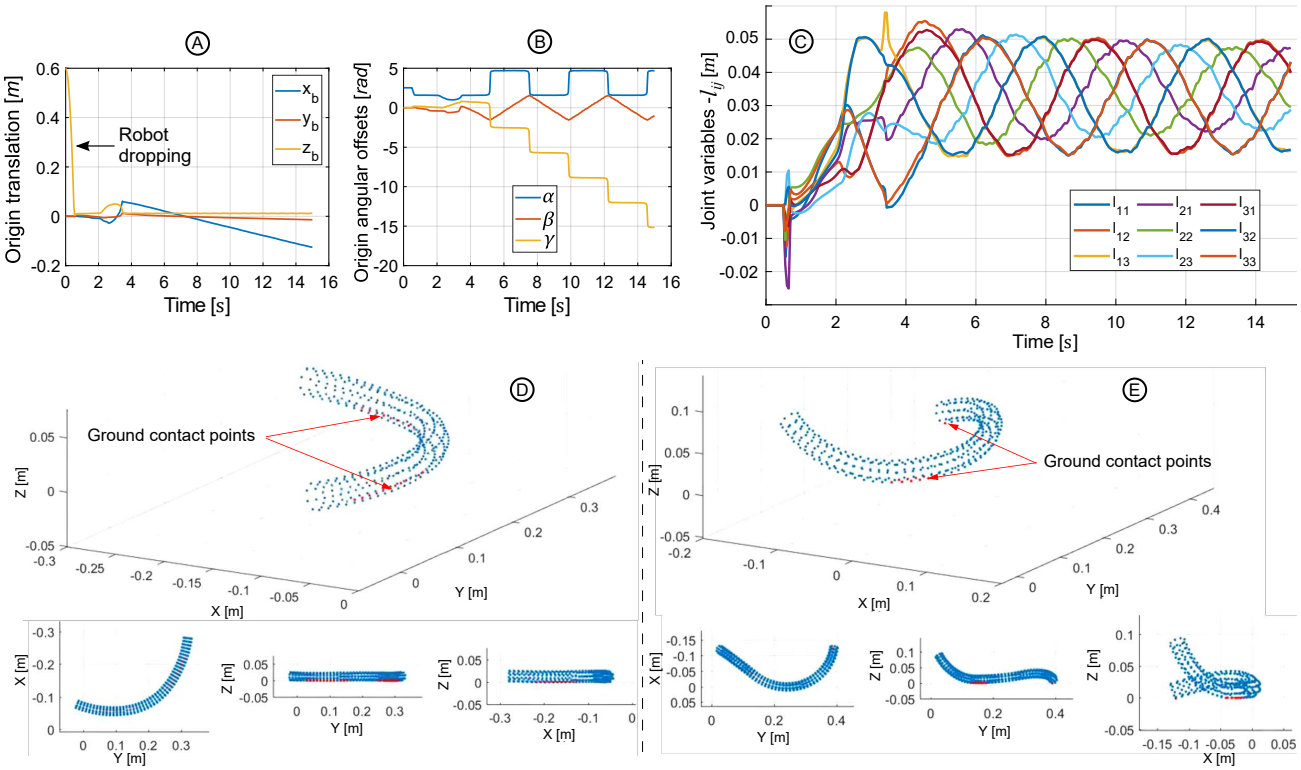

Figure 7.12: Dynamic model simulation outputs for spatial rolling – (A) position and (B) orientation changes of SRS origin, C) joint variables of complete SRS. Dynamic model implementation in an SRS numerical model and simulated locomotion gaits – (D) planar rolling and (E) spatial rolling.

B. Numerical Testing

In the simulation, first, we dropped the robot from a known height (0.6 m) and then engaged the SRS in rolling trajectories. The dropping test was carried out to evaluate the contact dynamic model as explained in the subsequent text. The displacement of the origin of $\{O_b\}$ is depicted in Figs. 7.12A and 7.12B. The figures visualize position (x, y, z) and orientation (α, β, γ) changes of the robot coordinate system origin (i.e., floating-base parameter changes) during a simulation period of 15 s with respect to spatial rolling. The joint variable output (l_{ij}) is presented in Fig. 7.12C. It closely resembles the trajectory input shown in Fig. 5.4B. Initial drop $(0-2\ s$ in Fig. 7.12A) helps us examine the validity of the contact dynamic model stated in Sec. 4.2.2 as follows. After the drop, it is clear that z stops at $z = 0$, assuring ground contact conditions. Additionally, Fig. 7.12A proves that, throughout the simulation, the robot stays above the ground. We recorded simulation data at 30 Hz sampling rate to ensure a smooth approximation of jointspace variable changes in simulation videos. Two separate movie frames of planar and spatial rolling simulations are presented in Figs. 7.12D and 7.12E.

Figure 7.13: The SRS pose progression for (A) planar and (B) spatial rolling gaits at 3 $bar - 0.50$ Hz.

Readers are referred to the video file at SRS-Dynamic-Multimedia to see the complete simulations. The simulation outputs show that the dynamic model replicates the desired gaits well, demonstrating the intended operation of ground contact dynamics.

C. Prototype Testing

The locomotion gaits are tested on the SRS prototype to compare and validate the results obtained in numerical testing. We tested the SRS prototype for planar and spatial rolling gaits on a carpeted floor with uniform friction. The jointspace trajectories are length changes of PMAs, and they must be actuated in order to obtain locomotion from the SRS prototype. The length changes of PMAs are a function of input pressures. Therefore, we adopted the approach used in [167] to establish the length-to-pressure mapping and supply pressure inputs accordingly. We applied the same jointspace trajectories used in dynamic model simulations (i.e., length parameters in Fig. 5.4B) to obtain pressure trajectories and actuate the SRS prototype. The locomotion trajectories were tested for 15 s at a maximum supply pressure of 3 bar and frequency 0.50 Hz, which are consistent with the simulation inputs. A 3 bar pressure ceiling was used based on PMAs' ability to achieve the required SRS deformation. The frequency range was chosen based on the operational bandwidth of PMAs to obtain meaningful locomotion. The SRS testing was video captured using a fixed camera station. The locomotion progression of the SRS during planar and spatial rolling gaits is shown in Figs. 7.13A and 7.13B respectively. Our video file at SRS-Dynamic-Multimedia shows the complete results of these

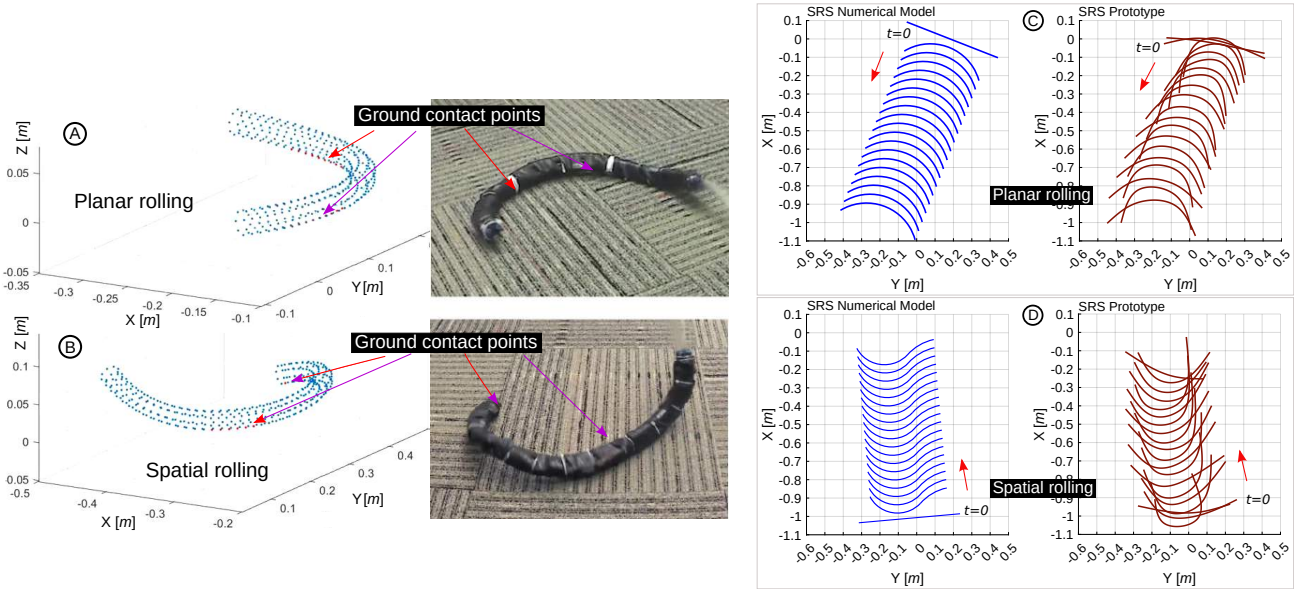

Figure 7.14: (A) and (B) – Ground contacts in dynamic model and SRS prototype. Contact points in the numerical model are shown by red color dots. (C) and (D) – Locomotion tracking of numerical model vs SRS prototype. Herein, the SRS neutral axis has been projected to $X-Y$ plane of O.

experiments. The results show that similar to the numerical testing, the SRS prototype replicated the desired locomotion trajectories well on the carpeted floor.

D. Discussion

Figures 7.14A and 7.14B show respective contact point mapping between dynamic model simulations and SRS prototype testing. Similar to the dynamic model simulations, we observed that the SRS prototype could successfully replicate two rolling gaits. Note that, here we applied the same jointspace trajectories to the numerical model and the SRS prototype. Hence, the replication of closely resembled locomotion patterns with contact points in both models qualitatively confirms the validity of the proposed dynamic model.

Table 7.6: SRS dynamic model validation: numerical and experimental model outputs.

Model	Travelling velocity (cms^{-1})			
	Planar rolling		Spatial rolling	
	V_x	V_y	V_x	V_y
SRS Numerical Model – V_N	3.51	9.39	0.67	7.77
SRS Prototype – V_P	3.31	9.01	0.61	7.12
Error [%] $= \frac{V_N - V_P}{V_N} \times 100$ %	5.70	4.05	8.96	8.37

We tracked numerical and experimental model outputs to quantify and compare the dynamic model performance. Figures 7.14C and 7.14D show the captured $X-Y$ displacement of the SRS during planar and spatial rolling gait replications. The left in each figure shows the $X-Y$ displacement of the numerical model. The experimental displacement data shown on the right were captured using the image perspective projection method reported in [167]. Based on displacement data, the calculated linear velocity components are presented in Table 7.6. Results in Table 7.6 show that the velocity components of the SRS numerical model closely follow (Error, $<$ 09 %) its counterpart, i.e., the SRS prototype, thereby quantitatively verifying the proposed dynamic model.

7.2.4 Validating Closed-loop Control of Soft Robotic Snake Locomotion

A. Testing SRS Prototype Control

In this section, we experimentally validate the proposed control scheme for the planar rolling locomotion trajectory of the SRS, as discussed in Chapter 6. We deployed the control system in the SRS prototype (Fig. 6.2) under actuation conditions identical to the soft module prototype testing, as reported in Sec. 6.2.4. Figure 7.15 shows the progression of the SRS with and without engaging the control system (i.e., open-loop and closed-loop) under both low and high actuation frequency–bending curvature combinations. Readers are referred to SRS-Control-Multimedia to see the results comprehensively. They show that when the control system is engaged, each SRS section uniformly maintains bending curvatures, whereas when it is not engaged, the moving direction is unclear, and the SRS sections show distorted bending. Additionally, we captured the SRS motion using optical markers attached to the SRS and Tracker 3.0 (Vicon, USA) motion capture system. Table 7.7 shows the computed mean velocities of the SRS with and without control. The Values in Table 7.7 indicate that when the SRS moves with closed-loop control, it attains higher locomotion speed, resulting in more efficient movement.

Table 7.7: Comparison of SRS locomotion performance with and without closed-loop control.

Actuating Frequency, f Hz]	**Bending Curvature,** ϕ $[rad]$	**Mean Velocity** $[cm/s]$	
		No Control	**With Control**
0.3	$\pi/12$	4.21	5.15
	$\pi/6$	3.61	3.98
0.6	$\pi/12$	8.21	9.91
	$\pi/6$	6.56	7.31

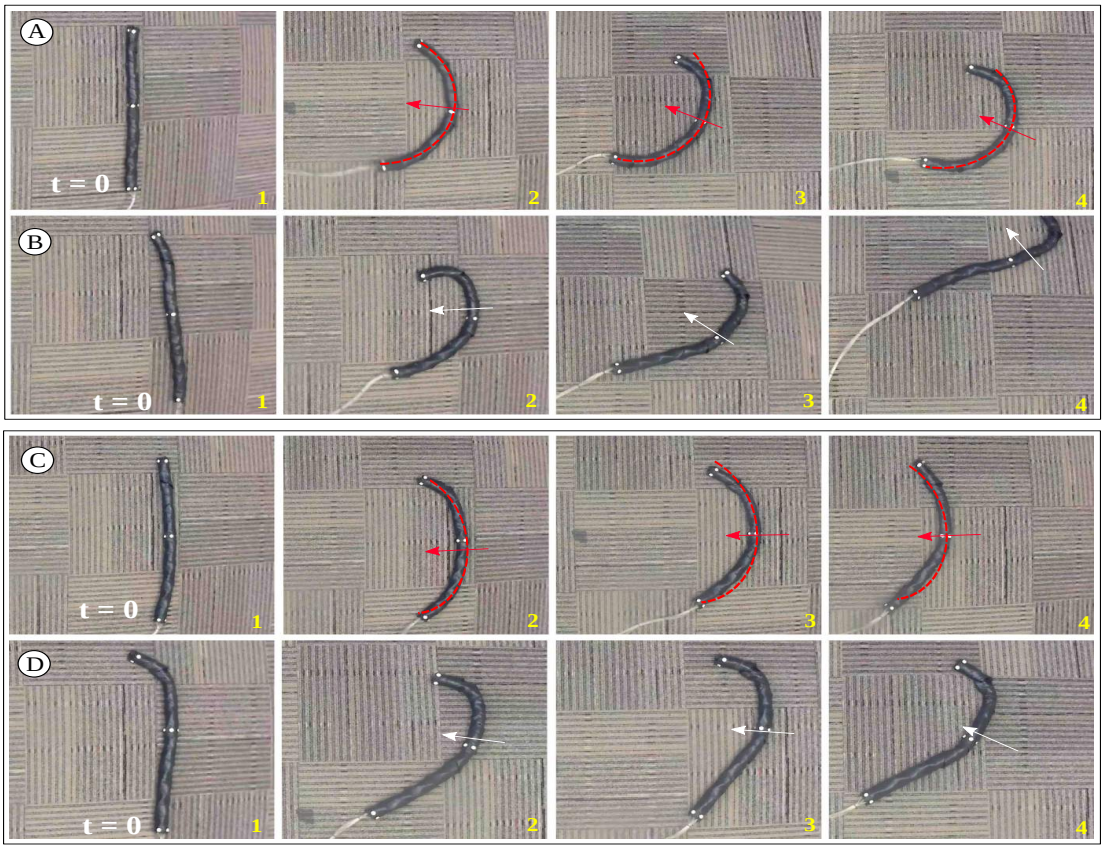

Figure 7.15: Experimental progression of SRS – (A) closed-loop and (B) open-loop actuation under the bending curvature, $\phi = \pi/6$, and actuation frequency, $f = 0.6\ Hz$. (C) Closed-loop and (D) open-loop actuation under the bending curvature, $\phi = \pi/9$ and actuation frequency, $f = 0.3\ Hz$.

B. Evaluating SRS Prototype Control

Figure 7.16 shows the controller performance under low actuation rate and bending, while Fig. 7.17 shows the controller performance under high actuation rate and bending. Table 7.8 provides the respective open-loop and closed-loop RMSEs for each SRS section. Figures 7.16 and 7.17 demonstrate that regardless of the actuation frequency or desired bending curvatures of each SRS section, the orientation angle, θ, exhibits a lower error compared to the bending angle, ϕ. This is evident from

Table 7.8: Controller performance: SRS prototype actuation.

Actuating Freq., f $[Hz]$	**Bending Curv., ϕ $[rad]$**	**SRS Section 1**				**SRS Section 2**				**SRS Section 3**			
		RMSE$_\theta$ $[deg.]$		**RMSE$_\phi$**$[deg.]$		**RMSE$_\theta$**$[deg.]$		**RMSE$_\phi$**$[deg.]$		**RMSE$_\theta$**$[deg.]$		**RMSE$_\phi$**$[deg.]$	
		NC	**WC**	**NC**	**WC**	**NC**	**WC**	**NC**	**WC**	**NC**	**WC**	**NC**	**WC**
0.3	$\pi/12$	4.85	3.55	10.2	5.61	4.21	3.87	8.96	4.67	4.85	3.42	6.69	4.21
	$\pi/6$	6.82	5.71	11.6	7.86	6.28	5.48	10.5	7.41	6.85	5.23	8.21	6.99
0.6	$\pi/12$	7.59	6.92	18.8	9.69	7.30	6.25	12.8	9.23	7.10	5.87	10.5	9.10
	$\pi/6$	9.91	7.91	19.9	10.9	9.09	7.13	13.0	9.39	8.81	7.22	11.2	9.86

NC - No Control, WC - With Control

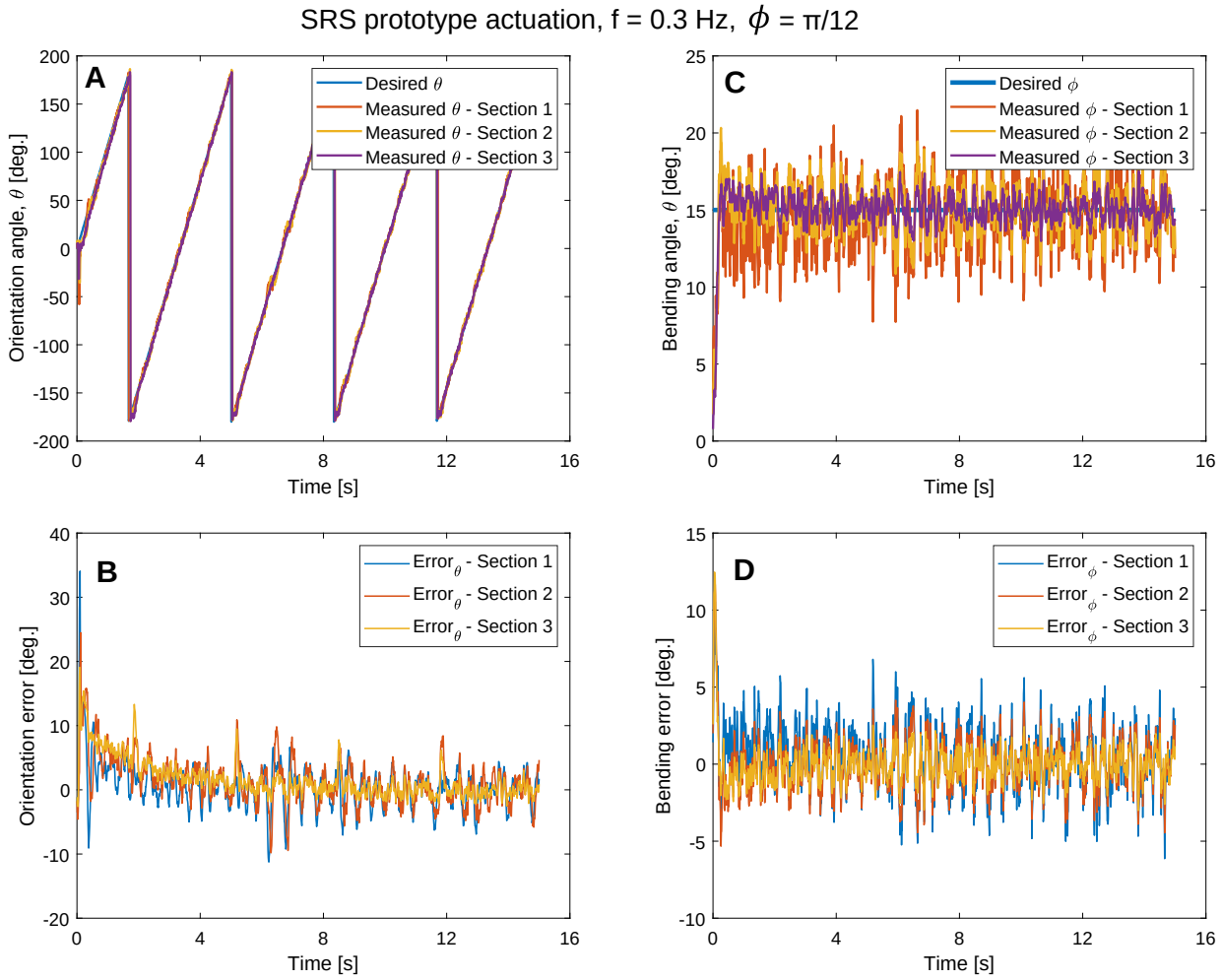

Figure 7.16: Experimental results of SRS prototype control, i.e., desired and actual trajectories of each SRS section under the bending curvature, $\phi = \pi/12$ at a lower actuation frequency, $f = 0.3\ Hz$.

the relatively low RMSE values recorded for θ in comparison to ϕ in Table 7.8. To further validate the controller performance quantitatively, we computed the error reduction percentage in jointspace, E [%], for each section, as defined by (6.1). The results are shown in Table 7.9. Additionally, we computed the error reduction percentage in taskpace using the motion tracking data, as presented in Table 7.10.

According to the data in Table 7.8, section 1 has recorded the largest error under open-loop (i.e., no control) actuation. Consequently, the data in Tables 7.9 and 7.10 show that the error reduction percentage decreases from the SRS base to the tip (i.e., from section 1 to section 3) under all actuation conditions proving the effect of control action. The reason behind the reported largest error in section 1 can be attributed to the fact that section 1 wraps all air supply tubes from other sections, thus

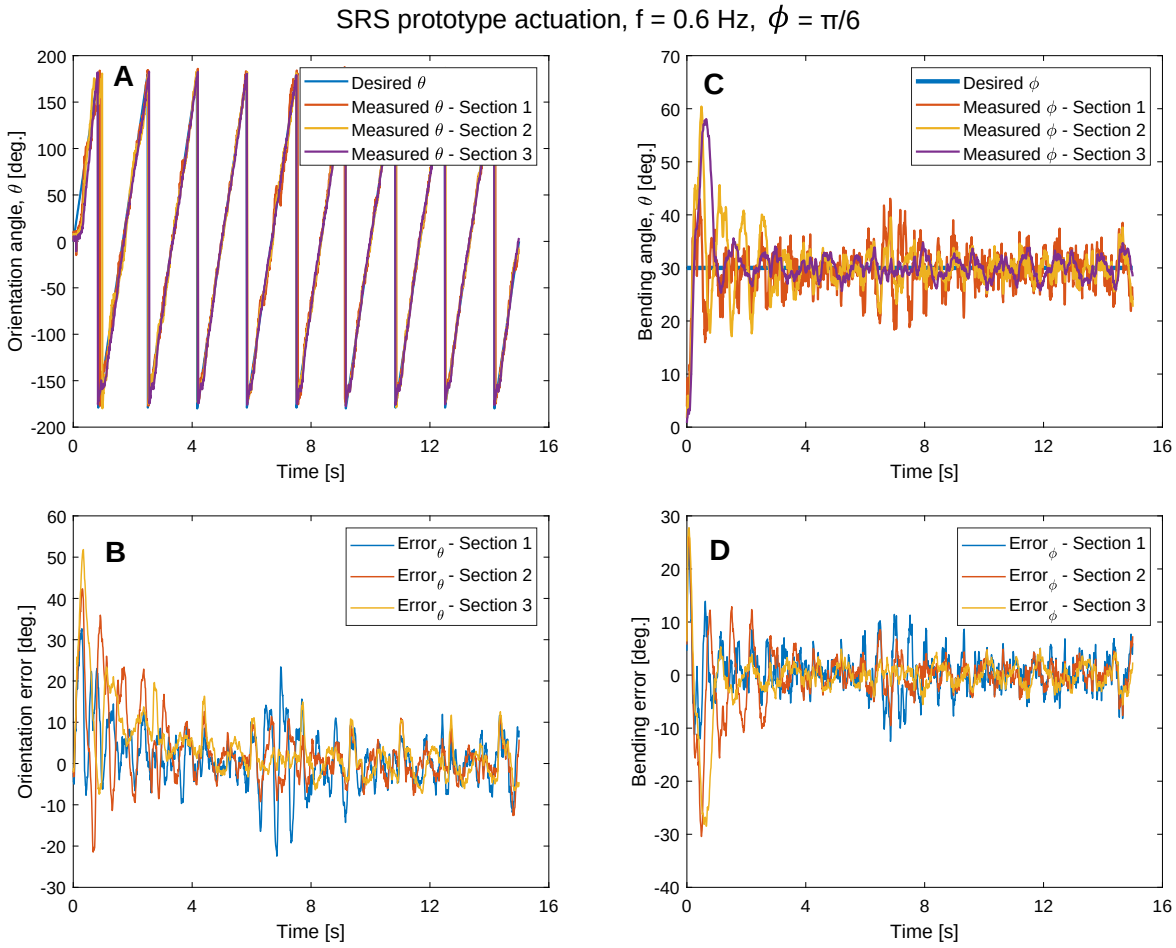

Figure 7.17: Experimental results of SRS prototype control, i.e., desired and actual trajectories of each SRS section under the bending curvature, $\phi = \pi/6$ at a higher actuation frequency, $f = 0.6\ Hz$.

presenting a larger obstacle for bending than the other sections. This hindrance is lower in section 2 than in section 1 (i.e., section 2 is less stiffer than section 1). Section 3 experiences zero hindrance as no wires wrap around that section. Despite that, the reported large error reduction percentages prove the robustness of the proposed controller. Finally, the error reductions reported in Table 7.10 confirm our initial control objective that the joinstpace SRS control can be effectively applied to maintain the desired SRS bending curvatures in taskpace.

Table 7.9: Error reduction through control actions: percentage decrease in jointspace error in the SRS prototype actuation.

Actuating Frequency, f $[Hz]$	**Bending Curvature, ϕ $[rad]$**	**SRS Section 1**		**SRS Section 2**		**SRS Section 3**	
		E_θ [%]	**E_ϕ [%]**	**E_θ [%]**	**E_ϕ [%]**	**E_θ [%]**	**E_ϕ [%]**
0.3	$\pi/12$	18.6	59.5	15.0	35.3	14.3	17.8
	$\pi/6$	19.4	60.3	15.3	36.3	15.5	18.6
0.6	$\pi/12$	24.9	64.1	17.4	37.6	17.0	19.8
	$\pi/6$	25.3	66.1	21.9	39.5	20.6	20.7

Table 7.10: Taskpace curvature error estimation in the SRS prototype control.

Actuating Frequency, f $[Hz]$	**Bending Curvature,** ϕ $[rad]$	**SRS Section 1**			**SRS Section 2**			**SRS Section 3**		
		$\mathbf{E}_{NC}$	$\mathbf{E}_{WC}$	**E** [%]	$\mathbf{E}_{NC}$	$\mathbf{E}_{WC}$	**E** [%]	$\mathbf{E}_{NC}$	$\mathbf{E}_{WC}$	**E** [%]
0.3	$\pi/12$	15.6	9.50	64.2	8.25	6.35	29.9	6.99	5.88	18.9
	$\pi/6$	17.7	10.8	63.9	9.85	7.73	27.4	6.61	5.75	15.0
0.6	$\pi/12$	14.9	9.21	61.8	8.85	7.22	22.6	7.85	6.85	14.6
	$\pi/6$	18.9	11.9	58.8	10.2	8.49	20.1	8.21	7.29	12.6

7.3 Validation of Soft-limbed Tetrahedral Robot Locomotion

7.3.1 Validating Pinniped Locomotion

A. Testing Methodology

We actuated each pinniped gait for 15 s with a 3 bar actuator pressure ceiling (based on PMAs' ability to achieve the required limb deformation). The frequency range, $\{0.75, 1.00, 1.25\}$ Hz was chosen based on the operational bandwidth of PMAs to replicate meaningful locomotion. With 03 frequency combinations, we conducted 54 experiments for 06 straight crawling gaits, 06 crawling-and-turning gaits, and 06 in-place turning gaits as detailed in subsequent sections.

B. Testing Pinniped Forward and Backward Crawling Gaits

We generated a total of 18 combinations of forward and backward crawling locomotion trajectories, with three gaits in each direction, using three different stride radii ($\rho_1 = 0.06$ m, $\rho_2 = 0.08$ m, $\rho_3 = 0.10$ m). Figures 7.18A and 7.18B show the progression of the robot during forward and backward crawling at the 0.10 $m - 1.00$ Hz stride radius-frequency combination. Complete videos of the experiments are included in our video file at Pinniped-Multimedia. To determine the robot's moving distance along the X and Y directions, we used the perspective image projection approach reported in [167]. This approach utilized video feedback and floor carpet geometry data to estimate the distances. Note that some deviation from the intended gait is expected due to the performance variations of the custom-built PMAs powering the soft limbs.

We present the performance of each crawling gait in terms of estimated robot speed, which is shown in Table 7.11. The experiments revealed that the robot achieved higher speeds at larger stride radii (0.10 m) and moderate actuation frequencies (1.00 Hz). This is because larger crawling strides generate stronger limb displacement torques on the floor than smaller strides. In addition, moderate

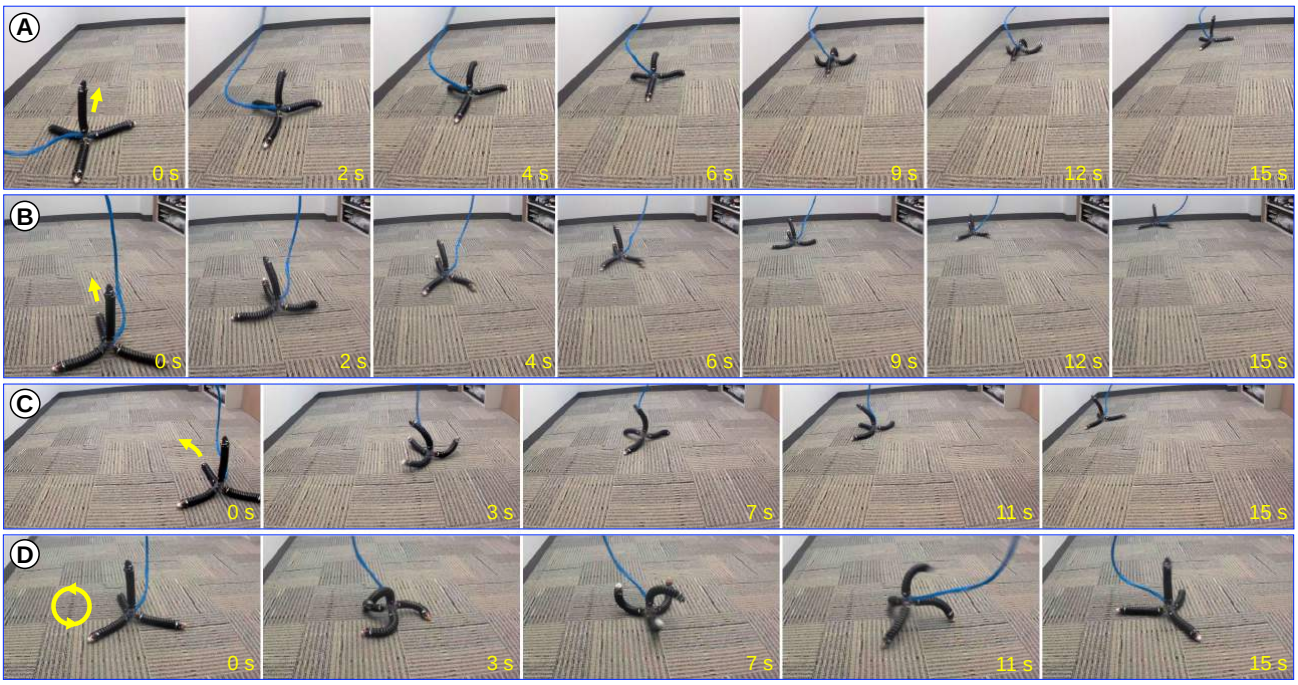

Figure 7.18: (A) Forward crawling, (B) backward crawling, (C) crawling-and-turning (leftward), (D) in-place turning (counterclockwise), at 0.10 m – 1.00 Hz.

actuation frequencies enable air pressure to reach the PMAs in a timely manner through the long pneumatic tubes, allowing for desired limb deformation without distortion of the torque amplitude. The highest recorded crawling speed was 16.9 cms^{-1} (0.65 body length/second), which is a 38-fold increase from the state-of-the-art reported in [19], 0.37cms^{-1}.

In forward crawling, the robot must perform additional limb deformations, as described in Sec. 5.2.1, in order to maintain balance and generate additional forward propulsion. As a result, forward crawling recorded lower speeds compared to backward crawling at all times. The accompanying video further demonstrates that although forward crawling resembles pinniped locomotion, it is less efficient in maintaining forward locomotion stability.

Table 7.11: Performance of pinniped straight crawling gaits.

Straight Gait	**Stride radius of crawling limbs (FR & FL)**								
	ρ_1 (0.06 m)			ρ_2 (0.08 m)			ρ_3 (0.10 m)		
	Freq. $[Hz]$			**Freq.** $[Hz]$			**Freq.** $[Hz]$		
	0.75	1.00	1.25	0.75	1.00	1.25	0.75	1.00	1.25
	Mean speed $[cm/s]$								
Fwd Crawling	5.34	7.57	7.21	7.53	10.2	9.81	9.41	11.9	10.9
Bwd Crawling	7.21	10.1	9.83	9.52	13.5	13.0	11.9	16.9	16.1

Table 7.12: Performance of pinniped crawling-and-turning gaits.

Turning Gait	**Stride radius of turning limb (B limb)**								
	ρ_1 (0.04 m)			ρ_2 (0.06 m)			ρ_3 (0.08 m)		
	Freq. $[Hz]$			**Freq.** $[Hz]$			**Freq.** $[Hz]$		
	0.75	1.00	1.25	0.75	1.00	1.25	0.75	1.00	1.25
	Angular speed per unit distance $[rad/(ms)]$								
Leftward Turn	1.13	1.72	1.70	1.59	2.24	2.06	2.22	2.89	2.41
Rightward Turn	1.15	1.68	1.65	1.62	2.31	2.11	2.35	2.92	2.49

Table 7.13: Performance of pinniped in-place turning gaits.

Turning Gait	**Stride radius of crawling limbs (FR, FL, B)**								
	ρ_1 (0.06 m)			ρ_2 (0.08 m)			ρ_3 (0.10 m)		
	Freq. $[Hz]$			**Freq.** $[Hz]$			**Freq.** $[Hz]$		
	0.75	1.00	1.25	0.75	1.00	1.25	0.75	1.00	1.25
	Angular speed $[rad/s]$								
Clockwise	2.75	3.29	3.09	3.01	3.55	3.41	3.35	3.76	3.51
Counterclockwise	2.81	3.35	3.12	3.08	3.69	3.53	3.42	3.82	3.59

C. Testing Pinniped Turning Gaits

We have successfully generated crawling-and-turning gaits for backward crawling locomotion (as described in Sec. 5.2.1). We created 03 leftward and 03 rightward turning trajectories by varying the stride radius of the B limb at values of ($\rho_1 = 0.04\ m$, $\rho_2 = 0.06\ m$, $\rho_3 = 0.08\ m$). For these gaits, the FR and FL limbs were actuated at a fixed stride radius of 0.10 m.

For in-place turning, we produced six trajectories to represent clockwise/counterclockwise turning under three stride radii ($\rho_1 = 0.06\ m$, $\rho_2 = 0.08\ m$, $\rho_3 = 0.10\ m$). During these gaits, all limbs, including the Head (H) limb, were actuated under the same stride radii as each crawling gait. Figs. 7.18C and 7.18D show the leftward crawling-and-turning gait and counterclockwise in-place turning gait, respectively. The performance of these trajectories is presented in Tables 7.12 and 7.13, respectively. We experimentally measured the turn angle and $X - Y$ floor displacement for all gaits using the method described in the straight crawling. We then calculated the angular speed per unit distance for crawling-and-turning gait and the angular speed for in-place turning gait. According to the data in Table 7.12, the effectiveness of turning increases with the stride radius of the turning limb. Similarly, the data in Table 7.13 indicates that the robot performs well in replicating in-place turning at higher stride radii, due to the increase in relative turn displacement torque with the applied trajectory stride radius.

7.3.2 Validating Tumbling Locomotion

A. Validating Tumbling on a Physics–Based Robot Simulation Model

Herein, we develop a Physics-based real-time simulation model of the tetrahedral robot to streamline the process of obtaining tumbling trajectories. It is used to test, fine-tune and validate the proposed locomotion method in advance before moving into the experimental testing.

1) Bullet Physics Engine

We utilized an open-source Physics engine, Bullet Physics to develop the tetrahedral simulation model [281]. It offers a collection of resources and software components for emulating the behavior of solid objects in motion, detecting collisions, and enabling physics-driven interactions within a virtual environment that replicates real-world physics characteristics. It includes functionalities like kinematic and dynamic simulations, friction models, gravitational effects, and contact forces. The Physics engine incorporates PyBullet, a Python interface designed for robotic simulations with a primary emphasis on rigid components and their joints [282]. However, it only accommodates simulations of inert soft materials such as fabric, rubber, foam, and other substances that display properties of softness and flexibility. The soft limb under consideration in this work is an active soft body that generates motions. In Bullet-Physics, the mass-spring-damper approach is effectively applied for modeling soft bodies. Herein, we utilized the same approach to model soft limbs for effectiveness [233].

2) Soft-limb and Tetrahedral Robot Simulation Models

A soft limb is formed by serially joining discrete rigid disks. In order to create a soft limb within the Bullet Physics environment, a URDF (Unified Robot Description Format) file that encompasses

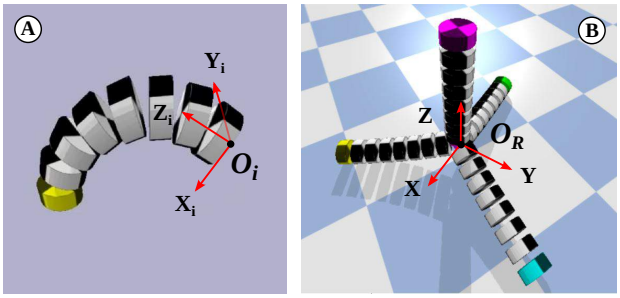

Figure 7.19: A) Soft limb PyBullet model. B) Tetrahedral PyBullet model.

both the physical and visual characteristics of the limb is created. Therein, masses of rigid disks, their positions and orientations, moments of inertia, joint types, joint positions and orientations, joint physics (stiffness, friction), etc., are defined. Additionally, the appearance of rigid disks is defined by setting a mesh target using 3D-modeling software, Blender. Using a URDF plugin installed in Blender, an XML-based URDF file is generated. It is then loaded into Python for simulations with the help of PyBullet.

By incorporating the physical details of the limb prototype given in Table 3.1, the soft limb PyBullet model is constructed using eight discrete rigid disks as shown in Fig. 7.19A. The total weight is evenly distributed among eight disks. Two revolute joints, controlled in position control mode through PyBullet, are placed along the X and Y axes between two rigid disks. The two revolute joints are sequentially actuated to manipulate the limb according to the given curve parameters (θ_i, ϕ_i in Sec. 4.1.1). The bending torque, as defined in (4.10), is uniformly distributed across all revolute joints. In position control mode, the physics engine automatically calculates and applies the corresponding directional torques to the revolute joints. The damping and bending stiffness coefficients of the soft limb are set following an experimental identification process outlined in our previous work [253]. A tetrahedral-shaped fixed joint is utilized to anchor four limbs and assemble the tetrahedral PyBullet model shown in Fig. 7.19B.

We characterized the soft limb PyButllet model to match the behavior of the soft limb prototype. Therein, first, we tested a circular trajectory on the limb prototype as demonstrated in our previous work [45]. Following this, an identical limb trajectory was applied to the PyBullet soft limb model. We obtained a comparable behavior on the PyBullet model by fine-tuning the bending stiffness and damping coefficients.

3) Testing Tumbling on Tetrahedral Simulation Model

The proposed limb actuation philosophy for tumbling in Sec. 5.2.2 are tested in the Tetrahedral PyBullet model to validate and fine-tune. The friction coefficients of the simulation floor are set as, $\mu_x = \mu_y = 0.6$, closely matching those of the actual floor (experimentally found in our previous work [183]), where the tetrahedral prototype will be tested. The gravitational acceleration is set to 9.81 ms^{-2}. Following the proposed tumbling strategy, the testing range of each limb parameter (θ_i, ϕ_i)

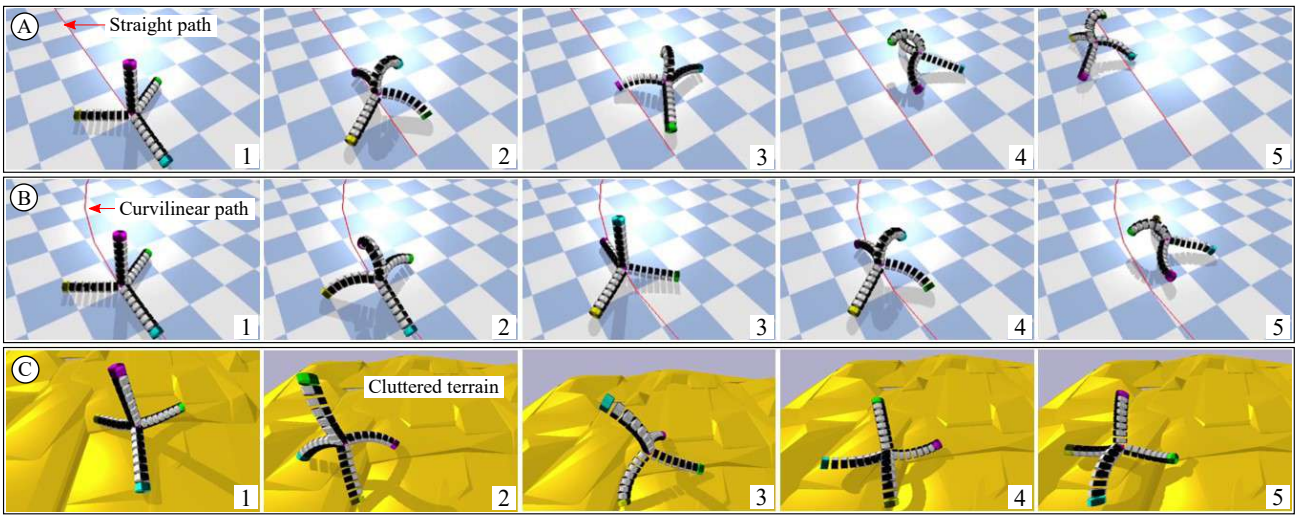

Figure 7.20: Progression of consecutive tumbling cycles on tetrahedral PyBullet model under, (A) straight, (B) curvilinear, and, (C) cluttered paths.

is computed using (4.5), based on empirically identified taskspaces, (x_i, y_i) of each limb as presented in our previous work [21]. For example, the testing range of stride radius, ρ_i given in (5.16) (i.e., radii of circular crawling trajectories of left and right limbs) is determined as $\rho_i \in [4, 10]$ cm based on the operating workspace of soft limbs. In the end, the joint position control method available in the PyBullet is applied to feed curve parameters into the PyBullet simulation model.

The testing range of limb actuating frequencies is set as, $f \in [0.25, 1.00]$ Hz based on the operating bandwidth of soft limb prototypes [45]. The tumbling ability of the PyBullet simulation model is iteratively tested for different combinations of limb parameters and frequency ceilings. Through repeated testing, we identified the optimized regions of each limb parameter approximated to the ceilings presented in Table 7.14. We observed that low limb actuation frequencies (0.25 $Hz < f < 0.50$ Hz) led to unsuccessful tumbling attempts. However, the tumbling was sustained at a critical threshold of $f = 0.55$ Hz and beyond. The reason behind this behavior is the inadequacy of low

Table 7.14: Optimized curve parameters of a tumbling cycle in PyBullet.

Limb	**Curve parameter**	**Optimized ceiling** $[rad]$	
		$0 < t \leq T/2$	$T/2 < t \leq T$
Head	θ_1	$-\pi$	0
	ϕ_1	$[0, 5\pi/12]$	0
Tail	θ_2	0	$-\pi$
	ϕ_2	$[0, \pi/3]$	$[0, \pi/4]$
Right	θ_3	$[0, -3\pi/4]$	0
	ϕ_3	$7\pi/18$	0
Left	θ_4	$[0, 3\pi/4]$	0
	ϕ_4	$7\pi/18$	0

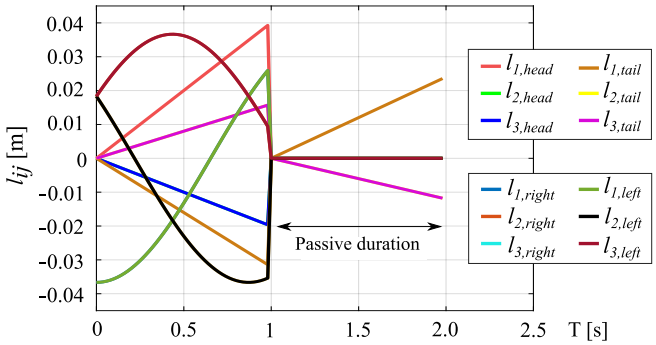

Figure 7.21: Joint variables of soft limbs during a single tumbling cycle.

limb actuation rates in generating the essential angular momentum to topple the robot. Next, we repeat the tumbling motion within the optimized trajectory margins to obtain straight and curvilinear locomotion simulations. Additionally, we simulated tumbling on a cluttered terrain characterized by obstacles, sharp edges, slopes, and varied frictional surfaces.

Here, for a given trajectory path (e.g., straight or curvilinear), the tumbling sequence is determined by the robot's operator. Since the robot rolls on the $X-Z$ plane (Fig. 5.9A), the operator can tumble the robot into a desired direction by inputting the limb parameters of the head and tail that operate on the $X-Z$ plane. We implemented the limb remapping approach proposed in Sec. 5.2.2 to transform the trajectories from the current orientation into a new orientation. Figures 7.20A, 7.20B, and 7.20C illustrate successive simulation frames depicting both straight and curvilinear tumbling, as well as tumbling on a cluttered terrain, in the PyBullet simulation model. The complete simulations are included in our supplementary file at Tumbling-Multimedia. The results show that the PyBullet simulation model successfully tracks straight, curvilinear, and cluttered paths via discrete tumbling locomotion.

B. Validating Tumbling on the Tetrahedral Robot Prototype

1) Testing Tumbling

Initially, the robot prototype is tested on a carpeted floor (Fig. 7.22 - flat terrain) that has nearly consistent friction. To actuate the prototype, the joint variables (l_{ij}) shown in Fig. 7.21 are generated by applying optimized limb parameters in Table 7.14 into (4.1). Next, l_{ij} should be mapped to actuation pressure trajectories. The joint variable – pressure mapping approach proposed in [45] is applied to obtain pressure trajectories.

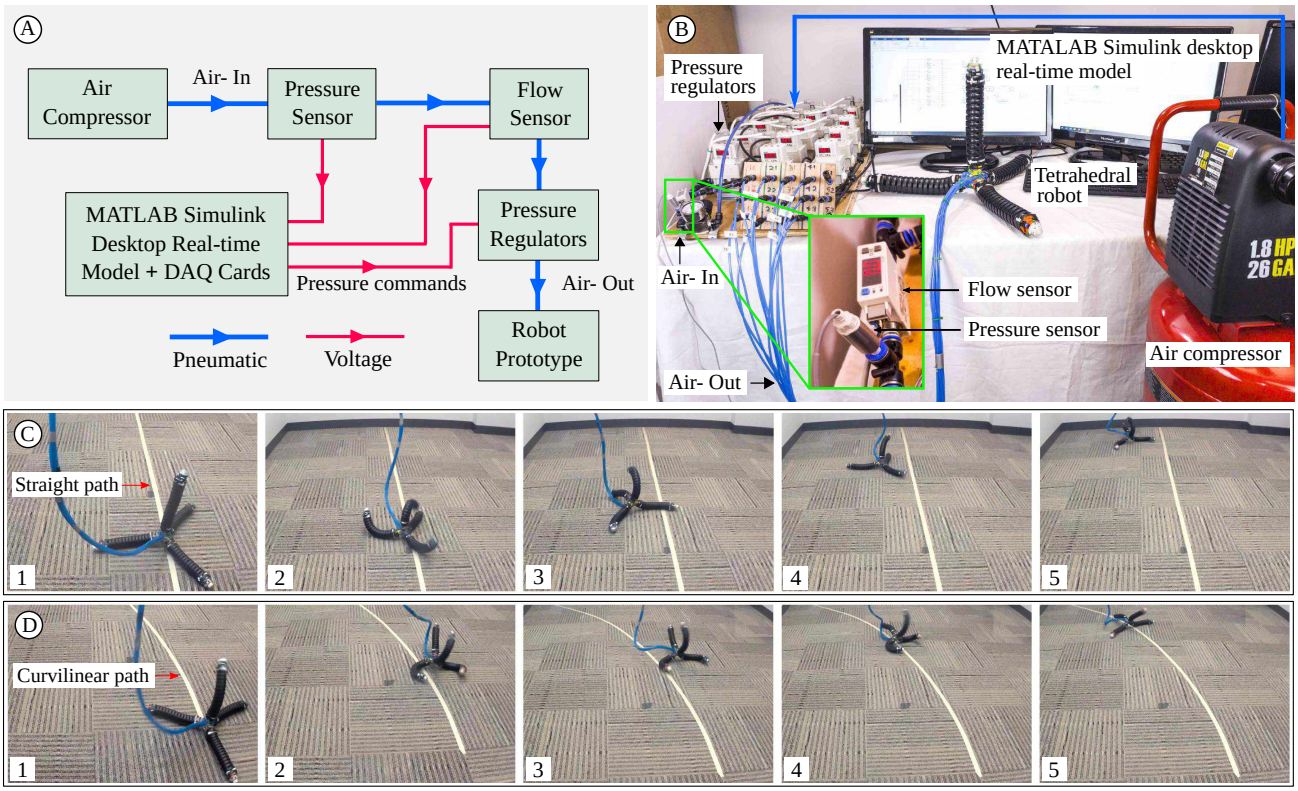

Figure 7.22: (A) Block diagram and (B) hardware components of the robot operating setup. Experimental progression of (C) straight and (D) curvilinear tumbling on flat terrain at 3 $bar - 0.75$ Hz, actuation pressure - frequency combination.

Figures 7.22A and 7.22B show the block diagram and hardware components of the robot actuation setup, respectively. The air pressure from the compressor is fed to 12 pressure regulators (ITV3050-31F3N3, SMC USA) via a pressure sensor and a flow sensor, corresponding to 12 PMAs of 04 limbs. The pressure regulators release air pressure based on voltage signals issued by an analog output data acquisition (DAQ) card (PCI-6703, NI USA). The DAQ card is connected to a MATLAB Simulink desktop real-time model where corresponding actuation pressure trajectories are set. Therein, the pressure values are mapped to the voltage signals applied to pressure regulators (i.e., pressure commands).

We tested the robot tumbling by applying the optimized curve parameters in Table 7.14 within the optimized actuation frequency region, $f \in [0.55, 1.00]$ Hz. We initiated the testing at the pressure ceiling, $p = 3$ bar, and the actuation frequency, $f = 0.55$ Hz. We found that a high-pressure ceiling ($p > 3.0$ bar) generated unexpected jerks due to over-stiffed limbs. Consequently, the pressure ceiling for subsequent testing was set at 3 bar. We further noted that low frequencies ($f < 0.55$ Hz) onto

PMAs cannot generate adequate forward momentum to tumble the robot, which is consistent with the testing results of the PyBullet model. Hence, the robot testing was repeated by increasing the frequency ceiling by 0.05 Hz steps. The robot started tumbling effectively at about 0.65 Hz and sustained it till about 0.90 Hz. We observed that high frequencies ($f > 0.90$ Hz) led to unsuccessful tumbling attempts. This is owing to the fact that high limb actuation rates result in incomplete limb deformation because those exceed the operational bandwidth of PMAs.

Figures 7.22C and 7.22D depict the trajectory tracking of straight and curvilinear tumbling on flat terrain, respectively, at a frequency of 0.75 Hz — the optimal frequency that produces the best tumbling motion. Figures 7.23A, 7.23B, 7.23C, and 7.23D demonstrate various testing scenarios for tumbling, including orientation correction, negotiating inclined surfaces (slope angle = 30°), cluttered terrains (fabric surface formed with underneath obstacles), and natural-like irregular terrains (sand, pebbles, and grass), respectively. Refer to Tumbling-Multimedia to see the complete tumbling videos.

2) Discussion

Discrepancies can be observed between the simulated behavior of the PyBullet model and the actual performance of the robot prototype in experiments. The reasons for that can be identified as follows. The robot prototype is bound by its operational limitations. For example, the inconsistency in pressure reaching PMAs can be attributed to the use of long pressure supply tubes, which act as a low-pass filter, limiting their ability to transmit rapid pressure changes in real-time. Additionally, the PyBullet soft limb model did not account for limb characteristics such as deadzone, hysteresis of PMAs, etc. that are present in the soft limb prototype.

C. Estimating Energy Consumption in Tumbling

1) Methodology

We investigated the energy usage of tumbling locomotion and compared it against the robot's conventional locomotion gait, i.e., crawling [21] (see Tumbling-Multimedia). If the robot is actuated by an input pneumatic pressure, P_{in} $[Nm^{-2}]$ with a volumetric air flow rate, $\dot{V}$ $[m^3s^{-1}]$, the power output of the pneumatic system can be computed as, $P_{in}\dot{V}$. Accordingly, the energy spent by the pneumatic system (or energy input to the robot), E is given by (7.1) where t denotes the robot actuation duration.

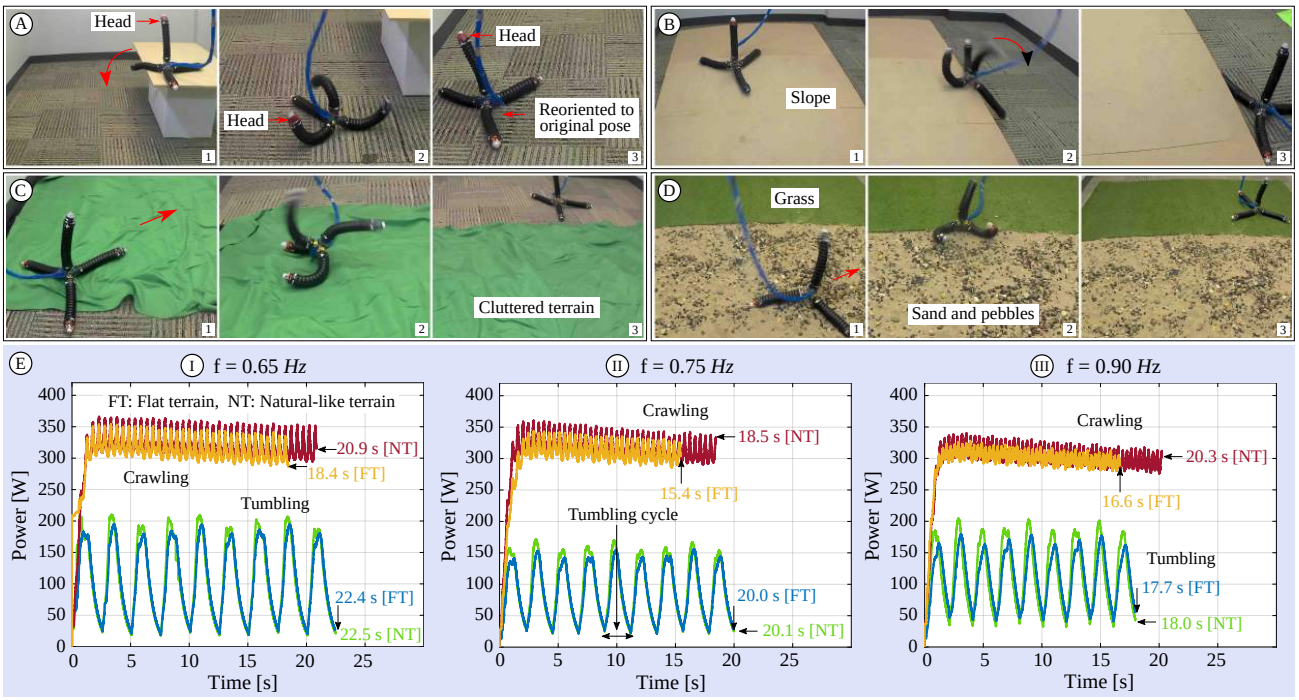

Figure 7.23: Robot testing for (A) orientation correction, (B) inclined surface, (C) cluttered terrain, & (D) natural-like irregular terrain. (E) Assessing power output of the pneumatic system involves tumbling & crawling at actuation frequencies of (I) 0.65 Hz, (II) 0.75 Hz, & (III) 0.90 Hz on flat & natural-like terrains.

$$E = \int_0^t P_{in}\dot{V}dt. \tag{7.1}$$

To measure the input air pressure and flow rate, a pressure sensor (PSE530-R07-L, SMC USA) and a flow sensor (PFM711-C6-E-M, SMC USA) are serially coupled at the air inlet of pressure regulators (Refer Figs. 7.22A and 7.22B). An analog input DAQ card (PCI-6255, NI USA) is interfaced with the MATLAB Simulink desktop real-time model to acquire sensor data that are generated as voltage signals.

We tumbled the robot a fixed straight distance (2.5 m) at low, mid, and high frequencies ($f = \{0.65, 0.75, 0.90\}$ Hz), independently on flat terrain (Fig. 7.22C) and recorded pressure input, flow rate, and traversal time during each locomotion cycle. Next, we repeated the same step for crawling under identical conditions. Subsequently, both tumbling and crawling actuations were repeated on natural-like irregular terrain (Fig. 7.23D). Figure 7.23E shows the computed power outputs of the pneumatic system (or power input to the robot) using (7.1). The crawling exhibits a slight downward slope in power output, which is a result of the drop in the flow rate from the air tank due to the loss of tank pressure because crawling draws air at a faster rate. Table 7.15 summarizes the respective energy

Table 7.15: Energy estimation of tumbling locomotion.

Locomotion gait	**Energy consumption** $[KJ]$					
	Flat terrain			**Natural-like terrain**		
	Frequency $[Hz]$			**Frequency** $[Hz]$		
	0.65	**0.75**	**0.90**	**0.65**	**0.75**	**0.90**
Crawling	5.71	4.60	4.87	6.52	5.71	5.58
Tumbling	2.33	1.70	2.01	2.40	1.82	2.10
Energy saving, E_{saving} [%]	59.2	63.0	58.7	63.2	68.1	62.4

outputs. The decrease in flow rate has no impact on the energy estimation because the flow rate is accurately measured.

2) Analysing Energy Consumption in Tumbling

According to Fig. 7.23E, the robot takes longer traversing the desired fixed distance via tumbling than crawling under each actuation frequency at all times. This is due to tumbling being a discrete locomotion gait that requires time to recover or stabilize between tumbles, whereas crawling can continue cyclically. The average moving speed of crawling and tumbling under 3 actuation frequencies on all terrains can be found as 13.8 cms^{-1} and 12.5 cms^{-1}, respectively. Here, the relative speed decrease in tumbling is 10.4%.

Based on the data in Table 7.15 tumbling uses lower energy than crawling at all times. Accordingly, we computed the energy efficiency of tumbling relative to crawling, given in the last row of Table 7.15, as

$$E_{saving}[\%] = \frac{E_{crawling} - E_{tumbling}}{E_{crawling}} \times 100. \tag{7.2}$$

According to Table 7.15, tumbling saves approximately 60% of energy on flat terrain and 65% on natural-like irregular terrain compared to crawling, irrespective of actuation frequencies and similar locomotion speeds. Tumbling significantly reduces floor friction by reducing contact surface area. In contrast, crawling, where continuous contact with the floor consumes significant energy due to distributed limb contacts. Additionally, not all limbs are continuously actuated during the entire tumbling cycle, as seen in Table 7.14 and Fig. 7.21. Limbs are active during the first half, contributing to the tumbling action, and passive during the second half. Consequently, the pneumatic system does not consume power throughout the entire tumbling cycle, unlike continuous crawling.

The lowest energy saving occurs at the highest limb actuation frequency, $f = 0.90\ Hz$, due to the increased work needed to overcome floor friction. At high frequencies, limbs cannot reach their full

deformation potential, given fast pressure changes. Conversely, moderate actuation frequencies enable full limb operation within their workspace. Therefore, Table 7.15 highlights the highest energy saving at the moderate frequency, $f = 0.75\ Hz$, identified as the optimal actuation frequency for tumbling. It is important to note that the energy saving at the lowest limb actuation frequency, $f = 0.65\ Hz$, falls between the highest and moderate actuation frequencies. At reduced limb actuation frequencies, the robot takes an extended time to reach its destination, as seen in Fig. 7.23E. Thus, the energy input to the robot increases due to the prolonged operating time of the pneumatic power system.

According to Table 7.15, the energy saving in tumbling locomotion on natural-like irregular terrains is higher than on flat terrains. Figure 7.23E illustrates that on both flat and natural-like irregular terrains, tumbling covers the same distance within comparable time intervals. This advantage of discrete locomotion modes like tumbling arises from dealing less with floor friction. Conversely, during crawling, the robot must negotiate surface variations in natural-like irregular terrain through distributed contact forces, leading to higher frictional resistance, which causes increased energy consumption compared to traversing flat terrain.

7.4 Validation of Soft-limbed Quadruped Locomotion

7.4.1 Validating Quadruped Crawling

A. Experimental Methodology

The experimental setup employed to validate the locomotion gaits is similar to the one used for SRS actuating in Fig. 7.6. We used 15 pressure regulators corresponding to 15 PMAs (Each module has 3 PMAs). The quadruped was tested on a carpeted floor with approximately uniform friction. The gait trajectories were actuated for 15 s with a pressure amplitude of 3 bar and frequencies of $f \in \{0.5, 0.75, 1.0\}\ Hz$. The pressure amplitude and the frequency range were chosen based on PMAs' ability to provide a desired limb deformation within their operational bandwidth. We chose three stride radii ($\rho_a = 0.06\ m$, $\rho_b = 0.08\ m$, $\rho_c = 0.1\ m$) and nine phase shifts ($\omega_k \in \{0, \frac{\pi}{6}, \frac{\pi}{4}, \frac{\pi}{3}, \frac{\pi}{2}, \frac{2\pi}{3}, \frac{3\pi}{4}, \frac{5\pi}{6}, \pi\}\ rad$) within the workspace of the soft limb to obtain locomotion trajectories. We executed the robot testing according to the following pipeline.

i. Choose a locomotion gait <– {straight locomotion, in-place turning, locomotion with differential strides, locmotion with body bending, general locomotion}.

ii. Choose a phase shift, ω_k <– $\{0, \frac{\pi}{6}, \frac{\pi}{4}, \frac{\pi}{3}, \frac{\pi}{2}, \frac{2\pi}{3}, \frac{3\pi}{4}, \frac{5\pi}{6}, \pi\}$ rad.

iii. Choose a limb stride radius, ρ <– $\{\rho_a = 0.06,\ \rho_b = 0.08,\ \rho_c = 0.1\}$ m.

iv. Apply the inverse kinematic model in Section 4.1.2 and obtain jointspace variables (i.e., length changes) of each limb for respective locomotion gait – phase shift – limb radius combination.

v. Apply length – pressure mapping from Fig. 7.26 (detailed in Section 7.4.1) and obtain actuation pressure trajectories.

vi. Choose an actuation frequency, f <– $\{0.5, 0.75, 1.0\}$ Hz.

vii. Set actuation pressure – frequency combination in the MATLAB Simulink Desktop Real-Time model.

viii. Apply the corresponding voltage signal required to release the air pressure in the pressure regulators via the data acquisition card.

B. Mapping Length Changes to Actuating Pressures

In the presented robotic system, the length of the modules can change due to the extension-mode pneumatic artificial muscles (PMAs) located inside them. However, due to the inextensible backbone, these length changes can sometimes be negative. The experimental setup, on the other hand, can only provide positive pressure commands. To address this issue, the authors proposed a method to convert negative length values to positive ones without affecting the module bending. This is achieved by utilizing the decoupled stiffness and shape variation of the modules.

To convert negative length values to positive ones, the authors added a length offset and set the minimum length change to zero. For each limb, the trajectory of each PMA was considered separately, and the minimum value of the length change for each PMA was determined. Then, the positive length changes were obtained by subtracting the minimum value from each length change. These positive length changes were subsequently normalized around the maximum positive value to ensure

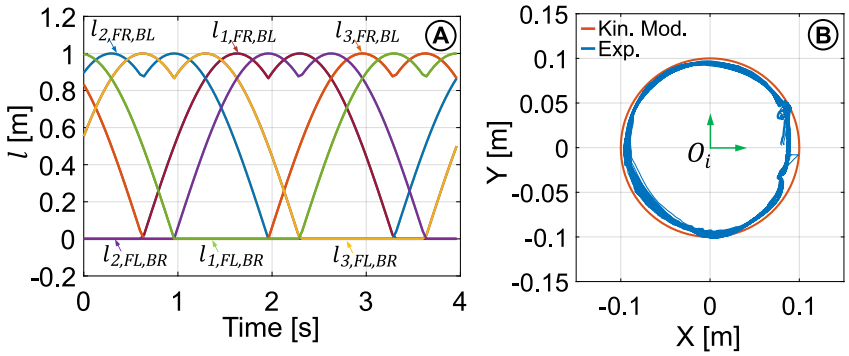

Figure 7.24: (A) At straight locomotion ($\omega = 90°$, $\rho = 0.1\ m$), positively converted and normalized length changes of four limbs. (B) Kinematic model and experimental model outputs of a soft module.

the uniformity of length changes in all limbs. It is important to note that no length changes occur in the body (Limb B) since it is kept straight under straight motion. The straightness is maintained by applying equal pressure amplitudes for all three PMAs. The converted length changes for four limbs at $\omega_k = \frac{\pi}{2}\ rad$ and $\rho_j = 0.1\ m$ under straight motion are shown in Fig. 7.24A.

The length changes of PMAs depend on the input pressures; however, the length-pressure relationship is highly nonlinear and hysteretic [242]. It is worth noting that the crawling motion of the robot can be relatively fast compared to the typical bandwidth of the PMAs used [283]. To establish the length-pressure relationship of the PMAs, we conducted experiments using the setup shown in Fig. 7.25. First, we applied a triangular pressure trajectory (within the actuation frequency of the robot) to a PMA, denoted by l_{ji}, and measured the bending angle ϕ_j while maintaining θ_j at zero. The bending angle ϕ_j was computed (Fig. 7.26A) using a motion tracking system (G4, Polhemus USA) with three 6-DoF trackers and applying the inverse kinematics model given by (4.5). Next, the values of θ_j and ϕ_j were converted to the length change l_{ji} of the actuated PMA using (4.1). We repeated these steps for actuation frequencies of $f \in \{0.5, 0.75, 1.0\}\ Hz$, and the obtained length-pressure variation is shown in Fig. 7.26B. We then computed the mean line of each curve to establish the linear relationship given by $p_{ji} = K \cdot l_{ji} + C$ and generated the pressure trajectories corresponding to the locomotion trajectories. Here, $p_{ji}\ [bar]$ is the pressure, $K\ (94, 93, 72)$ is the proportional gain, $l_{ji}\ [m]$ is the length change of the PMA, and $C\ (0.5, 0.6, 0.9)$ is the intercept or the deadzone of the PMA. From the plots, we can see that their linear relationship at different frequencies is very similar. Hence, we used the average line to map length changes into pressure trajectories required for limb actuation in subsequent experiments under different phase shift – stride radius – frequency combinations.

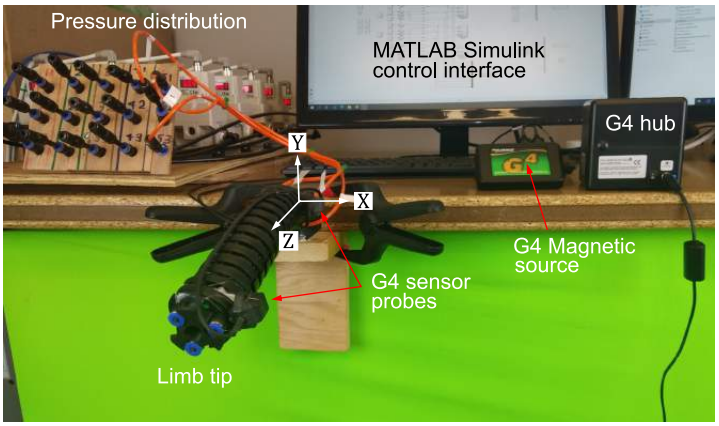

Figure 7.25: Experimental setup for (1) mapping the relationship between limb length and pressure, and (2) validating the kinematic model of a soft limb.

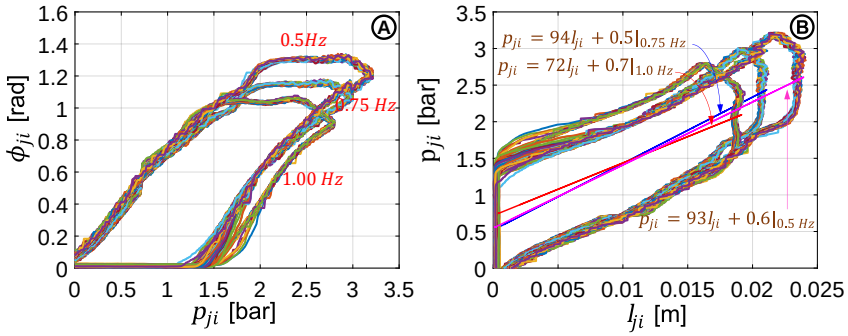

Figure 7.26: Hysteretic behavior of PMAs: (A) Bending of PMAs under actuation pressure, (B) Mapping of length change (l) with respect to actuation pressure (P).

C. Validating Soft Limb Kinematics for Crawling

The circular trajectory of a soft module was recorded experimentally using the setup depicted in Fig. 7.25 and compared with the output of the kinematic model. The joint variables required to generate a desired locomotion trajectory of $\rho = 0.1\ m$ were first obtained and then converted to pressure trajectories to actuate the limb prototype several cycles within the robot actuation frequencies, $f \in \{0.5, 0.75, 1.0\}\ Hz$. The limb tip position of each actuation relative to the limb's base was recorded using the Polhemus G4 motion tracking system, and Fig. 7.24B shows the recorded mean tip positions (X, Y) and the kinematic model output. Although the experimental model slightly diverged from the kinematic model, both models showed relatively close trajectories. The soft limb's trajectory error was computed as the root mean square error, RMSE = 0.04. This low trajectory error confirms the viability of the kinematic model. It should be noted that the observed divergence in the experimental model is due to unmodeled characteristics such as deadzone, hysteresis, gravity, etc., in PMAs.

Table 7.16: Experimentally recorded straight crawling gaits.

Phase gait $[\omega_k]$	**Estimation**	**Stride radius**								
		ρ_a [0.06 m]			ρ_b [0.08 m]			ρ_c [0.10 m]		
		Freq. $[Hz]$			**Freq.** $[Hz]$			**Freq.** $[Hz]$		
		0.50	0.75	1.00	0.50	0.75	1.00	0.50	0.75	1.00
		Mean speed$-V$ $[cm/s]$								
0	Exp. V.	5.68	8.10	7.88	7.24	10.3	9.12	9.28	13.1	11.0
	T_{err} [RMSE]	0.41	0.49	0.29	0.36	0.31	0.28	0.25	0.24	0.32
$\pi/6$	Exp. V.	5.52	7.83	7.56	6.95	9.99	8.82	9.02	12.9	10.5
	T_{err} [RMSE]	0.49	0.53	0.35	0.38	0.36	0.33	0.32	0.31	0.36
$\pi/4$	Exp. V.	5.45	7.71	7.26	6.81	9.87	8.62	9.02	12.7	10.2
	T_{err} [RMSE]	0.54	0.62	0.66	0.41	0.33	0.41	0.31	0.40	0.57
$\pi/3$	Exp. V.	5.39	7.65	7.11	6.62	9.68	8.48	8.95	12.5	9.98
	T_{err} [RMSE]	0.50	0.42	0.63	0.48	0.34	0.35	0.44	0.39	0.55
$\pi/2$	Exp. V.	5.32	7.55	6.98	6.45	9.41	8.21	8.81	12.2	9.80
	T_{err} [RMSE]	0.52	0.44	0.51	0.44	0.41	0.39	0.33	0.48	0.51
$2\pi/3$	Exp. V.	4.88	6.88	6.35	5.91	8.62	7.56	8.12	11.1	8.99
	T_{err} [RMSE]	0.30	0.42	0.39	0.32	0.38	0.29	0.36	0.29	0.34
$3\pi/4$	Exp. V.	4.65	6.62	5.99	5.65	8.22	7.22	7.72	10.4	8.59
	T_{err} [RMSE]	0.46	0.48	0.69	0.48	0.57	0.46	0.58	0.54	0.50
$5\pi/6$	Exp. V.	4.41	6.32	5.92	5.56	7.99	7.10	7.50	9.90	8.32
	T_{err} [RMSE]	0.61	0.56	0.43	0.31	0.55	0.30	0.46	0.52	0.51
π	Exp. V.	4.22	6.08	5.83	5.44	7.86	6.91	7.10	8.80	8.23
	T_{err} [RMSE]	0.56	0.49	0.51	0.43	0.51	0.38	0.42	0.35	0.44

D. Validating Straight Crawling

In accordance with Section 5.3.1, 27 combinations of straight locomotion trajectories were generated for three stride radii ($\rho_a = 0.06\ m$, $\rho_b = 0.08\ m$, $\rho_c = 0.1\ m$) and nine phase shifts ($\omega_k \in \{0, \frac{\pi}{6}, \frac{\pi}{4}, \frac{\pi}{3}, \frac{\pi}{2}, \frac{2\pi}{3}, \frac{3\pi}{4}, \frac{5\pi}{6}, \pi\}\ rad$) and validated under three actuation frequencies ($f \in \{0.5, 0.75, 1.0\}\ Hz$). Figure 7.27-Left illustrates the robot's progression during straight locomotion for five phases at $0.1\ m{-}0.5\ Hz$ stride radius-frequency combination. The complete experimental videos are available in Quadruped-Crawling-Multimedia. Table 7.16 indicates the experimentally recorded speed and the trajectory tracking error, T_{err} for each straight gait. To estimate the robot displacement along the X, Y directions, we utilized video feedback and geometric blocks on the carpeted floor with the perspective image projection method reported in [167], [180]. By utilizing $X - Y$ displacement data, we computed the trajectory tracking error as the root mean square error (RMSE) between the desired and the estimated locomotion trajectories. We observed that at higher ω_k, the robot exhibited more stability in maintaining its straight-line motion. However, for the lowest gait ($\omega_k = 0$), which closely resembled a jumping-like behavior, we observed a slight divergence in its heading (i.e., the first gait in Fig. 7.27-Left). This is further witnessed by the low T_{err} recorded at higher ω_k. The results show that the robot performs

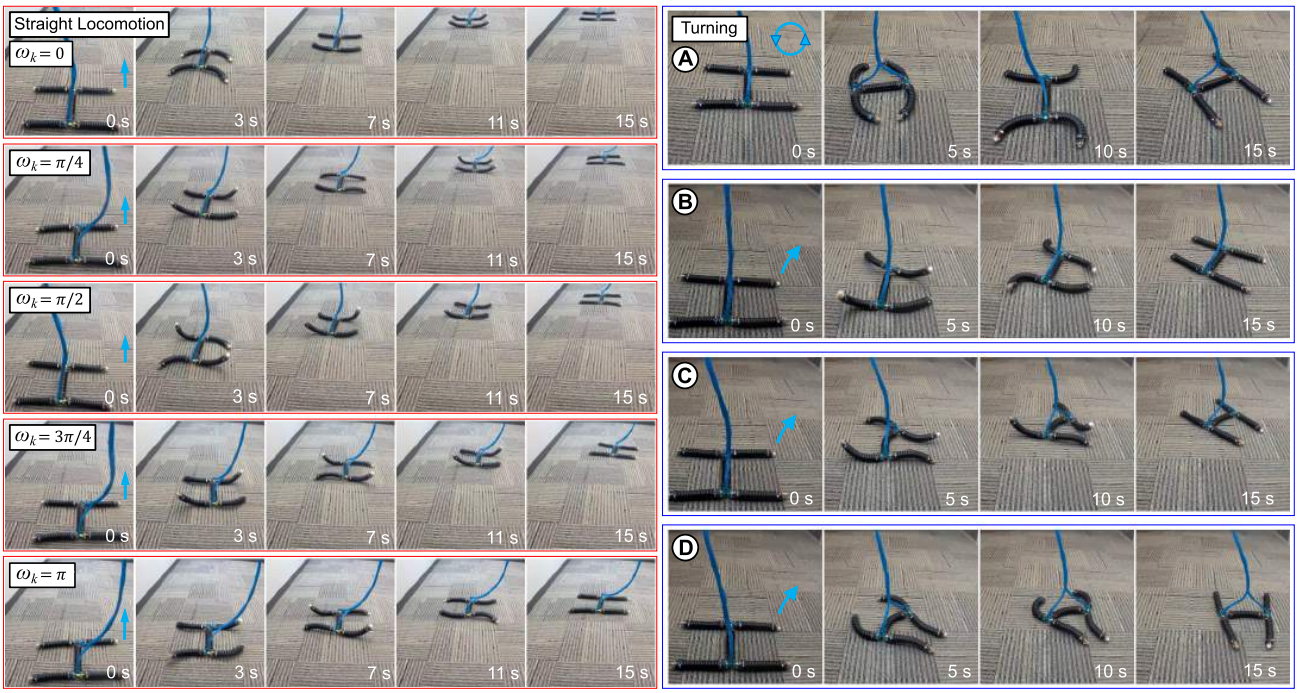

Figure 7.27: Left: Various gaits with different phase (ω_k) for straight locomotion with a 0.1 $m - 0.5$ Hz stride radius-frequency combination. Right: (A) Counterclockwise in-place turn at 0.1 $m - 0.5$ Hz, (B) Locomotion with differential strides; rightward turn at $0.06, 0.1$ $m - 0.5$ Hz, (C) Locomotion with body bending; rightward turn at 0.06 $m - 0.5$ Hz, (D) Locomotion combining differential strides and body bending; rightward turn at $0.06, 0.1$ $m - 0.5$ Hz.

well for straight locomotion gaits, and we further observed that the robot's moving speed is primarily influenced by ω_k. According to Table 7.16, lower ω_ks result in higher speeds, which is in agreement with the gait model in (5.19). Limb pairs generate lower resulting stride torque during the stance phase at higher ω_ks, as they interact with the floor in more asynchronous time intervals. In contrast, at lower ω_k, limb pairs tend to generate more stride torque on the floor, as illustrated in Fig. 5.12.

To predict robot speeds (V), we used the gait model in (5.19), and compared the predicted speeds with the experimentally recorded speeds in Table 7.16 to evaluate the model's validity. However, since η in (5.19) was unknown, we interpolated η using a few experimental data points in Table 7.16, as explained below. If ω_k and V were known, we applied (5.19) to obtain η. Accordingly, we used recorded V at $\omega_k \in \{0, \frac{\pi}{2}, \pi\}$ rad in Table 7.16 to compute η and fit the quadratic polynomial curves shown in Fig. 7.28. Based on curve fittings, we interpolated η for the remaining $\omega_k \in \{\frac{\pi}{6}, \frac{\pi}{4}, \frac{\pi}{3}, \frac{2\pi}{3}, \frac{3\pi}{4}, \frac{5\pi}{6}\}$ rad values. According to Fig. 7.28, when the actuation frequency was low ($f \in \{0.5, 0.75\}$ Hz), there was only a slight discrepancy among their locomotion efficiencies. However, when the actuation frequency was high (1 Hz), efficiencies significantly dropped, and the discrepancy widened. This was because,

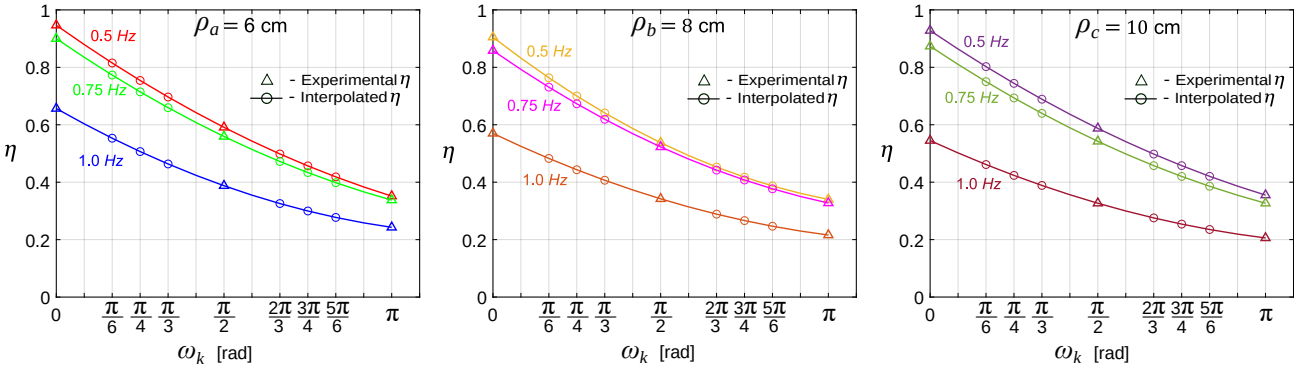

Figure 7.28: Interpolation of locomotion efficiency (η) for different stride radii – phase shift – frequency combinations of straight locomotion gait.

Table 7.17: Performance of straight crawling models.

Phase gait $[\omega_k]$	**Model output**	**Stride radius**								
		ρ_a [0.06 m]			ρ_b [0.08 m]			ρ_c [0.10 m]		
		Freq. $[Hz]$			**Freq.** $[Hz]$			**Freq.** $[Hz]$		
		0.50	0.75	1.00	0.50	0.75	1.00	0.50	0.75	1.00
		Mean speed$-V$ $[cm/s]$								
$\pi/6$	Pred. V.	5.70	8.12	7.74	7.13	10.2	9.02	9.22	13.2	10.8
	$P_{error}[\%]$	3.25	3.53	2.35	2.54	2.38	2.17	2.14	2.11	2.39
$\pi/4$	Pred. V.	5.66	8.04	7.59	7.00	10.1	8.86	9.21	13.0	10.6
	$P_{error}[\%]$	3.62	4.15	4.35	2.71	2.23	2.71	2.09	2.68	3.77
$\pi/3$	Pred. V.	5.58	7.87	7.42	6.84	9.90	8.68	9.12	12.8	10.4
	$P_{error}[\%]$	3.34	2.82	4.23	3.18	2.26	2.33	2.96	2.65	3.70
$2\pi/3$	Pred. V.	4.98	7.08	6.52	6.04	8.84	7.71	8.32	11.3	9.20
	$P_{error}[\%]$	2.00	2.82	2.61	2.15	2.49	1.91	2.37	1.95	2.28
$3\pi/4$	Pred. V.	4.80	6.84	6.28	5.84	8.55	7.45	8.03	10.8	8.89
	$P_{error}[\%]$	3.09	3.15	4.60	3.22	3.83	3.06	3.89	3.60	3.37
$5\pi/6$	Pred. V.	4.59	6.56	6.09	5.67	8.29	7.23	7.73	10.2	8.61
	$P_{error}[\%]$	4.08	3.76	2.86	2.04	3.66	2.00	3.06	3.48	3.44

at high frequencies, we attempted to actuate soft limbs beyond their responsive bandwidth, resulting in insufficient time for soft limbs to fully bend (i.e., the desired stride length was not fully realized). Having interpolated η, we then applied (5.19) and computed the predicted robot speed and prediction error, $P_{error}[\%] = \frac{V_{predicted} - V_{actual}}{V_{predicted}} \times 100$ for each gait as given in Table 7.17. The reported P_{error}, which was less than 5% at all times, validated the accuracy of the derived gait model in (5.19). Furthermore, it showed that the interpolated η values were quite accurate. This was because we used empirical data to establish η curves in Fig. 7.28.

Table 7.18: Performance of crawling and in-place turning gaits.

Estimation	**Stride radius**					
	ρ_a [0.08 m]			ρ_b [0.10m]		
	Frequency [Hz]			**Frequency** [Hz]		
	0.50	0.75	1.00	0.50	0.75	1.00
	Angular speed of clockwise turn [rad/s]					
Pred. V.	0.273	0.394	0.347	0.381	0.526	0.442
Exp. V.	0.223	0.331	0.281	0.315	0.445	0.369
T_{err} [RMSE]	02.74	02.41	02.84	02.61	02.32	02.48
P_{error}[%]	18.28	16.04	18.93	17.40	15.46	16.53
	Angular speed of counterclockwise turn [rad/s]					
Pred. V.	0.273	0.394	0.347	0.381	0.526	0.442
Exp. V.	0.225	0.328	0.284	0.319	0.441	0.371
T_{err} [RMSE]	02.63	02.52	02.71	02.45	02.43	02.41
P_{error}[%]	17.54	16.80	18.06	16.35	16.22	16.07

E. Validating Crawling and In-place Turning

We generated 12 trajectories to represent clockwise/anticlockwise turning under two different stride radii ($\rho_a = 0.06\ m$, $\rho_b = 0.08\ m$), and three frequencies ($f \in \{0.5, 0.75, 1.0\}\ Hz$) using the in-place turning gait. Table 7.18 provides the performance metrics of these trajectories, and Fig. 7.27-Right (A) visualizes the progression of the counterclockwise in-place turn at $0.1\ m - 0.5\ Hz$ stride radius – frequency combination. We measured the angular speed of the robot using the adopted method of straight locomotion in each gait. To evaluate the derived turning model in Sec. 5.3.1, we compared the model output with the experimental results. The data in Table 7.18 shows that the in-place-turning model in (5.20) computes angular speeds with a P_{error} less than 19% at all times. Furthermore, the P_{error} values are consistent for both clockwise and anticlockwise turns. It should be noted that η_π is required for use in all gait models. We estimated η_π from η at $\omega_k = \pi\ rad$ in Fig. 7.28.

F. Validating General Crawling

We categorized locomotion with differential strides, body bending, and their combined motion under general locomotion (Sec. 5.3.1). To test locomotion with differential strides, we generated two trajectories representing leftward/rightward turning with a stride radius pair of 0.06 m and 0.1 m. For testing locomotion via bending the body module without changing the stride radius ($\rho_{FR} = \rho_{FL} = \rho_{BL} = \rho_{BR} = 0.06\ m$), we generated two trajectories replicating leftward/rightward turning at a body bending angle of $\varphi = 15°$. We calculated φ using (5.24) to obtain the same turning effect (i.e., same turn radius,

Table 7.19: Performance of general crawling gait models.

Estimation	**Frequency** $[Hz]$			**Frequency** $[Hz]$		
	0.50	0.75	1.00	0.50	0.75	1.00
	Angular speed $[rad/s]$					
Pred. V.	0.078	0.113	0.108	0.078	0.113	0.108
	Turn left with stride			**Turn right with stride**		
Exp. V.	0.063	0.092	0.088	0.064	0.091	0.087
T_{err} [RMSE]	02.91	02.74	02.78	02.71	02.88	02.91
$P_{error}[\%]$	19.38	18.29	18.49	18.10	19.18	19.42
	Turn left with body			**Turn right with body**		
Exp. V.	0.066	0.096	0.091	0.067	0.097	0.092
T_{err} [RMSE]	02.33	02.21	02.36	02.14	02.13	02.22
$P_{error}[\%]$	15.55	14.74	15.71	14.27	14.20	14.79
	Turn left: stride & body			**Turn right: stride & body**		
Exp. V.	0.072	0.104	0.099	0.071	0.103	0.098
T_{err} [RMSE]	01.18	01.14	01.24	01.38	01.28	01.39
$P_{error}[\%]$	07.87	07.63	08.30	09.15	08.52	09.23

r_ρ given in (5.22)) as in the previous gait, i.e., locomotion with differential strides. Similarly, for testing the combined locomotion gait, where we combine locomotion with differential strides and body bending to efficiently turn the robot, we generated two turning trajectories replicating leftward/rightward turning while maintaining the same turn radius, at a body bending angle of $\varphi = 15^\circ$ and a stride radius pair of 0.06 m and 0.1 m. We validated all aforementioned trajectories under three actuation frequencies ($f \in \{0.5, 0.75, 1.0\}$ Hz). Fig. 7.27-Right visualizes the progression of the above locomotion gaits at 0.06 m, 0.1 m, and 0.5 Hz stride radii-frequency combination, and Table 7.19 provides their performance metrics. In each gait, we measured the robot's angular speed using the adopted method of straight locomotion.

Table 7.19 shows that the locomotion with differential stride exhibited the highest P_{error}, at approximately 19% for each frequency, while the locomotion that combined differential stride with body bending exhibited the lowest P_{error}, at approximately 9% for each frequency. The locomotion with body bending exhibited P_{error} of approximately 15% for each frequency. Hence, the proposed modeling approach is more accurate for the locomotion gait that combines differential stride with body bending. Furthermore, the reported P_{errors} differ considerably across each model, primarily due to unmodeled characteristics specific to each gait, such as slipping and friction. It is worth noting that the P_{error} are consistent for both leftward/rightward turnings in each gait model.

G. Discussion

The analysis of the experimental results indicates that the robot performs optimally at a gait frequency of approximately 0.75 Hz and with higher stride radii combinations across all gaits. The moderate frequency actuation allows the soft modules to deform and assume the large stride radii while maintaining forward motion. Moreover, the larger stride radius generates higher limb displacement torque against the floor. It should be noted that P_{errors} and T_{errs} are consistent with each other across all gait categories and actuation parameters. This is obvious since speed variations and respective tracking deviations are correlated to each other. The data also shows that the P_{errors} of general locomotion gaits are relatively larger than those of straight locomotion gaits. The possible cause of this is the accuracy of η values used in computations. Therein, we applied the empirically estimated η at $\omega_k = \pi\ rad$ obtained from the straight locomotion gait (Fig. 7.28). However, the considered locomotion in this study is turning. If η was estimated based on empirical data of turning locomotion, the P_{errors} could have been substantially lower than current values. Analyzing P_{error} in each gait, it can be concluded that the accuracy of the interpolated η values has a significant impact on P_{error}. Therefore, the use of an appropriate empirical approach to find η has a greater impact on the validity of the derived gait models on the surface where the robot is actuated.

7.4.2 Validating Quadruped Trotting

A. Obtaining a Physics-Based Soft Quadruped Dynamic Model

In trotting, diagonal pairs of limbs touch the ground alternately, which contributes to dynamic stability. Additionally, there exists a brief moment when all four limbs may simultaneously contact the ground, especially at lower speeds, providing a transition phase for increased stability. To facilitate the described movements, the robot needs to generate adequate momentum in the direction of motion [277]. This requirement should be rigorously evaluated under dynamic conditions to ensure optimal performance. The inherent hysteresis and nonlinearity of PMAs pose challenges in deriving gait trajectories for generating the required momentum, particularly within the constrained bandwidth of PMAs. Thus, an empirical approach becomes necessary. Implementing such an empirical approach directly on the physical robot is impractical due to the vast search space resulting from numerous

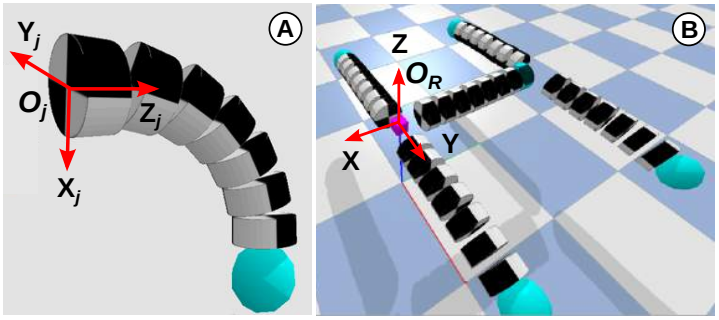

Figure 7.29: A) Soft limb PyBullet model, B) quadruped PyBullet model.

Table 7.20: Trotting parameter grid for PyBullet simulations.

ρ $[cm]$	D	x_d $[cm]$	f $[Hz]$	Δt $[s]$
4.0	0.1	7.0	0.25	1.67
5.0	0.2	8.0	0.35	0.95
6.0	0.3	9.0	0.50	0.67
7.0	0.4	10.0	0.65	0.51
8.0	0.5	11.0	0.80	0.42
9.0			0.95	
10.0			1.25	

parameters influencing its stability. In this context, we develop a comprehensive, physics-based real-time quadruped simulation model following the procedure outlined in Sec. 7.3.2. Figure 7.29 shows the obtained soft module and quadruped simulation models. This model allows us to optimize the parameterized trajectories to identify viable trajectories for subsequent testing on the actual robot proposed in Sec. 5.3.2.

B. Optimizing and Validating Trotting Trajectories in Quadruped Simulation Model

We first characterized the PyButllet soft limb model to match the dynamic response of the soft limb prototype for the fundamental limb trajectory (Fig. 5.13) proposed in Sec. 5.3. The testing procedure is outlined in Sec. 7.4.2. Actuating pressure trajectories of the limb prototype are mapped to the bending torques applied in the limb simulation model using (4.10). We iteratively modified the bending stiffness and damping coefficients of the PyBullet limb dynamic model to optimize the dynamic trajectory tracking of the limb prototype. The resulting trajectories are shown in Fig. 7.30D. Next, we apply different combinations of stride radius (ρ), duty cycle (D), position of the trajectory origin relative to limb base (x_d), limb actuation frequency ($f = 1/\tau\ Hz$), and time delay between diagonal limb pairs (Δt) derived in Sec. 5.3, to obtain stable locomotion in the PyBullet quadruped dynamic model.

Table 7.21: Optimized trotting parameters through PyBullet simulations.

Gait parameter	**Optimized region**
Trajectory stride radius, ρ	$4-8\ cm$
Duty cycle, D	$0.1-0.3$
Distance to the trajectory origin, x_d	$8-10\ cm$
Limb actuation frequency, $f=1/\tau$	$0.65-1.0\ Hz$
Time delay between diagonal limb pairs, Δt	$0.42-0.67\ s$

We set the friction coefficients of the simulation environment floor as, $\mu_x = \mu_y = 0.6$. They approximately match the friction coefficients of the actual floor (experimentally found in our previous work [183]), where the quadruped prototype will be tested. Based on the characterization and operating bandwidth of the soft limbs, we determined the testing range of the gait parameters as, $\rho \in [4, 10]\ cm$, $D \in [0.1, 0.5]$, $x_d \in [7, 11]\ cm$, and $f \in [0.25, 1.25]\ Hz$. For the above parameters, from (5.34), the testing range of Δt was computed as $\Delta t \in [0.42, 1.67]\ s$. We uniformly discretized each range and built the parameter grid shown in Table 7.20. Subsequently, we tested trotting performance via the quadruped dynamic model developed in Sec. 7.4.2 for each parameter combination. The model started trotting approximately at $\rho = 6\ cm$, $D = 0.1$, $x_d = 8\ cm$, $f = 0.65\ Hz$, and $\Delta t = 0.51\ s$. We observed that the robot tends to slip at the specified friction. Hence, friction coefficients were slightly (approximately 8%) increased to improve the stability. A 8% increase in the friction coefficients could be a reasoned choice based on the need for a slight improvement in stability without significantly departing from realistic conditions.

This simulation study revealed that low limb actuation frequencies ($0.25 < f < 0.65\ Hz$) led to unsuccessful trotting locomotion attempts. However, stability was maintained at a critical threshold of $f = 0.65\ Hz$ and beyond. The underlying cause for this behavior is the inadequacy of low limb actuation rates in generating the requisite forward momentum essential for sustaining dynamic stability during movement. We also noted that higher values of x_d (approximately 10 cm) contributed to improved trotting stability. This improvement stems from the effect of elevated x_d values causing limbs to pivot closer to the robot body, effectively redistributing mass and lowering both angular momentum and resultant torque generated by limb-ground reaction forces. This optimization aids in accurately tracking the gait trajectory while adhering to the assumption of constant curvature for limb bending. Conversely, lower values of x_d prompt a transition from trotting to crawling, as the limb tip extends farther from the robot body, aligning the trajectory origin (x_0, y_0) horizontally with the limb

origin (O_j). Notably, the success of quadruped trotting was constrained within narrower margins of D ($0.1 < D < 0.3$) and Δt ($0.42 < \Delta t < 0.67\ s$) due to their significant distortions of the original limb trajectory.

Top margins of ρ ($> 10\ cm$) and x_d ($> 11\ cm$) failed the trajectory generation (i.e., inverse kinematics failed) since they try to actuate the limb beyond its workspace. Table 7.21 gives the identified margins of each gait parameter that generated stable locomotion. Utilizing those optimized parameter margins, we tested the PyBullet dynamic model for turning trajectories proposed in Sec. 5.3.2. Figures 7.31A and 7.33A show successive simulation frames of straight locomotion and turning, respectively. The complete PyBullet simulations are included in Quadruped-Trotting-Multimedia.

C. Quadruped Prototype Actuating Setup

The block diagram and hardware components of the experimental setup configured for the quadruped actuation are shown in Figs. 7.30A and 7.30B, respectively. They are identical to the tetrahedral prototype actuating setup in Sec. 7.3.2. To actuate soft limbs and enable locomotion, joint variables (i.e., length trajectories such as those appeared in Fig. 5.14C) were converted into pressure trajectories and input via the pressure regulators in Fig. 7.30B. We employed the length-pressure mapping described in [45] to obtain pressure trajectories.

D. Testing Fundamental Trotting Trajectory on a Limb Prototype

The limb trajectory introduced in Fig. 5.13 underwent experimental testing using the setup depicted in Fig. 7.30C. Initially, curve parameters (θ_j, ϕ_j) and joint variables (l_{ji}) were computed in accordance with the desired fundamental trajectory parameters ($\rho = 8\ cm$, $D = 0.2$, and $x_d = 10\ cm$), following the methodology outlined in Sec. 5.3. Subsequently, the kinematic model in (4.3) was employed with θ_j and ϕ_j inputs to numerically derive the desired limb tip position $\{x_j, y_j\}$. This calculated trajectory was then transformed into pressure trajectories at the pressure ceiling of 300 kPa. The limb prototype shown in Fig. 7.30C was cyclically actuated at low, mid, and high frequency ranges ($f = \{0.25, 0.75, 1.25\}\ Hz$) independently over a duration of 20 s. During each actuation cycle, a motion tracker (6-DoF electromagnetic tracker, Polhemus G4 USA) recorded the spatial position of the limb tip $\{x_j, y_j\}$ relative to the limb's origin. Fig. 7.30D showcases a comparison between numerically

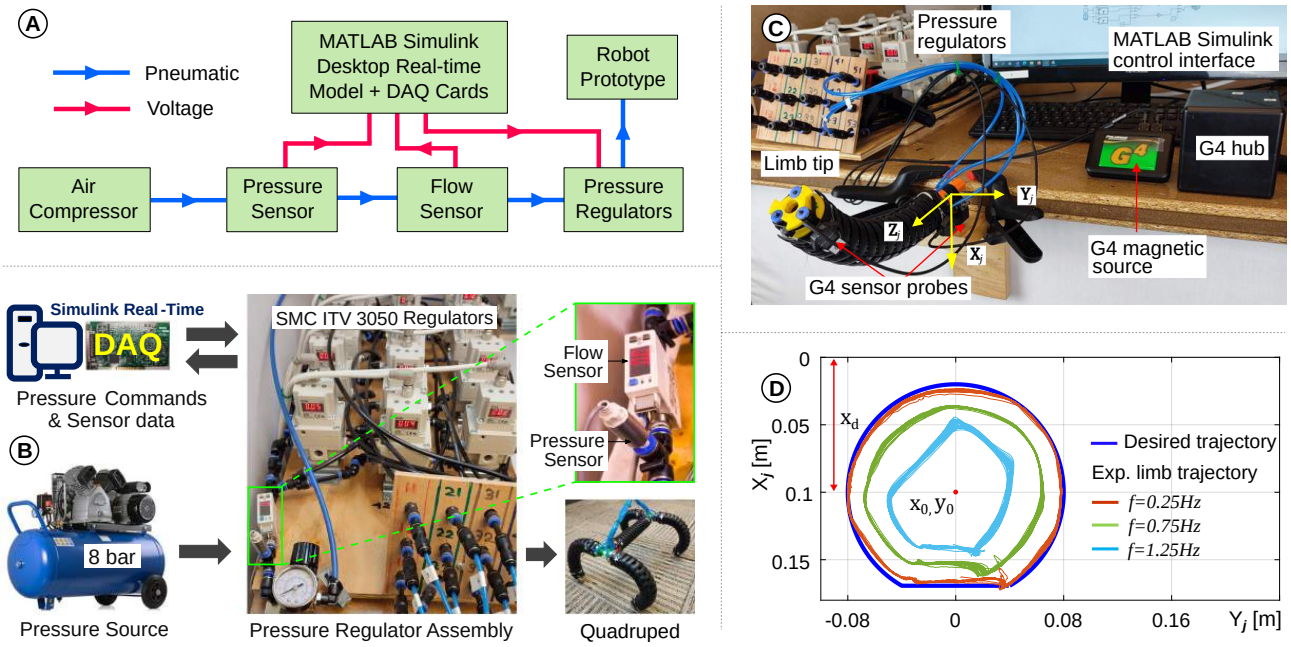

Figure 7.30: (A) Block diagram and (B) components illustrating the actuation setup for the quadruped prototype. (C) Experimental setup for testing fundamental limb trajectory. (D) Recorded trajectory profiles of a soft limb prototype.

obtained and experimentally recorded limb tip positions. The observations indicate that the recorded limb trajectory closely aligns with the desired trajectory at low frequencies ($f < 0.25\ Hz$), undergoes contraction into smaller profiles at mid frequencies ($0.25\ Hz < f < 1.00\ Hz$), and experiences distortion at high frequencies ($f > 1.00\ Hz$). This distortion arises due to the phenomenon where rapid pressure changes lead to incomplete limb deformation. Additionally, it is worth noting that the employed kinematic model does not encompass factors such as deadzones, hysteresis, and gravity, which are associated with the behavior of the limb prototype. Consequently, the irregularities observed in the trajectory within Fig. 7.30D are to be expected across all instances.

E. Validating Straight Trotting on the Quadruped Prototype

We used the optimized trajectory parameters in Table 7.21 as the baseline for the quadruped prototype testing. The quadruped was actuated for 10 s on a carpeted floor (see Fig. 7.31B). We initiated the locomotion in an unactuated pose where the quadruped is hanging at a certain distance above the ground. We used pressure supply tubes – bundled at the geometric center of the quadruped – to lift and keep the quadruped off the ground at the beginning. This pose ensures that the quadruped gained the initial stance force before locomoting. We estimated the desired hanging distance with the help of

the limb trajectory given in Fig. 5.13. Therein, the hanging distance equals to the ground distance, $x_g = x_d + \rho\cos(\varphi)$ measured along the $+X_j$ axis relative to the limb's origin at O_j. During locomotion, the pressure supply tube bundle is released and freely guided without impeding the robot movement (see Quadruped-Trotting-Multimedia).

The testing was initiated at the lower ceiling of parameters listed in Table 7.21 and the pressure ceiling of $p = 300\ kPa$. Different combinations of trajectory parameters within their optimized regions and pressure ceilings were applied until the quadruped attained its steady locomotion. During straight movements, the quadruped body is kept at straight by supplying identical pressure ceilings onto its 3 PMAs. The best locomotion was recorded at $\rho = 6\ cm$, $D = 0.2$, $x_d = 10\ cm$, $f = 0.80\ Hz$, $\Delta t = 0.42\ s$ and $p = 325\ kPa$. Figure 7.31B shows its progression. Complete videos of several experimental trials are included in Quadruped-Trotting-Multimedia. The quadruped moved with a slight divergence from its desired straight path. This was anticipated given the diversity of custom-designed PMAs that drive the soft limbs. The selection of the pressure ceiling relies on factors such as the characteristics of individually tailored PMAs, the entirety of the quadruped structure including the length of air supply tubes, limb actuating frequency, and so forth. We found that a low-pressure ceiling ($< 300\ kPa$) onto PMAs cannot provide adequate limb stiffness that can make the quadruped move while bearing its own weight. On the contrary, a high-pressure ceiling ($> 350\ kPa$) generated unexpected jerks due to over-stiffed limbs resulting in unsteady locomotion. The quadruped could not produce stable locomotion at the limb actuation frequency, 0.65 Hz recommended by PyBullet dynamic model due to inadequate forward momentum. Additionally, actuation frequencies above 1 Hz led to unstable movement, such as wobbling, due to the creation of incomplete limb trajectories. This instability arises because such frequencies surpass the operational bandwidth of PMAs. Refer to Quadruped-Trotting-Multimedia to witness the above failure scenarios.

Note that, even though the quadruped PyBullet model showed locomotion stability within specific regions of trajectory parameters at all times, the quadruped prototype did not perform similarly due to its operational limitations and unaccounted characteristics. Limb characteristics such as deadzone, hysteresis of PMAs, etc. were not included in the soft limb PyBullet model, but were inherently included in the soft limb prototype. Additionally, pressure arrival onto PMAs is not consistent since long pressure supply tubes cannot transmit fast pressure changes in real-time.

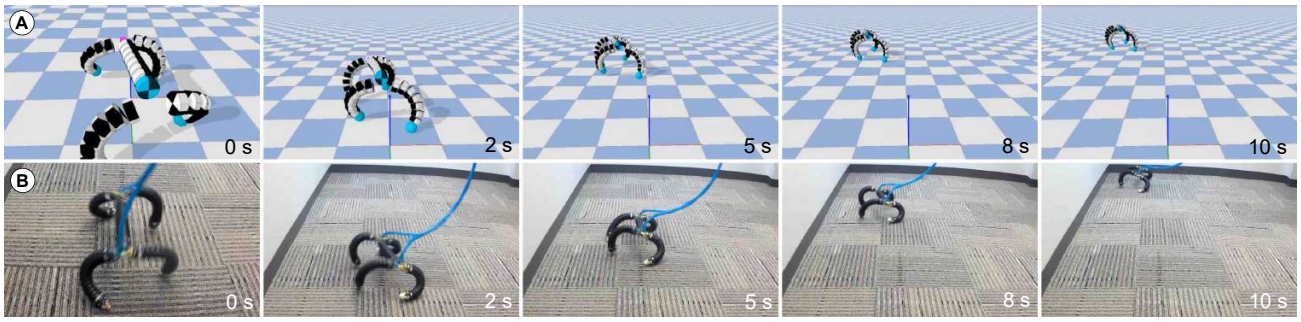

Figure 7.31: Straight locomotion at $\rho = 6\ cm$, $D = 0.2$, $x_d = 10\ cm$, $f = 0.80\ Hz$, and $\Delta t = 0.42\ s$: (A) PyBullet simulation model, (B) quadruped prototype.

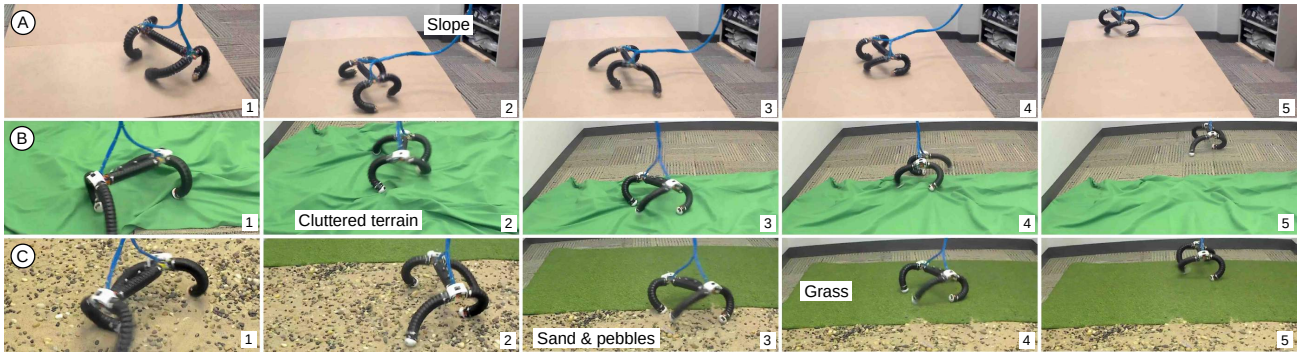

Figure 7.32: Testing the quadruped prototype on various terrains: (A) inclined surface, (B) cluttered terrain (fabric with underlying obstacles), and (C) natural-like uneven terrain (with sand, pebbles, and grass).

Table 7.22 shows the recorded locomotion speeds of the PyBullet model and the quadruped prototype for straight motion under identical trajectory parameters. We utilized video feedback from front and overhead cameras, along with floor geometry, to estimate the robot's displacement on the X-Y plane. This estimation was achieved by employing an image projection method akin to the one described in [167]. According to the results in Table 7.22, the speed error between the two models is less than 11 %. Overall, quadruped models demonstrated fast locomotion gaits well.

Additionally, we expanded the robot prototype testing into uneven and irregular terrains, as depicted by Fig. 7.32, including slopes (inclination = 40°), cluttered terrain (fabric with underlying obstacles), and natural-like uneven terrain with obstacles such as sand, pebbles, and grass by applying optimized gait parameters from the PyBullet simulations. Our experimental results (See Quadruped-Trotting-Multimedia) confirm the robot's ability to locomote under these varied uneven conditions.

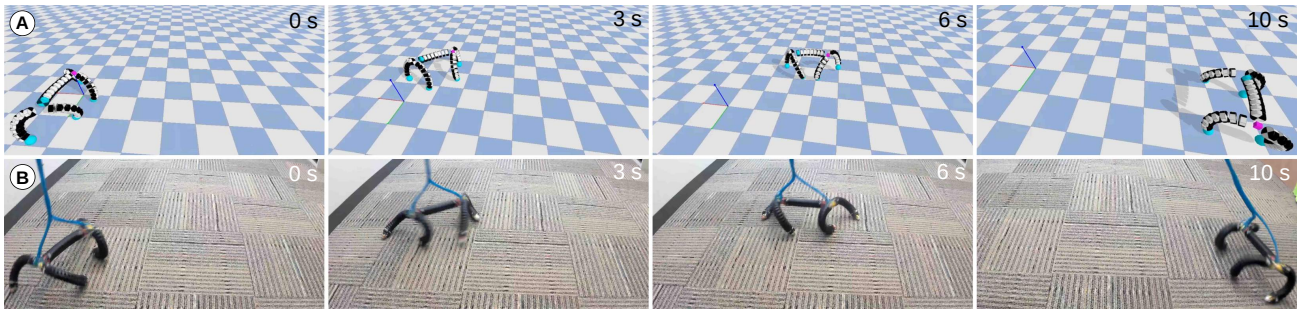

Figure 7.33: Rightward turn at $\rho_I, \rho_O = 4, 6\ cm$, and body bending, $\phi_B = 37.2°$ in (A) PyBullet simulation model, (B) quadruped prototype. Herein, trajectory parameters; D, x_d, f, and Δt unchanged from straight motion.

F. Validating Trotting-and-Turning

We tested the quadruped turning by applying proposed turning trajectories in Sec. 5.3.2 within the optimized range of trajectory parameters given in Table 7.21. We initiated the testing at the pressure ceiling, 325 kPa, and the actuating frequency, 0.80 Hz since those gave stable locomotion for the straight motion (Sec. 7.4.2). The testing was repeated for three amplitudes of turn radius ($\lambda = \{40, 50, 60\}\ cm$) and leftward/rightward turn directions. During turning, we bend the robot body to accommodate differential turn radii on inward and outward limbs (Sec. 5.3.2). It causes to increase in the active DoF of the quadruped from 12 (straight motion) to 15 (turning). Because of that, the quadruped turning showed relatively unsteady locomotion compared to its straight motion. Figure 7.33B visualizes the progression of the rightward turning at a turn radius, 40 cm and Table 7.23 provides turning performances. For every gait, the robot's angular speed in relation to its turn radius was estimated using the method described for straight motion in Sec. 7.4.2. The results show that the quadruped leverages its body bending to effectively turn while moving similar to its counterpart, PyBullet model. When the turn radius is low, the quadruped efficiently turned recording a higher angular speed per turn radius.

There exists slight discrepancies between the dynamic responses of the PyBullet dynamic model and the experimental results of the robot prototype. For instance, the heel contact of the PyBullet model appears as a point contact whereas, in the robot prototype, it appears as distributed contact even though the results closely agree with each other. This is owing to the fact that soft robots (such as the soft limbs herein) can conform to the environment to find stability. Further, soft robots have a higher stability margin or error tolerance than the continuum limbs modeled through rigid body

Table 7.22: Performance of straight trotting.

Model	**Speed** $[cm/s]$
Quadruped PyBullet model	44.4
Quadruped prototype	39.8
Error [%]	10.3

Table 7.23: Performance of trotting-and-turning.

Model	**Rightward turn**			**Leftward turn**		
	Turn radius $[cm]$			**Turn radius** $[cm]$		
	40	50	60	40	50	60
	Angular speed per turn radius $[rad/ms]$					
Quadruped PyBullet model	2.36	1.64	1.16	2.27	1.57	1.11
Quadruped prototype	1.99	1.40	1.02	1.92	1.36	0.99
Error [%]	15.7	14.9	12.5	15.4	13.3	10.5

approximations in PyBullet. Because of such reasons, the robot prototype showed a slightly higher oscillatory behavior in each trotting cycle than the PyBullet model. These discrepancies are reflected by the error margins recorded in Tables 7.22 and 7.23.

G. Estimating Energy Consumption in Trotting

We examined the energy consumption during trotting locomotion and contrasted it with the conventional crawling gait of the robot presented in Sec. 7.4.1 [45]. When the robot is powered by pneumatic pressure, P_{in} $[Nm^{-2}]$, and its volumetric air flow rate, $\dot{V}$ $[m^3s^{-1}]$, the power output of the pneumatic system can be computed as $P_{in}\dot{V}$ $[W]$. Consequently, the energy expended by the pneumatic system (or the energy input to the robot), denoted as E, is determined by (7.1), with t representing the duration of robot actuation.

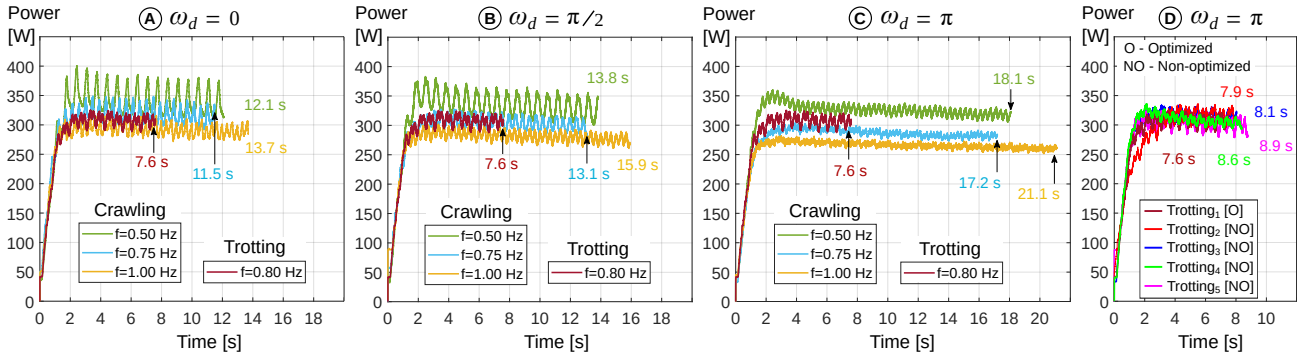

Figure 7.34: Power output of the pneumatic system at phase gaits; (A) $\omega_d = 0$, (B) $\omega_d = \frac{\pi}{2}$ and, (C) $\omega_d = \pi$ rad under different actuation frequencies for crawling and optimized trotting gaits. (D) Power output of optimized and non-optimized trotting gaits. Here "optimized" refers to the one that gives the most stable locomotion and "Non-optimized" refers to the ones that give unstable locomotion.

Following the energy estimation procedure outlined in Sec. 7.3.2, we connected a pressure sensor (PSE530-R07-L, SMC USA) and a flow sensor (PFM711-C6-E-M, SMC USA) to gauge the input air pressure and volumetric flow rate, as shown in Figs. 7.30A and 7.30B. First, we actuated the robot for trotting over a fixed straight distance of 3.0 m within the optimized trajectory parameters and recorded the pressure input, air flow rate, and traverse time. Secondly, we repeated the same step for trotting under several combinations of non-optimized trajectory parameters, as listed in column 2 of Table 7.24, to investigate the effect of trajectory optimization on energy consumption. Therein, we isolated actuation frequency, f, and duty cycle, D, as variable non-optimized trajectory parameters since their impact was significant for trotting stability based on simulation results in Sec. 7.4.2. The testing range of these non-optimized parameter values was kept within a close margin to the optimized value, as significantly deviated non-optimized values do not allow the quadruped to locomote with reasonable stability, as evidenced by failure scenarios (see Quadruped-Trotting-Multimedia). Table 7.24 provides the computed energy consumption under each optimized and non-optimized trotting condition.

Thirdly, we repeated the same step for crawling under identical conditions. The prior work in [45] demonstrated crawling under 9 phase shifts ($\omega_d \in \{0, \frac{\pi}{6}, \frac{\pi}{4}, \frac{\pi}{3}, \frac{\pi}{2}, \frac{2\pi}{3}, \frac{3\pi}{4}, \frac{5\pi}{6}, \pi\}\ rad$) between diagonal limb pairs and 3 actuation frequencies ($f \in \{0.5, 0.75, 1.0\}\ Hz$). In this work, for estimating the energy consumption during crawling, we opted for lower, middle, and upper bounds of $\omega_d \in \{0, \frac{\pi}{2}, \pi\}\ rad$ along with the same actuation frequencies as representative boundary points. Table 7.25 gives the computed energy output under each crawling gait.

Figures 7.34A, 7.34B, and 7.34C depict the power outputs of the pneumatic system (equivalent to the power input to the robot) based on (7.1) for crawling and optimized trotting gaits. The crawling motion displays a subtle decline in power output, attributed to the reduction in volumetric flow rate from the air tank caused by the diminishing tank pressure, as crawling leads to a faster air intake rate. However, the reduction in flow rate does not affect the accuracy of the energy estimation since the flow rate is precisely measured.

Figure 7.34D compares the power output of the optimized (i.e., the most stable) trotting gait against various non-optimized (i.e., unstable) trotting gaits. When these results are combined with the estimated energy consumption in Table 7.24, it is evident that both higher ($f = 0.9\ Hz$) and lower ($f = 0.7\ Hz$) actuation frequencies cause the robot to consume more energy compared to the

Table 7.24: Energy estimation in trotting gaits.

Trotting type	**Optimized/ Non-optimized gait parameters**	**Energy consumption** $[KJ]$
Trotting_1 [O]	$f = 0.8\ Hz,\ D = 0.20$	2.14
Trotting_2 [NO]	$f = 0.8\ Hz,\ D = 0.15$	2.23
Trotting_3 [NO]	$f = 0.8\ Hz,\ D = 0.25$	2.19
Trotting_4 [NO]	$f = 0.9\ Hz,\ D = 0.20$	2.49
Trotting_5 [NO]	$f = 0.7\ Hz,\ D = 0.20$	2.57

O - Optimized (stable), NO - Non-optimized (unstable)

Table 7.25: Energy estimation in crawling gaits.

Actuating frequency $[Hz]$	**Phase shift in crawling gait** $[rad]$		
	$\omega_d = 0$	$\omega_d = \pi/2$	$\omega_d = \pi$
	Energy consumption $[KJ]$		
0.50	3.89	4.40	5.70
0.75	3.46	3.80	4.75
1.00	3.85	4.34	5.47

optimized actuation frequency ($f = 0.8\ Hz$). The reason for this is that at lower actuation rates, the robot spends more time covering a fixed distance, resulting in prolonged operation of the pneumatic system. Conversely, at higher rates, the trajectory becomes distorted, making it difficult for the robot to cover the distance efficiently. Additionally, the data shows that the duty cycle has a minimal impact on energy consumption since we chose a variation range close to the optimized value. Larger variations in the duty cycle prevent the robot from achieving trotting.

H. Analyzing Energy Efficiency in Trotting

Figure 7.34 indicates that the robot dedicates a considerably lower duration to covering the specified fixed distance via trotting compared to crawling, regardless of the actuation frequency or limb phase shift of the crawling. Consequently, the data presented in Tables 7.24 and 7.25 demonstrates that trotting consistently records a reduced energy input to the robot compared to crawling. The trotting has a smaller duty cycle than crawling, hence its floor contacts are minimal. Conversely, owing to the

Table 7.26: Energy saving of trotting against crawling.

Trotting type	**Phase shift in crawling gait** $[rad]$								
	$\omega_d = 0$			$\omega_d = \pi/2$			$\omega_d = \pi$		
	Freq. $[Hz]$			**Freq.** $[Hz]$			**Freq.** $[Hz]$		
	0.50	0.75	1.00	0.50	0.75	1.00	0.50	0.75	1.00
	Energy saving - $E_{saving}[\%]$								
Trotting_1 [O]	45.0	38.2	44.4	51.4	43.7	50.7	62.5	54.9	60.9
Trotting_2 [NO]	42.7	35.5	42.1	49.3	41.3	48.6	60.9	53.1	59.2
Trotting_3 [NO]	43.7	36.7	43.1	50.2	42.4	49.5	61.6	53.9	59.8
Trotting_4 [NO]	36.0	28.0	35.3	43.4	34.5	42.6	56.3	47.6	54.5
Trotting_5 [NO]	33.9	25.7	33.2	41.6	32.4	40.8	54.9	45.9	53.0

increased number of distributed floor contacts, crawling demands a significant amount of energy to overcome friction. We computed the energy efficiency of trotting relative to crawling as

$$E_{saving}[\%] = \frac{E_{crawling} - E_{trotting}}{E_{crawling}} \times 100. \tag{7.3}$$

Table 7.26 summarizes the corresponding energy efficiencies of both optimized and non-optimized trotting gaits. The results demonstrate that optimized trotting consistently saves the maximum percentage of energy compared to non-optimized conditions at all times. Accordingly, the optimized-trotting approximately saves energy, on average, 42 %, 48 %, and 59 % under phase shifts, 0, $\pi/2$, and π, respectively. The data aligns with the observation that the energy consumption of crawling increases as the phase shift, ω_d rises from 0 to π. The crawling reported in [45] demonstrated that higher ω_d values lead to lower speeds (see crawling videos in Quadruped-Trotting-Multimedia). Therefore, because of the prolonged operating time of the pneumatic system, higher ω_ds have resulted in increased energy expenditure, thereby contributing to higher energy savings in trotting.

According to Fig. 7.34, during each phase shift of crawling, the power amplitude decreases as the frequency increases from 0.50 Hz to 1.00 Hz. This is because higher actuation rates require rapid pressure changes, thereby compelling the pneumatic system to deliver power at shorter intervals. Moreover, a similar trend can be observed as the phase shift increases from 0 to π. The reason for this is that at higher phase shifts, all limbs are operated asynchronously, forcing the pneumatic system to maintain a uniform power supply compared to the cyclic pattern observed at lower phase shifts.

It should also be noted that, during each phase shift of crawling, the lowest energy consumption is observed at the moderate actuation frequency, 0.75 Hz. This is attributed to the fact that moderate actuation frequencies enable the limbs to attain their complete deformation range, delivering the required work with minimal energy.

7.4.3 Validating Closed-loop Control of Quadruped Trotting

In this section, we validate closed-loop control system of the quadruped proposed in Chapter 6. We deployed the control system with the gains given in Table 6.5 to test the locomotion performance of the quadruped prototype. Note that we optimized controller gains to achieve the best performance

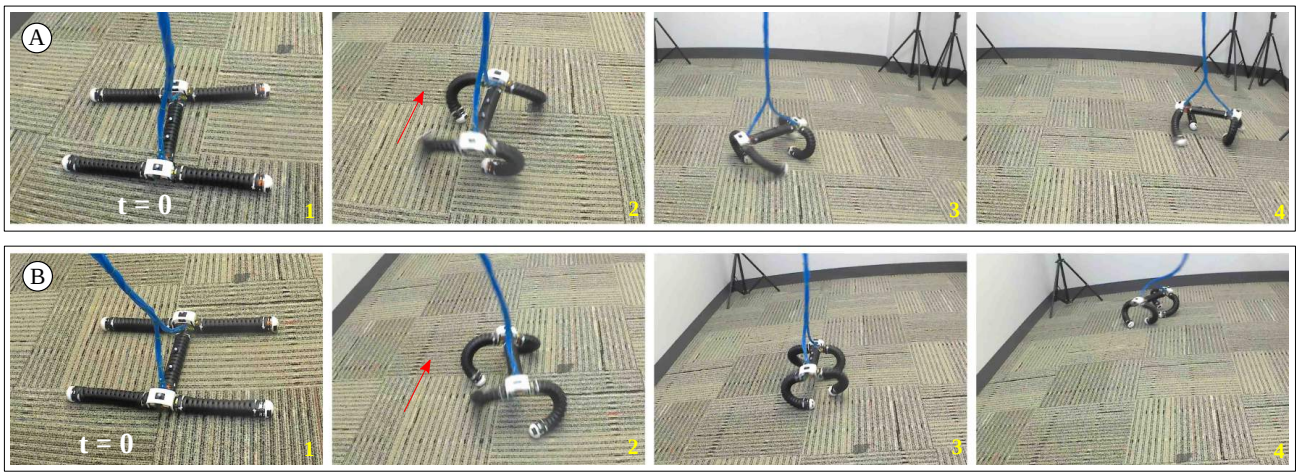

Figure 7.35: Experimental progression of trotting under (A) open-loop and (B) closed-loop control.

Table 7.27: Controller performance: soft quadruped prototype testing.

Limb	**RMSE**$_\theta$ [*deg.*]			**RMSE**$_\phi$ [*deg.*]		
	WC	**NC**	**E** [%]	**WC**	**NC**	**E** [%]
Front Right	7.91	6.55	20.7	22.2	16.6	33.6
Front Left	7.64	6.25	22.2	21.0	15.5	35.5
Back Right	7.77	6.41	21.2	21.9	16.1	36.0
Back Left	8.59	6.99	22.9	24.9	17.9	39.0

WC - With Control, NC - No Control

of the trotting gait parameters found through pyBullet Dynamic model optimizations (see Sec. 7.4.2). Figure 7.35 shows the progression of the quadruped prototype with and without engaging the control system. The complete videos are available in the web repository, Quadruped-Control-Multimedia. These videos demonstrate that the quadruped locomotion is more streamlined when the control system is fully applied to each limb. Additionally, Fig. 7.36 visualizes the jointspace performance and controllers' engagement in each limb actuation. Table 7.27 provides the respective RMSE for the limb orientation and the bending angle at limb level, both with and without control. The RMSE of limb orientation remains within a margin of error of 07° whereas, the RMSE of limb bending remains within a margin of error 19°. The error reduction percentage for θ remains approximately at 22 %, while it stays at 38 % for ϕ. The higher error margin in limb deformation is attributed to the fact that the trotting trajectory undergoes non-uniform deformation compared to uniform gait trajectories such as quadruped crawling or SRS rolling. Overall, these results, along with multimedia evidence, demonstrate the effectiveness of engaging the feedback control system for quadruped locomotion.

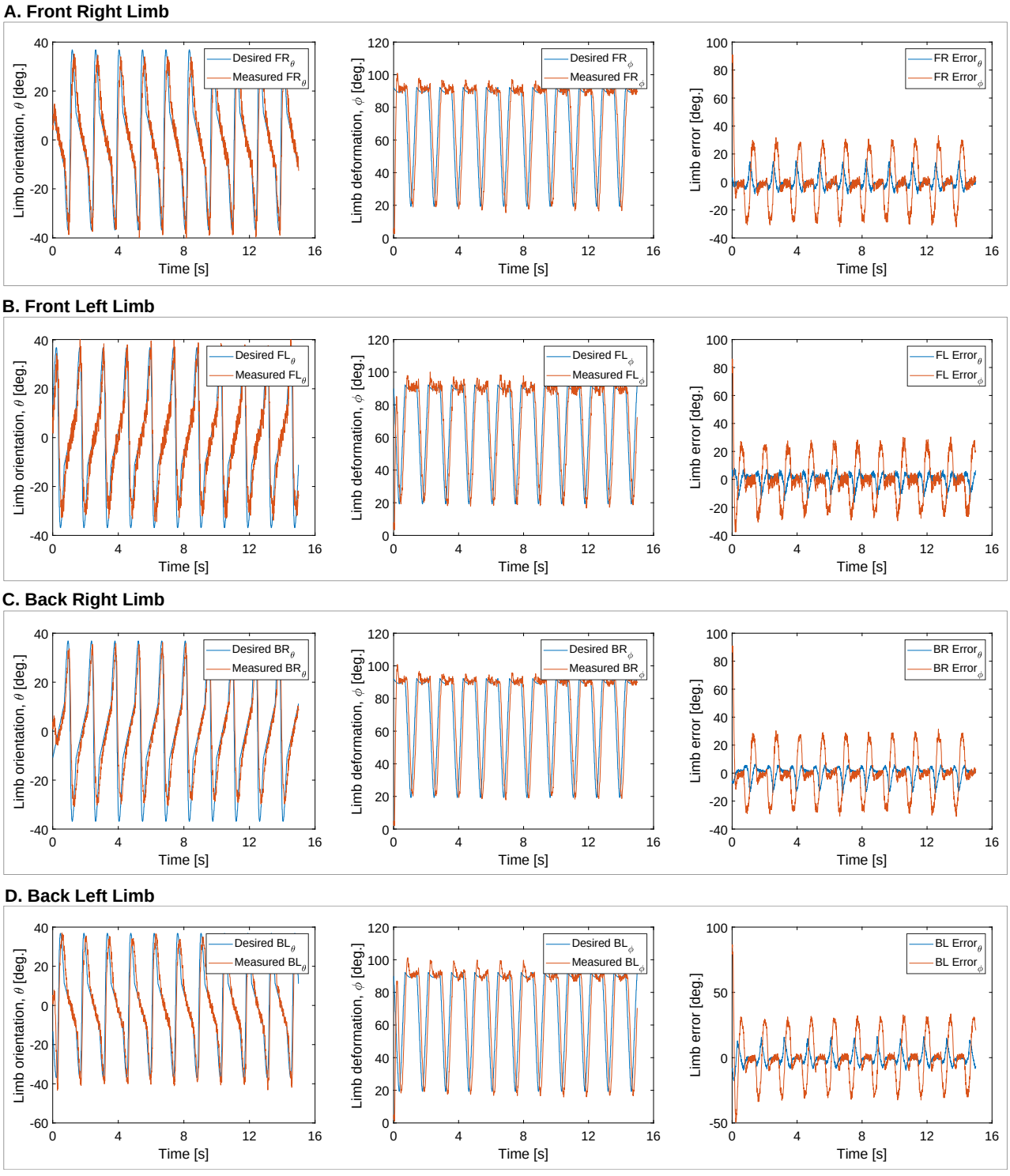

Figure 7.36: Experimental results of controlling the trotting trajectory of each limb in the quadruped prototype.

7.4.4 Chapter Summary

This chapter detailed the experimental validation of the proposed soft module and soft mobile robot topologies. The soft module was validated for its improved stiffness range and decoupled stiffness and shape control. The SRS was validated for various locomotion trajectories, including sidewinding, serpentine, planar rolling, helical rolling, and curved surface locomotion. Additionally, the proposed dynamic model of the SRS was validated. The tetrahedral robot was validated for pinniped and tumbling locomotion trajectories, while the quadruped robot was validated for crawling and trotting trajectories. The validation studies also included closed-loop control of the SRS planar rolling and quadruped trotting gaits. The subsequent chapter concludes the dissertation.

Chapter 8

Conclusion

8.1 Overview

This dissertation has explored the design, modeling, and validation of various soft mobile robot topologies. It has contributed to notable advancements in the field of soft robotics, particularly in the use of hybrid soft modules (integrating soft and stiff elements) as soft limbs, the development of novel locomotion gaits, and the validation of these innovations through both experimental and simulation-based methods. This chapter summarizes each research study undertaken within the dissertation and outlines the overarching conclusions and future research directions.

8.2 Summary of Work

8.2.1 Hybrid Soft Robots Incorporating Soft and Stiff Elements [254]

In this study, we introduced a novel hybrid soft module that integrates rigid and soft components inspired by the biological design of spider monkey tails. By incorporating an inextensible articulable rigid backbone with pneumatic muscle actuators, the soft module demonstrated an approximate 100 % increase in stiffness compared to purely soft robots. This design allowed for independent control of stiffness and shape, validated through the application of a soft robotic gripper. The results highlight the potential of hybrid soft modules in applications requiring adaptive stiffness, combining high stiffness range with natural compliance and task space performance.

8.2.2 A Novel Variable Stiffness Soft Robotic Gripper [253]

This research proposed a novel soft robotic gripper employing the proposed hybrid soft module that has independent shape and stiffness control capabilities. Detailed design and kinematic models were developed, and empirical data was utilized for precise control. Experimental validation through various tests demonstrated the gripper's ability to sustain rotational and linear motion with grasped objects, and improve grasping quality through stiffness control. These findings underscore the potential of variable stiffness control in enhancing soft robotic grippers' performance in adaptive grasping tasks.

8.2.3 Soft Robotic Snake Locomotion: Modeling & Experimental Assessment [167]

This study focused on a 3-section SRS capable of replicating various snake locomotion gaits. The SRS prototype was fabricated based on the modular design concept of soft robots from previous studies. The development of a full floating base kinematic model and optimization-derived jointspace trajectories enabled the successful replication of serpentine, inward rolling, and outward rolling gaits. While serpentine gait did not produce meaningful displacement due to uniform friction, rolling gaits achieved successful locomotion. This study was pivotal in demonstrating the feasibility of rolling locomotion in SRS for the first time.

8.2.4 Dynamic Modeling and Validation of Soft Robotic Snake Locomotion [183]

Building on previous work, this study introduced a dynamic model with point-based contact dynamics for the 3-section SRS prototype. The model successfully replicated planar and spatial rolling gaits, both in simulations and experimental tests. The consistency between numerical and experimental results validated the proposed dynamic model, setting the stage for future work on additional snake locomotion gaits.

8.2.5 Wheelless Soft Robotic Snake Locomotion: Study on Sidewinding and Helical Rolling Gaits [180]

This study introduced a four-section SRS, achieving locomotion via spatial deformation without relying on friction anisotropy. The SRS prototype design exemplifies the serial arrangement of hybrid soft modules. The robot, with its 12-DoF, demonstrated sidewinding and helical rolling gaits through a

comprehensive kinematic model and optimization-based inverse kinematic approach. Experimental validation confirmed the feasibility and effectiveness of these gaits, paving the way for future dynamic modeling studies.

8.2.6 Soft Robotic Snake Locomotion on Curved Surfaces [284]

This study explored a novel approach to SRS locomotion using distributed contacts on curved cylindrical surfaces utilizing the 4-section SRS prototype proposed in the previous study. It systematically parameterized and generated locomotion trajectories suitable for various scenarios, demonstrating versatility and practicality. Investigating gripping forces exerted by these contacts enhanced understanding of SRS locomotion mechanics. Experimental validation with the SRS prototype confirmed the efficacy of the trajectories across diverse configurations, validating the robustness of the locomotion strategy.

8.2.7 Study on Soft Robotic Pinniped Locomotion [21]

This research focused on a soft-limbed robot that mimics pinniped locomotion. The robot prototype was fabricated in the tetrahedral topology utilizing the hybrid soft modules proposed in previous studies. It demonstrated the parallel arrangement of hybrid soft modules. Through kinematic models and task-space trajectories, the robot demonstrated successful crawling and turning gaits under various conditions. This work sets the foundation for future development of dynamic gaits and closed-loop control systems for pinniped locomotion.

8.2.8 Tumbling Locomotion of Tetrahedral Soft-limbed Robots [22]

Extending the previous work on pinniped locomotion, this study introduced an energy-efficient tumbling gait for the tetrahedral soft-limbed robot. This novel locomotion mode, validated through simulations and prototype testing, showcased enhanced maneuverability, adaptability to challenging terrains, and energy conservation. This was the first study on energy estimation in soft-limbed robot locomotion.

8.2.9 Soft Steps: Exploring Quadrupedal Locomotion with Modular Soft Robots [45]

This study presented a modular soft-limbed quadruped, detailing its design and kinematic models. The quadruped prototype showcased the serial-parallel arrangement of hybrid soft modules. Through task-space and jointspace trajectory analysis, the robot demonstrated successful replication of various gaits under different conditions. The low prediction error in experimental results validated the proposed gait modeling approach, highlighting the reliability of the modular design.

8.2.10 Efficient Trotting of Soft Robotic Quadrupeds [200]

Expanding the previous work, this study proposed dynamically-stable trotting locomotion for the soft quadruped. Using a Physics-enabled virtual environment for optimization, the study demonstrated energy-efficient trotting gaits, validated through experimental testing. The results confirmed that physics-based simulation environments can effectively support the realization of dynamically-stable locomotion in soft robots.

8.2.11 Closed-loop Control of Soft Mobile Robots [285], [286]

This study employed the closed-loop control system to effectively manage the locomotion of the SRS and the quadruped. Wireless sensors were integrated to measure the bending curvatures of the SRS body and the quadruped limbs. The measured trajectory parameters were compared and adjusted in real-time to align with the desired locomotion trajectories. The results demonstrated that closed-loop controlled locomotion trajectories outperformed open-loop control trajectories tested previously, significantly enhancing locomotion towards field applications.

8.3 Future Research Directions

Future research should focus on extending dynamic modeling, enhancing autonomy through onboard power and sensing, implementing dynamic control, and developing path planning. Additionally, exploring new locomotion modes will further broaden the capabilities and field applications of soft mobile robots.

The closed-loop control systems introduced in this dissertation demonstrated the control of planar rolling gaits in SRSs. These control systems were implemented based on kinematic modeling. Future advancements should focus on developing control systems based on dynamic modeling to manage not only planar locomotion gaits but also spatial locomotion gaits of SRSs, aiming for more accurate and robust locomotion control. Additionally, exploring new locomotion modes for SRSs, such as multimodal and bio-inspired locomotion, and extending capabilities to vertical and tapered surfaces, will broaden the range of applications.

Soft mobile robots should be designed for untethered operation. To achieve this, integrating onboard sensing and power systems will be crucial, along with developing efficient energy management systems. Transitioning power autonomy from pneumatic actuation to electromechanical actuation is essential for untethered operation. Therefore, hybrid soft modules should be redesigned to accommodate electromechanical actuation with onboard power, actuators (e.g., motors), cables/tendons, etc. This redesign will support the integration of necessary components for fully autonomous and versatile soft mobile robots.

The design, trajectory generation, control methods, and validation of soft-limbed robots must be enhanced for testing in unstructured unpredictable environments. Expanding the testing of these mobile robots for field applications such as search and rescue operations and environmental monitoring is essential. Innovations in materials and fabrication, including the use of smart materials, advanced 3D printing, and improved durability, will further enhance the functionality and longevity of soft robots. These advancements will pave the way for versatile and adaptive solutions across various applications.

Bibliography

[1] D. Rus and M. T. Tolley, "Design, fabrication and control of soft robots," *Nature*, vol. 521, no. 7553, p. 467, 2015.

[2] G. M. Whitesides, "Soft robotics," *Angewandte Chemie Intl. Edition*, vol. 57, no. 16, pp. 4258–4273, 2018.

[3] M. Calisti, G. Picardi, and C. Laschi, "Fundamentals of soft robot locomotion," *Journal of The Royal Society Interface*, vol. 14, no. 130, 2017.

[4] B. Mazzolai, F. Carpi, K. Suzumori, *et al.*, "Roadmap on soft robotics: Multifunctionality, adaptability and growth without borders," *Multifun. Materials*, 2022.

[5] S. Chen, Y. Cao, M. Sarparast, *et al.*, "Soft crawling robots: Design, actuation, and locomotion," *Adv. Material Technologies*, vol. 5, no. 2, p. 1 900 837, 2020.

[6] F. Ahmed, M. Waqas, B. Javed, *et al.*, "Decade of bio-inspired soft robots: A review," *Smart Materials & Struct.*, 2022.

[7] N. El-Atab, R. B. Mishra, F. Al-Modaf, *et al.*, "Soft actuators for soft robotic applications: A review," *Adv, Intel. Sys.*, vol. 2, no. 10, p. 2 000 128, 2020.

[8] S. Aracri, F. Giorgio-Serchi, G. Suaria, *et al.*, "Soft robots for ocean exploration and offshore operations: A perspective," *Soft Robotics*, vol. 8, no. 6, pp. 625–639, 2021.

[9] E. W. Hawkes, L. H. Blumenschein, J. D. Greer, and A. M. Okamura, "A soft robot that navigates its environment through growth," *Science Robotics*, vol. 2, no. 8, eaan3028, 2017.

[10] T. T. Oshiro, "Soft robotics in radiation environments: A prospective study of an emerging automated technology for existing nuclear applications," 2018.

[11] C. S. X. Ng and G. Z. Lum, "Untethered soft robots for future planetary explorations?" *Adv, Intel. Sys.*, p. 2 100 106, 2021.

[12] Y. Zhang, P. Li, J. Quan, L. Li, G. Zhang, and D. Zhou, "Progress, challenges, and prospects of soft robotics for space applications," *Adv, Intel. Sys.*, p. 2 200 071, 2022.

[13] F. Schmitt, O. Piccin, L. Barbé, and B. Bayle, "Soft robots manufacturing: A review," *Frontiers in Robotics and AI*, vol. 5, p. 84, 2018.

[14] M. Kondoyanni, D. Loukatos, C. Maraveas, C. Drosos, and K. G. Arvanitis, "Bio-inspired robots and structures toward fostering the modernization of agriculture," *Biomimetics*, p. 69, 2022.

[15] A. L. Gunderman, J. A. Collins, A. L. Myers, R. T. Threlfall, and Y. Chen, "Tendon-driven soft robotic gripper for blackberry harvesting," *IEEE Robo & Auto. Letters*, pp. 2652–2659, 2022.

[16] Z. Ye, G. Pang, K. Xu, *et al.*, "Soft robot skin with conformal adaptability for on-body tactile perception of collaborative robots," *IEEE Rob. & Auto. Letters*, pp. 5127–5134, 2022.

[17] S. Mao, E. Dong, H. Jin, M. Xu, and K. Low, "Locomotion and gait analysis of multi-limb soft robots driven by smart actuators," in *IEEE/RSJ Intl. Conf. on Intelligent Robots and Systems (IROS)*, 2016, pp. 2438–2443.

[18] J. M. Bern, P. Banzet, R. Poranne, and S. Coros, "Trajectory optimization for cable-driven soft robot locomotion.," in *Robotics: Science & Systems*, vol. 1, 2019.

[19] Y. Wang, J. Wang, and Y. Fei, "Design and modeling of tetrahedral soft-legged robot for multi-gait locomotion," *IEEE/ASME Transactions on Mechatronics*, 2021.

[20] D. M. Perera, D. D. Arachchige, S. Mallikarachchi, *et al.*, "Teleoperation of soft modular robots: Study on real-time stability and gait control," in *IEEE Intl. Conf. on Soft Rob. (RoboSoft)*, 2023.

[21] D. D. Arachchige, T. Varshney, U. Huzaifa, *et al.*, "Study on soft robotic pinniped locomotion," in *IEEE/ASME Intl. Conf. on Adv. Intel. Mechatronics (AIM)*, 2023, pp. 65–71.

[22] D. D. Arachchige, D. M. Perera, U. Huzaifa, I. Kanj, and I. S. Godage, "Tumbling locomotion of tetrahedral soft-limbed robots," *IEEE Robotics and Automation Letters*, 2024.

[23] M. T. Tolley, R. F. Shepherd, M. Karpelson, *et al.*, "An untethered jumping soft robot," in *2014 IEEE/RSJ Intl. Conf. on Intelligent Robots and Systems*, 2014, pp. 561–566.

[24] I. S. Godage, T. Nanayakkara, and D. G. Caldwell, "Locomotion with continuum limbs," in *IEEE/RSJ Intl. Conf. on Intel. Rob. & Sys. (IROS)*, 2012, pp. 293–298.

[25] S. Mao, E. Dong, L. Zhou, *et al.*, "Design and gait analysis of a tortoise-like robot with soft limbs," in *Assistive Robotics: 18th Intl. Conf. on CLAWAR*, World Scientific, 2016, pp. 215–223.

[26] Y. Li, Y. Chen, T. Ren, Y. Li, and S. H. Choi, "Precharged pneumatic soft actuators and their applications to untethered soft robots," *Soft robotics*, vol. 5, no. 5, pp. 567–575, 2018.

[27] X. Huang, K. Kumar, M. K. Jawed, Z. Ye, and C. Majidi, "Soft electrically actuated quadruped (seaq)—integrating a flex circuit board and elastomeric limbs for versatile mobility," *IEEE Rob. & Auto. Letters*, vol. 4, no. 3, pp. 2415–2422, 2019.

[28] M. A. I. Kalın, C. Aygül, A. Türkmen, J. Kwiczak-Yiğitbaşı, B. Baytekin, and O. Özcan, "Design, fabrication, and locomotion analysis of an untethered miniature soft quadruped, squad," *IEEE Rob. & Auto. Letters*, vol. 5, no. 3, pp. 3854–3860, 2020.

[29] Y. Kim, Y. Lee, and Y. Cha, "Origami pump actuator based pneumatic quadruped robot (oparo)," *IEEE Access*, vol. 9, pp. 41 010–41 018, 2021.

[30] H. Tanaka, T.-Y. Chen, and K. Hosoda, "Dynamic turning of a soft quadruped robot by changing phase difference," *Front. in Rob. & AI*, vol. 8, p. 629 523, 2021.

[31] S. T. Muralidharan, R. Zhu, Q. Ji, L. Feng, X. V. Wang, and L. Wang, "A soft quadruped robot enabled by continuum actuators," in *IEEE Intl. Conf. on Automation Science and Engineering (CASE)*, 2021, pp. 834–840.

[32] B. Xia, J. Fu, H. Zhu, Z. Song, Y. Jiang, and H. Lipson, "A legged soft robot platform for dynamic locomotion," in *IEEE Intl. Conf. on Rob. & Auto. (ICRA)*, 2021, pp. 11 812–11 819.

[33] S. Gong, J. Wu, T. Zheng, W.-M. Zhang, and L. Shao, "Untethered cable-driven soft actuators for quadruped robots," in *IEEE Intl. Conf. on Mechatronics & Machine V. in P. (M2VIP)*, 2021, pp. 417–422.

[34] M. G. Atia, A. Mohammad, A. Gameros, D. Axinte, and I. Wright, "Reconfigurable soft robots by building blocks," *Advanced Science*, p. 2 203 217, 2022.

[35] Q. Ji, S. Fu, K. Tan, *et al.*, "Synthesizing the optimal gait of a quadruped robot with soft actuators using deep reinforcement learning," *Rob. & Computer-Integrated Manufact.*, 2022.

[36] M. Wu, X. Xu, Q. Zhao, *et al.*, "A fully 3d-printed tortoise-inspired soft robot with terrains-adaptive and amphibious landing capabilities," *Adv. Material Technologies*, p. 2 200 536, 2022.

[37] R. F. Shepherd, F. Ilievski, W. Choi, *et al.*, "Multigait soft robot," *Proceedings of the national academy of sciences*, vol. 108, no. 51, pp. 20 400–20 403, 2011.

[38] M. T. Tolley, R. F. Shepherd, B. Mosadegh, *et al.*, "A resilient, untethered soft robot," *Soft Robotics*, vol. 1, no. 3, pp. 213–223, 2014.

[39] A. A. M. Faudzi, M. R. M. Razif, G. Endo, H. Nabae, and K. Suzumori, "Soft-amphibious robot using thin and soft mckibben actuator," in *IEEE Intl. Conf. on Adv. Intel. Mech. (AIM)*, 2017.

[40] Y. Tang, Y. Chi, J. Sun, *et al.*, "Leveraging elastic instabilities for amplified performance: Spine-inspired high-speed and high-force soft robots," *Science advances*, vol. 6, no. 19, 2020.

[41] L. Schiller, A. Seibel, and J. Schlattmann, "Toward a gecko-inspired, climbing soft robot," *Frontiers in neurorobotics*, vol. 13, p. 106, 2019.

[42] L. Schiller, A. Seibel, and J. Schlattmann, "A gait pattern generator for closed-loop position control of a soft walking robot," *Front. in Rob. & AI*, vol. 7, p. 87, 2020.

[43] N. Zhu, H. Zang, B. Liao, *et al.*, "A quadruped soft robot for climbing parallel rods," *Robotica*, vol. 39, no. 4, pp. 686–698, 2021.

[44] L. Schiller and A. Seibel, "Remote control of a soft walking robot," in *IEEE Intl. Conf. on Soft Rob. (RoboSoft)*, 2021, pp. 535–538.

[45] D. D. Arachchige, D. M. Perera, S. Mallikarachchi, I. Kanj, and I. S. Godage, "Soft steps: Exploring quadrupedal locomotion with modular soft robots," *IEEE Access*, 2023.

[46] A. A. Stokes, R. F. Shepherd, S. A. Morin, F. Ilievski, and G. M. Whitesides, "A hybrid combining hard and soft robots," *Soft Robotics*, vol. 1, no. 1, pp. 70–74, 2014.

[47] A. Poungrat and T. Maneewarn, "A starfish inspired robot with multi-directional tube feet locomotion," in *IEEE Intl. Conf. on Robo. & Biomim.(ROBIO)*, 2017, pp. 712–717.

[48] D. Drotman, S. Jadhav, M. Karimi, P. de Zonia, and M. T. Tolley, "3d printed soft actuators for a legged robot capable of navigating unstructured terrain," in *IEEE Intl. Conf. on Rob. & Auto. (ICRA)*, 2017, pp. 5532–5538.

[49] D. Drotman, M. Ishida, S. Jadhav, and M. T. Tolley, "Application-driven design of soft, 3-d printed, pneumatic actuators with bellows," *IEEE/ASME Tran. on Mechatronics*, 2018.

[50] D. Drotman, S. Jadhav, D. Sharp, C. Chan, and M. T. Tolley, "Electronics-free pneumatic circuits for controlling soft-legged robots," *Science Robotics*, vol. 6, no. 51, 2021.

[51] M. Feng, D. Yang, C. Majidi, and G. Gu, "High-speed and low-energy actuation for pneumatic soft robots with internal exhaust air recirculation," *Authorea Preprints*, 2022.

[52] Y. Li, T. Ren, Y. Li, Q. Liu, and Y. Chen, "Untethered-bioinspired quadrupedal robot based on double-chamber pre-charged pneumatic soft actuators with highly flexible trunk," *Soft Robotics*, vol. 8, no. 1, pp. 97–108, 2021.

[53] S. Li, S. A. Awale, K. E. Bacher, *et al.*, "Scaling up soft robotics: A meter-scale, modular, and reconfigurable soft robotic system," *Soft Robotics*, vol. 9, no. 2, pp. 324–336, 2022.

[54] L. Sun, J. Wan, and T. Du, "Fully 3d-printed tortoise-like soft mobile robot with muti-scenarios adaptability," *Bioins.& Biomimetics*, 2023.

[55] P. Kaarthik, F. L. Sanchez, J. Avtges, and R. L. Truby, "Motorized, untethered soft robots via 3d printed auxetics," *Soft Matter*, vol. 18, no. 43, pp. 8229–8237, 2022.

[56] J. Ketchum, S. Schiffer, M. Sun, P. Kaarthik, R. L. Truby, and T. D. Murphey, "Automated gait generation for walking, soft robotic quadrupeds," in *IEEE/RSJ Intl. Conf. on Intelligent Robots and Systems (IROS)*, 2023, pp. 10 245–10 251.

[57] Y. Yang, S. Yan, M. Dai, Y. Xie, and J. Liu, "A quadrupedal soft robot based on kresling origami actuators," in *Chinese Intelligent Automation Conference*, Springer, 2023, pp. 417–426.

[58] Y. Ansari, A. L. Shoushtari, V. Cacucciolo, M. Cianchetti, and C. Laschi, "Dynamic walking with a soft limb robot," in *Conference on Biomimetic and Biohybrid Systems*, Springer, 2015.

[59] Z. Xiong, Y. Su, and H. Lipson, "Fast untethered soft robotic crawler with elastic instability," in *IEEE Intl. Conf. on Rob. & Auto. (ICRA)*, 2023, pp. 2606–2612.

[60] A. Yin, H.-C. Lin, J. Thelen, B. Mahner, and T. Ranzani, "Combining locomotion and grasping functionalities in soft robots," *Adv, Intel. Sys.*, vol. 1, no. 8, p. 1 900 089, 2019.

[61] C. Majidi, R. F. Shepherd, R. K. Kramer, G. M. Whitesides, and R. J. Wood, "Influence of surface traction on soft robot undulation," *The Intl. Journal of Rob. Research*, 2013.

[62] P. Wharton, T. L. You, G. P. Jenkinson, *et al.*, "Tetraflex: A multigait soft robot for object transportation in confined environments," *IEEE Robotics and Automation Letters*, 2023.

[63] M. Ishida, J. A. Sandoval, S. Lee, S. Huen, and M. T. Tolley, "Locomotion via active suction in a sea star-inspired soft robot," *IEEE Rob. & Auto. Letters*, pp. 10 304–10 311, 2022.

[64] N. N. Goldberg, X. Huang, C. Majidi, *et al.*, "On planar discrete elastic rod models for the locomotion of soft robots," *Soft robotics*, vol. 6, no. 5, pp. 595–610, 2019.

[65] Z. Liu, Z. Lu, and K. Karydis, "Sorx: A soft pneumatic hexapedal robot to traverse rough, steep, and unstable terrain," in *IEEE Intl. Conf. on Rob. & Auto. (ICRA)*, 2020, pp. 420–426.

[66] Z. Liu and K. Karydis, "Position control and variable-height trajectory tracking of a soft pneumatic legged robot," in *IEEE/RSJ Intl. Conf. on Intel. Rob. & Sys. (IROS)*, 2021.

[67] Q. Shao, X. Dong, Z. Lin, *et al.*, "Untethered robotic millipede driven by low-pressure microfluidic actuators for multi-terrain exploration," *IEEE Rob. & Auto. Letters*, pp. 12 142–12 149, 2022.

[68] Q. Ji, S. Fu, L. Feng, G. Andrikopoulos, X. V. Wang, and L. Wang, "Omnidirectional walking of a quadruped robot enabled by compressible tendon-driven soft actuators," in *IEEE/RSJ Intl. Conf. on Intelligent Rob. & Sys. (IROS)*, 2022, pp. 11 015–11 022.

[69] S. Mao, E. Dong, S. Zhang, M. Xu, and J. Yang, "A new soft bionic starfish robot with multi-gaits," in *IEEE/ASME Intl. Conf. on Advanced Intelligent Mechatronics*, 2013, pp. 1312–1317.

[70] S. Mao, E. Dong, H. Jin, *et al.*, "Gait study and pattern generation of a starfish-like soft robot with flexible rays actuated by smas," *Journal of Bionic Eng.*, vol. 11, no. 3, pp. 400–411, 2014.

[71] H. Jin, E. Dong, M. Xu, C. Liu, G. Alici, and Y. Jie, "Soft and smart modular structures actuated by shape memory alloy (sma) wires as tentacles of soft robots," *Smart Materials & Structures*, vol. 25, no. 8, 2016.

[72] H. Jin, E. Dong, G. Alici, *et al.*, "A starfish robot based on soft and smart modular structure (sms) actuated by sma wires," *Bioins. & biom.*, vol. 11, no. 5, 2016.

[73] W. L. Scott and D. A. Paley, "Geometric gait design for a starfish-inspired robot using a planar discrete elastic rod model," *Adv, Intel. Sys.*, vol. 2, no. 6, p. 1 900 186, 2020.

[74] H. Lee, Y. Jang, J. K. Choe, *et al.*, "3d-printed programmable tensegrity for soft robotics," *Science Robotics*, vol. 5, no. 45, eaay9024, 2020.

[75] K. Suzumori, "Elastic materials producing compliant robots," *Robots and Autonomous Systems*, vol. 18, no. 1-2, pp. 135–140, 1996.

[76] K. Suzumori, F. Kondo, and H. Tanaka, "Applications of flexible microactuators to walking robots," in *Video proc. of IEEE Intl. Conf. on Rob. & Auto.*, 2003.

[77] J. Waynelovich, T. Frey, A. Baljon, and P. Salamon, "Versatile and dexterous soft robotic leg system for untethered operations," *Soft Robotics*, vol. 3, no. 2, pp. 64–70, 2016.

[78] J. M. Florez, B. Shih, Y. Bai, and J. K. Paik, "Soft pneumatic actuators for legged locomotion," in *IEEE Intl. Conf. on Robo. & Biomim.(ROBIO)*, 2014, pp. 27–34.

[79] M. Calisti, A. Arienti, F. Renda, *et al.*, "Design and development of a soft robot with crawling and grasping capabilities," in *IEEE Intl. Conf. on Rob. & Auto. (ICRA)*, 2012, pp. 4950–4955.

[80] K. HASE, T. Akagi, S. Dohta, T. Shinohara, W. Kobayashi, and S. Shimooka, "Development of six-legged mobile robot using tetrahedral shaped pneumatic soft actuators," *JFPS Intl. Journal of Fluid Power Sys.*, vol. 15, no. 1, pp. 33–39, 2022.

[81] J. Zou, Y. Lin, C. Ji, and H. Yang, "A reconfigurable omnidirectional soft robot based on caterpillar locomotion," *Soft robotics*, vol. 5, no. 2, pp. 164–174, 2018.

[82] H. Lu, M. Zhang, Y. Yang, *et al.*, "A bioinspired multilegged soft millirobot that functions in both dry and wet conditions," *Nature communications*, vol. 9, no. 1, p. 3944, 2018.

[83] H. Gu, Q. Boehler, H. Cui, *et al.*, "Magnetic cilia carpets with programmable metachronal waves," *Nature communications*, vol. 11, no. 1, p. 2637, 2020.

[84] H. Lu, Y. Hong, Y. Yang, Z. Yang, and Y. Shen, "Battery-less soft millirobot that can move, sense, and communicate remotely by coupling the magnetic and piezoelectric effects," *Advanced Science*, vol. 7, no. 13, 2020.

[85] X. Yang, R. Tan, H. Lu, and Y. Shen, "Starfish inspired milli soft robot with omnidirectional adaptive locomotion ability," *IEEE Rob. & Auto. Letters*, vol. 6, no. 2, pp. 3325–3332, 2021.

[86] D. Sun, J. Zhang, Q. Fang, *et al.*, "Analysis and control for a bioinspired multi-legged soft robot," *Biomimetic Intel. & Robotics*, vol. 2, no. 1, p. 100 030, 2022.

[87] M. Xie, Y. Feng, H. Nabae, and K. Suzumori, "A soft crawling robot that can self-repair material removal and deep lengthwise cuts, actuated by thin mckibben muscles," *IEEE Robotics and Automation Letters*, 2024.

[88] B. A. Trimmer, H.-T. Lin, A. Baryshyan, G. G. Leisk, and D. L. Kaplan, "Towards a biomorphic soft robot: Design constraints and solutions," in *IEEE RAS & EMBS Intl. Conf. on Biomedical Robot. & Biomechatronics (BioRob)*, 2012, pp. 599–605.

[89] S. Rozen-Levy, W. Messner, and B. A. Trimmer, "The design and development of branch bot: A branch-crawling, caterpillar-inspired, soft robot," *The Intl. Journal of Rob. Research*, vol. 40, no. 1, pp. 24–36, 2021.

[90] X. Sheng, H. Xu, N. Zhang, N. Ding, X. Zhu, and G. Gu, "Multi-material 3d printing of caterpillar-inspired soft crawling robots with the pneumatically bellow-type body and anisotropic friction feet," *Sensors & Actuators A: Physical*, vol. 316, 2020.

[91] T. Umedachi, M. Shimizu, and Y. Kawahara, "Caterpillar-inspired crawling robot using both compression and bending deformations," *IEEE Robo. & Auto. Letters*, pp. 670–676, 2019.

[92] C. Mc Caffrey, T. Umedachi, W. Jiang, *et al.*, "Continuum robotic caterpillar with wirelessly powered shape memory alloy actuators," *Soft robotics*, vol. 7, no. 6, pp. 700–710, 2020.

[93] D. K. Patel, X. Huang, Y. Luo, *et al.*, "Highly dynamic bistable soft actuator for reconfigurable multimodal soft robots," *Adv. Material Technologies*, vol. 8, no. 2, p. 2 201 259, 2023.

[94] E.-F. M. Henke, S. Schlatter, and I. A. Anderson, "Soft dielectric elastomer oscillators driving bioinspired robots," *Soft robotics*, vol. 4, no. 4, pp. 353–366, 2017.

[95] B. Grossi, H. Palza, J. Zagal, C. Falcón, and G. During, "Metarpillar: Soft robotic locomotion based on buckling-driven elastomeric metamaterials," *Materials & Design*, p. 110 285, 2021.

[96] Y. Guo, J. Guo, L. Liu, Y. Liu, and J. Leng, "Bioinspired multimodal soft robot driven by a single dielectric elastomer actuator and two flexible electroadhesive feet," *Extreme Mechanics Letters*, vol. 53, p. 101 720, 2022.

[97] S. Wu, Y. Hong, Y. Zhao, J. Yin, and Y. Zhu, "Caterpillar-inspired soft crawling robot with distributed programmable thermal actuation," *Science Advances*, vol. 9, no. 12, eadf8014, 2023.

[98] A. A. Calderón, J. C. Ugalde, J. C. Zagal, and N. O. Pérez-Arancibia, "Design, fabrication and control of a multi-material-multi-actuator soft robot inspired by burrowing worms," in *IEEE Intl. Conf. on robotics & biomim. (ROBIO)*, 2016, pp. 31–38.

[99] N. Cheng, G. Ishigami, S. Hawthorne, *et al.*, "Design and analysis of a soft mobile robot composed of multiple thermally activated joints driven by a single actuator," in *IEEE Intl. Conf. on Rob. & Auto. (ICRA)*, 2010, pp. 5207–5212.

[100] J. Cao, L. Qin, J. Liu, *et al.*, "Untethered soft robot capable of stable locomotion using soft electrostatic actuators," *Extreme Mechanics Letters*, vol. 21, pp. 9–16, 2018.

[101] T. Duggan, L. Horowitz, A. Ulug, E. Baker, and K. Petersen, "Inchworm-inspired locomotion in untethered soft robots," in *IEEE Intl. Conf. on Soft Rob. (RoboSoft)*, 2019, pp. 200–205.

[102] E. B. Joyee and Y. Pan, "A fully three-dimensional printed inchworm-inspired soft robot with magnetic actuation," *Soft robotics*, vol. 6, no. 3, pp. 333–345, 2019.

[103] T. Li, Z. Zou, G. Mao, *et al.*, "Agile and resilient insect-scale robot," *Soft Robotics*, vol. 6, no. 1, pp. 133–141, 2019.

[104] W. Wang, J.-Y. Lee, H. Rodrigue, S.-H. Song, W.-S. Chu, and S.-H. Ahn, "Locomotion of inchworm-inspired robot made of smart soft composite (ssc)," *Bioins. & biom.*, 2014.

[105] P. Wu, W. Jiangbei, and F. Yanqiong, "The structure, design, and closed-loop motion control of a differential drive soft robot," *Soft robotics*, vol. 5, no. 1, pp. 71–80, 2018.

[106] Z. Tang, J. Lu, Z. Wang, W. Chen, and H. Feng, "Design of a new air pressure perception multi-cavity pneumatic-driven earthworm-like soft robot," *Autonomous Robots*, 2020.

[107] J. W. Booth, D. Shah, J. C. Case, *et al.*, "Omniskins: Robotic skins that turn inanimate objects into multifunctional robots," *Science Robotics*, vol. 3, no. 22, 2018.

[108] T. Hu, X. Lu, and J. Liu, "Inchworm-like soft robot with multimodal locomotion using an acrylic stick-constrained dielectric elastomer actuator," *Adv, Intel. Sys.*, vol. 5, no. 2, p. 2 200 209, 2023.

[109] Y. Zhang, D. Yang, P. Yan, P. Zhou, J. Zou, and G. Gu, "Inchworm inspired multimodal soft robots with crawling, climbing, and transitioning locomotion," *IEEE Transactions on Robotics*, vol. 38, no. 3, 2021.

[110] P. Karipoth, A. Christou, A. Pullanchiyod, and R. Dahiya, "Bioinspired inchworm & earthworm like soft robots with intrinsic strain sensing," *Adv, Intel. Sys.*, vol. 4, no. 2, p. 2 100 092, 2022.

[111] L. Xu, R. J. Wagner, S. Liu, *et al.*, "Locomotion of an untethered, worm-inspired soft robot driven by a shape-memory alloy skeleton," *Scientific Reports*, vol. 12, no. 1, p. 12 392, 2022.

[112] Q. Xu and J. Liu, "Dynamic research on nonlinear locomotion of inchworm-inspired soft crawling robot," *Soft Robotics*, 2023.

[113] H. Dong, H. Yang, S. Ding, T. Li, and H. Yu, "Bioinspired amphibious origami robot with body sensing for multimodal locomotion," *Soft Robotics*, vol. 9, no. 6, pp. 1198–1209, 2022.

[114] Z. Xu, L. Hu, L. Xiao, H. Jiang, and Y. Zhou, "Modular soft robotic crawlers based on fluidic prestressed composite actuators," *Journal of Bionic Engineering*, pp. 1–13, 2024.

[115] S. Seok, C. D. Onal, R. Wood, D. Rus, and S. Kim, "Peristaltic locomotion with antagonistic actuators in soft robotics," in *IEEE Intl. Conf. on Rob. & Auto. (ICRA)*, 2010, pp. 1228–1233.

[116] S. Seok, C. D. Onal, K.-J. Cho, R. J. Wood, D. Rus, and S. Kim, "Meshworm: A peristaltic soft robot with antagonistic nickel titanium coil actuators," *IEEE/ASME Transactions on Mechatronics*, vol. 18, no. 5, pp. 1485–1497, 2012.

[117] R. Das, S. P. M. Babu, S. Palagi, and B. Mazzolai, "Soft robotic locomotion by peristaltic waves in granular media," in *IEEE Intl. Conf. on Soft Rob. (RoboSoft)*, 2020, pp. 223–228.

[118] R. Das, S. P. M. Babu, F. Visentin, S. Palagi, and B. Mazzolai, "An earthworm-like modular soft robot for locomotion in multi-terrain environments," *Scientific Reports*, p. 1571, 2023.

[119] B. Liu, Y. Ozkan-Aydin, D. I. Goldman, and F. L. Hammond, "Kirigami skin improves soft earthworm robot anchoring and locomotion under cohesive soil," in *IEEE Intl. Conf. on Soft Robotics (RoboSoft)*, 2019, pp. 828–833.

[120] T. Manwell, B. Guo, J. Back, and H. Liu, "Bioinspired setae for soft worm robot locomotion," in *IEEE Intl. Conf. on Soft Rob. (Robosoft)*, 2018, pp. 54–59.

[121] A. Menciassi, S. Gorini, G. Pernorio, L. Weiting, F. Valvo, and P. Dario, "Design, fabrication and performances of a biomimetic robotic earthworm," in *IEEE Intl. Conf. on Robotics and Biomimetics*, 2004, pp. 274–278.

[122] Z. G. Joey, A. A. Calderón, and N. O. Pérez-Arancibia, "An earthworm-inspired soft crawling robot controlled by friction," in *IEEE Intl. Conf. on Robo. & Biomim.(ROBIO)*, 2017.

[123] M. P. Nemitz, P. Mihaylov, T. W. Barraclough, D. Ross, and A. A. Stokes, "Using voice coils to actuate modular soft robots: Wormbot, an example," *Soft robotics*, pp. 198–204, 2016.

[124] C. D. Onal, R. J. Wood, and D. Rus, "An origami-inspired approach to worm robots," *IEEE Transactions on Mechatronics*, vol. 18, no. 2, pp. 430–438, 2012.

[125] Y. O. Aydin, J. L. Molnar, D. I. Goldman, and F. L. Hammond, "Design of a soft robophysical earthworm model," in *IEEE Intl. Conf. on Soft Rob. (RoboSoft)*, 2018, pp. 83–87.

[126] Z. Tang, J. Lu, Z. Wang, G. Ma, W. Chen, and H. Feng, "Development of a new multi-cavity pneumatic-driven earthworm-like soft robot," *Robotica*, vol. 38, no. 12, pp. 2290–2304, 2020.

[127] T. Du, L. Sun, and J. Wan, "A worm-like crawling soft robot with pneumatic actuators based on selective laser sintering of tpu powder," *Biomimetics*, vol. 7, no. 4, p. 205, 2022.

[128] M. H. Rezaei, M. R. Kolani, S. A. M. Jalali, and M. Zareinejad, "Earthworm-inspired in-pipe soft robot (esr): Design, modeling, and implementation," in *RSI Intl. Conf. on Robotics and Mechatronics (ICRoM)*, 2022, pp. 125–131.

[129] T. Umedachi, V. Vikas, and B. A. Trimmer, "Highly deformable 3-d printed soft robot generating inching and crawling locomotions with variable friction legs," in *IEEE/RSJ Intl. Conf. on Intel. Rob. & Sys. (IROS)*, 2013, pp. 4590–4595.

[130] T. Umedachi, V. Vikas, and B. Trimmer, "Softworms: The design and control of non-pneumatic, 3d-printed, deformable robots," *Bioins. & biom.*, vol. 11, no. 2, p. 025 001, 2016.

[131] W. Huang, Z. Xu, J. Xiao, W. Hu, H. Huang, and F. Zhou, "Multimodal soft robot for complex environments using bionic omnidirectional bending actuator," *IEEE Access*, 2020.

[132] K. Jung, J. C. Koo, Y. K. Lee, H. R. Choi, *et al.*, "Artificial annelid robot driven by soft actuators," *Bioins. & biom.*, vol. 2, no. 2, S42, 2007.

[133] D. E. Martinez-Sanchez, X. Y. Sandoval-Castro, N. Cruz-Santos, E. Castillo-Castaneda, M. F. Ruiz-Torres, and M. A. Laribi, "Soft robot for inspection tasks inspired on annelids to obtain peristaltic locomotion," *Machines*, vol. 11, no. 8, p. 779, 2023.

[134] H. Yuk, D. Kim, H. Lee, S. Jo, and J. H. Shin, "Shape memory alloy-based small crawling robots inspired by c. elegans," *Bioins. & biom.*, vol. 6, no. 4, p. 046 002, 2011.

[135] A. Sabbadini, M. A. Atalla, and M. Wiertlewski, "Simple and fast locomotion of vibrating asymmetric soft robots," *Soft Robotics*, 2023.

[136] S. Lee, I. Her, W. Jung, and Y. Hwang, "Snakeskin-inspired 3d printable soft robot composed of multi-modular vacuum-powered actuators," in *Actuators*, MDPI, vol. 12, 2023, p. 62.

[137] A. Rafsanjani, Y. Zhang, B. Liu, S. M. Rubinstein, and K. Bertoldi, "Kirigami skins make a simple soft actuator crawl," *Science Robotics*, vol. 3, no. 15, 2018.

[138] A. Rafsanjani, L. Jin, B. Deng, and K. Bertoldi, "Propagation of pop ups in kirigami shells," *Proceedings of the National Academy of Sciences*, vol. 116, no. 17, pp. 8200–8205, 2019.

[139] G. Gu, J. Zou, R. Zhao, X. Zhao, and X. Zhu, "Soft wall-climbing robots," *Science Robotics*, vol. 3, no. 25, eaat2874, 2018.

[140] M. Malley, M. Rubenstein, and R. Nagpal, "Flippy: A soft, autonomous climber with simple sensing and control," in *IEEE/RSJ Intl. Conf. on Intel. Rob. & Sys. (IROS)*, 2017.

[141] L. Qin, X. Liang, H. Huang, C. K. Chui, R. C.-H. Yeow, and J. Zhu, "A versatile soft crawling robot with rapid locomotion," *Soft robotics*, vol. 6, no. 4, pp. 455–467, 2019.

[142] W. Zhang, W. Zhang, and Z. Sun, "A reconfigurable soft wall-climbing robot actuated by electromagnet," *Intl. Journal of Adv. Rob. Sys.*, vol. 18, no. 2, p. 1729, 2021.

[143] G. Chen, T. Lin, G. Lodewijks, and A. Ji, "Design of an active flexible spine for wall climbing robot using pneumatic soft actuators," *Journal of Bionic Eng.*, vol. 20, no. 2, pp. 530–542, 2023.

[144] W. Zhang, W. Zhang, and Z. Sun, "A modular soft wall-climbing robot using electromagnetic actuator," in *IEEE Annual Intl. Conf. on CYBER Tech. in Auto., Control, & Intel. Sys. (CYBER)*, 2019, pp. 730–733.

[145] L. P. Pratap, P. M. Shailendrasingh, A. Anand, and V. Tharun, "Wall climbing robot using soft robotics," in *IEEE Intl. Conf. on Power, Control, Signals & Inst. Eng. (ICPCSI)*, 2017.

[146] Y. Tang, Q. Zhang, G. Lin, and J. Yin, "Switchable adhesion actuator for amphibious climbing soft robot," *Soft Robotics*, vol. 5, no. 5, pp. 592–600, 2018.

[147] Y. Zhang, L. Ge, J. Zou, H. Xu, and G. Gu, "A multimodal soft crawling-climbing robot with the controllable horizontal plane to slope transition," in *IEEE/RSJ Intl. Conf. on Intel. Robot and Systems (IROS)*, 2019, pp. 3343–3348.

[148] Y. Jiang, D. Chen, H. Zhang, F. Giraud, and J. Paik, "Multimodal pipe-climbing robot with origami clutches and soft modular legs," *Bioins. & biom.*, vol. 15, no. 2, p. 026 002, 2020.

[149] Y. Sakuhara, H. Shimizu, and K. Ito, "Climbing soft robot inspired by octopus," in *IEEE Intl. Conf. on Intel. Sys. (IS)*, 2020, pp. 463–468.

[150] B. Zhang, Y. Fan, P. Yang, T. Cao, and H. Liao, "Worm-like soft robot for complicated tubular environments," *Soft robotics*, vol. 6, no. 3, pp. 399–413, 2019.

[151] R. Xie, M. Su, Y. Zhang, M. Li, H. Zhu, and Y. Guan, "Pisrob: A pneumatic soft robot for locomoting like an inchworm," in *IEEE Intl. Conf. on Rob. & Auto. (ICRA)*, 2018.

[152] X. Liu, M. Song, Y. Fang, Y. Zhao, and C. Cao, "Worm-inspired soft robots enable adaptable pipeline and tunnel inspection," *Adv, Intel. Sys.*, vol. 4, no. 1, p. 2 100 128, 2022.

[153] Y. Lin, Y.-X. Xu, and J.-Y. Juang, "Single-actuator soft robot for in-pipe crawling," *Soft Robotics*, vol. 10, no. 1, pp. 174–186, 2023.

[154] J. Wan, L. Sun, T. Du, *et al.*, "A bionic pipe-crawling soft robot based on the pneumatic silicone actuator," in *Journal of Physics: Conference Series*, IOP Publishing, vol. 2355, 2022, p. 012 003.

[155] W. Yu, X. Li, D. Chen, *et al.*, "A minimally designed soft crawling robot for robust locomotion in unstructured pipes," *Bioins. & biom.*, vol. 17, no. 5, p. 056 001, 2022.

[156] Z. Zhang, X. Wang, S. Wang, D. Meng, and B. Liang, "Design and modeling of a parallel-pipe-crawling pneumatic soft robot," *IEEE access*, vol. 7, pp. 134 301–134 317, 2019.

[157] G. Singh, S. Patiballa, X. Zhang, and G. Krishnan, "A pipe-climbing soft robot," in *IEEE Intl. Conf. on Rob. & Auto. (ICRA)*, 2019, pp. 8450–8456.

[158] F. Xu, J. Quansheng, Y. Lu, and G. Jiang, "Modelling of a soft multi-chambered climbing robot and experiments," *Smart Materials & Struct.*, vol. 30, no. 3, p. 035 009, 2021.

[159] M. S. Verma, A. Ainla, D. Yang, D. Harburg, and G. M. Whitesides, "A soft tube-climbing robot," *Soft robotics*, vol. 5, no. 2, pp. 133–137, 2018.

[160] A. Kanada, F. Giardina, T. Howison, T. Mashimo, and F. Iida, "Reachability improvement of a climbing robot based on large deformations induced by tri-tube soft actuators," *Soft robotics*, vol. 6, no. 4, pp. 483–494, 2019.

[161] Q. Hu, E. Dong, and D. Sun, "Soft modular climbing robots," *IEEE Trans. on Robotics*, 2022.

[162] Q. Hu, E. Dong, G. Cheng, H. Jin, J. Yang, and D. Sun, "Inchworm-inspired soft climbing robot using microspine arrays," in *IEEE/RSJ Intl. Conf. on Intel. Rob. & Sys. (IROS)*, 2019.

[163] L. Li, P. Ma, Y. Jiang, *et al.*, "Research on a tubular climbing robot induced by tri-tube soft actuators," in *IEEE Intl. Conf. on Robo. & Biomim.(ROBIO)*, 2019, pp. 2189–2194.

[164] N. Mendoza and M. Haghshenas-Jaryani, "Combined soft grasping and crawling locomotor robot for exterior navigation of tubular structures," *Machines*, vol. 12, no. 3, p. 157, 2024.

[165] A. D. Horchler, A. Kandhari, K. A. Daltorio, *et al.*, "Peristaltic locomotion of a modular mesh-based worm robot: Precision, compliance, and friction," *Soft Robotics*, pp. 135–145, 2015.

[166] L. Li, C. Zhao, S. He, Q. Qi, S. Kang, and S. Ma, "Enhancing undulation of soft robots in granular media: A numerical and experimental study on the effect of anisotropic scales," *Biomimetic Intelligence and Robotics*, p. 100 158, 2024.

[167] D. D. Arachchige, Y. Chen, and I. S. Godage, "Soft robotic snake locomotion: Modeling and experimental assessment," in *IEEE Intl. Conf. on Auto. Sci. & Eng. (CASE)*, 2021, pp. 805–810.

[168] T. D. Ta, T. Umedachi, and Y. Kawahara, "Design of frictional 2d-anisotropy surface for wriggle locomotion of printable soft-bodied robots," in *IEEE Intl. Conf. on Rob. & Auto. (ICRA)*, 2018.

[169] W. Zhao, J. Wang, and Y. Fei, "A multigait continuous flexible snake robot for locomotion in complex terrain," *IEEE/ASME Transactions on Mechatronics*, pp. 3751–3761, 2021.

[170] C. Branyan, C. Fleming, J. Remaley, *et al.*, "Soft snake robots: Mechanical design and geometric gait implementation," in *IEEE Intl. Conf. on Robo. & Biomim.(ROBIO)*, 2017, pp. 282–289.

[171] Y. Cao, Y. Liu, Y. Chen, L. Zhu, Y. Yan, and X. Chen, "A novel slithering locomotion mechanism for a snake-like soft robot," *Jnl. of the Mechanics & Physics of Solids*, 2017.

[172] C. Branyan, R. L. Hatton, and Y. Mengüç, "Snake-inspired kirigami skin for lateral undulation of a soft snake robot," *IEEE Rob. & Auto. Letters*, vol. 5, no. 2, pp. 1728–1733, 2020.

[173] X. Qi, H. Shi, T. Pinto, and X. Tan, "A novel pneumatic soft snake robot using traveling-wave locomotion in constrained environments," *IEEE Robo. & Auto. Letters*, pp. 1610–1617, 2020.

[174] C. Branyan, A. Rafsanjani, K. Bertoldi, R. L. Hatton, and Y. Mengüç, "Curvilinear kirigami skins let soft bending actuators slither faster," *Front. in Rob. & AI*, vol. 9, 2022.

[175] X. Qi, T. Gao, and X. Tan, "Bioinspired 3d-printed snakeskins enable effective serpentine locomotion of a soft robotic snake," *Soft Robotics*, 2022.

[176] C. Branyan and Y. Menğüç, "Soft snake robots: Investigating the effects of gait parameters on locomotion in complex terrains," in *IEEE/RSJ Intl. Conf. on Intel. Rob. & Sys. (IROS)*, 2018.

[177] M. Lopez and M. Haghshenas-Jaryani, "A muscle-driven mechanism for locomotion of snake-robots," *Automation, MDPI*, vol. 3, no. 1, pp. 1–26, 2022.

[178] M. Haghshenas-Jaryani, "Dynamics and computed-muscle-force control of a planar muscle-driven snake robot," in *Actuators, MDPI*, vol. 11, 2022, p. 194.

[179] Y. B. Kim, S. Yang, and D. S. Kim, "Sidewinder-inspired self-adjusting, lateral-rolling soft robots for autonomous terrain exploration," *Advanced Science*, p. 2 308 350, 2024.

[180] D. D. Arachchige, D. M. Perera, S. Mallikarachchi, I. Kanj, Y. Chen, and I. S. Godage, "Wheelless soft robotic snake locomotion: Study on sidewinding and helical rolling gaits," in *IEEE Intl. Conf. on Soft Rob. (RoboSoft)*, 2023, pp. 1–6.

[181] F. Rozaidi, E. Waters, O. Dawes, J. Yang, J. R. David, and R. L. Hatton, "Hissbot: Sidewinding with a soft snake robot," in *IEEE Intl. Conf. on Soft Rob. (RoboSoft)*, 2023, pp. 1–7.

[182] X. Zhou, Y. Zhang, Z. Qiu, Z. Shan, S. Cai, and G. Bao, "Locomotion control of a rigid-soft coupled snake robot in multiple environments," *Biomimetic Intelligence and Robotics*, 2024.

[183] D. D. Arachchige, S. Mallikarachchi, I. Kanj, *et al.*, "Dynamic modeling and validation of soft robotic snake locomotion," in *IEEE Intl. Conf. on Control, Auto. & Robotics (ICCAR)*, 2023.

[184] H.-T. Lin, G. G. Leisk, and B. Trimmer, "Goqbot: A caterpillar-inspired soft-bodied rolling robot," *Bioins. & biom.*, vol. 6, no. 2, p. 026 007, 2011.

[185] W.-B. Li, W.-M. Zhang, H.-X. Zou, Z.-K. Peng, and G. Meng, "A fast rolling soft robot driven by dielectric elastomer," *IEEE/ASME Transactions on Mechatronics*, pp. 1630–1640, 2018.

[186] W.-B. Li, W.-M. Zhang, Q.-H. Gao, *et al.*, "Electrically activated soft robots: Speed up by rolling," *Soft Robotics*, vol. 8, no. 5, pp. 611–624, 2021.

[187] N. S. Usevitch, Z. M. Hammond, M. Schwager, A. M. Okamura, E. W. Hawkes, and S. Follmer, "An untethered isoperimetric soft robot," *Science Robotics*, vol. 5, no. 40, 2020.

[188] X. Wang, Z. oBo, C. Guo, J. Wu, Y. Liu, and W. Sun, "A magnetic soft robot with rolling and grasping capabilities," *Proceedings of the Institution of Mech. Engineers, Part C: Journal of Mechanical Eng. Science*, 2022.

[189] J. Wang, Y. Fei, and Z. Liu, "Fifobots: Foldable soft robots for flipping locomotion," *Soft Robotics*, vol. 6, no. 4, pp. 532–559, 2019.

[190] J. Wang and Y. Fei, "Design and modelling of flex-rigid soft robot for flipping locomotion," *Journal of Intell. & Robot Sys.*, pp. 379–388, 2019.

[191] R. Chen, X. Zhu, Z. Yuan, H. Pu, J. Luo, and Y. Sun, "A bioinspired single actuator-driven soft robot capable of multi-strategy locomotion," *IEEE Transactions on Robotics*, 2024.

[192] Z. Zheng, P. Kumar, Y. Chen, *et al.*, "Scalable simulation and demonstration of jumping piezoelectric 2-d soft robots," in *IEEE Intl. Conf. on Rob. & Auto. (ICRA)*, 2022, pp. 5199–5204.

[193] A. Fernandes Minori, S. Jadhav, H. Chen, S. Fong, and M. T. Tolley, "Power amplification for jumping soft robots actuated by artificial muscles," *Frontiers in Robotics and AI*, vol. 9, p. 844 282, 2022.

[194] J. Sun, B. Tighe, and J. Zhao, "Tuning the energy landscape of soft robots for fast and strong motion," in *IEEE Intl. Conf. on Robotics and Automation (ICRA)*, 2020, pp. 10 082–10 088.

[195] R. Chen, Z. Yuan, J. Guo, *et al.*, "Legless soft robots capable of rapid, continuous, and steered jumping," *Nature Communications*, vol. 12, no. 1, p. 7028, 2021.

[196] M. Loepfe, C. M. Schumacher, U. B. Lustenberger, and W. J. Stark, "An untethered, jumping roly-poly soft robot driven by combustion," *Soft Robotics*, vol. 2, no. 1, pp. 33–41, 2015.

[197] B. Liao, H. Zang, M. Chen, *et al.*, "Soft rod-climbing robot inspired by winding locomotion of snake," *Soft robotics*, vol. 7, no. 4, pp. 500–511, 2020.

[198] J. Walker, T. Zidek, C. Harbel, *et al.*, "Soft robotics: A review of recent developments of pneumatic soft actuators," in *Actuators, MDPI*, vol. 9, 2020, p. 3.

[199] M. T. Tolley, F. ShepherdRobert, C. GallowayKevin, J. WoodRobert, M. WhitesidesGeorge, *et al.*, "A resilient, untethered soft robot," *Soft robotics*, 2014.

[200] D. D. Arachchige, D. M. Perera, S. Mallikarachchi, I. Kanj, and I. S. Godage, "Efficient trotting of soft quadrupeds," *IEEE Transactions on Automation Science & Eng.*, 2024, [In revision].

[201] Z. Xu, L. Hu, and Y. Zhou, "Pneumatic soft robotic crawler integrated with a precurved actuator enables fast locomotion," in *IEEE Intl. Conf. on Robo. & Biomim.(ROBIO)*, 2022, pp. 507–512.

[202] H. Kim, S. Cho, D. Kam, *et al.*, "Tendon-driven crawling robot with programmable anisotropic friction by adjusting out-of-plane curvature," *Machines*, vol. 11, no. 7, 2023.

[203] Y. Hao, S. Zhang, B. Fang, F. Sun, H. Liu, and H. Li, "A review of smart materials for the boost of soft actuators, soft sensors, and robotics applications," *Chinese Journal of Mechanical Eng.*, vol. 35, no. 1, pp. 1–16, 2022.

[204] J.-H. Lee, Y. S. Chung, and H. Rodrigue, "Long shape memory alloy tendon-based soft robotic actuators and implementation as a soft gripper," *Scientific reports*, vol. 9, no. 1, pp. 1–12, 2019.

[205] J. Hwang and W. D. Wang, "Shape memory alloy-based soft amphibious robot capable of seal-inspired locomotion," *Adv. Material Technologies*, vol. 7, no. 6, p. 2 101 153, 2022.

[206] Y. Guo, L. Liu, Y. Liu, and J. Leng, "Review of dielectric elastomer actuators and their applications in soft robots," *Adv, Intel. Sys.*, vol. 3, no. 10, p. 2 000 282, 2021.

[207] J. Guo, C. Xiang, A. Conn, and J. Rossiter, "All-soft skin-like structures for robotic locomotion and transportation," *Soft robotics*, vol. 7, no. 3, pp. 309–320, 2020.

[208] H. Wang, Z. Zhu, H. Jin, R. Wei, L. Bi, and W. Zhang, "Magnetic soft robots: Design, actuation, and function," *Journal of Alloys and Compounds*, p. 166 219, 2022.

[209] Y. Lee, F. Koehler, T. Dillon, *et al.*, "Magnetically actuated fiber-based soft robots," *Advanced Materials*, p. 2 301 916, 2023.

[210] N. Bira, P. Dhagat, and J. R. Davidson, "A review of magnetic elastomers and their role in soft robotics," *Front. in Robo. & AI*, vol. 7, 2020.

[211] M. Eshaghi, M. Ghasemi, and K. Khorshidi, "Design, manufacturing and applications of small-scale magnetic soft robots," *Extreme Mechanics Letters*, vol. 44, p. 101 268, 2021.

[212] Z. Ren and M. Sitti, "Design and build of small-scale magnetic soft-bodied robots with multimodal locomotion," *Nature Protocols*, vol. 19, no. 2, pp. 441–486, 2024.

[213] R. Wang, J. Wang, Z. Zhu, and D. Wang, "Multimodal magnetic soft robots enabled by bistable kirigami patterns," *IEEE/ASME Transactions on Mechatronics*, 2024.

[214] E. B. Joyee, A. Szmelter, D. Eddington, and Y. Pan, "3d printed biomimetic soft robot with multimodal locomotion and multifunctionality," *Soft Robotics*, vol. 9, no. 1, pp. 1–13, 2022.

[215] Y. Ju, R. Hu, Y. Xie, *et al.*, "Reconfigurable magnetic soft robots with multimodal locomotion," *Nano Energy*, vol. 87, p. 106 169, 2021.

[216] Q. Ze, S. Wu, J. Nishikawa, *et al.*, "Soft robotic origami crawler," *Science advances*, 2022.

[217] F. Xu, K. Ma, T. Gong, Z. Jiang, and C. Hu, "Design and testing of a magnetic soft crawling robot with multimodal locomotion driven by three-dimensional magnetic fields," *IEEE Transac. on Instrumentation and Measurement*, 2024.

[218] R. F. Shepherd, A. A. Stokes, J. Freake, *et al.*, "Using explosions to power a soft robot," *Angewandte Chemie International Edition*, vol. 52, no. 10, pp. 2892–2896, 2013.

[219] C. Armanini, F. Boyer, A. T. Mathew, C. Duriez, and F. Renda, "Soft robots modeling: A structured overview," *IEEE Transactions on Robotics*, 2023.

[220] I. S. Godage, D. T. Branson, E. Guglielmino, G. A. Medrano-Cerda, and D. G. Caldwell, "Dynamics for biomimetic continuum arms: A modal approach," in *IEEE Intl. Conf. on Robo. & Biomim.(ROBIO)*, 2011, pp. 104–109.

[221] I. S. Godage, G. A. Medrano-Cerda, D. T. Branson, E. Guglielmino, and D. G. Caldwell, "Dynamics for variable length multisection continuum arms," *The Intl. Journal of Robotics Research*, vol. 35, no. 6, pp. 695–722, 2016.

[222] R. J. Webster III and B. A. Jones, "Design and kinematic modeling of constant curvature continuum robots: A review," *The Intl. Journal of Robotics Research*, pp. 1661–1683, 2010.

[223] M. Bergou, M. Wardetzky, S. Robinson, B. Audoly, and E. Grinspun, "Discrete elastic rods," in *ACM SIGGRAPH 2008 papers*, 2008, pp. 1–12.

[224] C. Schaff, A. Sedal, S. Ni, and M. R. Walter, "Sim-to-real transfer of co-optimized soft robot crawlers," *Autonomous Robots*, pp. 1–17, 2023.

[225] D. Kim, S.-H. Kim, T. Kim, *et al.*, "Review of machine learning methods in soft robotics," *Plos one*, vol. 16, no. 2, e0246102, 2021.

[226] X. Wang, Y. Li, and K.-W. Kwok, "A survey for machine learning-based control of continuum robots," *Frontiers in Robotics and AI*, p. 280, 2021.

[227] M. Ishige, T. Umedachi, T. Taniguchi, and Y. Kawahara, "Exploring behaviors of caterpillar-like soft robots with a central pattern generator-based controller and reinforcement learning," *Soft robotics*, vol. 6, no. 5, pp. 579–594, 2019.

[228] P. S. Gonthina, M. B. Wooten, I. S. Godage, and I. D. Walker, "Mechanics for tendon actuated multisection continuum arms," in *IEEE Intl. Conf. on Rob. & Auto. (ICRA)*, 2020.

[229] J. Li, Z. Teng, J. Xiao, A. Kapadia, A. Bartow, and I. Walker, "Autonomous continuum grasping," in *IEEE/RSJ Intl. Conf. on Intel. Robots & Systems*, 2013, pp. 4569–4576.

[230] J. Li and J. Xiao, "Progressive planning of continuum grasping in cluttered space," *IEEE Transactions on Robotics*, vol. 32, no. 3, pp. 707–716, 2016.

[231] W. McMahan, B. A. Jones, and I. D. Walker, "Design and implementation of a multi-section continuum robot: Air-octor," in *IEEE/RSJ Intl. Conf. on Intel. Rob. & Sys. (IROS)*, 2005.

[232] B. H. Meng, D. D. Arachchige, J. Deng, I. S. Godage, and I. Kanj, "Anticipatory path planning for continuum arms in dynamic environments," in *IEEE Intl. Conf. on Robotics and Automation (ICRA)*, 2021, pp. 7815–7820.

[233] A. Amaya, D. D. Arachchige, J. Grey, and I. S. Godage, "Evaluation of human-robot teleoperation interfaces for soft robotic manipulators," in *IEEE Intl. Conf. on Robot & Human InteRobotics Commun. (RO-MAN)*, 2021, pp. 412–417.

[234] D. G. Caldwell, G. A. Medrano-Cerda, and M. Goodwin, "Control of pneumatic muscle actuators," *IEEE Control Systems Magazine*, vol. 15, no. 1, pp. 40–48, 1995.

[235] D. Trivedi, A. Lotfi, and C. D. Rahn, "Geometrically exact models for soft robotic manipulators," *IEEE Transactions on Robotics*, vol. 24, no. 4, pp. 773–780, 2008.

[236] J. Fras, J. Glówka, and K. Althoefer, "Instant soft robot: A simple recipe for quick and easy manufacturing," in *IEEE Intl. Conf. on Soft Robotics (RoboSoft)*, IEEE, 2020, pp. 482–488.

[237] I. S. Godage, G. A. Medrano-Cerda, D. T. Branson, E. Guglielmino, and D. G. Caldwell, "Modal kinematics for multisection continuum arms," *Bioins. & biom.*, vol. 10, no. 3, p. 035 002, 2015.

[238] K. C. Galloway, Y. Chen, E. Templeton, B. Rife, I. S. Godage, and E. J. Barth, "Fiber optic shape sensing for soft robotics," *Soft robotics*, vol. 6, no. 5, pp. 671–684, 2019.

[239] M. E. Giannaccini, C. Xiang, A. Atyabi, T. Theodoridis, S. Nefti-Meziani, and S. Davis, "Novel design of a soft lightweight pneumatic continuum robot arm with decoupled variable stiffness and positioning," *Soft robotics*, vol. 5, no. 1, pp. 54–70, 2018.

[240] M. E. Allaix, M. A. Bonino, S. Arolfo, M. Morino, Y. Mintz, and A. Arezzo, "Total mesorectal excision using the stiff-flop soft and flexible robotic arm in cadaver models," *Soft & Stiffness-controllable Robotics Solutions for Minimally Invasive Surgery: STIFF-FLOP Approach*, 2018.

[241] D. Caldwell, G. Medrano-Cerda, and M. Goodwin, "Braided pneumatic actuator control of a multi-jointed manipulator," in *IEEE Systems Man and Cybernetics Conference-SMC*, 1993.

[242] I. S. Godage, D. T. Branson, E. Guglielmino, and D. G. Caldwell, "Pneumatic muscle actuated continuum arms: Modelling and experimental assessment," in *IEEE Intl. Conf. on Robotics and Automation*, 2012, pp. 4980–4985.

[243] J. Gray, "The mechanism of locomotion in snakes," *Journal of experimental biology*, 1946.

[244] W. Zhen, C. Gong, and H. Choset, "Modeling rolling gaits of a snake robot," in *IEEE Intl. Conf. on Rob. & Auto. (ICRA)*, 2015, pp. 3741–3746.

[245] Y. Yamauchi, Y. Ambe, H. Nagano, *et al.*, "Development of a continuum robot enhanced with distributed sensors for search and rescue," *ROBOMECH Journal*, vol. 9, no. 1, pp. 1–13, 2022.

[246] D. L. Hu, J. Nirody, T. Scott, and M. J. Shelley, "The mechanics of slithering locomotion," *Proceedings of the National Academy of Sciences*, vol. 106, no. 25, pp. 10 081–10 085, 2009.

[247] C. D. Onal and D. Rus, "Autonomous undulatory serpentine locomotion utilizing body dynamics of a fluidic soft robot," *Bioins. & biom.*, vol. 8, no. 2, p. 026 003, 2013.

[248] M. Luo, M. Agheli, and C. D. Onal, "Theoretical modeling and experimental analysis of a pressure-operated soft robotic snake," *Soft Robotics*, vol. 1, no. 2, pp. 136–146, 2014.

[249] M. Luo, Y. Pan, E. H. Skorina, *et al.*, "Slithering towards autonomy: A self-contained soft robotic snake platform with integrated curvature sensing," *Bioins. & biom.*, 2015.

[250] M. Luo, E. H. Skorina, W. Tao, *et al.*, "Toward modular soft robotics: Proprioceptive curvature sensing and sliding-mode control of soft bidirectional bending modules," *Soft robotics*, 2017.

[251] M. Luo, R. Yan, Z. Wan, *et al.*, "Orisnake: Design, fabrication, and experimental analysis of a 3-d origami snake robot," *IEEE Rob. & Auto. Letters*, vol. 3, no. 3, pp. 1993–1999, 2018.

[252] Z. Wan, Y. Sun, Y. Qin, *et al.*, "Design, analysis, and real-time simulation of a 3d soft robotic snake," *Soft Robotics*, 2022.

[253] D. D. Arachchige, Y. Chen, I. D. Walker, and I. S. Godage, "A novel variable stiffness soft robotic gripper," in *IEEE Intl. Conf. on Auto. Sci. & Eng. (CASE)*, 2021, pp. 2222–2227.

[254] D. D. Arachchige and I. S. Godage, "Hybrid soft robots incorporating soft and stiff elements," in *IEEE Intl. Conf. on Soft Rob. (RoboSoft)*, 2022, pp. 267–272.

[255] Q. Xiao, M. Musa, I. S. Godage, H. Su, and Y. Chen, "Kinematics and Stiffness Modeling of Soft Robot With a Concentric Backbone," *Journal of Mechanisms and Robotics*, 2022.

[256] M. Azizkhani, A. L. Gunderman, I. S. Godage, and Y. Chen, "Dynamic control of soft robotic arm: An experimental study," *IEEE Rob. & Auto. Letters*, vol. 8, no. 4, pp. 1897–1904, 2023.

[257] I. S. Godage, R. J. Webster, and I. D. Walker, "Center-of-gravity-based approach for modeling dynamics of multisection continuum arms," *IEEE Transactions on Robotics*, 2019.

[258] H. B. Gilbert and I. S. Godage, "Validation of an extensible rod model for soft continuum manipulators," in *IEEE Intl. Conf. on Soft Rob. (RoboSoft)*, 2019, pp. 711–716.

[259] H. F. Al-Shuka *et al.*, "Active impedance control of bioinspired motion robotic manipulators: An overview," *Applied bionics & biomechanics*, 2018.

[260] S. K. Talas, B. A. Baydere, T. Altinsoy, C. Tutcu, and E. Samur, "Design and development of a growing pneumatic soft robot," *Soft Robotics*, vol. 7, no. 4, pp. 521–533, 2020.

[261] Y. Sun, A. Abudula, H. Yang, *et al.*, "Soft mobile robots: A review of soft robotic locomotion modes," *Current Rob. Reports*, pp. 1–27, 2021.

[262] X. Huang, K. Kumar, M. K. Jawed, *et al.*, "Chasing biomimetic locomotion speeds: Creating untethered soft robots with shape memory alloy actuators," *Science Robotics*, 2018.

[263] A. D. Marchese, C. D. Onal, and D. Rus, "Autonomous soft robotic fish capable of escape maneuvers using fluidic elastomer actuators," *Soft Robotics*, vol. 1, no. 1, pp. 75–87, 2014.

[264] P. Polygerinos, N. Correll, S. A. Morin, *et al.*, "Soft robotics: Review of fluid-driven intrinsically soft devices; manufacturing, sensing, control, and applications in human-robot interaction," *Advanced Engineering Materials*, vol. 19, no. 12, p. 1 700 016, 2017.

[265] C. Majidi, "Soft robotics: A perspective—current trends and prospects for the future," *Soft Robotics*, vol. 1, no. 1, pp. 5–11, 2014.

[266] J. Deng, B. H. Meng, I. Kanj, and I. S. Godage, "Near-optimal smooth path planning for multisection continuum arms," in *IEEE Intl. Conf. on Soft Rob. (RoboSoft)*, 2019, pp. 416–421.

[267] Y. Chen, L. Wang, K. Galloway, I. Godage, N. Simaan, and E. Barth, "Modal-based kinematics and contact detection of soft robots," *Soft Robotics*, vol. 8, no. 3, pp. 298–309, 2021.

[268] I. S. Godage, D. T. Branson, E. Guglielmino, and D. G. Caldwell, "Path planning for multisection continuum arms," in *IEEE Intl. Conf. on Mechatronics and Automation*, 2012, pp. 1208–1213.

[269] D. W. Marhefka and D. E. Orin, "Simulation of contact using a nonlinear damping model," in *IEEE Intl. Conf. on Rob. & Auto. (ICRA)*, IEEE, vol. 2, 1996, pp. 1662–1668.

[270] B. H. Meng, I. S. Godage, and I. Kanj, "RRT*-based path planning for continuum arms," *IEEE Robotics and Automation Letters*, vol. 7, no. 3, pp. 6830–6837, 2022.

[271] B. H. Meng, I. S. Godage, and I. Kanj, "Smooth path planning for continuum arms," in *IEEE Intl. Conf. on Robotics and Automation (ICRA)*, 2021, pp. 7809–7814.

[272] *Matlab curve fitting toolbox*, www.mathworks.com/help/curvefit/.

[273] X. Wu, X. Shao, and W. Wang, "Stable quadruped walking with the adjustment of the center of gravity," in *IEEE Intl. Conf. on Mechatronics and Automation*, 2013, pp. 1123–1128.

[274] I. S. Godage, R. Wirz, I. D. Walker, and R. J. Webster, "Accurate and efficient dynamics for variable-length continuum arms: A center of gravity approach," *Soft Robotics*, 2015.

[275] C. Kuhn and E. Frey, "Walking like caterpillars, flying like bats—pinniped locomotion," *Palaeob. and Palaeoenvironments*, vol. 92, pp. 197–210, 2012.

[276] A. Iscen, A. Agogino, V. SunSpiral, *et al.*, "Flop and roll: Learning robust goal-directed locomotion for a tensegrity robot," in *IEEE/RSJ Intl. Conf. on Intelligent Rob. & Sys. (IROS)*, 2014.

[277] A. Spröwitz *et al.*, "Towards dynamic trot gait locomotion: Design, control, and experiments with cheetah-cub, a compliant quadruped robot," *Intl. Journal of Robotics Research*, 2013.

[278] M. Luo, W. Tao, F. Chen, T. K. Khuu, S. Ozel, and C. D. Onal, "Design improvements and dynamic characterization on fluidic elastomer actuators for a soft robotic snake," in *IEEE Intl. Conf. on Technologies for Practical Robot Applications (TePRA)*, 2014, pp. 1–6.

[279] M. Luo, Y. Pan, W. Tao, F. Chen, E. H. Skorina, and C. D. Onal, "Refined theoretical modeling of a new-generation pressure-operated soft snake," in *Intl. Design Eng. Tech. Conference & Computers & Info. in Eng. Conference*, American Society of Mechanical Engineers, 2015.

[280] Y. Qin, Z. Wan, Y. Sun, E. H. Skorina, M. Luo, and C. D. Onal, "Design, fabrication and experimental analysis of a 3-d soft robotic snake," in *IEEE Intl. Conf. on Soft Robotics (RoboSoft)*, 2018, pp. 77–82.

[281] E. Coumans and Y. Bai, *Pybullet, a python module for physics simulation for games, robotics and machine learning*, http://pybullet.org, 2021.

[282] E. Coumans and Y. Bai, *Pybullet quickstart guide*, https://pybullet.org/wordpress/index.php/forum-2/, 2021.

[283] I. S. Godage, Y. Chen, and I. D. Walker, "Dynamic control of pneumatic muscle actuators," *arXiv preprint arXiv:1811.04991*, 2018.

[284] D. D. Arachchige, D. M. Perera, H. Umer, I. Kanj, and I. S. Godage, "Soft robotic snake locomotion on curved surfaces," *Journal of Soft Robotics (SoRo)*, 2024, [In review].

[285] D. D. Arachchige, H. Umer, I. Kanj, and I. S. Godage, "Application of closed-loop control for energy-efficient locomotion in soft robotic snakes," in *IEEE Intl. Conf. on Robotics and Automation (ICRA)*, [In preperation], 2025.

[286] D. D. Arachchige, H. Umer, I. Kanj, and I. S. Godage, "Closed-loop control of soft quadrupedal robots for discontinuous gaits," in *IEEE Intl. Conf. on Robotics and Automation (ICRA)*, [In preperation], 2025.